Dominic Zerulla

Spektroskopie molekularer Eigenschaften an Grenzflächen

Habilitationsschrift

Heinrich-Heine-Universität Düsseldorf

Inhaltsverzeichnis

1

Einleitung

Diese Habilitationsschrift faßt zwei verschiedene Themen zur Spektroskopie molekularer Eigenschaften an Grenzflächen zusammen. Beiden ist gemeinsam, daß angeregt durch Photonen Informationen über molekulare Eigenschaften oberflächenempfindlich abgefragt werden können.
Ein Ziel ist es dabei, die Eigenschaften geringer Mengen von Molekülen zu erfassen.

Im Grenzfall sind dies kleine Cluster oder sogar Einzelmoleküle. Ein weiteres Ziel von besonderem Interesse ist die Untersuchung molekularer Mechanismen auf Oberflächen. Letzteres ist zum Beispiel für katalytische Untersuchungen, biologische Prozesse an Membranen oder physikalische Grundlagenforschung von Bedeutung.

Die im Rahmen dieser Schrift verwendeten Methoden lassen sich im wesentlichen in zwei Klassen einteilen:

1. Photoelektronenspektroskopie und Nahstruktur der Röntgenabsorptionskanten,
2. Anregung und strahlender Zerfall von Oberflächen-Plasmon-Polaritonen.

Der ersten Klasse von Methoden ist gemeinsam, daß für ihre Anwendung Ultrahochvakuum (UHV) benötigt wird und sich die besten Ergebnisse an Synchrotronspeicherringen erzielen lassen[1]. Die Notwendigkeit im Vakuum zu arbeiten, erlaubt die Untersuchung nahezu perfekter Oberflächen mit geradezu modellhaftem Charakter. Sie schränkt auf der anderen Seite jedoch auch die mit diesen Methoden analysierbaren Systeme ein. Hier ist insbesondere die Relevanz und Übertragbarkeit der unter UHV-Bedingungen gemachten Messungen zu beachten. Beipielsweise zeigen Messungen unter UHV Bedingungen von katalytischen Systemen eine, wenn auch beschränkte, Übertragbarkeit auf technische Prozesse, während biologisch relevante Systeme unter diesen Bedingungen zerstört werden.
Die zweite Klasse der aufgeführten Methoden nutzt die Anregung von Oberflächenplasmonen Polaritonen (Surface Plasmon Polaritons, SPP's) durch Photonen. Hierbei muss erwähnt werden, daß die Anregung von SPP's mit Photonen ausserordentlichen Einschränkungen unterliegt: Eine Anregung eines SPP's in einem dünnen Metallfilm kann nicht durch direkte Bestrahlung mit Licht erzielt werden. Dieses wird besonders deutlich bei der Betrachtung der Dispersionsrelationen von Licht (Lichtgerade) und Oberflächenplasmonen, die keinen gemeinsamen Schnittpunkt aufweisen. Um eine Anregung trotzdem bewerkstelligen zu können, muss ein zusätzlicher **k**-Vektor parallel zur Oberfläche erzeugt bzw. der existente vergrössert werden. Eine Möglichkeit, speziell für glatte Metalloberflächen, ist die Verwendung einer ATR Konfiguration nach Räther-Kretschmann oder Otto. In beiden Techniken wird das Licht nicht direkt in die Metalloberfläche eingekoppelt, sondern unter Verwendung

---

[1] Es sei angemerkt, daß sich Photoelektronen Spektroskopie im Labormaßstab durchführen lässt, sich aber durch die am Synchrotronring nahezu frei wählbare Photonenenergie zusätzliche Möglichkeiten ergeben.

eines Prismas. Durch die höhere optische Dichte des Prismas kann nun die $k_{\|}$-Komponente erhöht werden und ein SPP angeregt werden. Die zweite Möglichkeit nutzt die Einkopplung an einer rauhen oder gezielt nanostrukturierten gitterartigen Oberfläche. Hierbei kann ein Pseudoimpuls, der von der Periodizität der Oberflächenstruktur herrührt genutzt werden, um die $k_{\|}$-Komponente zu vergrößern. Die additiven $k_{\|}$-Komponenten entsprechen hierbei den reziproken Gitterkonstanten der Oberflächenstruktur oder in anderen Worten deren Fourier-Komponenten.

Der Informationsgewinn durch SPP-Anregung kann direkt durch Bestimmung der benötigten Anregungsbedingungen erfolgen. Diese sind äußerst empfindlich gegenüber der Änderung der lokalen optischen Konstanten an der Grenzfläche und ermöglichen daher die Detektion von Molekülen in submonolagen Bedeckungen und der zeitlichen Verfolgung der entsprechenden Adsorptionskinetik. Indirekt kann die Anregung von SPP's aber auch dazu dienen, eine höhere Oberflächenempfindlichkeit für andere spektroskopische Techniken, insbesondere Raman- und Fluoreszenz-Spektroskopie, zur Verfügung zu stellen. Hierbei wird das SPP genutzt, ein extrem starkes, elektromagnetisches Nahfeld zu erzeugen. Bringt man Moleküle in dieses Feld, so werden diese intensiv angeregt. Daraus resultiert eine verstärkte Re-Emission. Hierdurch ergeben sich oberflächenempfindliche Varianten der bekannten Techniken.

Eine besondere Erwähnung verdient die Entwicklung von adaptiven Strukturen (sogenannten "Tuneable Quantum Wires for Plasmonic Excitation"), einem neuartigen Sensor, der die schnelle Veränderung seiner Oberflächenperiodizität erlaubt. Dieser ermöglicht für verschiedene Anregungswellenlängen eine Plasmonenanregung, ohne dabei den optischen Aufbau verändern zu müssen. Ein solcher Sensor ermöglicht beispielsweise kontinuierliche SPP-Anregung bei Durchstimmung der Anregungswellenlänge über große Bereiche, eine Eigenschaft, die zu völlig neuartigen spektroskopischen Methodiken führen wird. Weiterhin ist die Erzeugung von Nanostrukturen zur gezielten Veränderung des SPP Nahfelds Thema dieser Arbeit. Neben Aspekten der Grundlagenforschung werden auch die Theorie und Experimente von Oberflächenplasmonen auf ultraschnellen Zeitskalen behandelt.

Für die Evaluierung der zum zum Teil nanoskaligen Strukturen standen bei allen Untersuchungen hochauflösende, bildgebende Verfahren zur Verfügung. Zu diesen Verfahren gehören unter anderem die Rastertunnel- (STM) und die Rasterelektronen-Mikroskopie (REM) sowie die Rasterkraftmikroskopie (AFM). Im folgenden werden die auf den oben benannten Gebieten gemachten Ergebnisse zusammengefasst und erläutert.

2

Spektroskopievarianten im weichen Röntgenbereich zur Untersuchung von selbstassemblierenden organischen Systemen

Ein System, das sich zu Untersuchungen unter UHV-Bedingungen eignet, sind Self-Assembling Monolayers (SAM's). Diese zeigen als hervorstechende Eigenschaft ein hohes Maß an Selbstorganisation bei Adsorption an geeigneten Oberflächen. Sie können im allgemeinen aus Lösungen heraus präpariert aber auch im UHV verdampft werden. Ihre Präparation setzt nicht die Benutzung einer Filmwaage nach Langmuir-Blodget voraus. Die hier gemachten Untersuchungen basieren im Gegensatz zum Gros der internationalen Veröffentlichungen nicht ausschließlich auf dem Substrat Gold (oder vergleichbaren Münzmetallen), sondern wurden auf technologisch relevanteren III-V Halbleitersubstraten durchgeführt. III-V Halbleiter spielen aufgrund ihrer Bandstruktur z.B. eine wichtige Rolle in der Optoelektronik und bei dem Design schneller Oszillatoren. Eine strukturierte Monolage eines SAM's kann hier z.B. als Ätzmaske für hochdefinierte Strukturen (Größenordnung 10 nm) oder zur gezielten Immobilisierung von Antennenkomplexen genutzt werden. Als organische selbstassemblierende Moleküle wurde die Klasse der Alkanthiole ausgewählt, die sowohl in verschiedenen Längen als auch mit verschiedenen terminalen Funktionsgruppen erhältlich sind.

2.1 Struktur und Eigenschaften von selbstassemblierten Alkanthiolen auf III-V Halbleitern

Im Rahmen der gemachten Untersuchungen konnte festgestellt werden, daß Alkanthiole auf III-V (110)-Spaltflächen als Monolagen mit maximaler Dichte adsorbieren [1-3]. Weiterhin wurde gefunden, daß die länglichen Moleküle, analog zu den Untersuchungen auf Gold mit einem definierten Kippwinkel zur Substratoberfläche assemblieren. Die gefundenen Werte sind 32° für InP (110) und 15° für GaP (110)-Substrate [1, 3-4]. Die Winkel sind ein Resultat des Bestrebens der Moleküle, eine energieminimierte, dichteste Packung einzunehmen, wobei zusätzlich noch der Effekt der gezahnten all-trans konfigurierten Alkylketten zu beachten ist (sogenanntes: in-registry). Letztlich konnte unter Benutzung von X-ray Absorption Near Edge Structure (XANES) Spektroskopie, Soft X-ray Photoelectronspectroscopy (SXPS), X-ray Photoelectronspectroscopy Diffraction (XPD), Infrarotspektroskopie, Rastertunnelmikroskopie (STM), Elektrochemie und Dichtefunktional-Theorie (DFT) Rechnungen die vollständige innere Struktur der organischen Monolagen auf InP aufgeklärt werden [4-6]. Hierbei zeigte sich eine einzigartige, auf Metallen nicht gefundene, Eindomänen-Struktur der Alkanthiole auf III-V-Halbleitern [5]. Diese ist ein Resultat der von den "Dangling Bonds" der III-V Spaltflächen vorgegebenen Richtung, die auf Metallen so nicht vorhanden ist. Als Resultat findet man eine extrem hohe Ordnung der Monolagen mit einer Projektion der Ketten in eine der kristallographischen Hauptachsen des Halbleitersubstrats.[1, 3-5]

Zusätzlich zu der Struktur der Systeme wurde auch die Natur der Bindung zwischen dem organischen SAM und dem Halbleitersubstrat untersucht. Hierbei wurde die chemische Intuition bestätigt, daß die Bindung zwischen dem Schwefel der Thiolgruppe, nach Abspaltung eines Wasserstoff-Atoms, und allen Indium Atomen an der Spaltoberfläche geschieht [1, 5]. Hierbei wird die Oberflächen-Relaxation der InP und GaP Spaltflächen zum Großteil wieder aufgehoben. Im Zuge dieser Messungen wurde auch die konzentrationsabhängige Kinetik der Assemblierung bestimmt. Weiterhin konnten Selbstreinungseffekte der Thiol-Assemblierung beobachtet werden [2]. Diese ermöglichen letztlich die erfolgreiche Assemblierung einer reinen Alkanthiol-Monolage auf einer chemisch wenig inerten III-V Halbleiter-Spaltfläche aus einer Lösung heraus. Hierbei werden andere organische Moleküle von den III-V-Oberflächen von der energetisch günstigeren Thioladsorption verdrängt.

In diesem Rahmen wurde auch die Strukturierbarkeit solcher Filme untersucht.

Hierzu wurden drei verschiedene Verfahren, namentlich Röntgenlithographie, Elektronenstrahllithographie und Strukturierung durch Spannungspulse eines STMs, angewendet. Hierbei zeigte sich prinzipiell die Möglichkeit, insbesondere mit dem STM, Strukturbreiten in der Größenordnung von wenigen nm realisieren zu können [1]. Eine Untersuchung der Stellen mittels Rastertunnelspektroskopie (STS) und lateral hochauflösender Auger-Spektroskopie (AES), bei denen die organischen Moleküle entfernt wurden, ergab allerdings, daß selbige nicht vollständig frei waren. Es zeigte sich insbesondere bei Bestrahlung mit ionisierender Strahlung, daß sich neben der Ablösung von Molekülen eine chemische Veränderung der verbliebenden Moleküle nachweisen ließ. Die chemische Natur dieser strahlengeschädigten Spezies wird immer noch in der wissenschaftlichen Gemeinschaft diskutiert. Wir haben zu diesem Thema zeit- und dosisabhängige XPS Spektren veröffentlicht, die die Rate der Schädigung klar beschreiben [6]. Weiterhin haben wir die begründete Vermutung geäußert, es handele sich bei der neuen Spezies entweder um ein Disulphid oder einen Thioether (Dialkyl). Außerdem haben wir Vorschläge unterbreitet, diese Spezies von den Spaltoberflächen zu entfernen. Hierbei wurden elektrochemische Verfahren und thermische Verfahren getestet. Letztere können sogar in einem begrenzten Rahmen die strahlengeschädigte Spezies wieder zu einem Alkanthiol zurückwandeln und den Anteil der verbliebenen strahlengeschädigte Spezies von der Oberfläche entfernen. Elektrochemische Verfahren sind hingegen bestens geeignet die bestrahlten Bereiche zu reinigen und so das System weiteren Bearbeitungsschritten im Sinne der Erzeugung eines “Devices” zuzuführen.

2.2 Die Struktur von aromatischen Verbindungen auf Halbleiteroberflächen

Die bis hierher vorgestellten Untersuchungen begnügten sich mit der Untersuchung von verhältnismässig kleinen Molekülen. In Richtung der Untersuchung größerer und komplexerer Moleküle wurden die Alkanthiole durch sogenannte Mercaptobenzothiazole ersetzt. Diese verfügen über zwei Ringsysteme und zwei potentielle Schwefel-Bindungsstellen zum Substrat. Mercaptobenzothiazole werden in der Technik, z.B. als Flotationsmittel in der Erzgewinnung eingesetzt. Als Substrat wurde zusätzlich zu den bereits geschilderten Halbleitern, das optoelektronisch interessante CdS eingesetzt, speziell dessen CdS $(10\bar{1}0)$-Oberfläche [7].
Es konnte der Nachweis erbracht werden, daß auch diese Spezies auf den Halbleitersubstraten, unter Deprotonierung des Stickstoffatoms, chemisorbiert. Weiterhin konnte mit bereits oben erwähnten Methoden festgestellt werden, daß die Moleküle unter einem bestimmten Kippwinkel aufrecht auf der Oberfläche stehen. Die vom planaren Molekül aufgespannte Ebene kommt hierbei parallel zur $[\bar{1}2\bar{1}0]$- Richtung des CdS Einkristalls zu liegen [7].
Nach einer Oberflächenreaktion, die durch die photochemische Erzeugung von Elektronen-Loch-Paaren im Halbleitersubstrat ausgelöst wird, kann an der Oberfläche als Reaktionsprodukt Bis-(2-benzothiazolyl)disufid (BBTD) nachgewiesen werden. Zur Erklärung dieses Effektes wurde ein Modell entwickelt, das die gefundene Reaktion durch lichtinduzierte Ladungserzeugung in dem Halbleiter und den nachfolgenden Transport der Ladung entlang der Grenzfläche erklärt [7].

Im Sinne einer Steigerung der Komplexität der untersuchten Moleküle wurden nachfolgend erfolgreich Alkanthiole durch Aminosäuren ersetzt, die die Grundbausteine von Peptiden oder sogar Proteinen darstellen. Diese konnten ebenfalls erfolgreich auf Halbleiteroberflächen adsorbiert werden, obschon diese einen nicht so hohen Ordnungsgrad wie die Alkanthiole zeigen.

Proteine sind Kernbausteine in praktisch allen wichtigen Funktionen des menschlichen Körpers. Nahezu alle molekularen Transformationen, die den zellulären Metabolismus definieren, werden durch Proteine vermittelt. Proteine haben regulative Funktionen, senden Informationen an andere Zellkomponenten und kontrollieren intra- und extrazelluläre Funktionen (z.B. Enzyme und Antikörper). Weiterhin bilden sie die essentiellen strukturellen Komponenten in Zellen (z.B. Keratine). Der Träger von Information und Funktion ist in allen Fällen die Struktur der jeweiligen Proteine. Diese ist bei den meisten Peptiden oder Proteinen jedoch nur in wässriger Lösung stabil und verändert sich instantan wenn die Moleküle aus dieser Umgebung entfernt werden.

Die bisher hier vorgestellten Untersuchungsmethoden sind zur Bestimmung von biologischen Mechanismen daher ungeeignet. Da die Konzentration einer bestimmten Spezies von Biomolekülen in vivo zudem noch sehr gering ist, sollte die Methode biokompatibel, (oberflächen)empfindlich und nicht destruktiv sein. Des weiteren sollte auf aufwendige Markierung der Moleküle mit z.B. fluoreszenten Fremdmolekülen verzichtet werden können. Eine Technik, die alle geforderten Parameter in sich vereinigt, konnte nicht gefunden werden. So galt es eine neue Methode zu entwickeln.

3

Oberflächen-Plasmon-Polaritonen

Oberflächen Plasmon-Polaritonen zeigen bereits einige der geforderten Eigenschaften - z.B. eine erhöhte Oberflächenempfindlichkeit und ihre Einsetzbarkeit an der Grenzfläche zu einer wässrigen Lösung. SPP's sind Quasiteilchen und können als "mixed state" zwischen Nahfeld-Photonen und einer entlang der Grenzfläche propagierenden Elektronendichtewelle beschrieben werden. Hierbei kann, wie an späterer Stelle noch gezeigt werden wird, das SPP direkt mit z.B. an der Grenzfläche adsorbierten Molekülen wechselwirken.

3.1 Anregungsbedingungen

Eine Anregung von SPP's mit Licht anstelle von Elektronen bedarf besonderer Voraussetzungen. Vergleicht man die Dispersionsrelation von Oberflächenplasmonen mit der Kombination der möglichen $E/k_{\|}$ Werte für Licht in Vakuum (Lichtgerade), so muss festgestellt werden, daß keine Schnittpunkte der beiden Relationen existieren. Dies bedeutet, daß unter Energie- und Impulserhaltung keine Anregung von SPP's durch Licht direkt möglich ist. Trotzdem stehen zwei Techniken für die Anregung eines SPP's mit Hilfe von Photonen zur Verfügung. Diese kann erstens auf glatten Metallfilmen durch Einkopplung der Photonen aus einem optisch dichteren Medium erfolgen. Hierfür wird ein optischer Aufbau in ATR (attenuated total reflection) Konfiguration benötigt, wobei das Licht im allgemeinen durch ein Prisma eingekoppelt wird [8, 9]. Zweitens kann auf strukturierten Metallsubstraten ein Pseudoimpuls aus der reziproken Gitterkonstante genutzt werden, um die Anregungsbedingungen zu erfüllen [10, 11]. Dies wird insbesondere in der folgenden, vereinfachten Gleichung verdeutlicht:

$$\frac{\omega}{c}\sin(\alpha_{inc}) + l\frac{2\pi}{d} \overset{!}{=} \frac{\omega}{c}\sqrt{\frac{\epsilon_m}{\epsilon_m + 1}} \tag{3.1}$$

mit ϵ_m als dem Realteil der optischen Konstante, c der Vakuumgeschwindigkeit des Lichts, α_{inc} dem Einfallswinkel, ω der Kreisfrequenz und l der Diffraktionsordnung der periodischen Struktur.
Die benötigten Periodizitäten für Licht im sichtbaren Bereich liegen hierbei im mesoskaligen Bereich einiger hundert nm bis zu 2 μm. Beide Techniken werden in den folgenden Untersuchungen herangezogen.

3.2 Kohärenz und Kausalität von SPP vermittelten Prozessen

Zuerst sollte das Emissionsverhalten von Molekülen untersucht werden, die sich im Nahfeld eines SPP's befinden. Hierbei können prinzipiell elastische Streuung aber auch ineleastische Prozesse (Raman Streuung, Fluoreszenz) der Moleküle beobachtet werden.
In Abwesenheit von Streuung sollte die durch Licht erzeugte Elektronendichtewelle (SPP) unter Umkehrung der Anregungsbedingungen nach der mittleren Lebensdauer des SPP's wieder kohärent als Licht abgestrahlt werden. Diese Kohärenz bedingt in diesem Fall, daß die Einfallsebene des Lichtes und der Einkopplungswinkel relativ zur Oberflächennormalen erhalten bleiben.
Setzt man nun Streuung in dem dünnen Metallfilm voraus (z.B. an Rauheit), so geht ein Teil der Kohärenz verloren. Während der Winkel zur Oberflächennormalen weiterhin erhalten bleibt, da er unmittelbar in die An- und Abregungsbedingungen der Oberflächenplasmonen einfließt, geht die Information über die ursprüngliche

Einfallsebene verloren. Das wieder abgestrahlte Licht liegt daher auf einem Kegel mit einem Öffnungswinkel des ursprünglichen Anregungswinkels. Dieser Kegel wird ATR-Kegel genannt. Untersucht man nun die Polarisation des in diesen Kegel emittierten Lichtes, so mißt man linear polarisiertes Licht, das immer senkrecht auf dem Kegelrand liegt. Dieses Verhalten läßt unmittelbar den Rückschluß auf die Herkunft des Prozesses als Streuung der Elektronendichtewelle an dem dünnen Metallfilm zu [12].

Bringt man nun Moleküle in das Nahfeld dieses SPP's, so werden diese durch das Feld angeregt. Uns hatte sich an dieser Stelle die Frage gestellt: Ist die nun erfolgende, im allgemeinen rotverschobene, Re-emisssion der Moleküle noch kohärent zu den ursprünglichen Anregungsbedingungen? Oder handelt es sich hierbei um einen losgelösten Prozeß? Zu untersuchen war also die Kausalität der Transferkette von der Erzeugung eines SPP's bis zur Fluoreszenz oder Stokes-Raman-Emission der Moleküle im Nahfeld [12-13]. Hierzu wurde die räumliche Verteilung des frequenzverschobenen Lichtes untersucht. Das Ergebnis unterstreicht die Kohärenz des Gesamtvorgangs. Das monochromatische Anregungslicht wird unter einem Winkel α_{inc} auf der Prismenseite eingekoppelt, um an der abgewandten Metalloberfläche ein SPP auszulösen. Im Nahfeld dieses SPP's werden fluoreszente Moleküle immobilisiert. Diese werden von dem starken SPP-Nahfeld angeregt und emittieren daher ihrerseits rotverschobenes Licht. Dieses Licht wird nun aber nicht als Resultat der ungeordneten Lage der Moleküle auf diese Seite des Metallfilms semi-isotrop abgestrahlt, sondern auf der ursprünglichen Anregungsseite des SPP's. Die Emission erfolgt auch nicht unter dem vorherigen Anregungswinkel des SPP's, sondern unter einem Winkel der der Anregung des SPP's unter der neuen rotverschobenen Wellenlänge entspräche. Der Gesamtvorgang lässt sich also, trotz der Umweges über die Anregung von Farbstoffmolekülen, als kohärenter, stets den SPP-Bedingungen genügender Prozeß beschreiben [12-14]. Allerdings ist Vorsicht geboten, da die in der Ereigniskette liegende Fluoreszenz vibronische Relaxationen in ihren internen Mechanismen enthält. Diese sind im allgemeinen nicht kohärenz-erhaltend. Es ist daher auch denkbar, daß es sich um zwei getrennte Prozesse handelt. Der erste ist kohärent bis zur Anregung des Farbstoffmoleküls. Der zweite dieser Anregung folgende, rotverschobene Emissionsprozeß ist nicht im strengen Sinne kohärent, muss aber, um in ein SPP einzukoppeln, wieder dessen Anregungsbedingungen genügen. Die hohe Effizienz dieses Prozesses ließe sich durch die nur relativ geringe Frequenzverschiebung gegenüber dem bereits angeregten SPP erklären (Resonanz).

Die Kenntnis der Polarisation und der Abstrahlungsbedingungen von unter SPP Bedingungen angeregten Molekülen ist hierbei wichtig, um optimale Bedingungen für die Nutzung eines solchen Systems als Sensor zu gewährleisten. So kann z.B. die Unterdrückung des unerwünschten elastischen Streulichtes durch einfache Maßnahmen wie Aperturen und Polarisationsfilter erfolgen. Dieses ist insbesondere für die Kopplung von SPP-Anregung und Raman-Spektroskopie von entscheidender Bedeutung.

Angeregt durch eine Kooperation mit der Physikalischen Biologie (Prof. D. Riesner) der HHUD sollten die konformellen Änderungen von Proteinen in Membranen durch Raman-Spektroskopie untersucht werden. Hierbei waren vor allem die geringen Ramanstreuquerschnitte im Zusammenhang mit den niedrigen Konzentrationen von Proteinen in Membranen zu überwinden. Weiterhin galt es aus der Vielzahl der molekularen Vibrationen von Makromolekülen die gewünschten Informationen zu extrahieren. Die Methodik der Wahl war deshalb eine Kombination von SPP angeregter UV-Resonanz-Raman Spektroskopie. Die Anregung eines Oberflächenplasmons sollte hierbei die Oberflächenempfindlichkeit der Methode erhöhen. Hierbei war es wichtig die Abklinglängen des SPP's so zu wählen, daß ein vollständiges System aus biologischer Membran und adsorbierten/inkorporierten Proteinen gemessen werden konnte. Ein “first-layer” Effekt wie bei Surface Enhanced Raman

Scattering (SERS) konnte daher nicht genutzt werden, sondern ausschliesslich die elektromagnetische Komponente des SPP's. Weiterhin sollte durch elektronische Resonanzeffekte sowohl eine weitere Steigerung der Empfindlichkeit der Technik aber auch eine hohe Selektivität erreicht werden. Hierzu mußte eine Absorptionsbande gefunden werden, die unabhängig von der Art des Proteins ein indirekter Träger der Konformationseigenschaften ist. Diese wurde in der Absorption der Peptidbindung gefunden, die eine breite Absorptionsbande zwischen 180 nm und 240 nm mit einem Maximum nahe 190 nm zeigt. Um eine Dauerstrich-Laserquelle in diesem Bereich zu erzeugen, wurde die 413 nm Linie eines Kryptonlasers durch einen Ringlaser mit BBO-Kristall auf 206.5 nm verdoppelt. Außerdem steht seit neuestem der abstimmbare, frequenzvervierfachte Ausgang eines gepulsten (ns), Nd-YAG gepumpten Farbstofflasers mit Wellenlängen zwischen der atmosphärischen Absorption bei 198 nm und 240 nm zur Verfügung. Weiterhin wurde ein Echelle-Spektrometer in der 27. Ordnung und einer "Intensivierten CCD Kamera" (ICCD) mit "Advanced Solar Blind"-Photokathode zur Detektion verwendet. Um ein SPP bei diesen Wellenlängen anregen zu können, musste anstelle des üblicherweise verwendeten Silberfilms auf Aluminium gewechselt werden, da die Plasmafrequenz von Silber nicht hoch genug für die Anregung eines SPP's bei diesen Wellenlängen ist. Simulationen und Messungen mit den optimalen Aluminiumfilm- und Passivierungsdicken bei einer Anregung mit 514.5 nm ergaben eine Dicke von 20 nm für das Aluminium bei 47° Einfallswinkel. Der Verstärkungsfaktor des ATR-SPP-Aufbaus bei diesen Parametern betrug 28 [14]. Neuere Simulationen bei 206.5 nm zeigen eine optimale Schichtdicke von 15 nm Al und 2 nm Al_2O_3 bei höheren Einfallswinkeln. Weiterhin konnten Ramanspektren von Testsystemen bei Anregung mit 206.5 nm aufgenommen werden und zusätzlich die Ortsauflösung durch Kopplung an ein rasterndes Raman Mikroskop demonstriert werden [14].

Ein Nachteil der Anregung von SPP's auf glatten Filmen ist, daß die Informationen in Form von inelastisch gestreutem Licht über einen großen Winkelbereich gestreut werden. Speziell bei Anregung im UV-Bereich erreichen die halben Öffnungswinkel der emittierten ATR - Koni Werte zwischen 60° und 80°. Eine Optik zur Erfassung dieser Streustrahlung muss daher volle Akzeptanzwinkel von 120° bis 160° verarbeiten können. Da außerdem auch noch ein Prisma zur Anregung benötigt wird und ein Laserstrahl in einem definierten Winkel auf die Oberfläche gebracht werden muss (d.h. ein gewisser Mindestabstand zur fokalen Ebene wird benötigt), verfügen im UV selbst hochspezialisierte Mikroskopobjektive nicht über eine solche Numerische Apertur.

3.3 Abstimmbare Mesoskalige Strukturen

Eine Lösung dieser Problematik bietet der Wechsel von glatten zu periodisch strukturierten Metalloberflächen an. Hierbei ermöglicht, wie in Gleichung (1.1) gezeigt, ein zusätzlicher k-Vektor von der reziproken Gitterkonstante der periodischen Struktur die Anregung eines SPP's ohne den Umweg über eine ATR-Konfiguration. Durch geeignete Wahl der Periodizität können für festgelegte Wellenlängen auch Winkel nahe an der Oberflächennormalen gewählt werden. Strukturen dieser Art lassen sich hochpräzise durch Elektronenstrahllithographie auf verschiedenen Substraten (z.B. Silizium) erzeugen und anschließend mit dem gewünschten Metallfilm beschichten. Der Nachteil solcher Strukturen ist ihr hoher Preis und ihre geringe Flexibilität. Für einen gegebenen Einfallswinkel kann eine solche Struktur nur für eine einzige Wellenlänge ein SPP anregen. Um hier Abhilfe zu schaffen, haben wir abstimmbare mesoskalige Strukturen (Tuneable Mesoscale Structures) zur Anregung von Oberflächenplasmonen entwickelt [15-16]. Die besagten Strukturen verfügen über die Fähigkeit ihre Periodizität und damit auch den zusätzlichen Quasi-Impuls präzise

und über einen großen Bereich zu verändern.
Im folgenden wird kurz auf ihre Herstellung eingegangen:
Begonnen wird mit einem flexiblen Polymer, dessen Härte chemisch einstellbar ist: Polydimethylsiloxan (PDMS). Dieses wird durch spincoaten zu einem ca. 1 mm dicken Film verarbeitet. Anschließend wird dieser Film in einer mechanischen Streckvorrichtung um z.B. 50% seiner Gesamtlänge gedehnt und in dieser in ein Hochvakuum eingeschleust. Im Vakuum wird die Oberfläche danach mit Argon-Ionen bestrahlt. Diese erzeugen Bindungsaufbrüche aber auch ein neuvernetzen der Bindungen (Crosslinking). Nach dem Ausschleusen wird der Film aus der Spannvorrichtung genommen. Hierbei zieht sich das Polymersubstrat wieder zusammen, die ionenbestrahlte Oberfläche hat diese Fähigkeit jedoch verloren. Hieraus resultiert ein näherungsweise sinusförmiges Oberflächenprofil. Durch spezielle Beschichtungstechniken wird ein dickenmodulierter Metallfilm (Al, Ag, Au, Pt) aufgebracht. Wird nun das Substrat senkrecht zu den "Rillen" gestreckt, so bricht der Metallfilm entlang der dünnsten Linien auf. Als Resultat erhält man Metalldrähte, deren Abstände sich durch einfache mechanische Faktoren schnell und reproduzierbar einstellen lassen. Es entsteht also eine Struktur deren Periodizität (speziell im Hinblick auf die Modulation der optischen Konstanten) veränderbar ist. Ein solches System zeigt exemplarisch die Abbildung 1 in seiner ungestreckten (a) und um 20% gestreckten Form (b).

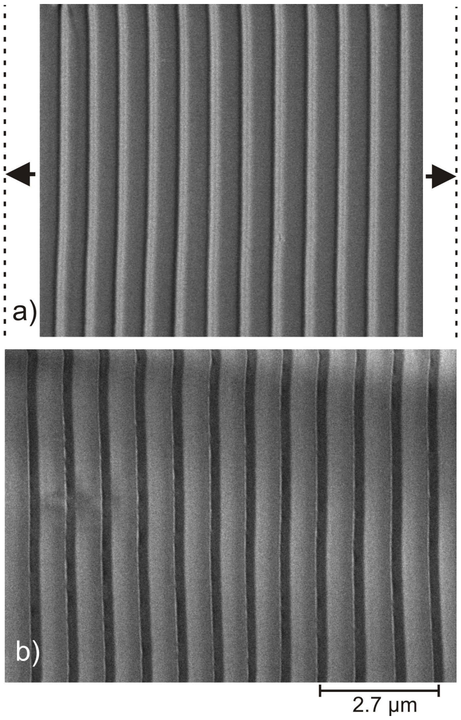

Abbildung 3.1. Rasterelektronenaufnahmen einer mit durchschnittlich 50 nm Silber beschichteten, periodischen Polymerstruktur a) ungestreckt, Periodizität 750 nm; b) 20 % gestreckt, Periodizität 900 nm.

Wir konnten nachweisen, daß solche Strukturen zur Anregung von Plasmonen geeignet sind [15-16]. Da die Periodizität um bis zu 50% variiert werden kann, gelingt das Anregen von SPP's z.B. in einem Bereich von 400 nm bis 600 nm ohne eine Veränderung des optischen Aufbaus. Offensichtlich ist eine solche Struktur zur Verwendung als selektiver Sensor besonders geeignet [17]. Erstmals ist es möglich eine kontinuierliche SPP Anregung bei Variation der Anregungswellenlänge über große Bereiche zu bekommen. Diese Systeme ermöglichen aber auch den Blick auf fundamentale Eigenschaften von Oberflächenplasmonen. Nicht nur lassen sich für jede Einfallswinkel/Wellenlängen Kombination, im Bereich der Abstimmbarkeit des Systems, SPP's anregen, sondern vor allem lassen sich fundamentale Eigenschaften von SPP's wie z.B. deren Propagationsgeschwindigkeit (Gruppengeschwindigkeit) und Abklinglängen bzw. -zeiten einstellen. Im folgenden werden die speziellen Eigenschaften abstimmbarer Systeme kurz beleuchtet. Zuerst sollte der Nachweis der Plasmonenanregung auf solchen Strukturen erbracht werden. Hierzu können beispielsweise winkelabhängige Reflektivitätsmessungen genutzt werden. Um echte SPP Anregung von anderen Verlustprozeßen unterscheiden zu können, vergleicht man Messungen mit s-polarisierter mit Messungen mit p-polarisierter Anregung. S-polarisiertes Licht (senkrecht zur Einfallsebene) kann die im wesentlichen longitudinale Elektronendichtewelle nicht anregen.

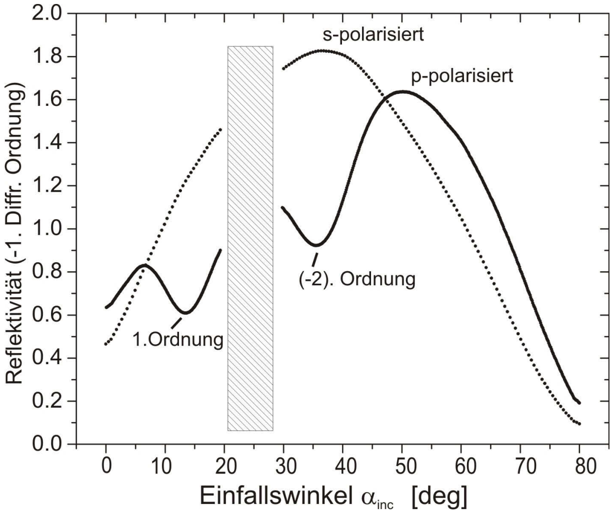

Abbildung 3.2. Messung der Reflektivität in der -1. Diffraktionsordnung gegen den Einfallswinkel α_{inc} für s- und p-polarisiertes Licht. Gitterkonstante ist konstant 780 nm. Der experimentelle Aufbau erlaubt aus geometrischen Gründen keine Messungen im schraffierten Bereich.

Abbildung 3.2 zeigt dabei nicht nur ein Minimum, das eindeutig die Anregung eines SPP's darstellt, sondern gleich derer zwei. Die entsprechende Erklärung findet man besonders anschaulich in Abbildung 3.3. Es handelt sich um eine Anregung in erster und eine Anregung in minus zweiter Ordnung. Die Ordnung l bezieht sich hier auf lk_G. Es sei angemerkt, daß sich in beiden Anregungen Plasmonen mit k_{SPP} bilden, allerdings mit verschiedenen Vorzeichen. Dies bedeutet, daß die beiden Plasmonen in entgegengesetzte Richtungen (antiparallel) propagieren. Je nach gewählter Gitterkonstante und gewünschter Wellenlänge können auch SPP Anregungen für höhere l nachgewiesen werden.

Im Folgenden soll die Abstimmbarkeit der vorgestellten Systeme demonstriert werden. Zu diesem Zweck werden Messungen für verschiedene Streckungen angefertigt, die die Lage der Minima abhängig von der realen Gitterkonstante bestimmen. Ein Beispiel für eine Serie solcher Messungen zeigt Abbildung 3.4.

Mit steigender Periodizität (Streckung) verschieben sich die Minima, bei einem Plasmon der ersten Ordnung zu größeren Einfallswinkeln, bei einem Plasmon der minus zweiten Ordnung zu kleineren Einfallswinkeln. Dieses Verhalten belegt im übrigen auch die in Abbildung 3.3 postulierten Anregungsmechanismen für die ge-

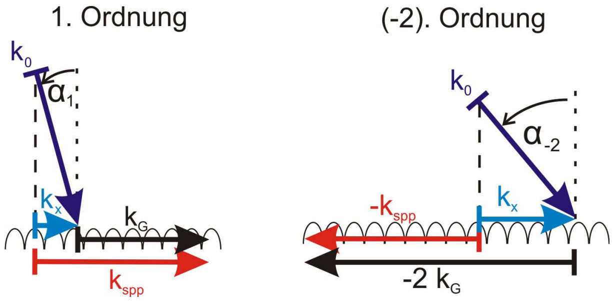

Abbildung 3.3. k-Vektor Diagramm zur Erklärung der gefundenen SPP Anregung: 1. Ordnung (links) und -2. Ordnung (rechts).

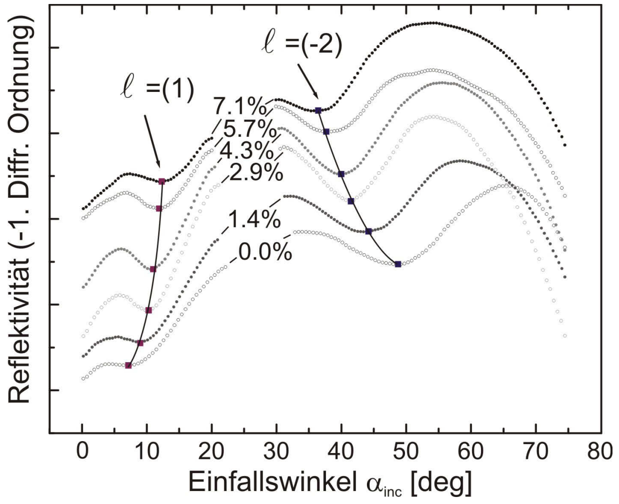

Abbildung 3.4. Serie zur Demonstration der Abstimmbarkeit der SPP Anregung für sechs verschiedene Streckungen.

zeigten Ordnungen. Im folgenden soll die Vorhersagbarkeit der Resonanzwinkel im Vordergrund stehen. Zuerst nähern wir uns dem Problem aus einem heuristischen Blickwinkel und versuchen die Resonanzwinkel mit einem möglichst einfachen Modell vorherzusagen. Dieses Modell berücksichtigt bei Streckung des Systems nicht nur die Veränderung der Periodizität sondern auch zusätzlich die Veränderung der räumlich gemittelten optischen Konstanten. Letzteres folgt aus dem höheren Anteil des Polymers an der Oberfläche durch das schrittweise voneinander Entfernen der metallischen Drähte bei Streckung.

Das hierbei prinzipiell immer noch mit makroskopischen Größen wie z.B. optischen Konstanten gerechnet werden darf, muss kritisch beleuchtet werden. Solange die Abstände der Drähte unterhalb der Wellenlänge des anregenden Lichts bleiben, kann ein solcher Ansatz sicherlich gerechtfertigt werden. Im Übrigen zeigen die Resultate in Abbildung 1.5 eine hervorragende Übereinstimmung mit den Messwerten aus verschiedenen Experimenten.

Obwohl der oben beschriebene, vergleichsweise simplistisch anmutende Ansatz zu erstaunlich präzisen Vorhersagen kommt, so ist er nur geeignet, die eigentlichen Resonanzwinkel vorherzusagen. Wenn auch die Effizienz, d.h. der tatsächliche Intensitätsverlauf oder sogar Eigenschaften wie Gruppengeschwindigkeit oder Propagationslängen ermittelt werden sollen, so ist der Zugriff auf die vollständige Dispersionsrelation des Systems bzw. dessen Bandstruktur nötig. Wir haben daraufhin in Kooperation mit Stephan Schwieger vom Lehrstuhl für Theoretische Physik I der

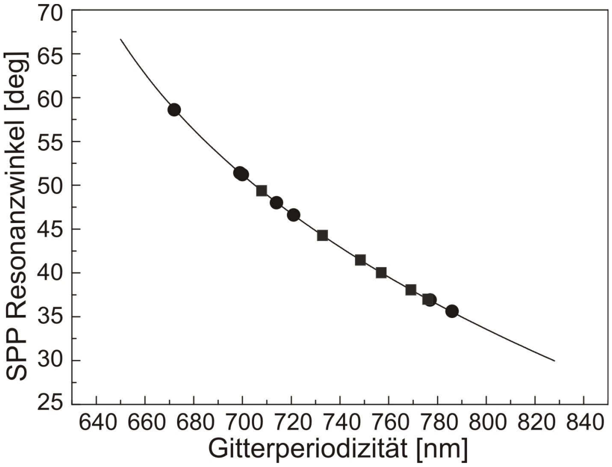

Abbildung 3.5. Lage der Minima gegen die streckungsabhängige Periodizität der Gitter. Die durchgezogene Linie stammt aus der im Text beschriebenen Modellrechnung.

TU Ilmenau (Erich Runge) die vollständige Lösung des Problems gesucht. Hierzu wird ein Algorithmus von Lochbihler und Depine genutzt, der die vollständige Lösung der Maxwell-Gleichungen nach einer Zerlegung des Lichtes in Partialwellen (z.B. in deren Fourierkomponenten) ermöglicht. Dieser Ansatz ist gültig für SPP's auf hochleitfähigen Materialien und damit uneingeschränkt für unsere Silber-Drähte bei den verwendeten Wellenlängen nutzbar. Hierbei sei betont, daß den Randbedingungen an den Silber-Polymer-Grenzflächen explizit Rechnung getragen wird. Als Resultat erhält man die vollständige Bandstruktur des Systems, die wir in Abbildung 1.6 in ein d(α_{inc}) Bild umgerechnet haben, um den direkten Vergleich mit unseren Messwerten zu ermöglichen.

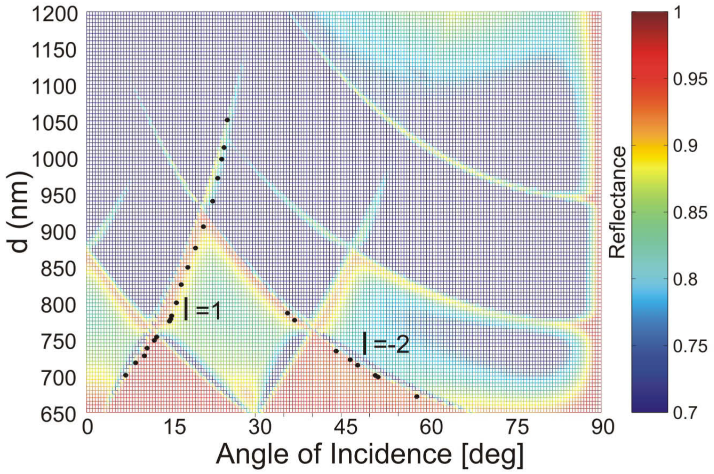

Abbildung 3.6. Simulation der "Bandstruktur" einer abstimmbaren Gitterstruktur mit 650 nm initialer Gitterperiodizität. Die eingezeichneten schwarzen Punkte stellen Messungen an einem solchen System dar.

Abbildung 3.6 zeigt eine sehr schöne Übereinstimmung zwischen Theorie und Experiment. Die gezeigte Bandstruktur ermöglicht nun die vollständige Kontrolle der SPP Anregung, der Propagation und der Wiederabstrahlung als Photonen. So können z.B. an Kreuzungspunkten verschiedener Ordnungen ultralangsame SPP's aber auch ultradispersive Plasmonen erzeugt werden. Die Gruppengeschwindigkeit der SPP's hängt nur vom gewählten $\partial\omega/\partial k$ ab.

Weiterhin ermöglichen die Simulationen nun die Erklärung des gesamten Intensitätsverlaufes, das Auffinden von SPP's an der Rückseite d.h. an der Metall-Polymer- zusätzlich zu der Metall-Luft-Grenzfläche, und eine Kontrolle der Phasenverschiebung zwischen normal reflektiertem und SPP re-emittiertem Licht. Letzteres kann dazu genutzt werden, um Maxima anstelle der sonst üblichen Minima unter Resonanzbedingungen zu erzeugen.

Außerdem lassen sich mit solchen Systemen die Lokalisierung von SPP's gezielt untersuchen. Beim erwünschten Aufreißen der Strukturen wird ein Übergang von einer korrugierten aber vollständig metallisierten Oberfläche zu separierten Nanodrähten vollführt. Hierbei kann kontinuierlich ein Plasmon angeregt werden und dessen Eigenschaften in-situ überprüft werden. Es soll hier vorweggenommen werden, daß sich die Eigenschaften des SPP's bei diesem Übergang erstaunlich gering ändern. Eine echte Lokalisierung des SPP's tritt in dem oben genannten Beispiel nicht auf. Ein solches Verhalten kann aber für größere Spaltbreiten theoretisch und experimentell gezeigt werden.

3.4 Wechselwirkungen von SPP's und elektrischen Strömen

Die longitudinale Elektronendichtewelle propagiert, vergleichbar mit anderen Wellenphänomenen, ohne die oszillierenden Ladungsträger im zeitlichen Mittel zu bewegen. In unserem Fall sind die Leitungselektronen in dem Metallfilm quasi-frei, vergleiche Blochs Theorie. Das heisst jedoch, daß im Extremfall die schwachen Rückstellkräfte dieser Elektronen nach Auslenkung durch die einkoppelnden Photonen zu einer winzigen aber auch im zeitlichen Mittel nicht verschwindenden Nettobewegung führen können. Diese Nettobewegung wäre durch die in ihr innewohnenden Ladungsverschiebung als kleiner Strom messbar. Kehrt man diesen Prozeß um, d.h. legt man einen Strom an den dünnen Metallfilm an, so würde man das Elektronengas mit einer Driftgeschwindigkeit versehen. Diese Driftgeschwindigkeit würde einen k-Vektor erzeugen, der prinzipiell zum Anpassen der Dispersionsrelation an die SPP Anregungsbedingungen geeignet wäre. Problematisch sind hier allerdings die experimentellen Details. Der dünne Film ist idealerweise bei Verwendung von Silber ca. 50 nm dick. Der einzige geometrische Parameter der variiert werden kann ist die Breite des Films. Da auf dem Film noch eine SPP Anregung mit einem Laser (typischer Spotdurchmesser 1-2 mm) vollführt werden soll, kann die Breite auch nicht beliebig schmal gewählt werden. Während breite Filme (1-2 cm) Widerstände in der Größenordnung 1Ω aufweisen, liegen schmale Filme (0.5 - 1 mm) bei ca. 20-40 Ω auf einer Länge von ca. 3 cm. Die Kontaktierung der Silberfilme ist hierbei kritisch und wurde mit spezial Kontaktpads gemacht, die ursprünglich für die Kontaktierung von LCD Displays hergestellt wurden. Dieser geringe Innenwiderstand unserer Proben erweisst sich hierbei im doppelten Sinne als nachteilig.

Erstens wollen wir ja einen zusätzlichen k-Vektor erzeugen, d.h. wir möchten den Elektronen eine möglichst hohe Geschwindigkeit mitgeben. Dies ist angesichts der geringen Innenwiderstände jedoch illusorisch. Die maximale Spannung die wir an einen solchen Film für längere Zeit anlegen konnten, war eine sinusförmige Wechselspannung mit einer V_{SS}=20 V. Zweitens ist das Messen ultrakleiner Ströme im femtoampere Bereich mit einem Hochleistungs-Elektrometer kein prinzipielles technisches Problem mehr. Allerdings versagen bei solch geringen Widerständen selbst

diese am theoretischen Limit arbeitenden Messgeräte. Daher haben wir folgenden Aufbau realisiert. Die Probe wurde in optische SPP-Anregungsbedingungen gebracht (genauer auf eine der Flanken mit hoher Reflektivitätsänderung), eine Wechselspannung angelegt und die Veränderungen der Reflektivität wurde mit der Hilfe eines hochempfindlichen Lock-In-Verstärkers detektiert. Die Referenz des Lock-In-Verstärkers wurde hierbei durch den Signalgenerator der modulierten Spannung gespeist. Als kritisch erwies sich auch die Abschirmung (Keithley Triax Systeme) konnte aber bei gleichzeitiger Senkung der Lock-In-Frequenz in den Griff bekommen werden.
Die Spannungsmodulation führt eindeutig zu einer Veränderung der Reflektivität des Surface Plasmon Resonance (SPR) Systems. Leider ist diese Änderung ungerichtet, d.h. unabhängig von der Richtung der angelegten Spannung (parallel oder antiparallel zur gewünschten SPP Propagation) ändert sich die Reflektivität immer in die gleiche Richtung (nur abhängig von der Ruheposition auf der Flanke des SPR Minimums). Dies bedeutet es handelt sich hier nicht um den erhofften zusätzlichen k-Vektor sondern um ein thermisch induziertes Verändern der optischen Konstanten. Bei 20 V fließen 0.5 - 1 A durch den nur 50 nm dicken Silberfilm! Der erhoffte Effekt ist also wesentlich kleiner als die thermische Veränderung der Probe. Um den thermischen Effekt unterdrücken zu können, haben wir vorgeschlagen eine kreuzförmige Silberschicht aufzudampfen. Hierbei werden vier Kontaktierungen an den Enden angebracht. Der Aufbau wird nun so gewählt, daß die Silberbahn zwischen zwei Kontakten genau senkrecht zur SPP Propagation liegt und daher nur thermische Effekte produziert, während das andere Paar in Propagationsrichtung liegt und daher thermische plus k-Vektor addierende Eigenschaften besitzen sollte. Die beiden Kanäle können mit dem Lock-In phasensensitiv detektiert und subtrahiert werden, wobei das thermische Signal herauskorrigiert werden soll. Die Messung des Restsignals ist jedoch extrem anspruchsvoll. Wir haben einen an das Problem angepassten Strom-Vorverstärker konzipiert, der nach der ersten 0.1 fA empfindlichen Stufe den DC Signalanteil abblockt und das Signal in einer zweiten Stufe weiter verstärkt. Diese zweite Stufe vollführt auch eine Strom-Spannungswandlung. Dieser Vorverstärker sitzt direkt im Detektorkopf und leitet das Verstärkersignal zum nV Lock-In-Verstärker. Der vollständige Nachweis des Effektes steht noch aus. Umgekehrt ist es jedoch gelungen, bei Bestrahlung der Metalloberfläche mit starken Kurzpulslasern einen sogenannten “Photon drag current” zu messen. Dieser “Photon drag current” ist der geforderte Netto-Strom aus dem Anfang dieses Abschnitts.

3.5 Nanopartikel und Streuung

Wir haben, um deren Brauchbarkeit für spektroskopische Zwecke zu testen, Goldkolloide mit sphärischen Formen als auch prolate d.h. stäbchenförmige Goldpartikel untersucht [17, 18]. Während erstere durchaus mit einfachen Mitteln synthetisiert werden können, möchten wir uns für letztere bei Carsten Sönnichsen (Universität Mainz) bedanken. Die Theorie der Wechselwirkung von Licht mit kolloiden Metallpartikeln ist bereits zu Beginn des vergangenen Jahrhunderts (1908) geschlossen von Gustav Mie dargelegt worden. Die mathematische Herleitung startet mit der Lösung von Maxwells Gleichungen und den notwendigen Randwertbedingungen. Diese werden dem Problem angepasst in Polarkoordinaten dargestellt und eine Lösung für die Wellenvektoren erhalten. Die Streukoeffizienten in einer Ebene ergeben sich bei der Erweiterung des Problems in das Fernfeld. Schließlich können die meßbaren Größen (Stokes Parameter) und die Formulierung der Phasenmatrix erhalten werden [17]:

$$\mathbf{P} = \begin{bmatrix} P_{11} & P_{12} & 0 & 0 \\ P_{12} & P_{11} & 0 & 0 \\ 0 & 0 & P_{33} & -P_{34} \\ 0 & 0 & P_{34} & P_{33} \end{bmatrix} \tag{3.2}$$

mit

$$P_{11} = \frac{4\pi}{2k^2\sigma_{sca}}(i_1(\theta) + i_2(\theta)), \tag{3.3}$$

$$P_{12} = \frac{4\pi}{2k^2\sigma_{sca}}(i_1(\theta) - i_2(\theta)), \tag{3.4}$$

$$P_{33} = \frac{4\pi}{2k^2\sigma_{sca}}(i_3(\theta) + i_4(\theta)), \tag{3.5}$$

$$P_{12} = \frac{4\pi}{2k^2\sigma_{sca}}(i_3(\theta) - i_4(\theta)). \tag{3.6}$$

Hier ist k der Wellenvektor, σ_{sca} ist der Wirkungsquerschnitt für Streuung, θ ist der Streuwinkel und i_j (j=1, 2, 3, 4) sind die Intensitätsfunktionen.

Die Größe der Partikel ist entscheidend für die Moden, die angeregt werden können. In kleineren Partikeln überwiegen sogenannte Dipol-Moden, die zu lokalisierten Plasmonen führen. In größeren Partikeln können höhere Moden angeregt werden, die zu propagierenden Plasmonen führen. Insbesondere letztere Plasmonen reagieren sehr empfindlich auf Änderung des lokalen Brechungsindexes. Umgekehrt heißt das, daß nur auf größeren Partikeln die Kinetik von Adsorptionen mittels SPR untersucht werden kann. Allgemein gilt, daß einfallendes Licht eine Oszillation der Elektronen gegen die Nuklei der Partikel verursacht. Die Resonanz resultiert aus den rückstellenden Coulomb Kräften, die der Separation entgegenwirken. Die Oszillationsfrequenz wird durch vier Faktoren bestimmt: Der Elektronendichte, der effektiven Elektronenmasse sowie Form und Größe der Nanopartikel.
Die Resonanz wird durch die Extinktions- und Streu-Effizienz Q_{ext}, Q_{sca} beschrieben:

$$Q_{ext} = 4x\Im m\left[g_d + \frac{x^2}{12}g_q + \frac{x^2}{30}(\epsilon_m - 1)\right] \tag{3.7}$$

$$Q_{sca} = \frac{8}{3}x^4\left[|g_d|^2 + \frac{x^4}{240}|g_q|^2 + \frac{x^4}{900}|\epsilon_m - 1|^2\right], \tag{3.8}$$

mit

$$g_d = \frac{\epsilon_2 - \epsilon_1}{\epsilon_2 + 2\epsilon_1} \tag{3.9}$$

$$g_q = \frac{\epsilon_2 - \epsilon_1}{\epsilon_2 + \frac{3}{2}\epsilon_1}. \tag{3.10}$$

Im folgenden präsentieren wir drei verschiedene Systeme und untersuchen diese bezüglich Proteinadsoption (Albumin, HSA): 60 nm sphärische Goldkolloide, 100 nm sphärische Goldkolloide und 20 nm x 60 nm prolate Goldkolloide. Die verschiedenen Kolloidsysteme wurden zuerst mittels Dialyse in hochreinem Wasser gereinigt und dann deren wellenlängenabhängige Streuung $Q_{sca}(\lambda)$ bestimmt und mit der Streutheorie verglichen. Abbildung 3.7 vergleicht die Messungen mit den entsprechenden Simulationen.

Die Übereinstimmung zwischen Theorie und Experiment ist beschränkt, aber insgesamt stimmen die Lage der Hauptmaxima gut überein. Es fallen insbesondere bei den sphärischen Kolloiden zusätzliche langwellig verschobene Maxima auf.

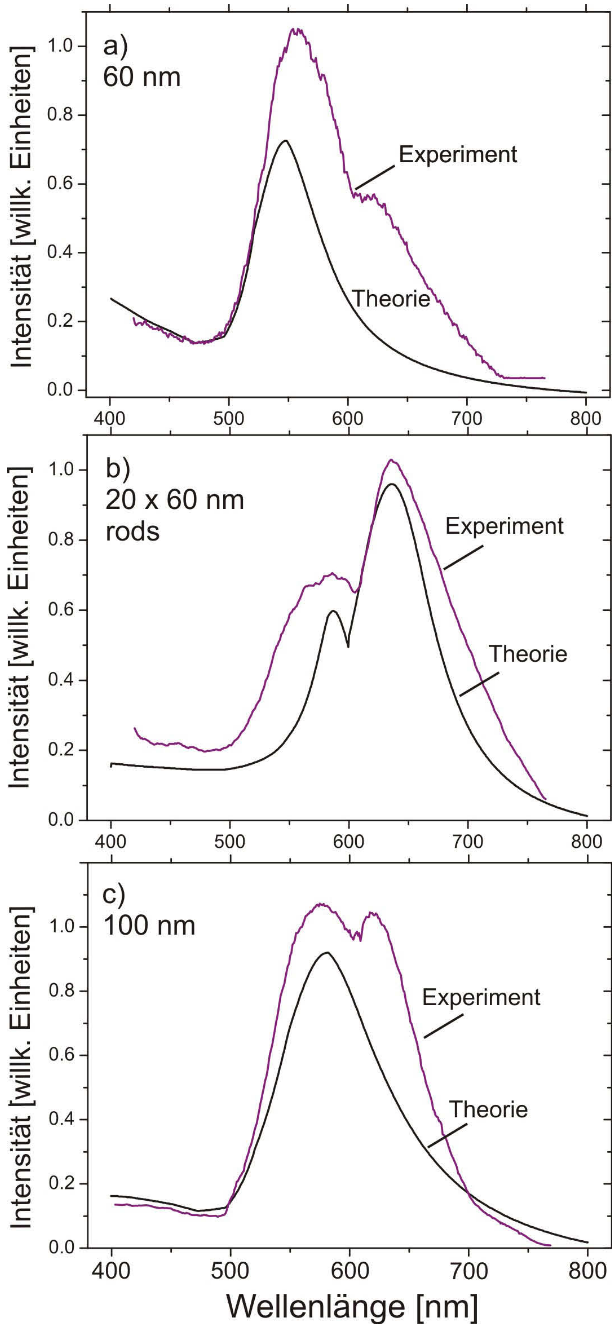

Abbildung 3.7. Vergleich der Streumessungen mit den theoretischen Mie-Streuungsdaten.

Mögliche Gründe für dieses Verhalten sind nicht monodisperse Größenverteilungen, Abweichungen von der sphärischen Form und im Falle der 100 nm Partikel Adsorption von Molekülen. Gibt man nun gezielt Albumin in die Lösung, so sollte man Veränderungen im Streuverhalten der Kolloide erkennen können. Die ensprechenden Messungen für die kleinen Partikel (60 nm und 20 nm x 60 nm) zeigt Abbildung 3.8.

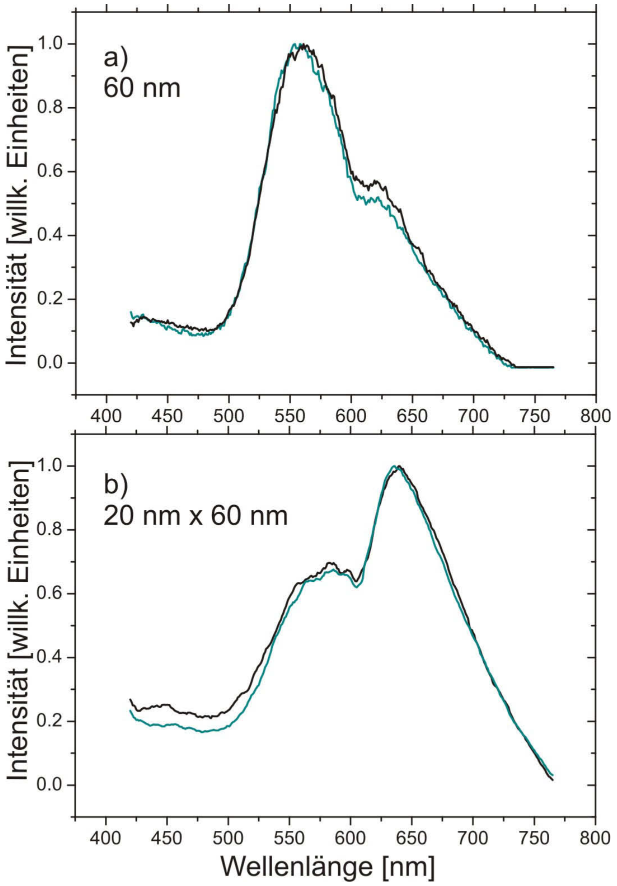

Abbildung 3.8. Vergleich der Streumessungen für die kleinen Partikel (60 nm und 20 nm x 60 nm) jeweils bevor und nachdem Albumin hinzugeführt wurde.

Offensichtlich können keine signifikanten Änderungen verfolgt werden. Der Grund hierfür ist das Kriterium für die minimale Größe der Partikel um adsorptionsempfindliche Mie-Streuung zu bekommen: $\lambda/10$. Machen wir den Gegentest und untersuchen die 100 nm durchmessenden Goldkolloide:

In Abbildung 3.9 zeigen sich deutliche Unterschiede, die sich im zeitabhängigen Streuverhalten widerspiegeln. Aus diesen Daten haben wir in [17] die kinetischen Konstanten bestimmt. Außerdem konnten durch numerische Fitverfahren die Größenverteilung der Goldkolloide abgeschätzt werden. Partikel mit Durchmessern zwische 80 nm und 200 nm eignen sich für sichtbares und nah-infrarotes Licht im Rahmen der Mie-Streuung. Es soll nicht verschwiegen werden, daß auch stabförmige Partikel geeignet sind. Ihre richtige Grösse vorausgesetzt streuen sie sogar stärker als sphärische Kolloide und zeigen auch eine höhere Empfindlichkeit gegenüber der Adsorption von Molekülen.

Zur Untersuchung von metallischen Einzelnanopartikeln haben wir eine "counterpropagating" Laserpinzette aufgebaut. Diese gestattet uns gezielt auch sub-

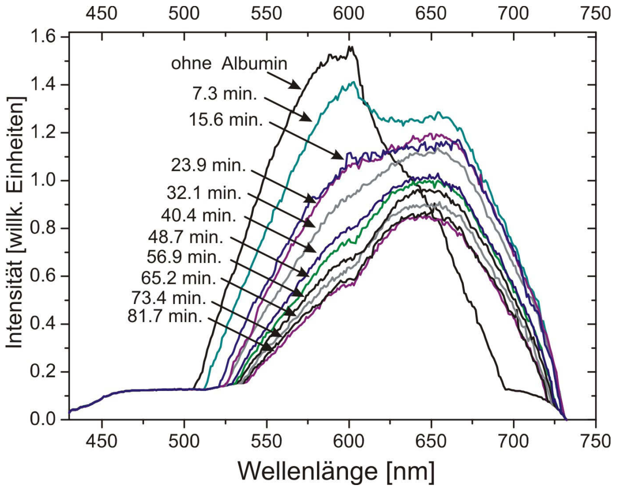

Abbildung 3.9. Vergleich der Streumessungen für die 100 nm durchmessenden Partikel bevor und nachdem Albumin hinzugeführt wurde.

wellenlängen Nanopartikel zu "greifen" und mit wellenlängenabhängiger Absorption, Mie-Streuung, Raman Streuung und SPP-Anregung zu untersuchen. Hierbei kann die Größenverteilung und Abweichungen von der Idealform des Ensembles ausgeschaltet werden und deshalb eine bessere Übereinstimmung zwischen Theorie und Experiment erzielt werden.

3.6 Maßgeschneiderte Nanostrukturen zum gezielten Design des SPP Nahfeldes

Offensichtlich ist es von Interesse möglichst hohe Feldverstärkungen auf möglichst kleinem Raum erzeugen zu können. Denkbar sind z.B. sogenannte Nanolichtquellen, die auf der Basis von SPP Anregungen auf nanostrukturierten Materialien ein hochdefiniertes Feld erzeugen [18]. Effekte dieser Art sind bereits schon von Gold- und Silberkolloiden bekannt, die sehr gerne als Surface Enhanced Raman Scattering (SERS) Sonden eingesetzt werden (siehe Abschnitt Nanopartikel und Streuung). Wieviel Kontrolle kann man über die Verteilung der elektromagnetischen Nah- und Fernfelder erlangen, wenn man vollständige Freiheit in dem Design der Nanostrukturen hat? Insbesondere ist es interessant die ausgetretenen Pfade von Objekten mit Kugel- oder Rotationssymmetrie zu verlassen. Durch eine Kooperation mit dem Tyndall Forschungszentrum in Cork (Irland) war es uns möglich auf Elektronenstrahlverfahren zur nahezu unbeschränkten Gestaltung von Oberflächen zurückzugreifen. Beispiele für so geschaffene Oberflächen sind in Abbildung 3.10 zu finden. Es handelt sich um rotationssymmetrische Ringstrukturen (zu Vergleichszwecken) und rotorartige Strukturen mit einer dreizähligen Symmetrieachse. Alle Strukturen sind silberbeschichtete Silizium-Substrate.

Die Anregungsbedingungen aus Gleichung (1.1) sehen im Fall eines zwei-dimensionalen Arrays wie folgt aus:

$$\frac{\omega}{c}\sin(\alpha_{inc}) + nG_x + mG_y \overset{!}{=} \frac{\omega}{c}\sqrt{\frac{\epsilon_m}{\epsilon_m+1}} \tag{3.11}$$

mit $(n,m)G_{x,y} = (n,m)\frac{2\pi}{d_{x,y}}$ und n, m ganze Zahlen. Aus der Definition der $G_{x,y}$ folgt, daß es sich bei ihnen um die reziproken Gittervektoren des Oberflächenarrays handelt. Hieraus wird bereits deutlich, daß die generellen Anregungsbedingungen

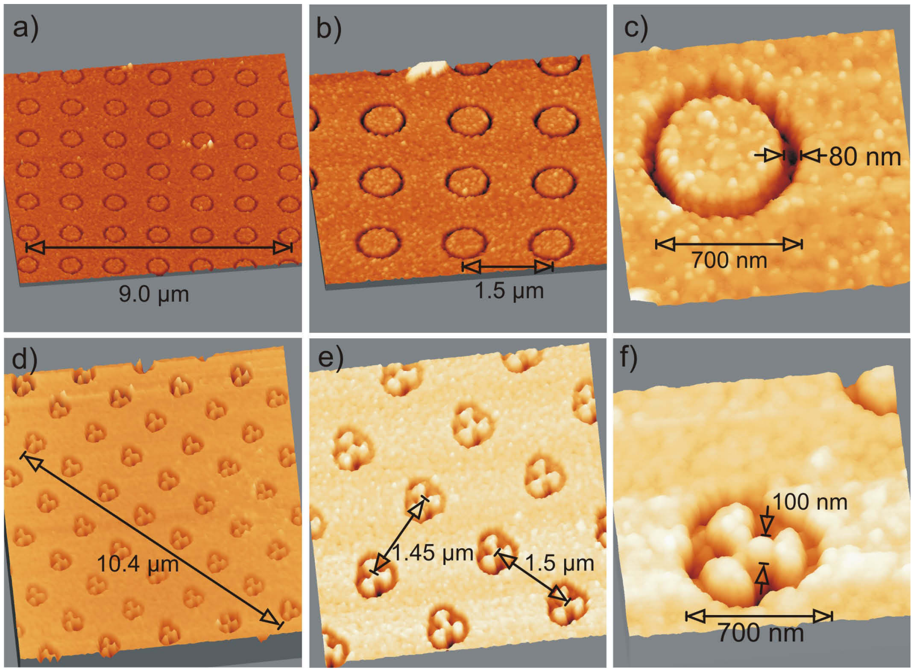

Abbildung 3.10. AFM Topographie von a)-c) Ringstrukturen und d)-f) Strukturen mit dreifacher Symmetrieachse.

für Plasmonen von der Periodizität der Strukturen abhängt. Die Frage die sich nun stellt ist: Welchen Einfluss hat die Form einer einzelnen Struktur auf die Anregungsbedingungen oder die Emission der SPPs?
Zuerst betrachten wir das Streubild von periodischen Arrays. Diese erzeugen ein Array von punktförmigen Streupunkten. Analysiert man ein individuelles Spotprofil dieser Streupunkte jedoch genau, so zeigt sich die reziproke Struktur der im Realraum streuenden Strukturen. Als Beispiel sei hier die fouriertransformierte der Strukturen mit 3-zähliger Symmetrieachse in Abbildung 3.11 angeführt.

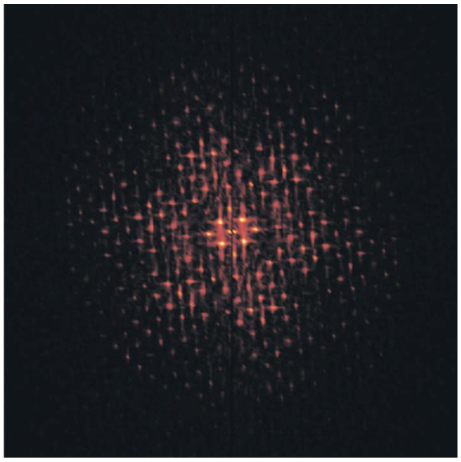

Abbildung 3.11. Zwei-dimensionale Darstellung der Fouriertransformierten des Rotors mit dreizähliger Symmetrie. Die Einzelpunkte in diesem Bild rühren aus der endlichen Zahl der für die Transformation benutzten Realraum-Strukturen her.

Insoweit ist das Ergebnis bekannt und lässt sich mit klassischer Streutheorie vorhersagen. Interessant wird es, wenn man nun einen Laserstrahl mit definiertem Winkel auf die Oberfläche einstrahlen lässt, so daß Gleichung 1.2 erfüllt wird. Man kann dann eine Plasmonenresonanz feststellen. Diese zeigt sich im Realraum dadurch, daß die Intensität des korrespondierenden Spots zu einem Minimum wird. Analysiert man die Polarisation des Lichtes in den verschiedenen Spots bei Anregung mit p-polarisiertem Licht, so stellt man fest, daß alle "nicht angeregten Spots" p-polarisiert sind aber der resonante Spot p- und s-Anteile enthält. Wir halten daher fest, daß Plasmonenanregung auf nanostrukturierten Arrays die Polarisationsrichtung der Emission verändern kann.

Vergleicht man nun ringförmige mit rotorförmigen Nanostrukturen, so zeigen sich auch in diesem Vergleich Unterschiede. Bei den rotationssymmetrischen Strukturen liegt das Maximum der SPP Anregung erwartungsgemäß in der reinen p-Richtung. Betrachtet man aber die rotorförmigen Strukturen so liegt das Anregungsmaximum bei diesen Strukturen nicht exakt in der p-Richtung, sondern entsprechend ihrer Symmetrie um - 30° oder +30° gedreht. Macht man die Gegenprobe, indem man die Probe um 90°, 180° und 270° dreht, so sieht man in allen vier Fällen unterschiedliches Verhalten. Letzteres kann wie folgt erklärt werden: Während die Strukturen eine dreizählige Symmetrieachse aufweisen so ist deren Anordnung bestenfalls mit einer vierzähligen Symmetrie ausgestattet. Beide Symmetrien zusammen bleiben daher bei Drehungen nicht erhalten. Dies erklärt auch die verschiedenen Ergebnisse bei Drehung um 90°, 180° und 270°. Es bleibt festzuhalten, daß die Form der Strukturen auch die Anregungsbedingungen verändern können. Insgesamt lassen sich verschiedene Einflüsse verschiedenen Kategorien zuordnen:

- Effekte, die die Anregung des SPPs beeinflussen. Hierzu gehören beispielsweise die Anordnung der Strukturen aber auch deren Form, da einzelne Strukturen auch resonant sein können vergleichbar mit Goldkolloiden. Insbesondere die hier vorgestellten Strukturen sind von einer Größenordnung und Form, die umlaufende SPPs und Bildung von Stehwellen unterstützen.
- Effekte, die die Propagation der Elektronendichtewelle beeinflussen. Hierzu gehören Kopplungseffekte zwischen Strukturen aber auch deren Symmetrie.
- Effekte, die die Wiederabstrahlung der SPPs als Photonen beeinflussen.

Ziel der Untersuchungen ist die Schaffung von Strukturen mit effizienter SPP-Anregung, deren Nahfeld räumlich eng begrenzte Maxima aufweisen.

3.7 SPP's auf ultra-schnellen Zeitskalen

Zur Berechnung der typischen Zeitskalen von SPP Prozessen werden Näherungen benutzt, die auch für die Berechnung der SPP Eindringtiefen und Propagationslängen Verwendung finden. Wir behandeln daher diese ebenfalls am Anfang dieses Abschnitts, bevor wir Theorie und Experimente auf ultra-schnellen Zeitskalen vorstellen.

3.7.1 Eindringtiefe

Um die Eindringtiefe von Oberflächenplasmonen in beide Materialien, entlang derer sie propagieren, zu quantifizieren, greifen wir auf folgende Formel zurück:

$$k_x^2 + k_{1z}^2 = \frac{\omega^2}{c^2}\epsilon_1$$

Ersetzt man hierin k_x^2 durch

$$k_x^2 = \left(\frac{\omega}{c}\right)^2 \frac{\epsilon_1 \epsilon_2}{\epsilon_1 + \epsilon_2}, \tag{3.12}$$

so erhält man nach einigen Umformungen und wegen der analogen Rechnung in Material 2 den allgemeinen Ausdruck in j

$$k_{jz}^2 = \left(\frac{\omega}{c}\right)^2 \frac{\epsilon_j^2}{\epsilon_1 + \epsilon_2}\ . \tag{3.13}$$

Insbesondere folgt daraus, dass $k_{jz} \in C$, da für Metalle $\epsilon_j \in C$ gilt. Der Wert der Größe k_{jz} besteht also aus einem Realteil, der der propagierenden ebenen Welle zugeordnet werden kann, sowie einem Imaginärteil, der die Dämpfung der elektromagnetischen Welle entlang der z-Achse beschreibt. Man bezeichnet als Eindringtiefe des Oberflächenplasmons im Material j, den Wert $\tilde{z}_j$, für den die Feldstärke der Welle auf den $\frac{1}{e}$ -ten Teil der Feldstärke bei $z = 0$ abgefallen ist.
Es wird daher definiert:

$$\tilde{z}_j = \frac{1}{\Im(k_{jz})}\ .$$

Weil man zur exakten Berechnung der Eindringtiefe nach dieser Formel die komplexe Wurzel von k_{jz} ziehen müsste, sich dies aber als kompliziert erweist, vernachlässigt man den Imaginärteil $\epsilon_1^{''}$ der dielektrischen Funktion $\epsilon_1 = \epsilon_1^{'} + i\epsilon_1^{''}$ des Metalls. Damit ergibt sich die Näherungsformel zu [20]

$$\tilde{z}_j = \frac{\lambda}{2\pi} \sqrt{\frac{\left|\epsilon_1^{'} + \epsilon_2\right|}{\Re(\epsilon_j)^2}}\ . \tag{3.14}$$

Beispiel

Für Plasmonen an einer Silber-Luft Grenzschicht, angeregt mit einem He-Ne Laser ($\lambda = 632.8\,nm$), ergibt sich damit die Eindringtiefe in Luft zu $390\,nm$ und in Silber zu $24nm$. Die Eindringtiefe im Metall ist in diesem Beispiel also um eine Größenordnung geringer als in Luft, denn elektromagnetische Felder können in Metall durch die im Vergleich zu Luft hohe Leitfähigkeit besser abgeschirmt werden.Der Verlauf der Eindringtiefe für verschiedene Wellenlängen ist in Abb. 3.12 gezeigt.

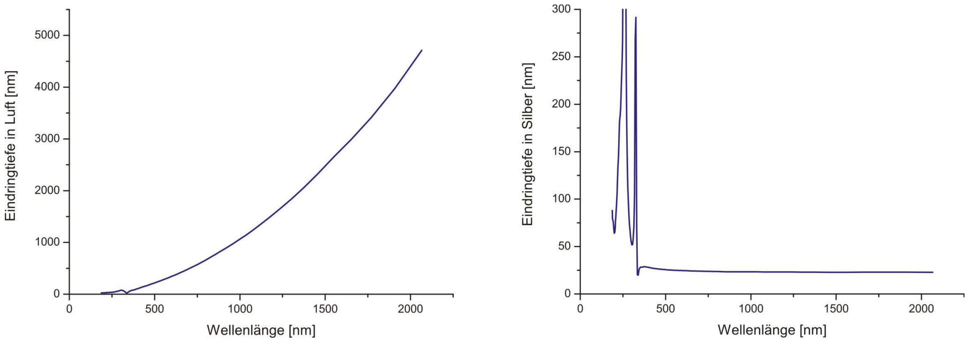

Abbildung 3.12. Verlauf der Eindringtiefe für Plasmonen in Luft und Metall in Abhängigkeit der Wellenlänge. Die Resonanzen bei Silber treten bei Frequenzen jenseits der Plasmafrequenz auf, die in Silber bei einer Wellenlänge von etwa $330\,nm$ liegt [21]. Hier dringt die elektromagnetische Welle ins Metall ein und kann sich darin ausbreiten.

3.7.2 Propagationslänge

Mit einer ähnlichen Überlegung lässt sich die Propagationslänge der Oberflächenplasmonen bestimmen. Entlang der Oberfläche wird die Ausbreitung des Plasmons durch die x-Komponente des Wellenvektors $\boldsymbol{k}$ gegeben. Da sie nach (3.12) komplex ist, wird das exponentielle Abklingen des Plasmons entlang der Oberfläche durch den Imaginärteil $\Im(k_x)$ beschrieben. Um nun die Länge zu berechnen, nach der die Feldstärke der elektromagnetischen Welle auf den $\frac{1}{e}$ -ten Teil der Feldstärke am Anregungspunkt abgefallen ist, muss zusätzlich noch die Ausdehnung des Plasmons in beide Richtungen entlang der x-Achse berücksichtigt werden. Als Abklinglänge L definiert man daher

$$L = \frac{2}{\Im(k_x)} \; .$$

Um auch hier wieder das Berechnen der komplexen Wurzel zu vermeiden zerlegt man nach [20] die x-Komponente des Wellenvektors $\boldsymbol{k}$ in $k_x = k_x^{'} + ik_x^{''}$. Dies geschieht unter der Annahme allein reeller Frequenzen ω, sowie einem kleinen Imaginärteil der dielektrischen Funktion gegenüber ihrem Realteil $\epsilon_1^{''} < \left|\epsilon_1^{'}\right|$. Somit ergibt sich für die Komponenten des Wellenvektors $\boldsymbol{k}$:

$$k_x^{'} = \frac{\omega}{c}\sqrt{\frac{\epsilon_1^{'}\epsilon_2}{\epsilon_1^{'}+\epsilon_2}} \; ,$$

$$k_x^{''} = \frac{\omega}{c}\left(\frac{\epsilon_1^{'}\epsilon_2}{\epsilon_1^{'}+\epsilon_2}\right)^{3/2}\frac{\epsilon_1^{''}}{2(\epsilon_1^{'})^2} \; .$$

Die Näherungsformel zur Berechnung der Propagationslänge wird dann zu

$$L = \frac{\lambda}{\pi\left(\frac{\epsilon_1^{'}\epsilon_2}{\epsilon_1^{'}+\epsilon_2}\right)^{3/2}\frac{\epsilon_1^{''}}{2\epsilon_1^{'2}}} \; . \tag{3.15}$$

Beispiel

Für das Beispiel der Plasmonen an einer Silber-Luft Grenzschicht bei $\lambda = 632,8\,nm$ liefert die Näherungsformel dann eine Propagationslänge von etwa $85\,\mu m$. Für verschiedene Anregungswellenlängen sind die Propagationslängen in Abb. 3.13 dargestellt.

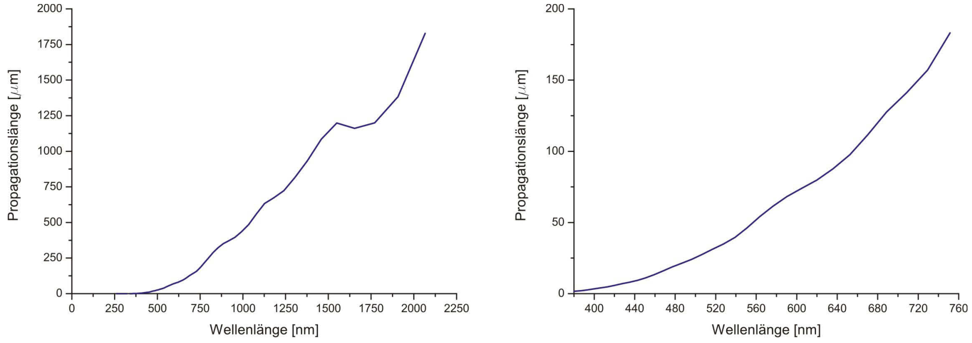

Abbildung 3.13. Die Propagationslänge der Oberflächenplasmonen für verschiedene Wellenlängen (links). Die Vergrößerung rechts beschränkt sich auf den sichtbaren Bereich.

3.7.3 Relaxationszeit

Um die Relaxationszeit τ, d.h. die Lebensdauer eines Oberflächenplasmons zu bestimmen, geht man analog vor: Die Plasmonenfrequenz ω wird als komplex angenommen, d.h. $\omega = \omega^{'} + i\omega^{''}$, wobei der Imaginärteil der Frequenz wieder einer Dämpfung entspricht. Damit ergibt sich als Lebensdauer der Plasmonen

$$\tau = \frac{1}{\Im(\omega)} \, .$$

Der Imaginärteil der Frequenz ω'' berechnet sich Näherungsweise durch $k_x^{''}$ über den Zusammenhang $\omega^{''} = ck_x^{''}$. Für die Relaxationszeit ergibt sich daher

$$\tau = \frac{\lambda}{2\pi c \left(\frac{\epsilon_1^{'}\epsilon_2}{\epsilon_1^{'}+\epsilon_2}\right)^{3/2} \frac{\epsilon_1^{''}}{2\epsilon_1^{'2}}} \, . \tag{3.16}$$

Beispiel

Plasmonen an der Silber-Luft Grenzschicht, die mit der Wellenlänge 632.8 nm eines He-Ne Lasers angeregt worden sind, haben demnach eine Lebensdauer von ca. 150 fs. Senkt man allerdings die Wellenlänge des anregenden Lichtes auf 400 nm so liegt Lebensdauer nur noch bei 12 fs. Abb. 3.14 zeigt die Entwicklung der Relaxationszeit in Abhängigkeit der Wellenlänge des anregenden Lichts.
Es ist bemerkenswert, daß Plasmonen zwar eine mesoskalige Propagationslänge besitzen, jedoch extreme Kurzzeitphänomene sind.
Bei der Auswertung der Formeln sowohl für die Propagationslänge als auch für die Relaxationszeit kann es vorkommen, dass für bestimmte Anregungswellenlängen eine negative Wurzel gezogen werden muss. Das ist ein Indiz dafür, daß das Metall bei diesen Wellenlängen Resonanzen besitzt, wie sie in Abb. 3.12 gezeigt werden. Physikalisch bedeutet dies, daß bei diesen Werten keine Plasmonen angeregt werden können, weil das Metall das Anregungslicht anderweitig absorbieren kann. Typischerweise tritt dieses Phänomen bei Anregungsfrequenzen, die der Plasmafrequenz entsprechen, und höher auf.

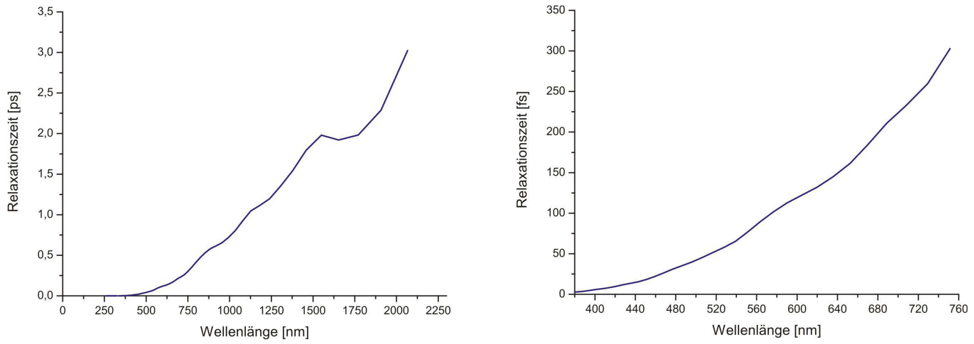

Abbildung 3.14. Die Relaxationszeit der Oberflächenplasmonen für verschiedene Wellenlängen (links). Die Vergrößerung rechts beschränkt sich auf den sichtbaren Bereich.

3.7.4 Ursachen für die Relaxation von Plasmonen

Der Zerfall der Oberflächenplasmonen nach einer gewissen Propagationslänge bzw. -zeit hat mehrere Ursachen, die im Folgenden einzeln besprochen werden. Dabei bestimmen die Relaxationsmechanismen ebenfalls die Effizienz der Plasmonenanregung mit.

- Interne Dämpfung
  Die interne Dämpfung wird durch $\Im(k_x)$ bestimmt. Die elektromagnetische Welle des Oberflächenplasmons wird im Metall von Elektronen-Loch Paaren an der Fermi-Kante begleitet [20]. Wenn diese rekombinieren, entstehen Phononen, d.h. Wärme. Außerdem kann die Rekombinationsenergie durch Emission von Photoelektronen abgegeben werden, falls sie größer als die Austrittsarbeit des Metalls ist. In Silber, das in dieser Arbeit ausschließlich verwendet wird, ist das jedoch nicht der Fall. Die Austrittsarbeit von Silber liegt höher als die frei werdene Rekombinationsenergie, so daß hier nur der Zerfallskanal der Phononen besteht.

- Strahlungsdämpfung
  Im Abschnitt "Eindringtiefe" wurde der Realteil der senkrecht zur Oberfläche stehenden z-Komponente des Vektors $\boldsymbol{k}$ vernachlässigt. Im Realfall lecken Plasmonen aber durchaus in z-Richtung, sowohl in das Metall, als auch in das umgebende Dielektrikum. Dort sorgt der, wenn auch gering vorhandene, Realteil $\Re(k_z)$ dafür, daß sie als propagierende Welle abgestrahlt werden. Die dadurch verlorene Energie wird Strahlungsverlust genannt.

Die oben vorgestellten Relaxationsmechanismen sind unabhängig von der Oberflächenbeschaffenheit des Metalls. Auf realen, d.h. rauhen Oberflächen kommen noch weitere Zerfallsprozesse hinzu.

- Abstrahlung an Rauheiten
  Statistische Rauheiten einer Oberfläche besitzen Quasiimpulskomponenten im $\boldsymbol{k}$-Raum. Sie bieten den Plasmonen Kopplungsmöglichkeiten und damit Gelegenheit zum Quasiimpulstransfer. Bei einer inelastischen Streuung an ihnen, kann sich der Quasiimpuls der Plasmonen so verändern, dass es möglich ist, die Plasmonenenergie als freie Photonen in den dielektrischen Halbraum abzustrahlen.
  Dieses Phänomen macht man sich im umgekehrten Fall auch zur Anregung der Plasmonen zu nutze, wie im Abschnitt "Design des SPP Nahfelds" vorgestellt wurde.

- Streuung an Rauheiten
  Ebenso können Plasmonen an Rauheiten elastisch streuen. Ohne Änderung des Betrages $|\boldsymbol{k}|$ ihres Quasiimpulses werden sie dabei aus ihrer Propagationsrichtung abgelenkt.

Als Abschätzung ergibt sich durch die Rauheitseffekte eine Reduktion von Propagationslänge und -zeit um den Faktor 2 [20].

Wie soeben gezeigt, sind Oberflächenplasmonen ultra-schnelle Phänomene auf Zeitskalen im Pico- bis Femtosekunden-Bereich. Um solche Phänomene zeitlich auflösen zu können, werden hochpräzise Doppelpuls-Interferometrietechniken angewendet [22]. Das Kreuzkorrelations-Signal wird dabei verwendet, um die Absorption und die Dispersion der Probe simultan zu messen. Dies ermöglicht auch die Messung der Gruppengeschwindigkeit aber speziell auch des "Chirps" und dessen Vorzeichen ohne Modellannahmen. Interessant ist auch, daß die zeitliche Auflösung der Experimente nicht meht länger von der Pulslänge des Lasers abhängt, sondern in der Größenordnung eines Zyklus' des Lichtfeldes liegt. Daher lassen sich prinzipielle Auflösungen in sub Femtosekunden erreichen. In diesen Experimenten wird ein zeitlich kurzer Laserpuls (z.B. 30 fs von einem Ti:Sa Oszillator) durch ein Mach-Zehnder (MZ) Interferometer geschickt, das zwei Pulse mit der Separation

$\varDelta L$ erzeugt. Das SPP Experiment wird in einen Arm des MZ Interferometers plaziert. Der Puls, der durch den anderen Arm geht, bleibt unverändert und wird als Referenz Puls genutzt. Das elektrische Feld mit der Frequenz ω kann im allgemeinen in der Frequenz-Domäne durch $A(\omega)\exp(i\omega t)$ ausgedrückt werden mit $A(\omega)$ der langsam variierenden Amplitudenfunktion. Die komplexe Amplitudenfunktion $A(\omega)$ beschreibt die spektrale Leistungsdichte des Referenzsignals und die relative Phasenbeziehung zwischen den Frequenzkomponenten. Die Summe des Referenzpulses und des Probenpulses ist gegeben durch:

$$E(t) = \int_{-\infty}^{+\infty} d\omega A(\omega) e^{i\omega t} + \int_{-\infty}^{+\infty} d\omega H(\omega) A(\omega) e^{i\omega(t+\varDelta L/c)} \tag{3.17}$$

wobei $\varDelta L/c$ die durch das MZ Interferometer eingeführte Verzögerung ist. Das erste Integral beschreibt den ungestörten Puls, das zweite den Probenpuls. Die Veränderung des Pulses durch das SPP wird durch die Transferfunktion $H(\omega)$ beschrieben. Im allgemeinen ist $H(\omega)$ eine komplexe Funktion in ω, die die Amplitude und relative Phasenbeziehungen der Frequenzkomponenten enthält. Die zwei Pulse werden in ein Michelson Interferometer geschickt. Das dort gewonnene Interferogramm ist das Autokorrelationssignal der zwei Pulse. Das Signal $I(\tau)$ ist gegeben durch:

$$\begin{aligned} I(\tau) &= \int_{-\infty}^{+\infty} dt E(t) E^*(t-\tau) && (3.18) \\ &= \int_{-\infty}^{+\infty} d\omega H(\omega) |A(\omega)|^2 e^{i\omega(\tau-\varDelta L/c)} && (3.19) \\ &+ \int_{-\infty}^{+\infty} d\omega (|A(\omega)|^2 + |H(\omega)A(\omega)|^2) e^{i\omega t} \\ &+ \int_{-\infty}^{+\infty} d\omega H(\omega)^* |A(\omega)|^2 e^{i\omega(\tau+\varDelta L/c)} \end{aligned}$$

wobei τ die durch das Michelson Interferometer eingeführte Verzögerung ist. Experimente zur Analyse der zeitabhängigen Antwortfunktion zeigen nun ein Verhalten bei dem ein Puls gefolgt von mindestens einem Echo aufgenommen wird. Der erste quasi-instantane Puls ist identisch mit der direkten spekulären Reflexion an der Metall-Grenzfläche, der zweite Puls ist die hiergegen verzögerte SPP-Re-Emission. Bei komplexeren Strukturen, wie z.B. Gittern, folgen noch weitere, schwächere Pulse, die mit den Laufzeiten in dem jeweiligen Gitter zusammenhängen. Die Fähigkeit, die Reflexion von der SPP Re-Emission zu trennen, ist sehr wichtig für die Analyse der SPP Anregungseffizienz. Bei langpulsiger oder CW Anregung interferiert das reflektierte Licht destruktiv mit dem SPP Licht. Daher ist das Minimum von klassischen SPR Kurven im allgemeinen nicht das Maximum der SPP Anregung, sondern beschreibt vielmehr eine Balance zwischen SPP und reflektiertem Licht. Diese Behauptung lässt sich auch durch Simulationen [14] und Nahfeldmessungen bestätigen.

3.8 Ausblick

Der Teil der Plasmonik, der sich mit linearer Optik zufriedenstellend beschreiben läßt, ist in seinen Grundzügen vollständig verstanden. Probleme bereiten hier allenfalls die konkreten Implementationen der Algorithmen, z.B. wenn die elektromagnetischen Felder im extremen Nahfeld-Bereich beschrieben werden sollen. Die meisten der zur Verfügung stehenden Techniken haben Probleme, wenn eine Grenzfläche in

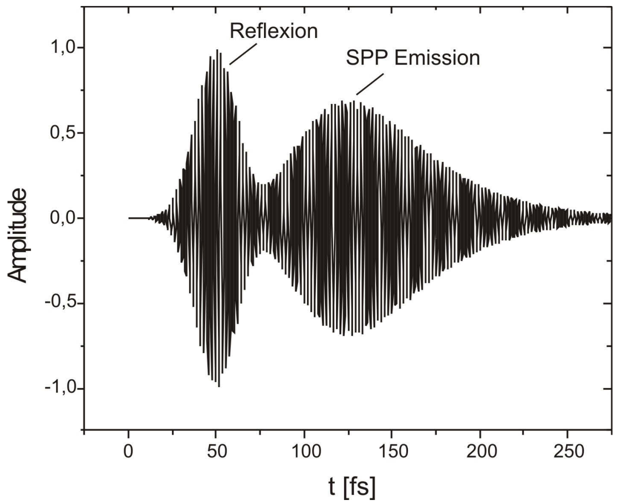

Abbildung 3.15. Simulation einer Reflexion mit verzögerter, überlagerter SPP Emission auf einem glatten, 50 nm dicken Silberfilm auf einer femtosekunden Zeitskala. Es existieren in der Zwischenzeit genauere und zutreffendere Simulationen und Messungen des Autors (Spectral Phase, PEEM) von SPPs auf Femtosekundenskalen.

ihren atomaren Details beschrieben werden soll. Dies sind jedoch mehr technische als physikalische Probleme.

Zu den physikalischen Problemem kommt man, wenn nicht-lineare optische Phänomene an metallischen Grenzflächen auftreten. Diese Phänomene entziehen sich bisher noch einer vollständigen theoretischen Beschreibung. Nicht-lineare optische Phänomene treten insbesondere bei der Verwendung extrem kurzer Laserpulse auf. Wie gezeigt stehen uns Methoden zur Nanostrukturierung als auch Techniken für zeitlich hochaufgelöste Messungen zu Verfügung. Die nächsten Schritte im Rahmen zweier bereits laufender Science Foundation Ireland (SFI) Research Frontier Projekte ("Nano-lightsource" und "Tuneable Light Confinement") und einer erwünschten Beteiligung am DFG Schwerpunktprogramm "Ultrafast Nanooptics" sehen daher die Erzeugung von Nahfeldemittern vor, die sich für neuartige sub-Beugungslimit Imaging-Techniken einsetzen lassen. Hierbei ist es notwendig, daß auch zeitlich ultraschnelle Phänomene mit diesen Methoden erfasst werden können und nicht-lineare optische Phänomene wie z.B. "Second Harmonic Generation" (SHG) an Nanostrukturen untersucht werden. Lateral und räumlich aufgelöste Untersuchungen können mit optischen Scanning Probe Techniken oder auch mit Photoemissions Elektronen Mikroskopie (PEEM) angefertigt werden. Ziele dieser Untersuchungen sind neue Einblicke in ultraschnelle Licht-Materie Wechselwirkungen aber auch neuartige Applikationen z.B. in den Bereichen Bildgebung und Sensorik. Ein wichtiger Aspekt der Untersuchungen ist hierbei auch die möglichst vollständige Kontrolle über die verwendeten Laserpulse im Hinblick auf deren Kohärenz, Zeitverhalten, dynamischer Wellenlängenverteilung (Stichwort chirping), Polarisation und Phase [23]. Durch maßgeschneiderte Pulsformen und Eigenschaften des anregenden Lichts können Licht-Materie Wechselwirkungen entscheidend beeinflusst werden (z.B. Resonanz mit einer Nanostruktur) und im weiteren in ihren Grundzügen besser verstanden werden.

A

Literaturverzeichnis

[1] D. Zerulla, Encyclopedia of Nanosciences, “Self assembly on semiconductors”, American Scientific Publishers ASP, Ed. H. Nalwa, ISBN 1-58883-001-2, **IX** (2004) 427-457.

[2] D. Zerulla, I. Uhlig, R. Szargan, T. Chassé: “Competing interaction of different thiol species on gold surfaces”, Surface Science 1998, **402-404**, 604-608.

[3] D. Zerulla, D. Mayer, K-H. Hallmeier, T. Chassé: “Angular resolved XANES-measurements of the polar and the azimuth orientation of alkanethiols on InP(110)”, Chem. Phys. Let. 1999, **311**, 8-12.

[4] T. Chassé, D. Zerulla, K.-H. Hallmeier “Angular Resolved X-Ray Absorption Near Edge Structure Investigation of Adsorbed Alkanethiol Monolayers on III-V(110) Surfaces”, Surf. Rev. Let. 1999, **6**, 1179-1186.

[5] D. Zerulla, T.Chassé, “Scanning Tunneling Microscopy and Spectroscopy of UHV-Deposited Dodecanethiolate Films on InP(110) Surfaces at Consecutive Doses: A Single Domain System”, Langmuir 2002, **18**, 5392-5399.

[6] D. Zerulla, T. Chassé: “X-ray Induced Damage of Self-Assembled Alkanethiols on Gold and Indium Phosphide”, Langmuir 1999, **15**, 5285-5294.

[7] D. Mayer, K. H. Hallmeier, D. Zerulla, R. Szargan in K. Wandelt, S. Thurgate eds., Topics in Applied Physics - Solid-Liquid Interfaces “SXPS and XANES Studies of Interface Reactions of Organic Molecules”, Springer 2003, Vol. **85**, 3-540-42583-7, (16 pages).

[8] A. Otto, “Excitation of surface plasma waves in silver by the method of frustrated total reflection”, Z. Physik 1968, **216**, 398–410.

[9] E. Kretschmann, H. and Raether, “Radiative decay of non-radiative surface plasmons excited by light”, Z. Naturforsch. 1968, **23A**, 2135–2136.

[10] R. W. Wood, “On a Remarkable Case of Uneven Distribution of Light in a Diffraction Grating Spectrum”, Proc. R. Soc. London 1902, **A18**, 269.

[11] R. H. Ritchie, E.T. Arakawa, J.J. Cowan, and R.N. Hamm, “Surface-plasmon resonance effect in grating diffraction”, Phys. Rev. Lett. 1957, **21**, 1530–1533.

[12] G. Isfort, K. Schierbaum, D. Zerulla, "Polarization Dependance of Surface Plasmon Polariton Emission", Phys. Rev. B **74**, 033404 (2006).

[13] G. Isfort, K.-D. Schierbaum, D. Zerulla, "Causality of Surface Plasmon Polariton Emission Processes" Phys. Rev. B **73**, 033408 (2006).

[14] D. Zerulla, G. Isfort, M. Kölbach, A. Otto, K. Schierbaum, "Sensing molecular properties by ATR-SPP Raman spectroscopy on electrochemically nanostructured sensor chips", Electrochimica acta 2003, **48**(20-22), 2943.

[15] S. Rehwald, M. Berndt, F. Katzenberg, S. Schwieger, E. Runge, K. Schierbaum, D. Zerulla, "Tuneable Nanowires: An Additional Degree of Freedom in Plasmonics", Phys. Rev. B (2007) (in print).

[16] D. Zerulla, S. Rehwald, Patent, "SPP Excited Tuneable Mesostructures as Biosensors", European Patent Office, filed October 8^{th} (2006).

[17] G. Doyle, B. Ashall, M. Galvin, M. Berndt, S. Crosbie, and D. Zerulla,"Mie Scattering and Surface Plasmon Based Spectroscopy for the Detection of Nanoparticle-Protein Interactions", Applied Physics, (2007) (in print).

[18] B. Ashall, M. Berndt, and D. Zerulla,"Tailoring SPP Propagation by Nanostructures with Specific Symmetry Properties", APL, (2007), submitted.

[19] M. Pfannmöller, and D. Zerulla,"Between Physics and Biology: A Review of Light Matter Interactions on the Nanoscale as Probes in Biological Applications", Plasmonics, (2007), accepted.

[20] H. Raether: *Surface Plasmons on Smooth and Rough Surfaces and on Gratings*, (Springer, Berlin Heidelberg 1988).

[21] F. Forstmann, R.R. Gerhardts: *Metal Optics near the Plasma Frequency*, (Springer, Berlin 1986).

[22] R.H.J. Kop and R. Sprik, "Phase-sensitive interferometry with ultrashort pulses", Rev. Sci. Instrum, 66(12) (1995).

[23] M. Aeschlimann, M. Bauer, D. Bayer, T. Brixner, F. Javier Carcia de Abajo, W. Pfeiffer, M. Rohmer, Ch. Spindler, F. Steeb, "Adaptive subwavelength control of nano-optical fields", Nature 446 (7133), 301, (2007).

ENN Encyclopedia of Nanoscience and Nanotechnology
www.aspbs.com/enn

Self-Assembled Monolayers on Semiconductor Surfaces

D. Zerulla
Heinrich-Heine-Universitaet Duesseldorf, Duesseldorf, Germany

CONTENTS

1. INTRODUCTION

Self-assembly is a very general principle in nature, as seen in the formation of for example, membranes from lipid molecules, or probably the most important paradigm, the living cell. Self-assembled monolayers (SAMs) are ordered molecular assemblies that are formed spontaneously by the adsorption of a surfactant. SAMs have recently attracted much attention because of the interesting opportunities for tailoring of solid surfaces. These monolayers exhibit unique chemical and structural properties. The formation of a SAM is initiated by bonding of a specific group of the organic molecule to the surface, followed by a rearrangement of the adsorbate layer with increasing coverage of the surface. This process is driven by intramolecular interactions between the adsorbed organics. Although self-assembly has attracted considerable attention over the last years, the subject has fairly old roots.

Pockels prepared monolayers at the air–water interface in the 19th century [1–4], followed by Rayleigh [5], Hardy [6], Deveaux [7], and others. Later, monolayers of amphiphilic molecules on the water surface were named after Langmuir [8, 9]. The first one to study the deposition of long-chain carboxylic acids on solid substrates was Blodgett [10, 11], who can be seen as the ancestor of our modern self-assembling systems, even if, around that time, amphiphilic monolayers were already used to control the wetting behavior of metal condenser plates in steam engines. Systematic research on self-assembling monolayers was performed later by Zisman [12] and Dewar [13]. For further information regarding the history of organic monolayers, we refer to [14, 15].

In the 1980s, the field of wetting and surface modification underwent a revival, and the great potential of thin organic films was recognized, which led to a very large number of publications in the following years [16–20].

Highly ordered organic films are very promising initial or intermediate states in order to achieve well-characterized tailoring of surfaces. Well-defined chemical modification and control of surfaces and interfaces are also essential for a variety of applications of semiconducting materials, as in photocatalysis, optoelectronic, and photovoltaic devices [21–23]. Recently, alkanethiolate films were also investigated on semiconductors because of their application potential for such purposes. But to date, still much less is known about alkanethiolate films on surfaces of compound semiconductors compared to the extensively studied surfaces of gold, silver, and copper. Passivation of GaAs surfaces using adsorbed thiols has been reported by Lunt et al. [24]. A study on alkanethiols on a chemically prepared InP(100) surface has been published by Gu et al. [25]. We will present very detailed results on the character, structure, passivating properties, and patterning of alkanethiols on III–V semiconductor surfaces in this chapter.

In contrast to the numerous publications in the field "self-assembling systems on coinage metals," the number of papers dealing with self-assembling on semiconductors is by far lower. In this chapter, the very detailed results on metals are sometimes used, to be compared with the results on semiconductors. This comparison allows us to judge if a self-assembling feature is a more general feature or a specific one for semiconductors. However, the main focus of this chapter is self-assembling and nanostructuring on semiconductors. Furthermore, this review is written from a surface-science perspective, with the focus on the fundamental principles governing the growth and structures

ISBN: 1-58883-065-9/$35.00

Encyclopedia of Nanoscience and Nanotechnology
Edited by H. S. Nalwa
Volume 9: Pages (427–457)

of self-assembling monolayers. While this naturally puts the emphasis on chemically simple compounds (e.g., thiols), we also outline the rich opportunities in the areas of lateral patterning, chemical functionalization, chelating compounds, and some technological applications. For the used surface-science techniques, we refer to well-known textbooks.

The chapter is organized as follows. In Section 2, the basic facts about the systems, the sample preparation techniques, and self-assembly are discussed. Section 3 deals with thiols on different III–V semiconductors, the most discussed and, in our opinion, the most fruitful combination. This includes speed of assembly, passivating properties, and a very detailed discussion of the structure of these systems. Section 4 is dedicated to the structuring of self-assembling systems. We present different approaches to structuring, but also discuss in detail the mechanisms behind the different technologies. Section 5 briefly describes systems which have not been discussed in the previous sections in order to give an as complete as possible review on the topic. Section 6 closes this chapter with a general discussion, and we conclude with an outlook and some open issues.

2. ORGANIC SELF-ASSEMBLIES

The most often used organic species in self-assembly is the *n*–alkanethiol molecule. Alkanethiols CH_3–$(CH_2)_{n-1}$–SH (alkyl chain length *n*) are well known to form SAMs on metals like gold, silver, or copper [16, 26–31]. The self-assembly of the alkanethiols results in a unique arrangement regarding a rather well-defined polar angle of the chains with respect to the surface normal of the metallic substrates. The head group contains a sulphur atom which binds to the substrates by splitting off the hydrogen atom [32–34]. The backbone of the molecule is an alkyl chain which is, in its most simple form, terminated by a methyl end group. Since the bonds in the alkyl chain are only σ (single) bonds, they permit rotation around the bond axis, and therefore the chain has a high degree of freedom apart from the symmetric all-trans conformation. Instead of the terminating methyl group, other groups can be used as a substitute (e.g., –OH, –COOH). Depending on the chemical character of the groups, the assembled monolayer has a hydrophobic or more hydrophilic behavior.

Instead of the saturated alkyl chain, double bonds or even aromatics can be introduced. The head group may also consist of any molecule which binds to the substrate of interest. There have been numerous reports on the properties of such monolayers on metal surfaces, including their structure, chemical properties, and applications for the structuring of surfaces. In contrast to metal surfaces, very few investigations so far have considered the adsorption of alkanethiols on semiconductor surfaces. This lack of knowledge is also in contrast to the large body of investigations which deal with the modification of semiconductor surfaces using inorganic sulphur compounds [33–37]. Reports have been given on the influence of alkanethiols on Schottky barrier heights on metal–semiconductor contacts and on the passivating properties of adsorbed thiols on semiconductor surfaces [35, 37].

Besides thiols in *n*–alkanethiols, often-used head groups are sulphonic and phosphorus acids. Another popular example is organosilicon monolayers (e.g., alkyltrichlorosilane) on hydroxylated surfaces, which are well ordered, but typically do not exhibit the degree of long-range order observed for thiols on coinage metals and III–V semiconductor surfaces [38–41]. A compilation of the most often used SAMs and their structure is shown in Table 1. For more details, we refer to Section 5.

2.1. Substrates

With the advent of the transistor in 1947 (Bardeen and Shockley, Bell Laboratories), semiconductors became more and more important in technological development. Nowadays, practically no modern technological device runs without semiconductors. While silicon (Si) is the basic material for most electronic devices (e.g., processors) [42–49], III–V semiconductors are the materials of choice for optoelectronic devices. Recently, the development of, for example, organic light emitters (OLEDs) and other organic devices demonstrates the necessity of combining and structuring organic–semiconductor systems.

Semiconductor compounds consisting of elements of the third (B, Al, Ga, In, Tl) and fifth row (N, P, As, Sb, Bi) of the periodic system, that is, the so-called III–V semiconductors GaAs, InP, or $Al_xGa_{1-x}As$, are frequently used in

Table 1. Structure of some frequently used SAMs.

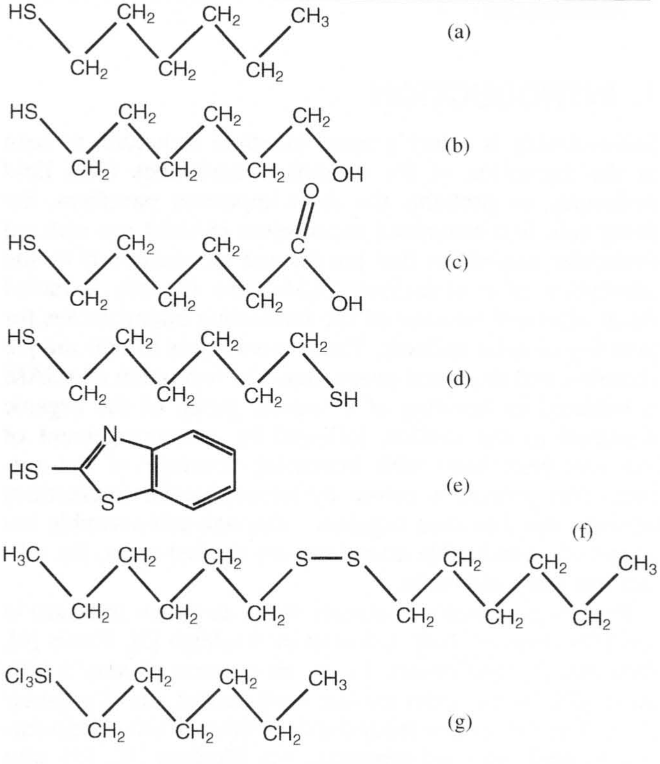

Note: (a) *n*–alkanethiol, (b) ω–mercaptoalkanol, (c) ω–mercaptoalkane carboxylic acid, (d) α, ω–alkanedithiol, (e) mercaptobenzothiazole, (f) 1,1′–dialkyl–disulfide, (g) alkyltrichlorosilane. For the purpose of illustration, the chain length is set to $n = 6$.

modern optoelectronic devices, such as light-emitting diodes (LEDs), semiconductor lasers, optoelectronic modulators, or light detectors. The reason for using these materials in optics rather than the most widely employed Si is the difference in band structure: many III–V semiconductors have a direct bandgap, resulting in very efficient optical absorption or emission. Silicon is an indirect bandgap semiconductor which, in its crystalline form, has only a few optical applications. The specific optical properties of III–V semiconductors are given by their band-structure characteristics. The wavelength of luminescence (e.g., the color of the LED) is determined by the width of the forbidden gap between the valence and conduction bands. The efficiency of such devices is strongly related to the effective mass or density of states for the carriers in each band.

Because of the above-mentioned optoelectronic properties, the most prominent compound semiconductors are gallium arsenide (GaAs), gallium phosphide (GaP), gallium nitride (GaN), indium arsenide (InAs), and indium phosphide (InP) [50a, 50b]. Heterostructures of alternating thin layers of the above compounds are made in order to tune their optoelectronic properties [50b].

Most semiconductor surfaces used for research are made from high-quality single crystals which are produced by Czochralski or Bridgman techniques. In the case of III–V semiconductors, two surface orientations are of utmost importance. First is the (110) surface, which is the natural cleavage plane. Cleaving a III–V semiconductor along this plane results in surfaces with the highest grade of perfection. For more details, for example, surface relaxation, we refer to [50, 51]. Second is the (001) surface, which is the technologically used plane for etching processes in the electrooptical industry [35–37].

The crystals are typically doped (naturally or artificially) with carrier concentrations of 10^{-15}–$10^{-18}/\text{cm}^3$ in order to make them useful for technical applications. The influence of the carrier concentration on the binding of organic self-assembling monolayers is weak, and thus will be ignored in this review.

2.2. Sample Preparation and Self-Assembly

2.2.1. Sample Preparation and Self-Assembly from Solutions

The alkanethiols (most typically hexadecanethiol or dodecanethiol 95–99.5%) were dissolved in isooctane, ethanol (absolute), or hexadecane. The typical concentrations were in the range of 10^{-3}–10^{-5} M. More polar species (e.g., mercaptobenzothiazole, MBT; see Section 4) were dissolved in an aqueous solution with 5% ethanol. After immersion times of 24–36 h, the samples were rinsed with fresh solvent, dried under a nitrogen stream, and inserted into, for example, the spectrometer immediately. As substrates, either prenotched bars of Czochralski-grown and crystallographically oriented single crystals were used or, for the purpose of comparison, gold films were prepared using a Knudsen cell in UHV (base pressure: 2×10^{-10} mbar), evaporating gold (Goodfellow, 99.999 + %) onto a freshly cleaved slice of muscovite mica. The mechanism behind the self-assembly process on gold was first published by Poirer and Pylant [52]. The corresponding mechanism from dilute solutions on semiconductors will be investigated in Section 3.1, and for vapor deposition in the following paragraph.

2.2.2. Sample Preparation and Self-Assembly in UHV

The alkanethiol (e.g., dodecanethiol Aldrich, 98%) was let into the preparation chamber by means of a sapphire-sealed leak valve (Vacuum Generators VG, U.K.), which is inert to sulphur-containing species. In order to minimize the content of dissolved oxygen in the alkanethiol, the liquid was degassed by several repeated pumping, purging (with N_2, 99.999%, Messer Griesheim, Germany), and freezing cycles, before passing the leak valve. The valve and its surrounding should be slightly heated (35–45 °C) to prevent condensation and physisorption of the alkanethiol molecules on the inner sealing surfaces of the leak valve [53]. Besides spectroscopic techniques, a scanning tunneling microscope (STM) was used to investigate the adsorbed systems in UHV. Because of the active properties of the freshly cleaved InP(110) surface, all experiments (at least with submonolayer coverage) had to take place in UHV. Therefore, the STM head, which was constructed on a CF-100 flange, had to be mounted inside a UHV chamber. The base pressure in the recipient was $2 * 10^{-10}$ mbar using a combination of a turbo molecular and a rotary pump. For the sake of low vibration, this combination could be shut down. In this case, we used a liquid-nitrogen-cooled Titan sublimation pump and an ion getter pump instead. These were able to maintain good vacuum conditions without generating vibrations. When the TSP was cooled with liquid nitrogen, the pressure went down to $5 * 10^{-11}$mbar. The tungsten tips were self-made with the help of a two-step procedure (see [22, 54–58]). Because of additional control of the current direction of the last applied sine wave, the tips are also free from covering oxide layers. Following this procedure, the tips were rinsed with tridest H_2O, and were directly inserted into the vacuum chamber. A self-constructed system allowed not only changing the samples, but also changing up to seven tips at one time, without breaking the vacuum. The supporting X-ray photoelectron diffraction (XPD) and X-ray photoelectron spectroscopy (XPS) measurements were made with an Escalab 220 iXL (Vacuum Generators VG, U.K.) spectrometer, equipped with a monochromatized Al Kα source and a computer-controlled microstage.

The comparative SXPS spectra were recorded at the BESSY synchrotron storage ring in Berlin at the undulator beamline TGM-5, using a VG Baby-Aries spectrometer.

As an example for consecutive adsorption of thiols in UHV, the coverage and order of dodecanethiolate molecules on InP(110) surfaces was investigated by Zerulla et al. [53] and on gold by Widrig et al. [59] and Poirer et al. [60]. In the following paragraph, the coverage and structure of the adsorbed molecules are controlled by spectroscopic means and STM investigations depending on the dodecanethiol dose. Starting from the clean, cleaved semiconductor surface, the STM images show the different states of order in the self-assembling films with molecular/atomic resolution.

Additionally, STS was applied, in order to distinguish covered and uncovered regions with high lateral resolution. Further proof is given by (S)XPS and XPD spectra, obtained from measurements at the synchrotron storage ring BESSY and high-resolution laboratory sources, at all consecutive stages of adsorption. The first straightforward step in the investigation of vacuum-deposited alkanethiols on III–V semiconductors was to monitor the clean, freshly cleaved (UHV conditions) semiconductor surface itself via STM. Depending on the polarity of the tip with respect to the substrate surface, the STM image shows either the positions of the indium or the phosphorus atoms [61–63]. The surface was recorded with a positive tip, therefore showing the filled "dangling bonds" of the phosphorus atoms. The distances of the atoms were analyzed in the [001] and [1–10] directions of the surface. These measured distances of 590 and 420 pm are close to the ideal distances of 587 and 415 pm, respectively, which can be taken from [35–37, 64]. The difference between ideal and measured distances are well in the limit of the temperature-dependent reproducibility of the STM piezocrystals, which were calibrated before with the help of a highly ordered pyrolytic graphite (HOPG) surface. It should be mentioned that surface-relaxation effects have an influence on the height offset of the topmost phosphorus atoms with respect to the indium atoms (I–P), but no effect on the P–P distances within the first layer [35–37, 65].

Further STM investigations on a larger scale show only minor distortions of the surface in the form of small steps (typical height 1–6 atoms). Typically, the surfaces are free from defects for lateral dimensions as large as 1 mm^2. For the typical lateral scale of atomic-resolved STM graphs, this, in fact, allows for the investigation of adsorbates on regions without any substrate defects.

STS measurements of various positions on such freshly cleaved InP(110) surfaces lead to a composite I/U spectrum. The shown spectrum is a result of 256 independent recorded spectra, which have been added to suppress random noise. The main characteristic feature of these spectra is the very good visible bandgap, which is about 1.3 eV at room temperature in the case of InP [53]. In our experiments, the line shape of the spectra was independent of the exact lateral position of the STM tip; therefore, it still represents a more macroscopic feature of the semiconductor, and not an atomic behavior—even if the lateral resolution in the normal image mode achieved atomic resolution. Surface-sensitive (S)XPS studies of these cleaved surfaces, which are proof of their cleanness, are presented in [53, 64–67].

After the characterization of the clean InP(110) surface, a systematic, consecutive, dose-dependent treatment with dodecanethiol molecules was applied to the semiconductor surface. First, a dose of 1 Langmuir dodecanethiol was applied. The result of this treatment was the complete loss of resolution in the STM graphs. The reason for this behavior is probably that dodecanethiol molecules are bounded via the sulphur atoms to the indium atoms [66, 67]. The alkyl chains, on the other hand, only adhere loosely to the surface. Because of the sparse density of the molecules at 1 Langmuir (sticking coefficient <1), sufficient space remains between the molecules. When the STM tip scans across such a molecule, the alkyl chain is moved by the tip. Therefore, a clear STM image could not be obtained.

Nevertheless, the adsorbed molecules can be traced with the help of XP spectroscopy. The spectra show the expected C1*s*/S2*p* intensity ratio of 12:1 (corrected with the respective sensitivity factors and the spectrometer transmission function) for dodecanethiol, while the total signal strength (e.g., C1*s*) of the adsorbed molecules is far below the well-known intensity expected for a typical monolayer (see [32]).

The measured relative and absolute intensities are proof for nonoverlapping molecules with a sparse density at the surface.

This behavior changes if a larger dose of dodecanethiol is applied. It is possible at 100 Langmuir to get a good resolved graph again. The situation is displayed in Figure 1. It shows a dense monolayer of "lying" dodecanethiol molecules. Note that the chains are not randomly distributed, but mostly pointing into a crystallographic main axis (to prevent disturbances by the scanning tip, and therefore misinterpretations, the main axis of the InP crystal was not chosen parallel to the image boundaries, but turned 15° counterclockwise).

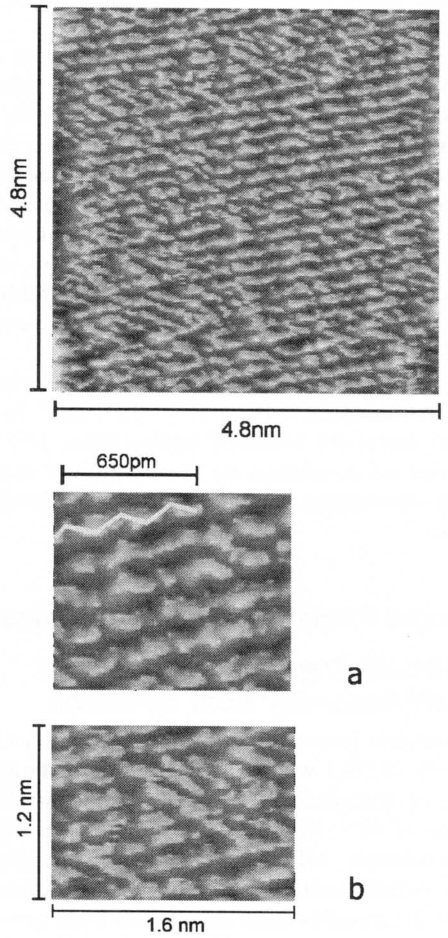

Figure 1. STM picture at 100 Langmuir dodecanethiol ($U_T = 2.4$ V; $I_T = 500$ pA). (a) STM-picture at 100 Langmuir dodecanethiol (enlarged). The all-trans conformation of a single molecule has been graphically emphasized. (b) STM picture at 100 Langmuir dodecanethiol (enlarged). The picture shows a region where some chains are misaligned. Reprinted with permission from [53], D. Zerulla and T. Chassé, *Langmuir* 18, 5392 (2002). © 2002, American Chemical Society.

Figure 1a (enlarged part of Fig. 1) shows the structure of the alkyl chains (all-trans conformation), which can also be resolved in some regions. While most of the chains are pointing into the [001] direction of the substrate, upon closer inspection, it can be seen that some chains point partially into other directions (see Fig. 1b). This can easily be explained by the following fact: because of the σ bondings between the carbon atoms in the alkyl chains, turning of molecular parts around these bonding axes is permitted. While the all-trans conformation is the energetically lowest form, other conformations will occur at room temperature, whose total energies are only slightly higher. Once lying on the surface at high densities, these conformations are also stabilized by the neighboring molecules within the dense package. To confirm the above thesis, it is necessary to investigate all possible geometrical variations which might occur on the surface. Assuming that the orientation of all of the In–S bondings between the substrate and the thiol molecules point into the [001] direction of the substrate due to the InP(110) surface (we will discuss this later), the number of alternate conformations projected onto the surface is limited, at least if the permitted values of the C–C angles are low in number, because of the state of adsorption at the surface. This means that, besides the pure all-trans conformation which is shown in Figure 1a, it should be possible to find a limited number of molecules in slightly differing conformations (e.g., only one turn around one bonding axis, leading to a change in one angle in the carbon backbone in contrast to an all-trans conformation), and therefore a differing orientation of their main axis after the deviating bond. This case is shown in Figure 1b. Further geometric analysis of the STM graphs reveals that the measured bonding angles between the carbon atoms in all-trans conformation molecules are larger then 110° (about 130–140°). First, this is a result of the slightly changed conformation of the molecules, while being physisorbed at the surface. The necessary structure to reach a minimum of total energy for a physisorbed alkyl chain (carbon in sp^3 hybridization) does not have a perfect planar carbon backbone parallel to the semiconductor surface. Second, the STM imaging mode projects this three-dimensional molecule into the two-dimensional space, resulting in images of molecules which seem to deviate from the octahedrally bonded situation.

A further proof that the STM graph displays "lying" molecules is given by angular-resolved XPS measurements. Here, the ratio between the C1*s* and the S2*p* peak intensity does not change while varying the take-off angle. Besides, the pure C1*s* and S2*p* peak intensities at normal take-off angle do not allow for models other than "lying" molecules, especially if models of a higher thickness than a "lying" monolayer can be excluded due to the substrate (e.g., P2*p* or In4*d*) to adsorbate intensity ratio, for example, C1*s* (see adsorption step 3 in Figs. 4 and 5).

If the sulphur atoms were covered significantly by the alkyl chains, the (corrected) intensity ratio (C1*s*/S2*p*) would have to be higher than the measured ratio (12.2), which still displays approximately the stoichiometric ratio.

Increasing the dodecanethiol dose to 1000 Langmuir leads to the conditions shown in Figure 2. Inspection of this STM image reveals two different kinds of regions: the higher ones (brighter gray scales), which we interpret to consist of "standing" molecules, and the lower ones (darker gray scales), which are still formed by "lying" molecules, as can be seen at lower doses. Note that the STM graph still shows molecular resolution simultaneously in both kinds of regions at room temperature.

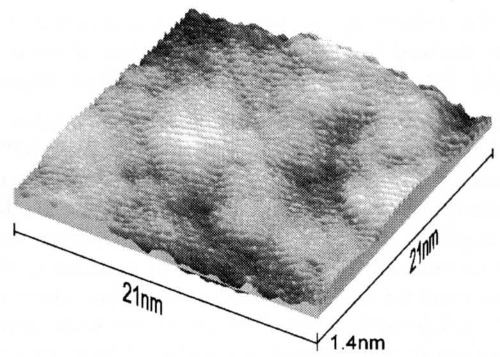

Figure 2. STM picture at 1000 Langmuir dodecanethiol ($U_T = 3.8$ V; $I_T = 250$ pA). Reprinted with permission from [53], D. Zerulla and T. Chassé, *Langmuir* 18, 5392 (2002). © 2002, American Chemical Society.

To ensure that both the "standing" and the "lying" regions do indeed consist of alkyl chains, both regions have been investigated via STS. The spectra are shown in comparison with an SXPS spectrum (excited at 55 eV with synchrotron radiation), recorded from surface-bonded alkyl chains, prepared from dilute solutions of dodecanethiol (Fig. 3) [32, 66, 68]. Despite the differences in excitation, the energetic positions of the peaks are identical. Both regions can therefore be assumed to be covered with dodecanethiols. The following arguments can be found to support the interpretation.

- From the STS–SXPS comparison, one can conclude that the whole surface is covered by dodecanethiol.
- The average height offset of the bright and dark regions of approximately 1.0–1.4 nm (taken from STM measurements) fits into the model of lying minus standing regions—taking the length of one dodecanethiol molecule (1.84 nm) and the expected angle from the surface normal of 34° into account [66, 67].

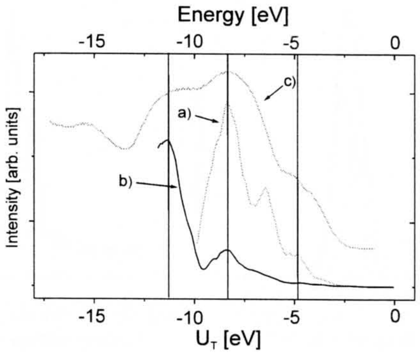

Figure 3. Locally resolved ST spectra of a DDT-covered region in comparison to an SXPS spectrum of a similar sample. Reprinted with permission from [53], D. Zerulla and T. Chassé, *Langmuir* 18, 5392 (2002). © 2002, American Chemical Society.

- In the following, we will present additional information, derived from detailed XPS studies of the substrate (In3*d*, P2*p*) and the adsorbate (C1*s*, S2*p*), respectively.

In order to obtain additional reliable information on the surface coverage, we performed highly resolved XPS measurements for all peaks of interest at all stages of adsorption. As an example, we provide the detailed XP spectra for step 3 (1 kLangmuir dose) in Figure 4. The intensity information was extracted from these spectra by calculating the true peak area from an elaborate fitting procedure which uses an iterative background subtraction combined with convoluted Voigt profiles in a multipeak algorithm. The corresponding residuals are also given in each graph. The extracted intensities for all stages of adsorption are given in Figure 5. Note that the data are normalized individually. That is, for example, the ratio between carbon and sulphur is always greater than 12. In Figure 5, the highest point (at step 4) of this ratio is normalized to 1 in order to display all graphs in the same diagram. This allows a detailed comparison between the individual intensities. A measure of the reliability of this method is given by the substrate intensities (In3*d*, P2*p*). In principle, both intensities should be identical in pairs at all points. In comparison to the magnitude of changes of the adsorbate intensities, this is true. Now, we focus on the carbon/sulphur ratio. In first-order approximation, the intensity of both elements should rise while more molecules are being adsorbed on the surface. The difference between both intensities in the course of adsorption is due the fact that the carbon–alkyl chains are covering the binding sulphur atoms in a standing film, and therefore weaken the XPS intensity of the sulphur signal. This means that the higher the C/S ratio, the more "standing" is the ordered monolayer. Returning to the adsorption step at 1 kLangmuir this means that this film already shows a high degree of standing molecules, but compared to the last step (doses >10 kLangmuir), one finds that the degree of order is not at its maximum. This is exactly how we interpreted the STM graph before. The film is partially well ordered (standing), but has also some regions which have a lower density of adsorbed molecules (lying).

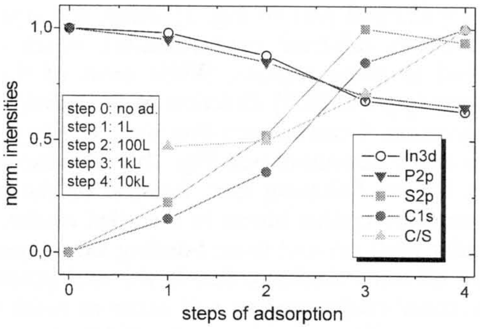

Figure 5. Comparison of the XPS intensities of adsorbate and substrate peaks and the carbon-to-sulphur ratio, derived from background-corrected peak areas at the different adsorption steps. Note that all measurements have been normalized individually. Reprinted with permission from [53], D. Zerulla and T. Chassé, *Langmuir* 18, 5392 (2002). © 2002, American Chemical Society.

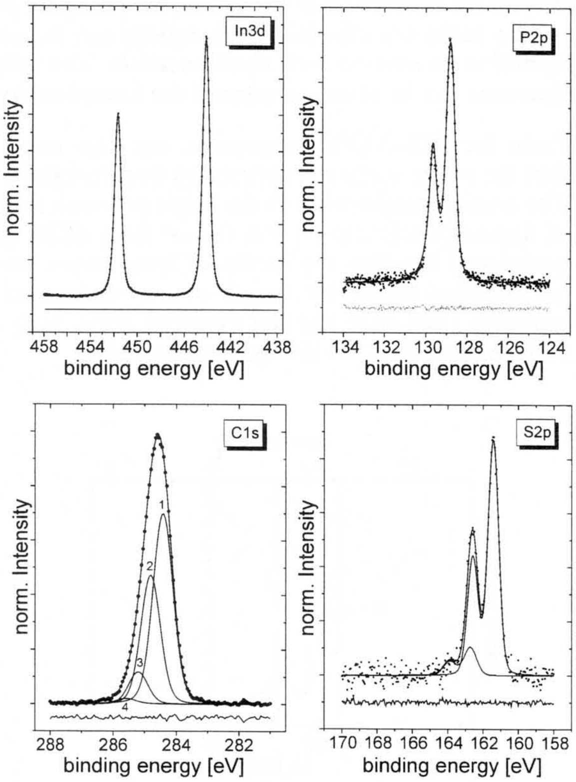

Figure 4. XPS spectra of DT on InP(110) at 1 kLangmuir. (a) In3*d*. (b) P2*p*. (c) C1*s*. (d) S2*p*. Reprinted with permission from [53], D. Zerulla and T. Chassé, *Langmuir* 18, 5392 (2002). © 2002, American Chemical Society.

Well-ordered self-assembling monolayers, which can be compared to systems prepared from dilute solutions, are also found. The required minimum dose for a quasifaultless monolayer is between 5000 and 10,000 Langmuir dodecanethiol. An example for such a system is shown in Figure 6. The SAM is prepared at 10,000 Langmuir dodecanethiol on a freshly UHV-cleaved InP(110) surface. The array of "standing" molecules appears faultless, although, on closer inspection, a small deviation in brightness (=height) is detectable. This effect might arise from some residual stress in the SAM, which itself comes from the exceptional three-dimensional tight packing of the alkanethiol molecules

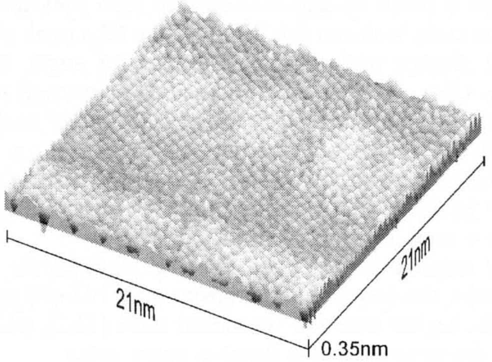

Figure 6. STM picture at 10 kLangmuir dodecanethiol (U_T = 3.8 V; I_T = 250 pA). Reprinted with permission from [53], D. Zerulla and T. Chassé, *Langmuir* 18, 5392 (2002). © 2002, American Chemical Society.

in the well-ordered "van der Waals stabilized" layer (see Section 3.3 and [66, 67]).

Note that neither the gray scale nor the z-axis scale of Figure 6 is equivalent to that of Figure 2, but is adjusted for more sensitivity in height display. Figure 7 shows an enlarged section of the former STM graph. Even on this scale, the monolayer appears well ordered. A small distortion of the graph can be found by comparing the resolution in the X and Y directions. This distortion could be caused by two points. First, the shape of the STM tip could be slightly asymmetric. Second, the tilted structure of the self-assembled monolayer in combination with the impact of the tip into the layer (Fig. 8) could cause such an effect. Because of some further tests with this tip and the knowledge of the inner structure of the monolayer [66, 67], we tend to interpret the distortion to be due to the "tilted" structure of the adsorbate, and not caused by imperfections in the shape of the tip.

The STM analysis of the adsorbate system is completed by a determination of the molecular spacing. For this purpose, not only was an exemplary determination on a "good fitting location" in real space made, but so was a complete two-dimensional fast Fourier transformation (FFT) [53]. The transformation allows us to judge the distances of all investigated molecules simultaneously, and to detect superlattices and repeating distortions in one image. Repeating structures in time (and therefore, due to the scanning, in space) are displayed as bright "spots" (accumulation points). The most prominent spots belong to the rectangular reciprocal surface unit cell of the underlying InP lattice, and are highlighted via white lines for better visibility. As far we can judge from numerous STM graphs, the adsorbed monolayer appears faultless and well ordered. But how can we be sure that the system under investigation is a unique, distortion-free monolayer system on larger scales? From STM measurements alone, it is practically impossible to obtain positive proof of the single-domain structure. If the area under investigation (STM) is successively made larger, there will be a certain point where the necessary molecular resolution will be lost. This is especially true if superlattices, and therefore domain boundaries, are missing, which has to be expected for single-domain structures. Proving the single-domain structure investigations on a macroscopic scale is necessary. For this, we refer to Section 3.3, where two different spectroscopic approaches have been chosen which are able to analyze structural aspects on macroscopic scales [66, 67].

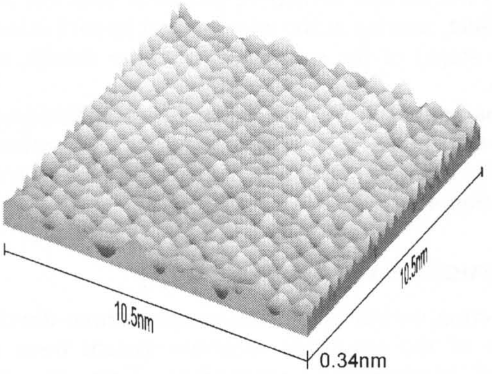

Figure 7. STM picture at 10 kLangmuir dodecanethiol (enlarged). Reprinted with permission from [53], D. Zerulla and T. Chassé, *Langmuir* 18, 5392 (2002). © 2002, American Chemical Society.

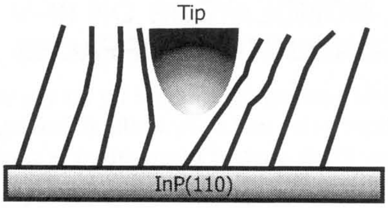

Figure 8. Model of the dodecanethiol–InP(110) system while measured by STM. Reprinted with permission from [53], D. Zerulla and T. Chassé, *Langmuir* 18, 5392 (2002). © 2002, American Chemical Society.

Summarizing the recent results for UHV deposition, four main phases of adsorption on InP(110) were found. First, at doses < 10 Langmuir, the surface is only sparsely covered, still permitting the alkyl chains to move "sideways" on the surface; therefore, no stable STM image was presented. Second, approximately at 10 Langmuir, a dense layer consisting of lying molecules is formed. The contact between the alkyl chains is stabilizing enough to give good resolution, even at room temperature. Third, at doses of 1 kLangmuir, parts of the monolayer start to stand up. This is done neither statistically nor individually, but in well-defined domains, while other regions are still flat on the surface. A comparison between the height of the standing and the lying molecules in the same graph permits us to deduce this difference precisely. From that, we can learn how deep the tip penetrates the organic layer.

From other papers concerned with the behavior of tip–surface interactions on organic films, it is well known that the tip might intrude into the organic layer while scanning [22, 56, 69]. This behavior is also to be expected for the STM parameters used here in connection with the insulating properties of the adsorbate system under investigation (See Section 2). Further proof is given by the height information of the different regions in Figure 2. The average height difference of the "standing" and the "lying" regimes is about 0.8 nm. Note that the given z axis in the graph denotes the maximum distance between the highest and lowest point; therefore, the average distance between neighboring regions is significantly lower. If the tip did not intrude into the layer, this distance would be about 1.5 nm (the height of a 34° tilted dodecanethiol monolayer) minus the height of a lying molecule, which should be near 0.2 nm. The result of 1.3 nm is significantly higher than the measured value of 0.8 nm; therefore, the tip intrudes about 0.5 nm into the layer, as is depicted in Figure 8.

In the last stage (dose >10 kLangmuir), a macroscopic "single-domain" monolayer covers the semicondoctor, which is virtually free from defects. All molecules have the well-defined tilt angle in the [001] direction of the InP (110) surface (see Section 3.3). The chain–chain distances, and therefore the tilt angle, reflect the lattice properties of the underlying semiconductor, which were additionally proved by an FFT analysis of the STM image and locally resolved tunneling spectra.

3. THIOL MONOLAYERS ON III–V SEMICONDUCTOR SURFACES

Thiols on III–V semiconductors are by far the most promising combination, as we will show in the following paragraphs of this section. Their ease of preparation is similar to thiols on gold (with some exceptions; see Section 2), and they form dense and therefore passivating (see Section 3.2) and highly ordered (see Section 3.3) monolayers which can be structured with the methods introduced in Section 3. But first, we will discuss the self-assembly and its speed, depending on the method of sample preparation, in the next paragraph.

3.1. Speed of Self-Assembly

While the adsorption under vacuum conditions is primarily a function of the differential pressure of the molecule species [53, 70], the adsorption from dilute solutions is easily traceable in the time domain [71]. Confining our systems to alkanethiols with lengths between 6 and 20 carbon atoms, the adsorption and self-assembling speeds are very similar. The methods to probe the degree of order or state of assembly can include in-line techniques which can be used without interrupting the self-assembling. This has been done by Grunze and Wöll, using second-harmonic generation (SHG) and sum-frequency generation (SFG) on the adsorption of thiols on gold [72].

The other class of experiments, that is, all surface-science techniques working under UHV conditions, needs an interruption of the assembling process. For gold and silver as substrates, this is not critical because they do not react with the atmospheric oxygen, but for semiconductors, this is not easily done. One method is to prepare as many samples as planned measurements, and to use each sample only one time. Despite the great efforts which are connected with this method, we chose to use it because it opened up the full choice of surface-science techniques [53, 64]. In the following, we present a time-dependent XPS analyzed study on the speed of self-assembly. Our concrete system is 1 mmol concentrated HDT in isooctane on InP (110).

The XPS intensities are presented in Figure 9. In the beginning, all signals, except the substrate-related signals, increase quickly until the alkyl chains start to cover the binding sulphur atoms of the thiol groups. This is the point where the ordering starts. After 24–36 h, the system does not change anymore. In order to be on the safe side, we chose assembly times >36 h for our experiments on well-ordered SAMs.

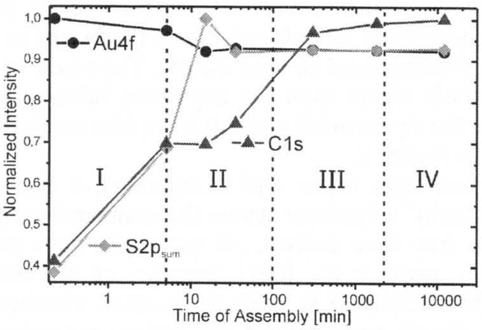

Figure 9. The self-assembling process is monitored via time-dependent XPS spectroscopy of the important substrate and adsorbate elements. Adsorbate: HDT in isooctane [64].

3.2. Passivating Properties

III–V semiconductors are not immune to oxygen. A freshly cleaved (110) surface, and of course other surfaces as well, would oxidize within fractions of a microsecond if not protected against atmosphere. Furthermore, if chemical etching is needed in the production of, for example, nanostructured devices (see Section 4), the monolayer should be able to resist the etching on the time scale of minutes. In the following, we will discuss the passivating properties of self-assembling monolayers on the example of alkanethiols on InP(110). First, we briefly note the preparation procedure which is necessary to make a monolayer free of defects (for more details regarding the preparation, we refer to Section 2). If the self-assembling takes place in a dilute solution, it is necessary to purge the solution first with nitrogen (or Ar) for about 20 min. Otherwise, the residual oxygen in the organic solvent immediately reacts with the substrate surface [32, 64]. But, if the prenotched crystal bars are cleaved in a degassed solvent, which contains μmol · mmol concentrated thiols, oxygen is absent, even in an extremely surface-sensitive SXPS measurement [32, 64]. In order to test the passivating properties of samples with fully assembled monolayers, we exposed the samples to atmosphere and humidity on time scales of hours, days, and even months.

While no changes of the samples were spectroscopically detectable within days, as judged from the SXPS sensitivity scale, on the time scale of a month, slight changes were detectable [64]. But even this slight change proved that at least 90% of the samples were not affected. These results show that readily assembled monolayers can be handled without further precautions in technological processes.

Then, we exposed similar samples to electrochemistry [64, 73]. At the start, a potential which was suitable for etching of the semiconductor was applied and changed to cyclic, while in parallel the current voltage (*CV*) ratio and the capacity were recorded. The results showed that the monolayer protects the semiconductor surface effectively [64, 73]. After some minutes, the monolayer showed the first degradation, but from the current density, it was clear that this is only a minor effect, starting at the edges and at imperfections (e.g., cleavage steps) of the substrate (for more details, refer to [64, 73]).

Summarizing the results, alkanethiol monolayers (for length >6) protect III–V semiconductor (110) surfaces well enough to be used as masks, especially if nanostructured (see Section 4).

3.3. Structure via Spectroscopy

In this section, we will analyze the complete three-dimensional structure of the adsorbate–substrate system from a multitude of spectroscopic approaches. First, we describe investigations of the X-ray absorption near-edge structure (XANES) of adsorbed hexadecanethiol monolayers on InP (110).

We will demonstrate that the self-assembly on III–V semiconductor surfaces results in a unique arrangement of the alkyl chains with a rather well-defined polar angle of the chains with respect to the surface normal. However, on the metal single-crystal surfaces investigated so far, the molecular orientation in the azimuthal direction is not uniform. This is because the surface symmetry permits the formation of several domains of differing azimuthal molecular orientation. Here, we report on self-assembled monolayers, which possess a very high degree of molecular order in both the polar and azimuthal orientation of the organic molecules with respect to the substrate. This unique feature has been observed during investigations of III–V (110) surfaces, which were performed in order to explore the self-assembling properties of compound semiconductor surfaces. These conclusions have been derived from the X-ray absorption near-edge structure XANES measurements taken at the carbon K edge (CK XANES), which have been carried out to determine the main structural features of the alkyl chains on InP (110). First, core-level photoemission XPS studies were performed in order to characterize the adsorbed organic layers of interest, which were prepared by adsorption from millimolar solutions of thiols in isooctane for durations of 24–36 h, according to Section 4.4. InP (110) faces were prepared by cleavage of prenotched bars in solution (see Section 4.4). As we will discuss in more detail in Section 4, essentially only one sulfur species is present on the freshly prepared SAMs in XPS and SXPS experiments. Also, taking into account the complete absence of oxygen-related features, even after contact with the atmosphere, we conclude that alkanethiols form stable and contamination-free monolayers on InP (110). Examples of other investigations on similar semiconductor surfaces can be found in [24, 25]. The XANES measurements in a partial electron yield mode on SAMs of adsorbed alkanethiols on InP 110 were carried out at the beamlines HE-TGM2 and PM5 of the BESSY I storage ring in Berlin. Figure 10 displays angular-resolved CK XANES of a monolayer, prepared by adsorption of hexadecanethiol (HDT). The absorption spectra were recorded at several incidence directions of the soft X-ray photons with respect to the surface normal polar angle (−60 to 80°). Here, the polarization vector of the linearly polarized synchrotron radiation was fixed in the azimuthal orientation to allow only variation parallel to the (110) plane. The spectra exhibit two main absorption peaks. The peak at the higher photon energy is attributed to σ^* C–C related resonance. The strong feature at the lower photon energies near the edge is mainly due to the σ^* C–H orbital [66, 67]. However, the well-resolved splitting that occurs at certain angles suggests a more complicated origin of this feature, which will not be discussed here. Notice the very good matching of the background for all of the spectra at both the lowest and highest photon energies. This is evidence for the reliability of the spectra following the flux-normalization procedure. The spectra show significant angular-dependent changes. In particular, the intensities of these features do not proceed in parallel, but they show pronounced maxima at quite different incidence angles, exhibiting nearly an inverse behavior. However, we will start focusing on the angular dependence of σ^* C–C related absorption, which contains information on the spatial orientation of the carbon backbone of the adsorbed molecules. Therefore, a peak shape analysis has been performed after subtracting an arctan-like step function which emulates the CK edge. In our special case, the exact position and width of this edge are not critical to the fit. The data in Figure 11 display the evolution of the absorption of the σ^* C–C resonance of the CK XANES of HDT (Fig. 10) in dependence on the photon incidence direction as characterized by the polar and azimuth angles. The data have been derived from σ^* C–C intensities obtained from the fits, following flux normalization of the recorded absorption spectra.

The solid line represents a fit curve to the experimental absorption values which will be explained later. The graph shown in Figure 11 reveals a clear minimum, as well as a maximum separated by about 90°. From the angular

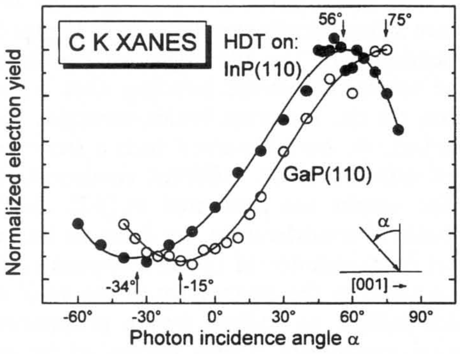

Figure 10. Series of normalized XANES absorption spectra of an adsorbed HDT monolayer on InP (110) with different polar angles. The retard potential of the partial yield detector was set to 150 V. Reprinted with permission from [66], D. Zerulla and T. Chassé, *Chem Phys. Lett.* 311, 8 (1999). © 1999, Elsevier Science.

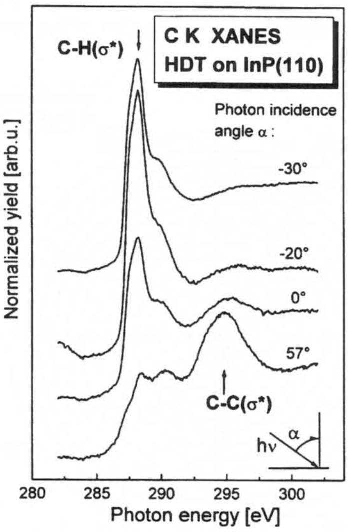

Figure 11. Plot of the absorption strength of the C–C(σ^*) resonances of HDT monolayers on InP and GaP in dependence on the polar angle. Normalization was performed as described in the text, and the maxima were set to 1. Error bars given for 0 and 80°. Reprinted with permission from [67], T. Chassé et al., *Surf. Rev. Lett.* 6, 1179 (1999). © 1999, World Scientific Publishing.

position of these extrema, the tilt angle can be determined to be about 34° from normal. Furthermore, we suggest from the nearly vanishing absorption in the minimum and high absorption in the maximum that a high degree of order has to be present in the layer. Note that the degree of linear polarization of the synchrotron beam itself is near 85%, and therefore not permitting, for example, the complete vanishing of the adsorption in the minimum, even if the order in the layer is perfect. In order to shed light on the azimuthal orientation of the chains, additional intensity data were obtained from a set of measurements taken at normal incidence (polar angle 0°), but varying azimuth angles of the sample 0–360° by rotating the sample with respect to its surface normal. The normalized intensities shown in Figure 12 in this manner also represent different orientations of the polarization vector with respect to the crystallographic directions in the surface plane. The graph clearly shows two striking absorption maxima at azimuth angles close to about 0 and 180°, and low absorption for polarization vector orientations far off these preferred angular directions. This very pronounced preference for strong X-ray absorption at polarization vector orientations about parallel to the (110) plane of InP (110) is rather exceptional. Although the graph of the experimental data is not exactly symmetric, this result provides strong evidence for a preferred tilt of the alkyl chains from normal toward the [001] direction. Because of the high anisotropy of this plot and the number of tested samples, we may essentially rule out averaging effects due to the possible existence of several domains possessing different tilt directions. This is important for the quantitative evaluation of the tilt angle because the data will only reveal the correct tilt angle if the azimuth polarization vector is chosen to correspond to a maximum in Figure 12, as has been done by recording the data displayed in Figure 11. In fact, the solid line in Figure 11 results from a fit to the experimental data following a $\cos^2$ function in dependence on the angle, as suggested by the matrix elements. This fit function has been slightly modified by a low-order polynomial in order to take into account an intensity decrease at highest incidence angles due to limited sample size. From the positions of the maximum and minimum in Figure 11, we can thus directly derive the tilt angle of the alkyl chains to be 34°+/−3°. The error has been estimated by taking into account both the sensitivity to intensity changes near normal incidence (Fig. 11), as determined from the slope of the fit curve, and the difference of the strength of the two opposite absorption maxima in Figure 12. Note, however, that the uncertainty in the azimuth angle of about 10° is much larger, unfortunately.

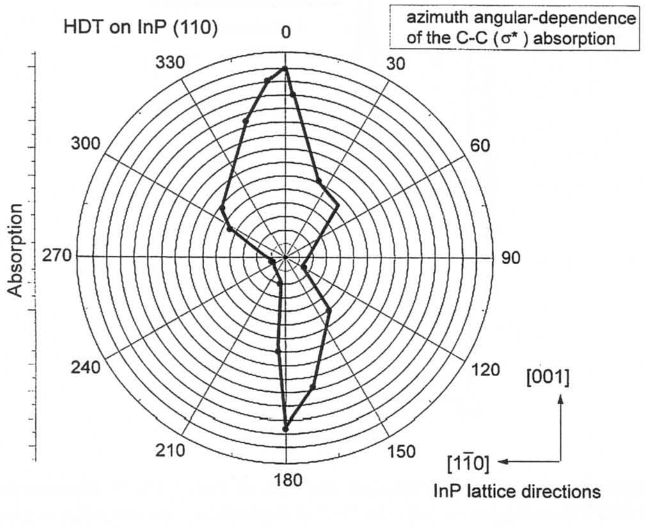

Figure 12. Plot of the changing absorption strength of the σ^* C–C resonance by varying the azimuthal angle while maintaining the polar angle at 0°. Reprinted with permission from [66], D. Zerulla and T. Chassé, *Chem Phys. Lett.* 311, 8 (1999). © 1999, Elsevier Science.

Thus, we cannot rule out slight deviations from an exact alignment within the (110) plane on this scale. Nevertheless, the experimental data presented above have clearly demonstrated the well-defined orientation of the adsorbed monolayer, resulting in an exceptionally high order of the adsorbed monolayer. To the best of our knowledge, a similarly pronounced preference of molecular orientation and high molecular order of alkanethiols has not been observed before on any other surface so far, including metal surfaces.

This strikingly high perfection of orientation of the adsorbed alkanethiol layers has to be discussed in terms of both adsorbate–substrate bonding and surface structure of the substrate. First, a preferential bonding of sulphur atoms to the surface indium atoms has been observed in several photoemission studies of inorganic sulphur species on InP (110) and InP (001) surfaces [35–37]. In particular, the formation of In–SH and P–H surface bonds has been reported in the case of the dissociative adsorption of H_2S on InP(110) [33, 34]. Second, we have performed synchrotron light-excited SXPS studies with alkanethiols on InP (110). These very surface-sensitive measurements also support the thesis of S–In bonding [73].

The rectangular surface unit cell of this zinc-blende type of substrate is characterized by In–In/P–P spacings along the [001] and [1–10] surface directions of 587 and 415 pm, respectively. The surface indium and phosphorus atom In–P bond lengths, 254 pm, are linked to form In–P zigzag chains within the InP (110) surface plane, which extend along the [1–10] direction. Thus, following structural arguments regarding the space requirements of the alkyl chains and their well-known tendency to form dense structures, a tilt of the alkyl chains toward [001] is indeed much more likely than toward [1–10]. These simple arguments fit very well with our observations regarding the tilt direction, which are schematically summarized in Figure 13. Further, a dependence of the tilt angle on the lateral distance of the sulphur–substrate bonding sites on the surface, and thus on the substrate lattice constant, has to be expected. In fact, we have observed such a trend by investigating thiol adsorption on different semiconductor surfaces, and the results are presented in [67]. Besides this purely geometrical consideration, we have to be aware of the structural inequivalence of the two opposite [001] surface directions due to the asymmetry of the In–P all-trans chains, which exhibit an indium and a phosphorus side. This structural asymmetry is also known to be responsible for the opposite spatial orientations of the empty and filled dangling bond orbitals of the surface indium and phosphorus atoms, respectively. Hence, it is reasonable to suggest that the experimentally observed preference of just one orientation of the alkyl chain has to be attributed to the

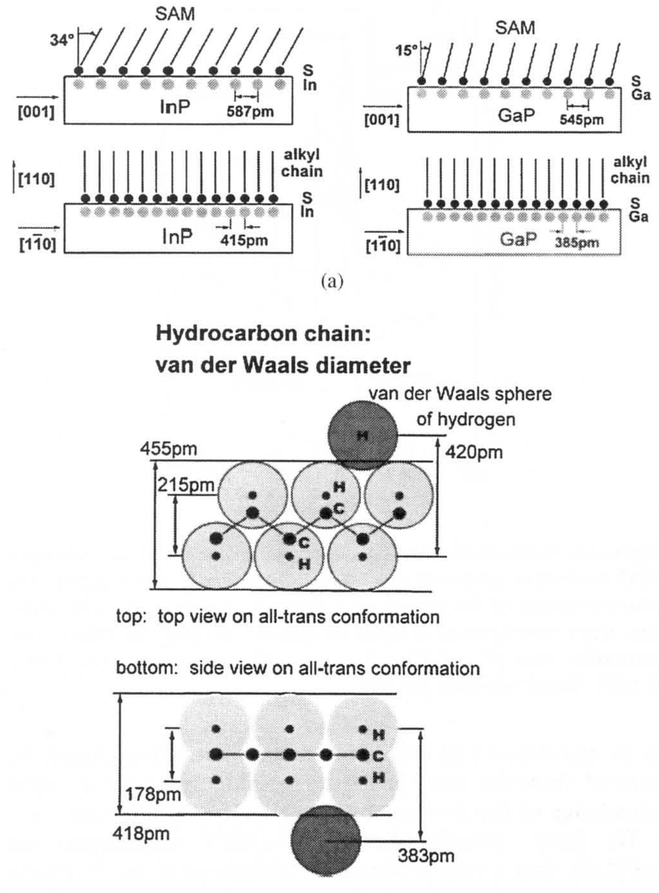

(a)

(b)

Figure 13. (a) Schematic structural model for the tilt orientation of the alkyl chains of HDT on InP(110) and GaP(110) (side views). Note that details of the local adsorption geometry are not reflected by this drawing. The surface indium and gallium atoms are included in order to emphasize the bonding to the sulphur atoms. The surface phosphorus atoms are not shown. (b) Schematic model of a hydrocarbon chain in an ideal all-trans conformation in combination with the hydrogen van der Waals radii. Space requirements due to the van der Waals interactions are provided by numbers. The reduction of these van der Waals dimensions by approaching an optimum registry is also indicated. Reprinted with permission from [67], T. Chassé et al., *Surf. Rev. Lett.* 6, 1179 (1999). © 1999, World Scientific Publishing.

orientation of these dangling bonds, most probably to the empty indium dangling bonds. Thus, structure as well as bonding constraints evidently force the adsorbed monolayer to adopt a uniquely well-defined structure, which allows us to propose the existence of single domains of the monolayer on InP (110), only limited by high-cleavage steps or other large defects of the cleaved substrate surface. Summarizing our results, we have observed the formation of a passivating, self-assembling organic monolayer on InP (110) by the adsorption of alkanethiols from the liquid phase. A tilt angle with respect to the sample normal of 34° and an azimuthal orientation parallel to the (110) plane of the InP lattice have been derived from the quantitative analysis of the XANES. The exceptionally well-defined orientation and high order within the adsorbed monolayer, as may be deduced from the strength and anisotropy of the X-ray absorption features, make this interface a candidate for a single-domain monolayer-adsorption system.

We will now extend the XANES measurements and discuss them in more detail. The structure of alkanethiol monolayers on III–V(110) surfaces was studied by analyzing the X-ray absorption near-edge structure (XANES) of the carbon K edge. Pronounced absorption maxima were observed for special orientations of the polarization vector of the radiation as revealed from angular-dependent measurements, suggesting a rather well-defined molecular axis of the alkyl chains. From quantitative evaluations of these angular dependences, the chains were found to be tilted from the normal toward the [001] direction of the (110) surfaces by 34 and 15° in the case of HDT adsorption on InP and GaP, respectively. The similarities as well as the differences in tilt angles between the substrates are discussed in terms of constraints imposed by the surface structure and lattice constants, as well as the space requirements of the van der Waals spheres of the adsorbed thiols. A unique feature observed on these monolayers is the nearly complete alignment of the alkyl chains with respect to the azimuthal orientation. We suggest that this adsorbate system represents the case of a single-domain orientation within the organic monolayer.

The spectra were recorded in a partial electron yield mode at a pressure of 5–8 $* 10^{-10}$ mbar. The retard potential of the partial yield detector was typically set to 50 V. All spectra were normalized with respect to the incident photon flux and the independently recorded background curve, which represents influences due to carbon contaminations on the optical elements of the beamline. The intensity calibration was performed by normalizing to the intensity difference between the spectrum background below the edge and at the highest energies, well above the resonances of interest. The orientation of the polarization vector of the soft X-rays was varied systematically by changing the incidence angle of the radiation with respect to the crystallographic orientations of the substrates in order to take advantage of the polarization dependence of the dipole matrix elements, which govern the absorption process.

Recent photoemission studies of the adsorption of alkanethiols (chain lengths $n = 10$–18) on InP(110) have demonstrated that alkanethiols form stable and contamination-free monolayers on this semiconductor surface [32]. This conclusion has been drawn from the complete absence of oxygen-related features in the spectra, even after contact with atmosphere, and the existence of essentially only one distinct sulphur species in freshly prepared thiol layers, which has been attributed to In–S bonds at the interface [32–37, 53, 66, 67]. Note that, from the chemical point of view, based on the experience outlined above as well as from the steric limitations due to the large space requirements of the alkyl chains, which will be discussed below, P–S bonds have been excluded via SXPS measurements, and will not be considered here [64]. In order to derive information on the intramolecular bonding, and most importantly on the structure of the adsorbed monolayer, we have investigated the X-ray absorption near-edge structure of the carbon K edge from alkanethiol SAMs on the cleavage faces of the III–V semiconductors InP and GaP.

Absorption spectra were recorded from SAMs of hexanethiol (HT) up to hexadecanethiol. Most complete datasets were gathered for the longer alkanethiols, which are well known to establish highly ordered SAM domains on metallic substrates like Au(111). In this paragraph, we will focus on the interpretation of these spectra, which were measured on the cleavage faces of InP and GaP. Figure 10 displays a set of CK XANES of a monolayer prepared by adsorption of HDT on InP(110). The absorption spectra in the figure were recorded at several incidence directions of the soft X-ray photons with respect to the surface normal, while keeping the azimuthal orientation of the polarization vector strictly parallel to the [001] surface direction. The spectra exhibit three absorption peaks. The broad peak at the highest photon energy, close to 295 eV, is attributed to the σ^* resonance, which is due to absorption by electron excitation from the C1s core level into the antibonding orbitals of the C–C bonds (hereafter called C–C(σ^*) resonance). The sharp peak at the photon energy of about 289 eV, close to the CK edge, mainly corresponds to the C–H(σ^*) resonance [68]. The third peak feature, which may be observed at about 2 eV higher energy compared to the latter, is much smaller in intensity. This peak feature appears much stronger in the absorption spectra for the shorter thiols, suggesting an origin due to the C–S bonds at the end of the alkyl chains. We emphasize the very good matching of the background for all of the spectra at both the lowest and highest photon energies, which is evidence for the reliability of the flux normalization procedure. Both C–C(σ^*) and C–H(σ^*) resonances show significant angular-dependent changes, which are reflected by the evident peak shape changes between the spectra. In particular, the intensity of the C–C(σ^*) resonance decreases when going from positive toward negative polar angles with respect to the surface normal. Note that there is no symmetry of the intensities with respect to the surface normal. Similar spectra of HDT monolayers on GaP(110) are shown in Figure 14. The overall shape of the spectra and the evolution of the intensities exhibit the same general trends as described above for HDT on InP(110). A noteworthy exception to this evident similarity is the smaller energy difference between C–C and C–H related resonances in the case of HDT on GaP. This energy difference is reduced by 0.7 eV (+/−0.3 eV) compared to HDT on an InP substrate. However, this difference calls for further statistical analysis of the whole body of experimental spectra and accompanying theoretical considerations, which will not be provided here. The C–C(σ^*) resonances contain the information on the spatial orientation of the carbon backbones of the adsorbed alkanethiols, which are of particular interest for the structure of the SAM. According to the dipole matrix elements for X-ray absorption, the intensity of the CK absorption resonance will be highest if the p contribution to the spatial orientation of the particular molecular orbital is parallel to the polarization of the X-ray light [74, 75]. The significant dependence of the resonance intensities on the polar angle of the photon incidence, and thus also the orientation of the polarization vector, as exhibited by the CK resonances in Figures 10, 11, and 14, indicates a preferential orientation of the carbon bonds of the organic adsorbates on both InP and GaP(110). Quantitative evaluation of the polar and azimuthal angles to be associated with this preferential orientation cannot be derived from the data in Figure 11 alone without detailed knowledge of the corresponding azimuth dependences.

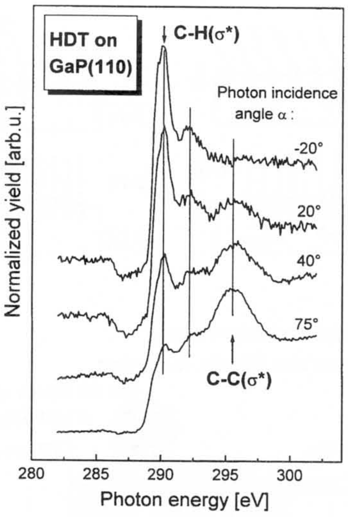

Figure 14. Normalized XANES absorption spectra of an adsorbed HDT monolayer adsorbed on GaP(110) at different polar angles. The retard potential of the partial yield detector was set to 50 V. Polarization vector and azimuth orientation parallel to [001]. Reprinted with permission from [67], T. Chassé et al., *Surf. Rev. Lett.* 6, 1179 (1999). © 1999, World Scientific Publishing.

We have recently shown, for HDT monolayers on InP(110), that a very pronounced anisotropy of the C–C(σ^*) resonance can be observed by rotating the azimuthal orientation of the polarization vector around the surface normal at normal photon incidence [66, 67]. In brief, the observed azimuthal dependence of the C–C(σ^*) intensity was strongly peaked along the two opposite [001] surface directions. The intensity nearly vanished far off these surface directions, in particular along [1–10]. Hence, a predominant orientation of the alkyl chains of HDT toward [001] was predicted [53, 66, 67]. In this manner, the anisotropies exhibited in Figures 10, 11, and 14, which were obtained for the particular azimuth with the highest C–C(σ^*) intensity, directly reflect a highly preferred orientation of the C–C bonds with respect to the surface normal, that is, a tilt angle of the alkanethiol chain. A peak shape analysis of the CK spectra has been performed in order to obtain quantitative data. An arctan-like step function was used to emulate the CK edge. In the special case of the C–C (σ^*) resonance and determination of its intensity, the exact position and width of this edge are not critical to the fit because this high-energy peak is already situated well above the threshold. The data in Figure 11 display the evolution of the absorption of the C–C (σ^*) resonance of the CK XANES of HDT (Figs. 10, 14) as a function of the photon incidence direction in terms of the polar and azimuth angles. The experimental data represent the intensities derived from the analysis of the spectral shapes, following appropriate flux normalization of the recorded absorption spectra. Closed and open circles denote data obtained from InP(110) and GaP(110), respectively. The solid lines represent fit curves to the experimental absorption values for SAMs on these two surfaces. The applied model functions for the fits represent the angular dependence by the term [$\cos^2 (90^\circ - (\alpha + \beta))$], essentially, including a single tilt angle $\beta > 0$ of the alkyl chains and the variable photon incidence angle α. The sign of the incidence angle α was arbitrarily chosen to obtain the maximum and minimum for $\alpha > 0$ and $\alpha < 0$, respectively.

The choice of this type of fit function is directly related to the polarization dependence of the absorption matrix elements and Fermi's golden rule [74]. We were able to neglect any effects due to azimuth orientation in the $\cos^2$ function because the experimental data to be analyzed were taken for the favored high-symmetry azimuth orientation, characterized by the polarization vector within the tilt plane, which is determined by the surface normal and the preferred [001] direction. The fit function has been slightly modified by a low-order polynomial in the case of the InP data in order to take into account an intensity decrease at highest incidence angles due to limited sample size. We further emphasize that no angular averaging was included in the fit functions (for example, regarding a range of tilt angles β or several distinct values for α), as might originate from differently oriented domains or from the absence of a preferential orientation. Nevertheless, the fit model matches the experimental data very well over the whole range of investigated incidence angles. We may conclude that a strongly preferred orientation of the alkyl chains exists with respect to the polar angle as well. The pronounced intensity maxima occurring only at certain azimuth and polar angles fix the observed preferential orientation in spherical coordinates by two independent angles, demonstrating the existence of a rather well-defined molecular axis of the hydrocarbon chain of the adsorbed thiol, which extends toward this direction. The data from InP show a clear minimum, as well as a maximum separated by about 90° (Fig. 11). From the angular positions of these extrema, the tilt angle β of this molecular axis of the HDT chain on InP(110) can be determined to be about 34°(+/−3°) from the surface normal toward [001]. In a completely analogous manner, we may determine a tilt angle of 15°(+/−3°) from the normal for HDT on GaP(110). We cannot draw any conclusion on preferred tilts toward the two opposite [001] directions, [001] or [00-1], from the XANES data alone. Although indistinguishable by LEED patterns, these two directions are not equivalent on III–V(110) surfaces because of the existence of the asymmetric In(Ga)P zigzag chains in the surface plane, which extend along [1-10]. This structural asymmetry is also known to be responsible for the opposite spatial orientations of the empty and filled dangling bond orbitals of the surface indium and phosphorus atoms, respectively. Hence, it is reasonable to suggest that the experimentally observed preference of just one orientation of the alkyl chain has to be attributed to the orientation of these dangling bonds, most probably to the empty indium dangling bonds. In fact, by combining analysis of the asymmetric features in the XPD patterns of InP with the XANES data, we have been able to identify the absolute tilt orientation as pointing from the indium side (sulphur-bonding site near indium due to In–S bonds) toward the phosphorus side of the same zigzag chain, as will be discussed in detail elsewhere [53, 64].

An independent check of the orientation of the hydrocarbon chain may be performed by analysis of the intensity evolution of the C–H (σ^*) resonances in the CK XANES. Figure 15 shows a comparison of the angular dependences of C–C (σ^*) and C–H (σ^*) resonances of HDT on InP(110), derived from the same set of spectra. The C–H (σ^*) resonance intensities were obtained by fitting Gaussians to the sharp low-energy peak only, after subtracting the arctan-like threshold function, characterized by a position at 289.5 eV and a full width at half maximum of 0.5 eV, and by excluding the contributions from the second, small resonance. Because of this fitting procedure, the C–H (σ^*) intensity is much more prone to error than the C–C (σ^*) resonance. Evidently, these intensities evolve roughly inversely. This result may also be confirmed for GaP by a glance at the spectra displayed in Figures 10 and 14 for InP and GaP, respectively.

An inverse behavior is in accordance with the above-mentioned proposal of a rather well-defined molecular axis. The individual bond angles C–C–H will be close to the tetrahedral angle due to the ideally adopted sp^3 hybridization of the carbon valence electrons. But in the case of an alkyl chain that extends along an axis, that is, in an ideal all-trans conformation, the C–H bond directions are expected to be 90° off the average C–C orientation, corresponding to the molecular axis. The slight deviation of the minimum/maximum positions of the two curves from a 90° difference may be related to some distortions of the chains. However, we have mentioned the much larger sources of errors for the C–H (σ^*) related resonance, and thus we cannot make any quantitative statements on the significance of this suggestion. Another argument for the presence of a high degree of molecular order in the HDT monolayer may be derived from the high anisotropy of the minimum/maximum intensity ratios of C–C (σ^*) angular dependencies. The absorption curves in Figure 11 were normalized by setting the maxima of the fit curves to 1.0 arbitrarily. Note that the degree of linear polarization of the synchrotron beam itself is near 85%. Therefore, complete vanishing of the absorption may not be expected, even if the order in the layer was perfect. Thus, we can also suggest, from the rather low values of absorption intensity in the minima of Figure 11, that a high degree of order regarding the orientation of the alkyl chain axis should be expected in the organic HDT layers on both investigated

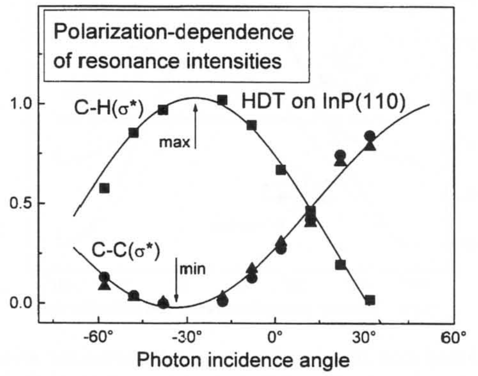

Figure 15. Comparison of the polar angle dependences of the intensities of C–C(σ^*) and C–H(σ^*) resonances for HDT on InP(110). Reprinted with permission from [67], T. Chassé et al., *Surf. Rev. Lett.* 6, 1179 (1999). © 1999, World Scientific Publishing.

substrates. Furthermore, we have performed simulations of the angular dependence in relation to simple models of the intramolecular structure, which are shown in Figure 16. The degree of polarization of the X-rays was assumed to be 100%, and the angular dependence was modeled by a bare $\cos^2$ function of the angle between the possible C–C bond orientations and the polarization vector of the radiation. An ideal all-trans conformation was adopted as a simplified model of a hydrocarbon. The highest absorption and the maximum anisotropy are obtained, as expressed by the minimum/maximum ratio (min = max = 0), for a hypothetical linear carbon atom chain. A tetrahedral C–C–C angle of 109.5° of a carbon zigzag chain within the plane of the variation of the polarization vector reduces and increases the absorption in the maximum and minimum, respectively, resulting in a dramatically reduced anisotropy (min = max = 0.5). The anisotropy would completely vanish (min = max = 1) in the other hypothetical case of a C–C–C angle of 90°, as shown in Figure 16. However, a minimum/maximum intensity ratio of 0.5 and larger would be in strong contrast to the much lower experimental values (min = max < 0.2) which may be taken from Figure 11. Another idealized hypothetical model considers a rotation of the C–C zigzags by 90° with respect to the plane determined by the polarization vector and molecular axis. The total intensity of the maximum is reduced within this model, but interestingly, the anisotropy remains high (min / max = 0). While this behavior would fit the observed high anisotropy in the polar angle dependence, it would be in contrast to the azimuthal anisotropy. Therefore, we may rule out the extreme cases of high-symmetry orientations of all-trans conformations with respect to [001] or [1–10]. In contrast, twisted alkyl chains or, to a certain extent, even some random orientations of individual C–C bonds of the chains fit the experimental observations much better. This result does not at all contradict the generally observed extremely well-defined orientation of the molecular axis. So far, the experimental data and the analysis presented above have clearly demonstrated the well-defined orientation of the adsorbed alkanethiol monolayers (HDT), resulting in an exceptionally high order of the adsorbed monolayers. To our knowledge, a similarly pronounced preference of molecular orientation and high molecular order of alkanethiols has not been observed before on any other surface, including metal surfaces. This strikingly high perfection of orientation of the adsorbed alkanethiol layers has to be discussed in terms of both adsorbate–substrate bonding and surface structure of the substrate. Preferential bonding of sulphur atoms to the surface indium atoms has been observed in several photoemission studies of sulphur species on InP(110) and InP(001) surfaces [35–37], and surface-sensitive core and valence level photoemission measurement of several alkanethiols on III–V(110) also support the thesis of S–In(Ga) bonding [33–37]. Thus, structural constraints by the substrates will be imposed by the different In–In (Ga–Ga) distances in the surface, which provide the links to the adsorbed thiols. The III–V(110) surfaces of zincblende structure possess a rectangular surface unit mesh. The unit mesh dimensions correspond to 587 and 544 pm along the [001], and to 415 and 385 pm along the [1–10] surface directions of InP(110) and GaP(110), respectively. This reflects the 7.9% larger lattice constant of InP. The unit mesh dimensions also correspond to the In–In (Ga–Ga) distances in the surface plane. Following straightforward structural arguments regarding the space requirements of the alkyl chains and their well-known tendency to form dense structures, a tilt of the alkyl chains toward [001] is indeed much more likely than toward [1–10]. These simple arguments fit our observations regarding the tilt direction very well, and are summarized in Figure 13(a) schematically. Further, a dependence of the tilt angle on the lateral distance of the sulphur–substrate bonding sites on the surface, and thus on the substrate lattice constant, has to be expected. This effect is clearly reproduced in our experiments by the smaller tilt angle of 15° on GaP compared to 34° on InP. From these data, we may estimate a vertical distance between the average molecular axes of 487 pm (InP) and 525 pm (GaP), in reasonable agreement with qualitative expectations.

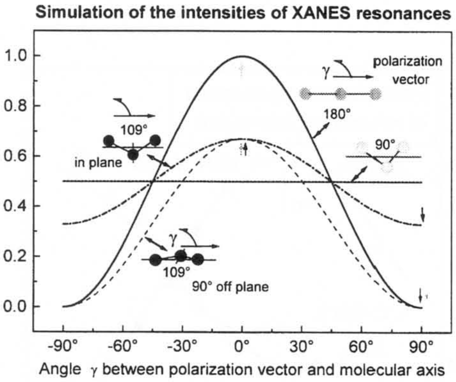

Figure 16. Simulation of the influence of intramolecular arrangement of the carbon atoms and the relative orientation of the C–C plane with respect to the polarization vector during an angular scan for hypothetical orientations of ideal all-trans conformation. Reprinted with permission from [67], T. Chassé, et al., *Surf. Rev. Lett.* 6, 1179 (1999). © 1999, World Scientific Publishing.

So far, this discussion has ignored the actual numbers for the space requirements of the alkyl chains, which essentially originate from the lateral dimensions of the covalently bound alkyl chains and the van der Waals radii of the hydrogen atoms (120 pm) of the organic molecule. The hydrogen atoms are mainly responsible for the intermolecular interactions between the hydrocarbon chains. The relevant data may be obtained from the schematic structures shown in Figure 13(b). It is evident that a problem exists regarding the space requirements of the chains parallel to [1–10], which is most serious for GaP because of the smaller lattice constant. However, by tilting or/and twisting the alkyl chains with respect to the molecular axis, an optimum registry of the van der Waals spheres of hydrogen atoms from neighboring chains may be obtained, which may significantly reduce the minimum van der Waals chain–chain distance from 418 down to 370 pm in the optimum case. Hence, by twisting the chains and adopting the optimum registry of hydrogen atoms between neighboring chains, the structural constraints imposed by the substrates may be essentially fulfilled. We suggest that the actually adopted tilt angles (34 versus 15°), as well as the resulting minor differences in average chain distances (487 versus 525 pm), may be affected by the need to reach an optimum registry in this direction too. We conclude that structural constraints will not prevent any Ga (In) surface atom from forming covalent bonds to the sulphur heads. This is an important result in terms of passivation of the surface indium (gallium) atoms. Otherwise, missing alkanethiols would permit easy oxidation of the unpassivated In (Ga) in air. Note that passivation of the P-surface sites has to proceed along another route. We further speculate that the need for optimum registry may additionally contribute to the excellent order of the chains in the layers. Summarizing our results, we have demonstrated the formation of a passivating, self-assembling organic monolayers on InP(110) and GaP(110) by adsorption of alkanethiols from the liquid phase. An exceptionally well-defined orientation and high order within the adsorbed monolayers on these semiconductor surfaces has been found by employing the angular dependences of CK XANES resonances. Tilt angles toward the [001] directions of the (110) surfaces with respect to the sample normal of 34 and 15° for InP and GaP, respectively, were obtained from quantitative analysis of the XANES. The considerable difference in lattice constants permitted us to draw some conclusions concerning the substrate influence in the case of these semiconductors. The bonding to the surface and surface structure, as well as intermolecular interactions, impose constraints, which evidently force the adsorbed monolayers to adopt a uniquely well-defined structure. The constraints result in single domains of the monolayers on the investigated III–V (110) surfaces, only limited by high-cleavage steps or other large defects of the cleaved substrate surface.

The sensitivity of XANES to determine the spatial orientation of the bonding axis (especially the C–C and C–H bonds at the CK edge) has been used to construct a model of the complete alkanethiol monolayer with respect to the underlying InP(110) lattice. The angular-dependent (in azimuth and vectorial angle) datasets have been measured, while averaging an area (spot size) of several mm^2, hence representing a truly macroscopic feature. Although the integration of spectral features over large regions has been made, the data reveal sharp angular-dependent changes. In particular, these changes are not symmetric with respect to different surface directions, which has to be expected for an oriented, single-domain system. More precisely, the following conclusions have been drawn from the XANES measurements.

- The angle between the surface normal and the tilted alkyl chains is 34° on InP(110) and 15° on GaP(110) [66, 67].
- The projection of this angle onto the surface lies along the [001] axis of the substrate, which has been confirmed by varying the azimuth angle parallel to the surface from 0 to 360° in 24 steps [66].
- Within the (001) plane, the chains are only tilted to one side of the surface normal, which is confirmed by varying the vectorial angle from −70 to +70° from the normal in more than 30 steps [53, 67].

From SXPS measurements which have been tuned for maximum surface sensitivity, it additionally has been proved that the chemical binding of SAM and the substrate takes place between the thiol sulphur and the indium, while the hydrogen atoms which are deprotonated in the binding process are connected to the phosphorus atoms [65]. The set of XPS intensities also supports the thesis of a well-ordered system. The C/S ratio is at its maximum, while the corresponding substrate intensities are at their minimum. To demonstrate the cleanness of the self-assembled system, we have presented an XPS-survey spectrum [32, 66, 67]. Only peaks which are related to the substrate (In, P) or the adsorbate (C, S) are present. No oxygen or other contaminants are detectable, which is proof of a good surface preparation.

We are now ready to sketch a complete model of the adsorbate–substrate system. However, to eliminate all possible objections to our conclusions, we will further prove the exceptional order of the SAMs by using X-ray photoelectron diffraction on exactly the same UHV-adsorbed alkanethiol film (either prepared in a solution or by vacuum deposition). For that, we made two sets of angular-dependent measurements at room temperature on spot sizes of several mm^2. The first one, with angular variations within the (001) plane, shows no significant deviations in intensity. But the second set (consisting of two independent series), which is made in the (1–10) plane, shows a clear peak at 34°, but not at −34° from normal (see Fig. 17). This peak comes from the so called "channeling" of the photoelectrons along the alkyl chains, and therefore describes the orientation of the chains. Note two important additional pieces of information, which can be derived from these measurements. First, the graph is not symmetric with respect to the surface normal (only one

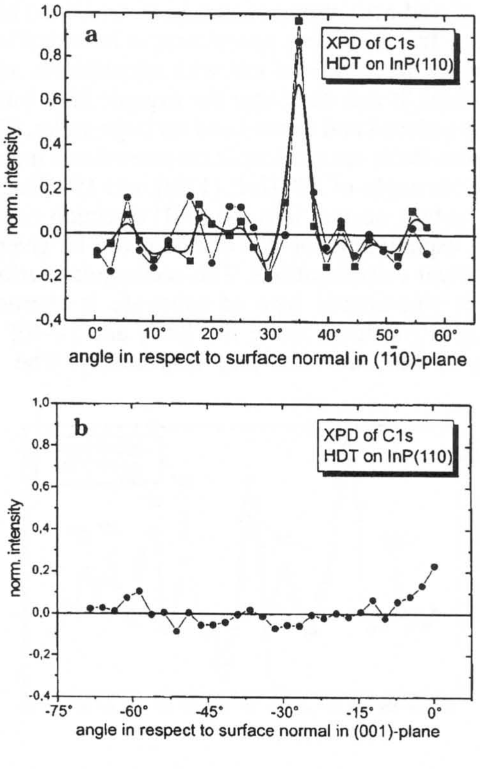

Figure 17. XPD experiment at the energy of the C1*s* peak: (a) along the (1–10) plane, (b) along the (001) plane of the InP lattice. Reprinted with permission from [53], D. Zerulla and T. Chassé, *Langmuir* 18, 5392 (2002). © 2002, American Chemical Society.

peak), and second, the peak is absent in the perpendicular plane. This again allows only one conclusion: the adsorbed monolayer is a single-domain system. Furthermore, from our analysis, one may conclude that fully assembled monolayers, prepared from solutions, and UHV-adsorbed monolayers at high doses (>10 kLangmuir) do form the same kind of structure on InP(110) surfaces. In order to complete the model of the spatial geometry of the adsorbate–substrate system, we are in need of the exact orientation of the substrate lattice with respect to the adsorbate. Having the exact orientation in space of the alkyl chains, the only missing parameter is the orientation of the substrate. From the previously shown XPD measurements on preoriented InP single crystals, it is clear that the alkyl chains lie in the (1–10) plane. The symmetry properties of the semiconductor lattice further allow the determination of "tilt direction" with respect to the sequence and spacing of the nonaxial-symmetric substrate lattice in the denoted plane. Hence, a second set of XPD measurements has been made along the (1–10) plane. In order to investigate the orientation of the substrate and not the adsorbate, the P2*p* peak instead of the C1*s* peak was chosen. The result of this experiment is depicted in Figure 18. Because of the unequivocal result, an interpretation using simple first-order scattering is sufficient. The matching of the first-order scattering model and the XPD peaks is illustrated in Figure 19. Taking all ascertained data from the measurements, we can now complete the structure of the single-domain adsorbate–substrate system. The resulting model, which is additionally confirmed by computer simulations, is shown in Figure 20.

The STM/STS results lead to further insights into the behavior of self-assembling monolayers on III–V(110) surfaces. From the preceding spectroscopic investigations [32, 66, 67], which were carried out with alkanethiols adsorbed from solutions, it was clear that the organic films build up a very highly ordered and dense layer on large scales. The data derived from these spectroscopic measurements include the molecular tilt angle of 34° [InP (110)] and 15° [GaP (110)] from the surface normal into the [001] direction of the substrate. An explanation for this behavior can be given solely by geometrical considerations. The rectangular surface unit cell of this zinc-blende type of substrate is characterized by In–In (P–P) spacing along the [001] and [1–10] surface directions of 587 and 415 pm, respectively. The surface indium and phosphorus atoms (In–P bond length 254 pm) are linked to form In–P zigzag chains within the InP(110) surface plane, which extend along the [1–10] direction. Thus, following structural arguments regarding the space requirements of the alkyl chains and their well-known tendency to form dense structures, a tilt of the alkyl chains toward [001] is indeed much more likely than toward [1–10]. These simple arguments agree very well with our above-mentioned observations regarding the tilt direction.

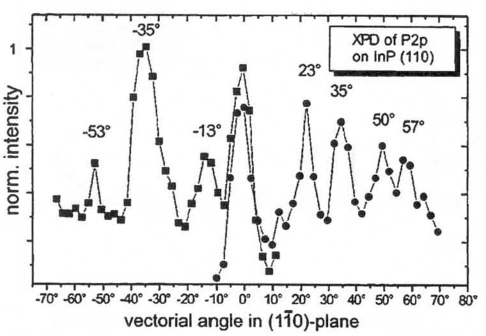

Figure 18. XPD experiment at the energy of the P2*p* peak along the (1–10) plane of the InP lattice. Reprinted with permission from [53], D. Zerulla and T. Chassé, *Langmuir* 18, 5392 (2002). © 2002, American Chemical Society.

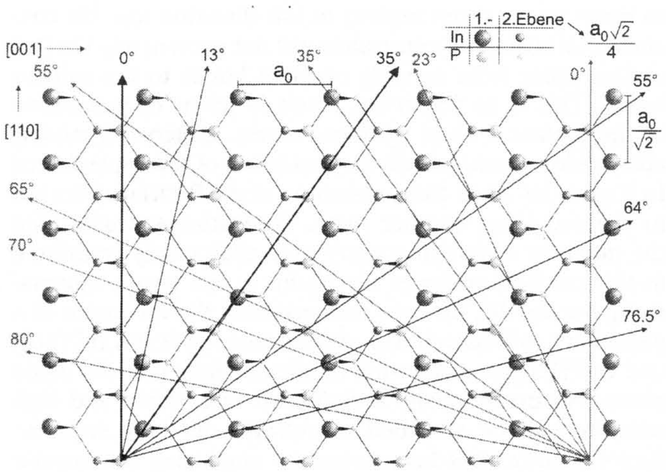

Figure 19. Illustration of the first-order scattering within the (1–10) plane. Reprinted with permission from [53], D. Zerulla and T. Chassé, *Langmuir* 18, 5392 (2002). © 2002, American Chemical Society.

Furthermore, a dependence of the tilt angle on the lateral distance of the sulphur–substrate bonding sites on the surface, and thus on the substrate lattice constant, had to be expected. In fact, we observed such a trend by investigating thiol adsorption on different semiconductor surfaces [53, 67].

Besides this purely geometrical consideration, we have to be aware of the structural inequivalence of the two opposite [001] surface directions due to the asymmetry of the In–P

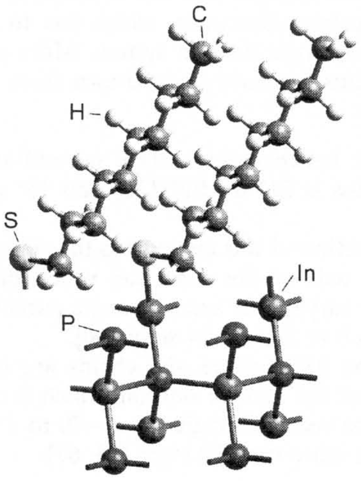

Figure 20. Model of the adsorbate–substrate system. Reprinted with permission from [53], D. Zerulla and T. Chassé, *Langmuir* 18, 5392 (2002). © 2002, American Chemical Society.

zigzag chains, which exhibit an indium and a phosphorus side. This structural asymmetry is also known to be responsible for the opposite spatial orientations of the empty and filled dangling bond orbitals of the surface indium and phosphorus atoms, respectively. Hence, it is reasonable to suggest that the experimentally observed preference of just one orientation of the alkyl chain has to be attributed to the orientation of these dangling bonds, that is, to the empty indium dangling bonds, which was proved by SXPS measurements [53, 67]. Thus, structure as well as bonding constraints evidently force the adsorbed monolayers to adopt a uniquely well-defined structure, which allows us to propose the existence of single domains of the monolayers on InP(110), only limited by high-cleavage steps or other large defects of the cleaved substrate surface.

Summarizing all data, we have proved macroscopically, from pure spectroscopic investigations [32, 66, 67], as well as microscopically from STM/STS measurements, the spatial structure of the complete adsorbate–substrate system. We have shown on self-assembling systems prepared from dilute solutions, as well as on systems prepared in UHV, that the whole layer under investigation is highly ordered and oriented into a specific direction, and therefore is a single-domain system on InP (110) and GaP (110).

Additionally, from the comparison of different preparation techniques (UHV deposition versus dilute solutions), it was possible to shed more light on the role of solvent molecules in the mechanism of self-assembly and the necessary doses. From the measurements with low doses, it is obvious that the preorientation of the alkyl chains, pointing toward the crystallographic [001] axis of the substrate, is induced by the empty (In) dangling bonds on the surface, while the tilt angle itself is a result of the dense package and the three-dimensional space requirements of the alkyl chains at higher doses.

The different stages of adsorption also give an explanation of the comparable high doses needed to obtain a densely packed layer despite the high reactivity, and therefore high sticking coefficient, of the surface. The reason for the requirement of higher doses is that the lying molecules on the semiconductor surface hinder the contact between new incoming molecules and the substrate surface itself. This is also the main reason for the differences in adsorption kinetics in comparison to adsorptions from solutions. There, the alkanethiols are expected to be kept afloat by the surrounding solvent molecules, and that is why they do not block the surface at low coverages. The corresponding results on gold surfaces are quite similar, but do not lead to single-domain systems; see, for example, [76].

4. NANOSTRUCTURING OF SAMs

In principle, self-assembling monolayers are stable against etching, act as lithographic resists, and can be combined with functional groups, to mention only a few examples. Because of the potential technical applications of such organized assemblies in a variety of fields, for example, chemical/optical sensors, these systems have been studied with increased attention for a number of years, and different techniques to structure the monolayers have been developed.

In this section, we will discuss different techniques that enable us to write structures with or into a self-assembled monolayer. Furthermore, we want to shed light on the mechanisms behind the different techniques in terms of changes in the molecular structure. Coarsely, the methods could be divided into techniques which remove parts of the monolayer (Sections 4.1, 4.2) or techniques which add molecules to the surface (Sections 4.3, 4.4).

4.1. X-Ray and *E*-Beam Lithography

Here we will discuss two methods whose origins are quite different. We do this because the final mechanism of the removal of molecules at the surface is the same in both techniques.

First, we discuss the influence of long-term X-ray irradiation on the structure and chemical state of a ready-assembled alkanethiol monolayer on InP (110) and Au (111). For this, we have performed an XPS study in order to investigate these effects. For the general preparation of the monolayer systems, we refer to Section 2. However, because we feel that it is an important point for the interpretation of the experiments, we have checked the surface quality on the gold films and on InP(110) using an ultrahigh-vacuum scanning tunneling microscope. According to these investigations, the gold surfaces are composed of large flat terraces, exhibiting typical dimensions of 200 nm × 200 nm. The terraces are separated by steps with a height of a few atomic distances. The largest part of the surface belongs to the terraces, which are almost free of defects. On the contrary, only a few single-cleavage steps, typically separated by distances of several micrometers, were found on InP(110), which thus exhibits very large, atomically flat terraces [64].

Thiol monolayers (1–decanethiol (DT), Aldrich, 96%; dodecanethiol (DDT), Fluka, 97%; hexadecanethiol, Fluka, 95%; octadecanethiol (ODT), Fluka, 97%) were prepared in a μM solution in isooctane (Merck, SupraSolv, for organic trace analysis). Before the solvent was used, it was purged with nitrogen for about 30 min to remove the dissolved oxygen. The indium phosphide crystals were cleaved in the above-described solutions. After immersion times of approximately 36 h, the samples were removed, rinsed with fresh solvent, dried under a gentle stream of nitrogen, and inserted into the spectrometer immediately.

The spectra were fitted by a least squares procedure with a model peak shape (Gaussian–Lorentzian convoluted functions) after background subtraction from experimental data using a Shirley-type function (using the software Unifit 2.1 by Hesse et al. [77]).

The samples were characterized by the core-level spectra of the substrates (Au4f, In3d, P2p) and of the organic films (C1s, $S2p$). However, for the purpose of this chapter, we mostly focus on the sulphur core levels of the organic adsorbates. First, we will present the data obtained for the adsorbed alkanethiol monolayers on gold. Figure 21 shows a set of $S2p$ spectra recorded from a DT layer on gold. From bottom to top, the spectra represent increasing accumulated irradiation time by X-rays up to a total of 8.5 h. The bottom spectrum in this figure, which corresponds to the shortest irradiation time, is dominated by a single, well-resolved

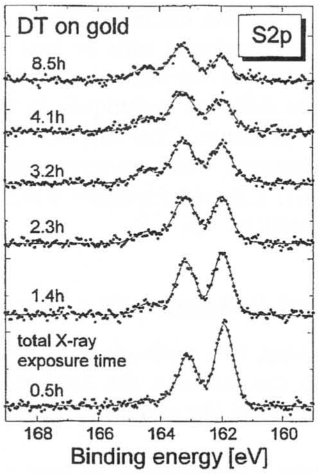

Figure 21. XPS S$2p$ spectra of DT on gold for different X-ray exposure times. The formation of a new chemical species and the loss of sulphur can be seen directly from the spectra as a function of time. Reprinted with permission from [32], D. Zerulla and T. Chassé, *Langmuir* 15, 5285 (1999). © 1999, American Chemical Society.

$S2p$ doublet structure. There is no signal from oxidized sulphur species observable, which would occur on the highest binding energies (BEs) on the left-hand side in Figure 21. But with an increasing interaction time of the X-rays with the adsorbed organic layer, the typical $2p_{3/2}/2p_{1/2}$ doublet branching ratio for XPS core-level spectra becomes increasingly distorted from this value, and an additional peak structure grows on the high-binding-energy side of the main peak structure. These changes of the spectral shape are evidence for the appearance of another sulphur species. This conclusion is supported by the peak-shape analysis of the spectra. Figure 22 shows two representative experimental spectra, together with the results of a peak-shape analysis using two doublet peaks for the fits of each sulphur spectrum. The corresponding fit components, the background lines, and the fit residuals have also been included in the figure. The fit-sum curves match the experimental data well, and the fit residuals appear to be randomly distributed, in this manner demonstrating the successful description of both experimental datasets by these two doublets. The initially dominating S$2p$ component (Fig. 22, bottom spectrum) at a binding energy ($S2p_{3/2}$ with respect to the Fermi level) of 161.92 eV evidently represents the sulphur head group of the thiolate, which bonds to the gold substrate (hereafter called sulphide component). The second sulphur component at the higher binding energy of 163.36 eV has reached the same relative intensity as the initial one in the top spectrum of Figure 22. It may be related to radiation-induced changes of the chemical bonding of the respective sulphur atoms. We have tested this hypothesis by switching off the X-ray tube for periods up to 12 h. After having resumed the irradiation, we could get about the same intensities from the sample surfaces as before the stop of the irradiation. This test has demonstrated that the chemical transformations that are indicated by the peak-shape changes are, in fact, X-ray induced (including X-ray excited secondary processes), and not solely due to storage of the layers in the UHV environment.

Hence, we will call this second sulphur doublet component radiation induced. The evolution of the chemical changes in the thiolate layer while continuously irradiated with X-rays is displayed in a quantitative manner by the sulphur component intensity ratios (radiation induced/sulphide) shown in Figure 23a on a longer exposure time scale. This ratio rises

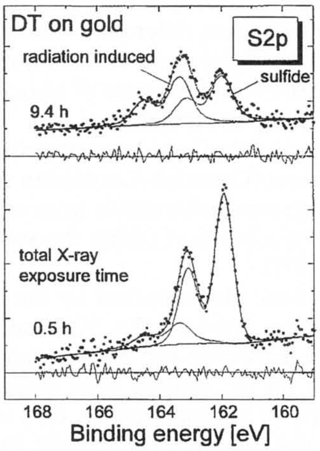

Figure 22. Peak-shape analysis of S$2p$ doublets (representing the sulphide and the radiation-induced species) from DT on gold, including the residuals for exposure times of 0.5 and 9.4 h. Reprinted with permission from [32], D. Zerulla and T. Chassé, *Langmuir* 15, 5285 (1999). © 1999, American Chemical Society.

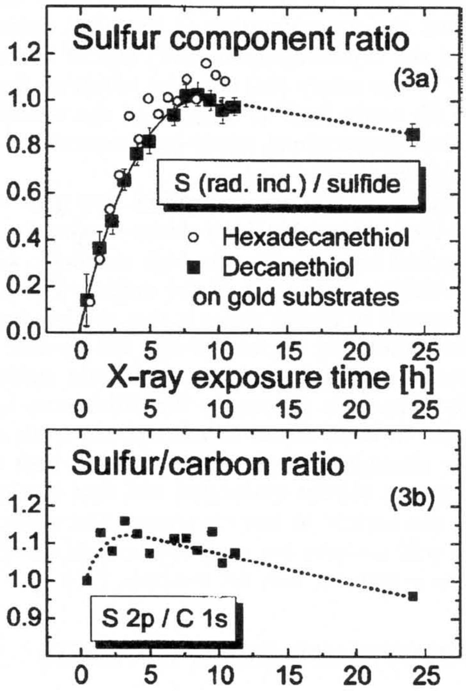

Figure 23. (a) Comparison of the irradiation time dependencies of the relative content of radiation-induced sulphur/sulphide of HDT and DT on gold. Note that extrapolating the data to $t = 0$ suggests a monolayer free of sulphur components other than sulphide from the adsorbed thiol. (b) Comparison of the sulphur/carbon intensity ratios of DT determined on gold. All absolute values have been normalized with respect to the Au4f peak. Reprinted with permission from [32], D. Zerulla and T. Chassé, *Langmuir* 15, 5285 (1999). © 1999, American Chemical Society.

fast during the initial stages of irradiation. Of course, the individual spectra and their intensities represent an average over the necessary recording time of about 30 min for a single high-quality spectrum, and thus the intensity ratio cannot be given for zero irradiation. However, tracing back the evolution of the data toward lower X-ray exposure gives a component intensity identical to or at least very close to zero for irradiation time $t > 0$. This suggests the absence of the second sulphur species at the initial stage of the XPS investigation. After having reached a maximum level at about 8–10 h of irradiation time by monochromatized X-rays, the intensity ratio exhibits a weak trend to decrease very slowly, in particular at the largest duration of X-ray exposures (24 h). It is important to note that the evolution of the sulphur component intensity ratio proceeds very similarly in the case of HDT and DT adsorption layers on gold (see Fig. 23a). This leads to the conclusion that these moderate differences in chain length are of less importance in the case of these radiation-induced chemical changes. But note that the intensity ratios measured for the HDT film exceed those for the DT film by about 5% typically. Normalized intensities of both the total C1*s* and S2*p* signals, as well as of the sulphide and the radiation-induced S2*p* components, are provided in Figure 24. A significant intensity loss of both the total sulphur and the carbon signal of the thiolate film with increasing X-ray exposure can be clearly observed. The decrease of the sulphur signal intensity proceeds fast during the initial stages of the X-ray exposure, but slows down considerably at later stages. The sulphur intensity decreases much slower beyond irradiation times of about 8–10 h, when it has reached about 60% of its initial value. These pronounced intensity changes cannot be explained by a rearrangement of the organic molecules of the adsorbate layer, but suggest a loss of adsorbate from the surface. Interestingly, the C1*s* intensity decreases at about the same rate (Fig. 24) during the whole investigation. There is only a slight increase of the sulphur/carbon ratio (Fig. 23b) by about 10–15% at intermediate irradiation times, which indicates more complex changes in the layer. This observation may indicate that parts of the alkyl chains have been removed from the adsorbed molecules by radiation-induced bond breaking and desorption or that part of the adsorbed organic molecules are more flat lying on the surface than in the well-ordered SAM. Both effects would increase the sulphur/carbon intensity ratio due to reduced sulphur signal attenuation by carbon. Another minor effect to be recently reported is a slight broadening of the C1*s* spectra toward lower BE after prolonged irradiation that has been attributed to chain damage due to double-bond formation possibly accompanying C–H bond breaking [78, 79]. Nevertheless, the major effect regarding the structural layer damage is the intensity decrease of both thiolate signals (C1*s*, S2*p*), which has to be attributed to a large extent to correlated losses of both sulphur and carbon from the surface. Note that all solid curves in Figure 24 have been drawn to guide the eyes only. In fact, the lines have been obtained by fitting the data with exponential functions. The best results have been found by using two exponential functions with characteristic time constants of about 2–3 h and about 100 h, respectively. We emphasize that similar time constants characterize the intensity loss of the total signals (S2*p*, C1*s*), as well as changes of the two individual sulphur component signals (radiation induced, sulphide). This observation strongly supports the assumption that chemical damage and structural damage are somehow correlated on gold substrates. The behavior of different adsorbed thiol molecules has been investigated in the range of alkyl chain lengths from $n = 10$ to $n = 18$ carbon atoms (only even numbers). All investigated layers exhibited the above-described effects. Small deviations in the data (e.g., shown in Fig. 23a) are visible, but not strong enough to be interpreted as significant influences from the deviating chain–chain interactions due to differences in the alkyl chain lengths. We have been able to visualize the structural damage of the adsorbate layers due to the extended X-ray exposure during our studies in SEM pictures, as shown in Figure 25a for the case of an ODT layer on gold.

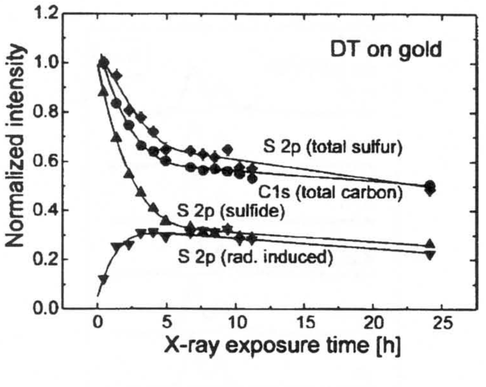

Figure 24. Normalized intensities of the carbon and the sulphur species from DT on gold. The intensities have been calculated from the average peak area of the fitted spectra. Normalizations have been made with respect to the Au4*f* peak of the substrate. This leads to a small overestimation of the loss because the substrate is not covered by the same effective layer thickness at longer exposure times. Reprinted with permission from [32], D. Zerulla and T. Chassé, *Langmuir* 15, 5285 (1999). © 1999, American Chemical Society.

The scanning electron microscopy (SEM) picture of the photoninduced damage of the thiol film was recorded using a VG LEG 1000 electron gun with a primary electron energy of 4 keV and the lowest possible current.

The elliptically shaped dark area represents the spot from the monochromatized X-ray source on the sample. The contrast in the picture is due to different electron reflectivities and secondary electron yields of the irradiated and nonirradiated parts of the thiolate film. The irradiated area can be clearly distinguished from the environment, but within this area, we notice gradual differences in contrast, which may be attributed to an inhomogeneous illumination by X-rays, and thus also inhomogeneous photon density. This renders the application of exact quantitative models for the characterization of the damage evolution difficult.

It should be mentioned that radiation-induced damage proceeds much faster by using nonmonochromatized X-ray sources. This result is quite reasonable, even if the X-ray power is chosen to give equivalent count rates for the photoelectron lines because of the additional photons from the bremsstrahlung and the X-ray satellites, and the much higher background of inelastically scattered and secondary electrons. Radiation-induced damage was also observed

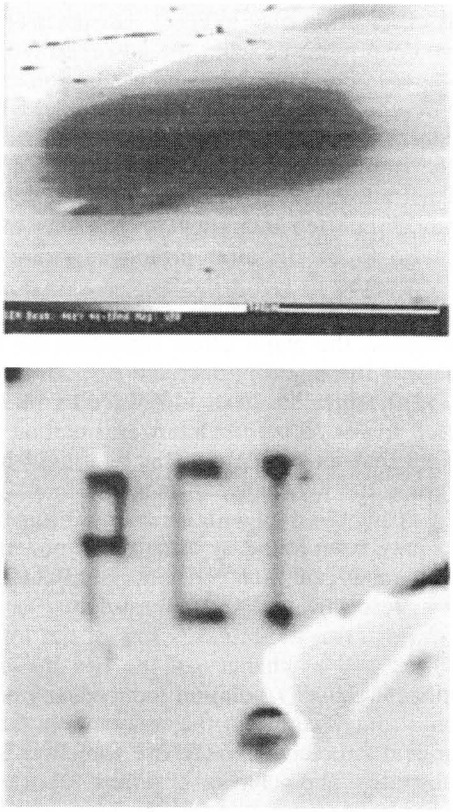

Figure 25. (top) SEM picture of an octadecanethiol monolayer on gold. The dark spot is due to the change of the SE yield by induced damage by the monochromatized X-ray source (1486.6 eV) to the adsorbate. The size of the spot is approximately 1000 μm × 250μm (primary electron energy was 4 keV). (bottom) SEM picture of a dodecanethiol monolayer on InP(110). The pattern "PCI" has been written by electron beam lithography, using a freely programmable electron gun at 10 keV. This picture demonstrates the ease of structuring an alkanethiol layer with electron beams. Reprinted with permission from [32], D. Zerulla and T. Chassé, *Langmuir* 15, 5285 (1999). © 1999, American Chemical Society.

after applying lower energy synchrotron radiation in the range of $h\nu = 50$–320 eV, as was used for X-ray absorption near-edge structure and soft X-ray photoelectron spectroscopy studies. Moreover, damage of SAMs was also found using electrons in the range of 10–14 eV, supplied by a flood gun, and we have further tested that electron beams <500 eV can damage the layer in the same way. These results ensure that low-energy and secondary electrons contribute to the layer damage. We have applied 4–10 keV electron beams of an Auger electron gun for laterally structuring the SAMs.

For example, the pattern "PCI" has been generated in a dodecanethiol monolayer (Fig. 25b). In fact, electron-induced damage has been reported before [80–82], and it has also been used for patterning purposes. To shed more light on the possible importance of substrate–layer interaction regarding the radiation-induced effects, we have also investigated adsorbed thiol monolayers on InP (110). This surface was chosen for comparison to the metallic gold surface because of the quite different surface structure and bonding of this covalent semiconductor with zinc-blende lattice, and finally because of the available experience in the interpretation of sulphur core-level spectra from several adsorption studies of inorganic sulphur species on InP [35–37, 66]. We have studied the composition and structure of such thiolate layers using XPS and XANES. Very pronounced angular dependencies were observed in the σ^*(C–C) and σ^* (C–H)-related structures in the near-edge region of the X-ray absorption spectra on alkanethiolate layers on InP(110) by varying both the polar and azimuth orientation of the sample with respect to the polarization direction of the synchrotron radiation. The data analysis has clearly shown that self-assembly also takes place on this surface, and it results in an excellently ordered organic monolayer. In contrast to gold substrates, where domains with different azimuth orientations of the alkyl chains exist on the surface, only the tilt orientation of chains parallel to the dangling bond directions of the surface atoms were observed on the cleavage face of indium phosphide. However, for both the XANES data and their detailed discussion, we refer to Section 3.

The adsorbed molecules form a dense monolayer on InP(110), as can be concluded likewise from the observed passivation of the semiconductor surface from oxidation by contact to air. This passivating effect is demonstrated by the complete absence of oxygen-related signals in the XPS core-level spectra (Fig. 26). A survey spectrum only shows photoelectron peaks of both the semiconductor substrate and the organic adsorbate on the background of inelastically scattered and secondary electrons [32]. For the purpose of this chapter, we will focus on the S2p spectra and the corresponding intensities as discussed for the gold substrates above. S2p spectra recorded from an HDT layer on InP(110) are provided in Figure 26. Cursory inspection by eye gives only evidence for a single doublet due to the sulphide component, which is present in all of the individual S2p spectra. But careful peak-shape analysis allows identification of a second sulphur component of low intensity at a higher binding energy. This small component also grows with increasing X-ray exposure, similar to the case of thiolate layers on gold. There have been several studies

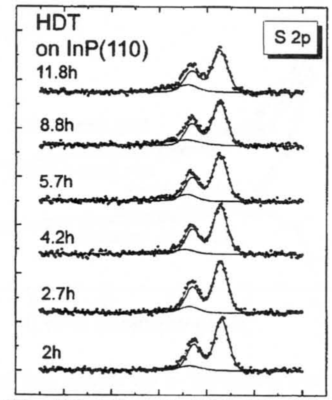

Figure 26. XPS S2p spectra of HDT on InP (110) recorded at different X-ray exposure times. Note the differences compared to alkanethiols on gold. Reprinted with permission from [32], D. Zerulla and T. Chassé, *Langmuir* 15, 5285 (1999). © 1999, American Chemical Society.

of inorganic sulphur species on both InP(001) and InP(110) surfaces [33–35, 37]. In–S bonds have been observed to dominate mostly, with sulphur components between 161 and 162 eV with respect to the Fermi level, depending on the detailed adsorption geometry and Fermi-level pinning. Polysulfidic sulphur was observed with binding energies near 163 eV. Dissociative adsorption has been verified in the case of H2S on InP (110), with P–H and In–SH surface bonds [33, 34]. The evolutions of both the changes in chemistry and composition of the adsorbed monolayer due to the radiation are displayed in a quantitative manner by normalized intensities and intensity ratios, as shown in Figure 27. Looking at the normalized intensities first, we may observe that both sulphur and carbon intensities decrease with increasing X-ray exposure. But this decrease is limited to less than 15% during the period of investigation (12 h). However, the evolution of sulphur and carbon intensities again proceeds about parallel. Furthermore, a small shift toward lower binding energies and a broadening of the C1*s* peak related to the alkyl chain, as was already mentioned for gold substrates, has also been detected on InP (110) in the very last stage of the irradiation process. Thus, there is again sufficient evidence for structural damage of the adsorbed films on indium phosphide. However, the loss of sulphur-containing molecules is strongly reduced under equivalent excitation conditions compared to the gold substrates discussed above.

Second, the sulphur component intensity ratio (radiation induced/sulphide) also increases with continuing irradiation with X-rays, but it increases much slower than that on the gold surface. At the final stages of the present investigations, this ratio does still increase, and there is no evidence for a reversal of this trend yet. In the case of the dataset presented in Figure 27, we have included periods of excitation by nonmonochromatized X-rays to enhance the radiation-induced effects. We have further extended our comparison of alkanethiol layers on gold films and on indium phosphide to the effects of electron beam patterning. It is very interesting to note that patterned structures were consistently smaller on InP substrates by 30–80% than on gold films under identical excitation conditions in the case of applied electron probes of a few 100 nm lateral size and 4–10 keV primary energy as used here. We explain this observation by a larger number of secondaries in the case of gold, and their larger lateral spread due to the higher electron backscattering in gold. We have been able to confirm these effects of higher backscattering of electrons in gold and the higher number of low-energy electrons at the surface compared to indium phosphide quantitatively in our Monte Carlo simulations, which were performed to support separate studies of patterning by electron beams. The Monte Carlo simulations of the electron trajectories were carried out in consideration of relativistic partial-wave calculations of elastic cross sections by solving the Pauli–Dirac equation, combined with Bethe's continuous slowing-down approximation and the Rao–Sahib–Wittrey approach at low energies.

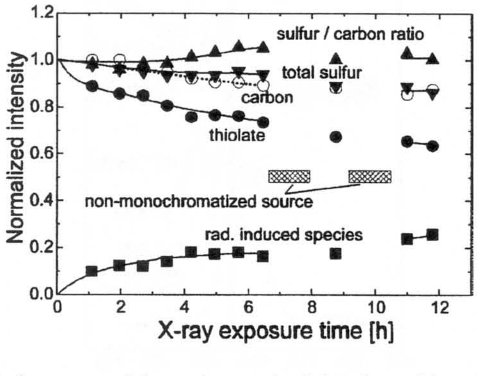

Figure 27. Summary of the carbon and sulphur intensities of HDT on InP (110). All absolute intensities have been normalized with respect to the In3*d* peak of the substrate. The diagonal hatched areas mark the points of time when the nonmonochromatized X-ray source has been used. Reprinted with permission from [32], D. Zerulla and T. Chassé, *Langmuir* 15, 5285 (1999). © 1999, American Chemical Society.

The higher number of low-energy electrons and the more pronounced backscattering accumulate and generate a high number of low-energy electrons in the surface region, which may introduce damage to the organic films. Thus, both the experimental observation of the substrate-dependent width of patterns in the organic films and the quantitative simulation of electron distribution in the samples provide further supporting evidence for the major importance of secondary electron damage of organic films. It is thus reasonable to suggest that the indirect damage by electrons seems to be very effective compared to direct damage by the X-rays, and thus is likely to dominate the damage, even in the SAMs investigated here. Moreover, care has to be taken in the application of structural probes that use ionizing radiation because of the possibility of damaging the layers by secondaries.

Summarizing this part, we may notice that evidence for both chemical and structural damage of the thiolate layers by extended exposure to X-rays was also observed on InP (110). The striking differences in the quantitative extent of these effects compared to gold substrates provide evidence for the importance of the different substrate–layer interactions and the different substrate properties.

The third part of the data will deal with the analysis of the chemical bonding using core-level spectroscopies. Besides the above-discussed thiolate monolayers on gold and indium phosphide, we have also investigated deposited films of pure dithiol (1,8-octanedithiol) and pure dialkyl or thioether (dioctadecyl-3,3′-thiodipropionate) and HDT as references.

Similar discussions regarding the nature of the adsorbed alkanethiols have been published by Jung et al. on gold [72], and by the author on gold and III–V semiconductors [32]. In the following, we will outline the experiments, main results, and their discussion.

To prepare reference samples for the chemical analysis, the undiluted disulfide DS (poly-octanedithiol, ...$-C_8-S-S-C_8-S-S-C_8-$..., Aldrich, 97+%; the disulfidic nature was additionally confirmed by Raman spectroscopy) and dialkyl DA (dioctadecyl 3,3′-thiodipropionate, $S[CH_2CH_2CO_2(CH_2)_{17}CH_3]_2$, Aldrich, 99%), as well as HDT were directly applied to a gold surface, and frozen down to liquid nitrogen temperature (LNT) under a protective gas atmosphere to minimize water adsorption. The samples were then inserted into the spectrometer immediately, while they were kept at LNT to prevent degassing of the molecules in UHV. This procedure leads to films which we will call later "thick films." Their thickness is much larger than 100 nm, which is proved optically and additionally by the fact that the substrate is no longer detectable by XPS measurements. The so-called "thin films" were prepared as follows. The frozen "thick films" were warmed in UHV until they reached room temperature. Thus, most of the film is degassed, and the substrate is detectable by XPS. In the case of long chain reference chemicals, the samples were removed from the UHV environment, and then additionally rinsed with isooctane. After that, the samples were inserted into the spectrometer again. Because of the substrate/adsorbate signal ratio, we estimate the "thin films" to have a thickness approximately up to 5–6 nm. Note that all molecules above the first ML are not supposed to be ordered, but are randomly distributed.

The reference chemicals have been chosen with regard to two aspects: first, because of their sulphur–carbon groups (R–S–S–R or R–S–R, respectively), and second, because of the existence of long alkyl chains which have been used to calibrate the spectra. The X-ray photoelectron spectra were recorded with a VG ESCALAB 220i-XL instrument irradiating the samples with monochromatized Al Kα radiation (22 mA, 10 kV). Spectra were recorded in normal emission, and with an angular averaging mode using an additional magnetic XL lens, if not stated otherwise.

The energy resolution was 0.45 eV (FWHM Ag$3d$). Binding energies (BE) have been referred to the Fermi energy. The energy scale of the spectrometer was calibrated by adjusting to EB (Au$4f_{7/2}$) 84.00 eV. The spot of the X-ray photons from the monochromatized X-ray source has a size of 1000 μm × 250 μm on the sample, with an approximate elliptic shape. Bremsstrahlung of a nonmonochromatized MgKα source (30 mA, 15 kV) has been used exceptionally to excite the Auger S KL$_{2,3}$L$_{2,3}$ and S$2p$ spectra, which were used for the chemical state plot. All binding energies in the chemical state plot have been referred to the C$1s$ energy of the alkyl chains, set to 284.60 eV. This allows correct relative adjustment of binding energies from species in highly insulating thick films which exhibit a charging shift of the energy positions.

The deposition of dithiol on gold, in the way described above, leads to the formation of thick films. These are expected to contain sulphur–sulphur bonds such as those in disulphides (DS) mostly, for example, a –C–S–S–C– group, which results in networks of polysulphides. Otherwise, the remarkable stability of these films in an ambient environment can hardly be explained. This assumption has been supported by the detection of specific vibrational modes in Raman spectra, which reveal typical fingerprints of disulphidic species. On the other hand, the dialkyl (DA) films contain –C–S–C– units. In addition to the thick films with, thicknesses in the range of several micrometers, thinner films with thicknesses in the range of only a few nanometers also were prepared by extensive treatment with solvents or partial desorption in UHV. The thickness of the latter films can be crudely estimated from the C$1s$ to Au$4f$ intensity ratios, which were observed roughly in the range of 0.3–3 in these cases. Charging effects were especially observed in the cases of the thick films because of the insulating nature of the adsorbed molecules. The charging-induced shifts in the very thick layers lead to a degeneration of the resolution due to the nonuniformities of the charging. Neither the use of a flood gun nor the change of the X-ray source and the lens modi could completely remove the inhomogeneous charging. However, this does not severely reduce the grade of information obtained. For the comparison of sulphur binding energies from different species and film thicknesses, the energy scales have been calibrated to set the C$1s$ signal of the alkyl carbon of all samples to EB = 284.60 eV to correct any kind of charging-induced shifts. A comparison of sulphur core-level spectra of HDT monolayers on gold and InP (110) and a thick film containing disulphide bonds (DS) is shown in Figure 28. The vertical line indicates the approximate position of the disulphidic S$2p_{3/2}$ components. The faint peak structure at the very high binding energy in the DS spectrum represents some oxidized sulphur. Quick inspection of the spectra by eye reveals that the binding energies of the radiation-induced signals from the monolayer fall quite close to the disulphide signal from the DS. This observation seems to support the hypothesis that the sulphur signal from the monolayers at the higher binding energy may represent disulphidic species, as has been suggested before [78, 79].

Furthermore, we have combined XPS spectra with X-ray-excited Auger electron spectroscopy (XAES) in order to derive Auger parameters, and to apply two-dimensional chemical state plots for chemical analysis of the sulphur bonding. In the "initial state–final state framework," the XPS core-level binding energies and the XAES Auger (kinetic) energies (AE) can be described essentially by the potential energy contribution on the site of the emitting atom due to the electron density distribution in the chemical environment and a relaxation or final state contribution, which characterizes the core-hole screening effects due to the transfer of screening charge or polarization of the environment following the core-hole generation. The Auger parameter α' according to Wagner corresponds to the sum of the BE and the AE [35–37]. The chemical shift $\Delta\alpha'$ of the Auger parameter reflects the changes of the relaxation or core-hole screening due to changes of the chemical bonding situation. Thus, the basic idea of application of Auger parameters and chemical state plots of binding and Auger energies is to use the additional information due to different

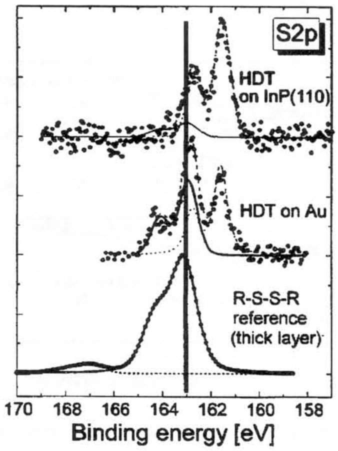

Figure 28. Comparison between the XPS spectra of HDT on InP (110) and gold and a thick layer of a reference disulphide (see text). Reprinted with permission from [32], D. Zerulla and T. Chassé, *Langmuir* 15, 5285 (1999). © 1999, American Chemical Society.

sensitivities to core-hole screening effects. In some cases, this may permit us to distinguish even between species, which have nearly identical binding energies. Figure 29 shows a chemical state plot, which presents the results from repeated measurements of three different adsorbate systems (HDT, DS, DA) and three different layer thicknesses (monolayer, thin film, thick film). The vertical axis represents the kinetic energy of the S $KL_{2,3}L_{2,3}(^1D)$ Auger peak. Binding energies are shown along the horizontal axis. The diagonal lines with slope $= -1.0$ represent identical values of the Auger parameter α', and thus the same relaxation or core-hole screening energy. There is a striking separation into two different groups of data sets in Figure 29. In the upper right corner, that is at the lowest BE and highest KE and thus the highest Auger parameter values, we observe the data points obtained from the sulphide signal of the HDT monolayer and a signal from the thin HDT films that we attribute to those HDT molecules of the thin film at the interface to gold. All other data points from DA, DS, and including the HDT thick film data, as well as the remaining data points from HDT thin films, may be found in the lower left corner of the chemical state plot. The significantly smaller KE and Auger parameter values of the latter data points suggest a much less effective core-hole screening compared to the sulphide in the HDT monolayer. The lowest KE and Auger parameter values were measured for the thick films of DS, DA, and HDT. This is reasonable in terms of the insulating nature of these films and the much reduced ability to screen the core hole compared, for example, to a metallic environment. Slightly higher Auger parameters are observed for thin films of DS, DA, and HDT. All datasets corresponding to DA films are shifted toward lower BE with respect to comparable film signals of other sulphur species. A shift to lower BE for dialkyl samples by 0.4 eV compared to similar disulphidic samples has already been reported in the early data compilations by Siegbahn [83] and Nefedov [84]. The relative shifts of about 0.5 eV to disulphides in our investigations are sufficiently large to distinguish DA species from the others. The thin-film HDT results are very similar to the thin-film DS data. We emphasize that the data, which represent the radiation-induced sulphur component of the irradiated SAMs, are very close to the thin DS film data. This observation is another fingerprint pointing to the disulphidic nature of the radiation-induced species in the monolayers. But most importantly, we may conclude from the huge difference in Auger parameters between sulphide and radiation-induced species that the sulphur atoms responsible for the latter signal are not bonded to the gold surface atoms anymore. Otherwise, the metallic substrate should provide a significant contribution to the core-hole screening energy, which is evidently not the case.

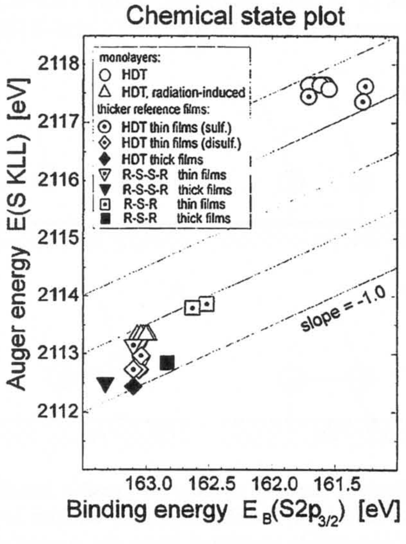

Figure 29. Chemical state plot including binding and Auger energies of three different adsorbates with different layer thicknesses in order to identify the radiation-induced species (see text). Reprinted with permission from [32], D. Zerulla and T. Chassé, *Langmuir* 15, 5285 (1999). © 1999, American Chemical Society.

In the following, we will discuss the experimental data. The adsorbed monolayers of alkanethiols on metals such as gold are known to exhibit long-term stability. However, it has been shown that extended irradiation by X-rays modifies alkanethiol monolayers on gold films in two ways. First, the chemical bonding of the sulphur atoms at the interface to gold is changed by partial breaking of the sulphur–substrate bonds. Second, the layer is structurally damaged, and loses adsorbate molecules. These results are in good agreement with very recent data by Jäger et al. [79] and Wirde et al. [78], and the appearance of radiation-induced damages of alkanethiolate SAMs on gold films now seems well established.

Besides, we will now focus on the comparison of gold film and InP substrates for the SAMs in order to derive conclusions on the effects contributing to the damage. The experimental observations at hand include the X-ray or radiation-induced changes of the spectra as indicated by the appearance of new spectral components, core-level line broadening and line shifts, total intensity changes, and intensity ratio modifications. These effects have been observed on both investigated substrates, as has been demonstrated in detail in the previous sections. However, there are significant differences regarding the quantitative extent in these effects, and in particular, differences in their evolution with X-ray irradiation time. Most striking is the comparably rapid chemical transformation of the sulphur and the significant loss of material from the SAMs on the gold films in the initial stages of the irradiation (time constant about 2–3 h). This rapid change in the initial stage is not observed on InP. Differences in substrate surface structure and related interface and organic film quality, substrate–layer bonding strength, and substrate-related excitations may contribute to this strikingly different behavior, and call for discussion. Bonding energies of 13.9 and 14 kcal/mol were derived for Au–methanethiol [30] and In–S [85], respectively, suggesting rather similar strengths of sulfur–substrate bonds for the substrates considered here. Note that In–S bonds are, in fact, preferentially formed after the adsorption of sulphur species on indium phosphide [35–37]. In a recent time-of-flight secondary ion mass spectrometry (TOF–SIMS) study of electron-stimulated damage of Langmuir–Blodgett (LB) monolayers and self-assembling monolayers, Rading et al. [86] have concluded that the strength of substrate–film bonding is of less importance for the desorption cross sections by ionizing radiation. Because of these results, we may reasonably conclude that the quantitative differences of the two substrates considered here should not mainly be related to substrate–film bonding.

The number of surface defects is much larger on evaporated gold films than on the cleavage face of indium phosphide. This was confirmed by STM, as has been mentioned above. Further, due to the existence of several domain types with different azimuthal orientations of the alkyl chains on gold, we may also expect more domains, and thus more adsorbed molecules at domain boundaries, to be present on this substrate. As was mentioned in the brief review of the XANES results, due to the unique azimuthal orientation of the thiolates on InP (110), considerably fewer domains should exist on this surface. But we cannot estimate the relative extent of these effects based on our results. Evidence for reduced order in SAMs on deposited gold films compared to gold single-crystal surfaces has recently been provided in electron energy loss spectroscopy (EELS) studies by Duwez et al. [87]. It has been shown that the stability of SAMs of adsorbed thiols is due to both the sulphur–substrate bonding and the van der Waals interchain interactions to a similar extent for chain lengths of about 10–20 C [28, 29]. Adsorbed molecules near defect sites experience much reduced stabilizing intermolecular interactions compared to those within well-ordered domains on a well-ordered substrate. From defective adsorbate sites, a desorption of rather complete adsorbate molecules after substrate bond breaking seems likely, which may explain that the losses of carbon and sulphur from the surface proceed in a rather correlated fashion. Predominant desorption from defective sites on the gold films may also contribute significantly to the observation of the different time scales that characterize the intensity evolution of the core levels, and thus the loss of organic material from the SAMs on gold in the initial stage (see Fig. 24). The significantly lower rates of material loss, which seem to govern the later stages of the radiation damage on gold films, and evidently the whole range of the irradiation of the SAMs on InP, may then be related to material loss from well-ordered areas. Radiation-induced cross linking of chains is another effect which may stabilize the organic layers against radiation-induced desorption. However, both the observed much faster and larger conversion of sulphur into the radiation-induced sulphur species on gold and the significantly larger increase of the S/C ratio as observed in the initial stage on gold films cannot be sufficiently explained by defect-site-related damage only. The increase of the S/C ratio has indicated partial destruction of the alkyl chains by bond scission, followed by desorption of separated hydrocarbons. Generally, bond breaking is due to vibronic or electronic excitations. In the present case, it is likely to be mostly due to rather localized electronic excitations. In particular, bond breaking in the alkyl chain is an intramolecular process, which is not expected to depend significantly on the substrate. Nevertheless, given the same types of adsorbed alkanethioles and the same photon flux, the larger increase of S/C on gold films indicates an influence of the substrate. We have demonstrated evidence for the importance of the low-energy electrons for the damage of the organic films. Völkel et al. [88] and our group now suggest that the observed difference in the development of S/C ratios may be due to a different number of secondaries originating from the X-ray excitation of the substrate, which may cause severe damage to the organic film. A higher number of secondaries from gold would also be in line with the observed faster chemical transformation of sulphur in the adsorbed alkanethiol layers on gold films, and is expected to contribute to the larger loss of organic material on this type of substrate too. Another important issue is that of the chemical nature and the adsorption geometry of the sulphur atoms of the adsorbed thiols. Our impact on that question remains limited because the XPS method may provide information on the chemical bonding, but it is only indirectly sensitive to structural sites via binding energy shifts. Nevertheless, by focusing on the radiation-induced changes, we have been able to present clear evidence for the disulphidic nature of the radiation-induced sulphur component, as previously suggested by Wirde et al. and Nuzzo et al. [78, 89]. This similarity of the radiation-induced peak to disulphidic or polysulphidic species may also be concluded by comparison to related adsorption studies of thiols and MBT on gold [31], and of several inorganic sulfur molecules on InP too [35–37]. Besides, from the analysis of the Auger data presented here, which included Auger parameters and the chemical state plot (Fig. 29), we have predicted that the radiation-induced sulphur is not strongly bonded to the gold substrate. From our experiments, the interpretation of the radiation-induced sulphur species as a dialkyl seems very unlikely. This problem is, however, linked to the ongoing discussion regarding the chemical nature of the sulphur species at the undamaged interface to gold. In Figure 30, we have sketched a few possible adsorption models, which emphasize the type of adsorbed species, but neglect any details of the local bonding geometries of sulphur on a gold surface. In contrast to the more generally assumed thiolate (RS–Au bonding, Fig. 30a) nature of the adsorbed thiols, there have been papers proposing the disulphidic nature of the adsorbed thiol layers (R–S–S–R bonding to Au via a disulphide group, Fig. 30b,c). These conclusions were derived from analysis of grazing incidence X-ray diffraction (GIXD [90]), X-ray standing wave (XSW [91]), and EELS [87] data

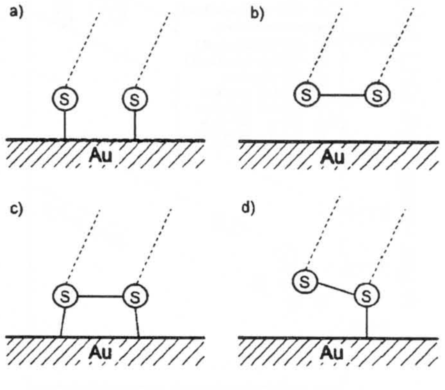

Figure 30. Schematic drawing of different possible bonding configurations of the thiol sulphur head groups: (a) thiolate bonding to the Au surface, (b) disulphide [stabilized above the Au surface by van der Waals forces (not shown)], (c) disulphide with additional dative bondings to the Au surface, (d) disulphide with one single dative bonding to the substrate (note the height offset between the two sulphur atoms). Reprinted with permission from [32], D. Zerulla and T. Chassé, *Langmuir* 15, 5285 (1999). © 1999, American Chemical Society.

obtained on Au (111) single crystals. Fenter et al. suggested that two inequivalent, but spatially close sulphur adsorption sites exist on Au (111), which led them to the conclusion of disulphides being bound on the gold. It has been proposed that different adsorption sites on transition metal surfaces with different coordination numbers will reflect insignificant BE shifts in core-level photoelectron spectra of the sulphur [92]; similarly, a suggestion has been made that inequivalent sites of the disulphide–sulphur atoms on Au (111) should also manifest in such chemical shifts [90]. However, within the limits of our experimental resolution, we cannot find evidence for another sulphur species different from the initial sulphur species (called sulphide), except the radiation-induced one on our gold films after thiol-solution preparation. Note that disulphides have been detected together with thiolate sulphur in photoemission studies of adsorbed alkanethiols on transition metal surfaces, but these observations were mostly limited to low temperatures and low dosages of alkanethiols from the gas phase [93]. To our knowledge, no photoemission study has reported adsorbed disulphides to appear at the binding energies corresponding to our sulphide species. Thus, there is no direct evidence from photoemission which would support disulphide models, and a characterization of the sulphide at the undamaged surface as a thiolate as shown in Figure 30a is most reasonable. Consequently, the disulphide component appears as a result of the radiation-induced effects in the organic film only. Such a prediction for disulphides contradicts neither the long-term stability of the disulphide species observed in our study nor the well-known much higher adsorption probability of disulphides compared to thiols because the strong intermolecular interactions between the neighboring hydrocarbon chains, possibly accompanied by some bending of chains necessary to allow linking of the sulphur atoms in the covalent bonding, may stabilize the disulphide in the film while suppressing retransformation to thiolates. Upon the continuing influence of radiation, even the S–S bonds may be destroyed, and from the radicals, thiolates can be formed again. In this manner, we may explain the fact that the disulphide contribution to the total sulphur signal does not grow further beyond a maximum value (close to 50% in our investigations), and it only changes to a very minor amount at higher irradiation times.

On the other hand, Fenter et al. have ruled out a significant influence of radiation damage on their GIXD and XSW results, which favor disulphides on the gold surface. They estimated a much smaller damage cross section (about 1/100) for the higher energy X-ray photons used in their study compared to photoemission studies using Al K X-rays, based on the energy dependence of the photoionization cross sections of core levels. We have demonstrated evidence for the importance of electrons generated in the substrate, and thus the X-ray energy dependence of the total quantum yields from the substrates rather than a single core-level photoionization cross section, for example, C1*s* of the film, should much better represent the variation of the damage with energy. According to the photon-energy-dependent electron yields for gold determined by Henke et al. [94], the yield at 8–10 keV (GIXD) is only a factor 2–3 smaller than at 1.5 keV (XPS), while at about 3 keV (XSW), it is even larger by a factor 2 than at the energy of the Al K X-rays. We cannot reasonably judge the second argument raised by Fenter regarding the photon flux because the information on photon flux, and in particular on the irradiated area, is incomplete, and the experimental geometries to be compared are quite different. Nevertheless, we feel that the quantitative estimations by Fenter need some reevaluation.

Significant damage of alkanethiol SAMs by X-rays (10 keV) under vacuum conditions was observed on a time scale of 14 days by GIXD [90], which is actually not too far off the time scale of 4 days determined for the long-term damage of the SAMs of gold (and similarly on InP) in our XPS investigations, keeping in mind the differences in damage cross sections (see above) and the different sensitivity to structural damage of the methods. This discussion has demonstrated that, presently, the effects of radiation damage on the sulfur at the interface may not yet be ruled out completely. Further, Jäger et al. [79] also have posed additional questions regarding the possible effects of adsorption-induced gold surface atom redistribution at the interface to the predicted presence of disulphides. Such thiol-induced reconstructions have, in fact, been reported for Cu (111) [95]. On the contrary, our XPS data may not completely rule out all kind of disulphides on gold. A possible adsorbate of this type has been sketched in Figure 30c. Sulphur is known to form a large variety of bonding configurations with metals, for example, in complexes, including disulphide groups and dative bonds [96]. Upon the damaging influence of radiation, such an adsorbed species as assumed in Figure 30c might transform into disulphides with a complete breaking of bonds to the gold substrate as in Figure 30b or a partial breaking of the sulphur–gold bonding with one sulphur atom remaining closely bound to the gold surface, as assumed in Figure 30d. In the latter case, photoemission spectra would represent the two sulphur components at the energies corresponding to disulphides and to the initial sulphide component, as is, in fact, observed after a few hours of irradiation. This latter bonding situation (Fig. 30d) would also fit the stability of the damaged organic layer and the almost similar intensities of the radiation-induced and sulphide component observed after some hours. Again, there is no direct evidence for such an adsorption from photoemission, and these explanations remain speculative and have to be proven. To allow an appropriate comparison of the existing experimental results and the corresponding adsorption models, both substrates (single crystals versus films) and the preparation methods (vacuum deposition versus deposition from solution) have to be chosen consistently, which has not yet been done. There is evidently a need for methods which offer stronger links between the purely structural and the chemical bonding information than is provided by application of GIXD/XSW or XPS/XAES alone. Investigations on gold complex compounds have demonstrated that XANES might be very promising in this context [97].

Summarizing, we have investigated the damage of alkanethiol SAMs on deposited gold films and InP(110) by X-rays using XPS, XAES, and SEM. Both chemical and structural damage of the adsorbed alkanthioles were observed on either of these substrates. But much stronger and faster development of the damage in the organic monolayers was observed on gold films compared to InP. This has been interpreted in terms of a higher defect density and larger effects of X-ray-generated electrons from the substrate on the organic layers in the case of gold. The importance of low-energy electrons for the damage and patterning of the layers has been emphasized. A radiation-induced new sulphur component has been clearly attributed to have a disulphide character using both binding and Auger energies. During the discussion, we have found more arguments supporting a thiolate-type SAM compared to disulphide models on gold.

In the preceding, we have focused on the molecular mechanisms of ionizing radiation. In order to use X-rays or electrons for structuring, it is not necessary to understand the underlying reactions. Electrons can be used directly to remove small parts of self-assembled monolayers, as shown before in the pattern "PCI." The drawback of this method is the very time-consuming sequential writing of the pattern which makes this method very highly prized and not suitable for mass production. Using X-rays instead requires a partial opaque mask. This mask needs to be transparent to X-rays, where parts of the SAM need to be removed and vice versa. The production of such a mask needs an additional type of lithography, for example, electron beams. The second drawback of both methods is that the irradiated parts are not completely free from covering molecules. This can be seen from our detailed spectroscopic investigation at the beginning of this paragraph. These remaining molecules can be removed by heating the sample in UHV [69] or electrochemical methods ([98] and Section 3.2).

Further related methods use UV light [99–102], near-UV light [103], visible light [104], and ion beams [105] for the photolithography of alkanethiol monolayers.

4.2. Scanning Probes

In the preceding section, we already demonstrated two different techniques for lateral structuring a molecule-covered surface. One of the most obvious ideas to write small structures into a self-assembled monolayer is to use scanning probe techniques like STM, AFM, or SECM.

An STM allows us to write structures by applying voltage pulses to the conducting tip while scanning. If the voltage is chosen high enough, small parts of the self-assembled monolayer are removed [22, 56–61, 88]. The voltage needs to surpass a certain threshold, which is typically in the range of 5–10 V, depending on the substrate–adsorbate combination. In order to demonstrate these technique, we have applied a voltage of 20 V at high currents (10 nA), and therefore near distances, while scanning a dodecanethiol layer on InP(110). The result is depicted in Figure 31. A 15 nm wide straight groove is shown, which is confined by sharp edges. The advantage of the technique is its very high resolution; its disadvantage is the low speed of writing, which is orders of magnitude slower than even *e*-beam lithography. An AFM can be used to literally scratch grooves into a monolayer [61]. Its advantage is that it allows structuring and scanning of topography of even thick nonconducting organic coatings due to the characteristics of its measurement principle. It should be mentioned that, instead of scratching the structures into the films, it could be used parallel to the STM technique if the AFM tip is coated with a metal and is correspondingly connected to a voltage source.

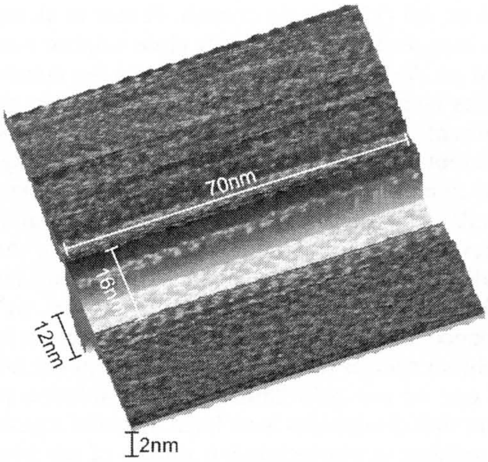

Figure 31. STM-nanostructured dodecanethiol monolayer on InP (110). $U = 20$ V; $I = 10$ nA.

The last microprobe technique which will be mentioned here is the SECM. Contrary to the STM technique, an ultramicroelectrode, a typically on its end flat-polished very thin Au or Pt wire which is coated by a nonconducting glass capillary, poses as a probe. The electrochemical technique is sensitive to redox reactions, and can also be used to deposit organics [98].

4.3. Microcontact Printing and Related Techniques

Microcontact printing (μPC) and related techniques use an old idea which has its roots in the late middle ages. Around the year 1444, Gutenberg invented the idea of using stamps for the purpose of typography. More than 500 years later, Kumar and Whitesides rediscovered this technique (with some changes) in order to transfer microstructured patterns of monolayers on surfaces [106].

The principle of microcontact printing is surprisingly easy. With the help of an elastic stamp of PDMS which is wetted by a self-assembling species, the pattern is transferred to the surface by contact. The technique allows different self-assembling species to be transferred by simply consecutively repeating the procedure with different stamps. Kumar and Whitesides where the first to invent this technique, using the system alkanethiolates on gold [106].

The greatest advantage of this method is its high speed, transferring one whole structure in one single fast stamping.

The time which is needed to obtain a highly ordered SAM from a 10 mM concentrated dodecanethiol in ethanol solution was investigated by Biebuyck et al., and was found to be as short as 0.3 s on Au (111) [21]. The typical time for a 2 mM concentrated HDT solution is between 10–20 s [107–109].

This ability makes the technique especially interesting for industrial applications. Microcontact printing is not the only method of "stamping" the pattern onto a substrate surface. In the following, we will list some further techniques with brief explanations in order to shed some light on the zoo of different techniques.

- Replica molding (REM): This technique deviates from conventional techniques by using a flexible (PDMS) mold. Its elasticity and small surface tension allow for easy removal of the mold after the process is completed The mold itself is produced by high resolving scanning electron lithography [110, 111].
- Microtransfer molding (μTM): The structured surface of a PDMS mold is coated with an appropriate polymer. Afterwards, the excess, which is everything above the mold surface, is removed. The advantage of this method is that nonplane surfaces can be coated, and the consecutive construction of complex three-dimensional structures is possible [112].
- Micromolding in capillaries (MIMIC): Here, the mold comes into contact with the surface first. The polymer (low viscosity) is distributed through the empty channels of the mold via capillary forces [113]. This technique is also very useful for nonplane surfaces, but it cannot produce isolated structures.
- Solvent-assisted micromolding (SAMIM): The last technique briefly described here is SAMIM, which can be seen as a combination of REM and imprinting. A PDMS mold is wetted with a dissolved polymer. After the mold is pressed onto the surface, the solvent dries out, the mold is removed, and the remaining polymer forms the desired structure [114].

This was only a very brief excursion on the topic of stamping. The author has ignored several variations of stamping techniques, as well as other techniques like laser ablation or inkjet printing because the discussion on the topic of lithography is a review of its own. Instead, we refer to the review on soft lithography of Xia and Whitesides [115] and citations therein.

4.4. Consecutive Chemical Reactions

In this last section on structuring, we will investigate the possibilities of creating mixed thiol films, consisting of two structurally and chemically very different thiol species. We will use the aliphatic hexadecanethiol and the aromatic 2-mercaptobenzothiazol (MBT). The competing interaction of both species after successive adsorption on gold is investigated using XPS.

The ability to produce mixed thiol films on surfaces, consisting of molecules with different electronic and chemical properties and combined with structuring in the nanometer scale, however, may lead to additional possibilities of application. Therefore, it is of interest to investigate the behavior of layers of aromatic thiols in comparison to layers formed by alkanethiols. MBT, known to form hydrophobic complexes with many metals, and therefore used as a corrosion inhibitor or a collector for mineral flotation [116, 117], was chosen for the studies presented here. Beside its aromatic character, MBT contains a nitrogen atom, which acts as an additional ligator atom in a chelate-type bonding at the surface, and can be used as tracer atom for identification of the adsorbed species. In connection to the experiments described above, the interaction between alkanethiols and hydrocarbon contamination, produced by sample transfer in air, was investigated. Because of the similarity of the behavior, it seems to be meaningful to discuss them in this context.

The preparation of the samples was described in detail in Section 2. The hexadecanethiol layer (Fluka, 95%) was prepared in a 10^{-3} M solution in isooctane (Merck, Supra-Solv, for organic trace analysis). The adsorption of MBT was carried out in a 10^{-4} M aqueous solution. After an immersion time of 30 min, the samples were rinsed with fresh solvent, dried under a nitrogen stream, and inserted into the spectrometer immediately. The X-ray photoelectron spectra were recorded with a VG ESCALAB 220i XL instrument irradiating the samples with monochromatized AlKa radiation (220 W, 22 mA, 10 kV). Spectra were recorded in normal emission and with angular averaging mode (XL lens), if not stated otherwise. The energy resolution was 0.45 eV. The spectra were fitted by a least squares procedure with a model of the peak shape (Gaussian–Lorentzian convoluted functions) after background subtraction from experimental data using a Shirley-type function. Binding energies are referred to Au4*f* (84.0 eV).

If a freshly produced gold film is treated with 10^{-4} M MBT solution, an S2*p* spectrum is recorded, as shown in Figure 32a. Two clearly separated components are found, representing the two differently bound sulphur atoms of the MBT molecule (Fig. 32a). The adsorption of MBT leads to deprotonation of most molecules, confirmed by the main component in the N1*s* spectrum with the binding energy of 399.0 eV, in comparison to the component of the not deprotonated molecules at 400.6 eV (Fig. 33a). Therefore, the low-energy component in the S2*p* spectrum (162.3 eV) can be attributed to the exocyclic sulphur of deprotonated and chemisorbed MBT. The second doublet at 163.9 eV is caused by the endocyclic sulphur. A partial oxidation of MBT to products containing sulphur–sulphur bonds like 2,2′-dithiobis(benzothiazole) is responsible for the deviation of the expected intensity ratio of 1:1 [31, 117, 118]. Both types of sulphur atoms in BBTD have nearly the same

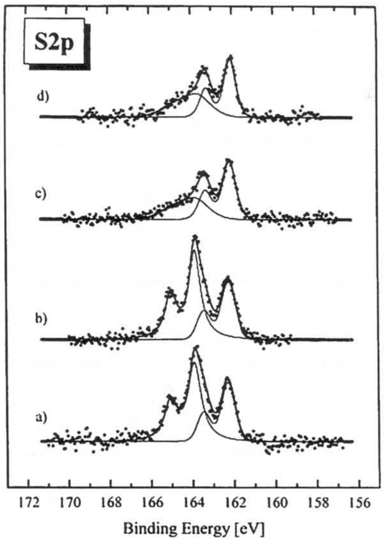

Figure 32. S2*p* spectra after succsessive treatment of an Au surface with: (a) MBT solution, (b) isooctane, (c) hexadecanethiol solution, and (d) MBT solution. Reprinted with permission from [31], D. Zerulla et al., *Surf. Sci.* 402–404, 604 (1998). © 1998, Elsevier Science.

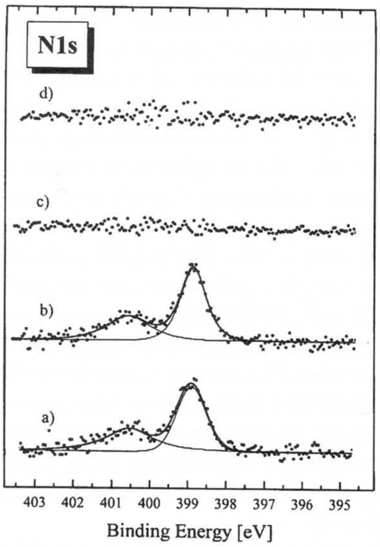

Figure 33. N1*s* spectra after successive treatment of an Au surface with: (a) MBT solution, (b) isooctane, (c) hexadecanethiol solution, and (d) MBT solution. Reprinted with permission from [31], D. Zerulla et al., *Surf. Sci.* 402–404, 604 (1998). © 1998, Elsevier Science.

ground state potential as the endocyclic sulphur in MBT, and cannot be distinguished by their binding energies [118]. After treatment of the MBT-covered sample in pure isooctane for 30 min, no significant changes in the S2*p* and N1*s* spectra were observed (Figs. 32b and 33b), thus excluding any effects caused by this solvent. Only the C1*s* spectrum (Fig. 34b) shows a decrease of the intensity of the signal assigned to aliphatic C–H bonds against the component caused by the aromatic rest, indicating a displacement of hydrocarbon contamination by isooctane. Next, the samples have been treated in an isooctane/hexadecanethiol solution (see Section 3). The changes in the spectra are remarkable. Figure 33c shows the complete absence of nitrogen on the sample surface. This can only be explained by supposing that MBT has been totally removed by the alkanethiol. This conclusion is supported by the S2*p* and C1*s* spectra in Figures 32c and 34c, respectively. These have changed to the typical signals expected for a monolayer of hexadecanethiol on gold. The C1*s* peak shows only one component, belonging to the alkane chain. The S2*p* reveals the typical two doublets for an alkanethiol. The first component at 162.1 eV belongs to the sulphide, which is responsible for the sulphur–gold bonding. The second and less intensive component (163.8 eV) is from disulphide groups. The generation of disulphide in alkanethiol monolayers may arise from air oxidation, but also from the effect of X-rays or electron irradiation. Extended investigations concerning these effects with different energies and intensities on alkanethiol monolayers have been carried out and will be published next. The data in Figures 32d, 33d, and 34d were obtained by exposing the already established alkanethiol film to an aqueous solution of MBT. In contrast to the reversed procedure described above, the surface remains completely covered with hexadecanethiol. Obviously, the adsorbed alkanethiol molecules are resistant against an MBT-containing solution because of the stabilizing effect of the hydrocarbon chain interaction that predominates with respect to the chelating effect of the MBT structure. Consistent with this phenomenon, the MBT adsorbate is completely removed from the gold surface by the hexadecanethiol-containing solution. A similar process to the replacement of the MBT layer by the hexadecanethiol has also been found for the hydrocarbon contamination mentioned at the beginning of this text. In [31], the removal of contamination from a gold surface after the sample has been dipped into a hexadecanethiol solution is demonstrated. The first spectrum shows carbon contamination (C–H and C–O bonds), which was due to exposing the sample to the atmosphere for several days. After a treatment in hexadecanethiol solution for 30 min, additional features of the alkane–carbon appear. The unchanged intensity of the contamination signal gives rise to the assumption that the removal of the carbon does not start until other adsorption sites have been occupied by the thiols. A further treatment for 90 min (total 2 h) removes the contamination and enhances the alkane signal. The last stage shows that an extended treatment (total 16 h) only slightly raises the intensity of the C1*s* signal, indicating a saturation of thiol adsorption with increasing density of the ordered layer. Summarizing, we have confirmed previous results on the ability of thiols to remove organic molecules from gold. In particular, by comparing the bonding of hexadecanethiol and MBT, we have been able to demonstrate that the specific binding of the thiol layers permits stronger bonding to gold, even in relation to other sulphur-containing molecules. This stabilization of a hexadecanethiol layer on a gold surface is believed to be strongly supported by hydrocarbon chain interaction, which is the well-known reason for the self-assembly. This enables the preparation of mixed films.

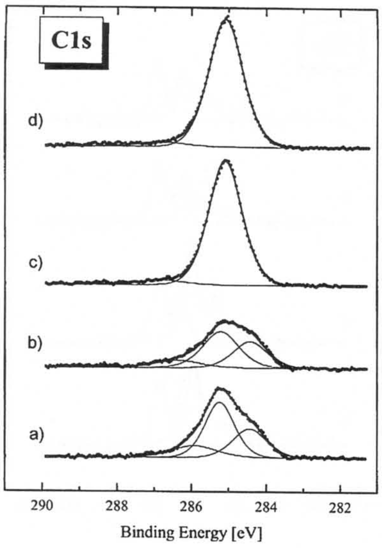

Figure 34. C1*s* spectra after successive treatment of an Au surface with: (a) MBT solution, (b) isooctane, (c) hexadecanethiol solution, and (d) MBT solution. Reprinted with permission from [31], D. Zerulla et al., *Surf. Sci.* 402–404, 604 (1998). © 1998, Elsevier Science.

Starting with a partially covering alkanethiol layer, produced, for example, by stamping the alkanethiol to the surface (see Section 4.3) [21], by different kinds of writing procedures or with the help of AFM/STM structuring (see Sections 4.1, 4.2) [22, 23], the free parts of the substrate can be covered subsequently with MBT by simply dipping the sample into an MBT solution, leaving the alkanethiol layer structurally undisturbed.

We found that hexadecanethiol displaces the MBT from gold surfaces, similar to the removal of carbon contamination by the alkanethiol. In contrast, MBT cannot replace the adsorbed alkanethiol layer. Therefore, the creation of mixed films has to start with a partial coverage of hexadecanethiol, followed by the MBT, which now can assemble to the uncovered surface without disturbing the alkanethiol.

5. MISCELLANEOUS SELF-ASSEMBLING SYSTEMS

While most of this chapter was focused on alkanethiols as self-assembling species, we will briefly describe further types of molecules which will also self-assemble on semiconductor surfaces.

First, there is the class of functionalized thiols which also consist of a sulphur head group and an alkyl chain, but the terminating group differs from the usual $-CH_3$ group. As long as the terminating group is small in size and does not bind to the semiconductor, we expect the same result as shown in this review. If the terminating group does bind to the substrate, we not only get reversed bounded molecules, but also loops where the head and the terminating group are bounded to the substrate [64]. Instead of exchanging the terminating group, one can change the head group which is responsible for the substrate–molecule binding. Instead of the thiol (–SH) group, sulphonic and phosphorus groups have been used. The choice of the head group should be made with respect to the substrate used. Thiols bind very well on coinage metals (Au, Ag, Cu) and III–V semiconductors, while sulphonic and phosphorus groups bind to oxidized metal surfaces, for example, Al (see Table 1). In the case of the technologically very important Si [42–49], the best choice is to use alkyltricholorosilanes, which give high-quality self-assembled monolayers on this substrate [38–41].

One of the many goals in using SAMs for technological applications is to construct assays for biological and medical sensors. This can be done in two ways. The first is to use well-known self-assembling species as building blocks in the construction of these assays. They may be used as spacers, to specifically bind biomolecules or as a structure-defining substrate themselves [119]. Second, some of the biological species can be used as self-assembling monolayers themselves. One example is the amino acid cysteine, which is able to bind on III–V semiconductor surfaces as well as on coinage metals by its sulphur side group [64]. However, this kind of molecule does not deliver highly ordered monolayers due to two facts. Its chain length is not large enough to have enough van der Waals interactions between neighboring molecules; therefore, one of the most important forces in self-assembly is too weak. Furthermore, it not only can bind with the sulphur, but also with the carboxyl group to most substrates. The result is a nearly unordered monolayer with only weak passivating properties compared to alkanethiols [64].

Table 2. References of semiconductor–SAM combinations in literature.

Substrate	Adsorbate(s)	Author(s)	Ref.
Si(100)	Alkyltrichlorosilane (docosyltrichlorosilane, octyltrichlorosilane)	Nuzzo, Chidsey, Grunze	[38–41, 123]
GaAs	Alkanethiols	Allara	[121–122]
InP(100)	Allkanethiols	Gu Waldeck	[25]
InP(110)	Alkanethiols, mercaptobenzothiazole	Zerulla	[53, 64, 66 67, 75]
GaP(110)	Alkanethiols	Zerulla Chassé	[67]
CdS (1010)	Mercaptobenzothiazole	Mayer Szargan	[75, 124]
PbS, FeS_2	Thiols	Schaufuß, Szargan	[118]

In general, all species that fulfill the following simple rules are likely to form highly ordered self-assembling monolayers:

- a chain length >6 (best: 12–24) [120]
- only one group which binds to the substrate
- the space requirements of the molecules are smaller than the lattice constants of the substrates (more precisely, the distance between binding sites on the substrate).

Of course, these rules ignore complicated molecule–molecule and molecule–substrate interactions, but will suffice in most cases. A compilation of references of semiconductor–SAM combinations in the literature is shown in Table 2. Note that the number of investigations of SAMs on semiconductors is by far lower than on coinage metals. A more detailed treatment, including structure and electronic properties, can be found in Section 4.

6. CONCLUSION

The self-assembly of thiols and related molecules on semiconductors leads to highly ordered systems. Independent of the preparation technique (solution/evaporation), it results in stable, passivating monolayers. For the example of alkanethiols on InP(110), proof is given that the self-assembly leads to single-domain systems with exceptional order. Furthermore, different techniques have been presented which may be used to write structures into the self-assembled monolayers on nanometer scales.

Additionally, even the possibility of constructing monolayers from different self-assembling species was demonstrated. Comparing the results on semiconductor (110) surfaces with those on Au (111), we can conclude that the ease of preparation, passivating properties, and structure are similar. Moreover, it can be stated that the perfection of the adsorbed monolayers is even higher on the semiconductor (110) surfaces than on gold, at least regarding InP (110).

As a future prospect, we suggest using the combination of thiols and a III–V (110) surface in order to construct nanodevices with specifically tailored properties.

GLOSSARY

Chemical vapor deposition (CVD) Technique used to deposit coatings, where chemicals are first vaporized, and then applied using an inert carrier gas such as nitrogen.

Langmuir–Blodgett Name of a nanofabrication technique used to create ultrathin films (monolayers and isolated molecular layers), the end result of which is called a "Langmuir–Blodgett film."

Nanoimprinting Sometimes called soft lithography. A technique that is very simple in concept, and totally analogous to traditional mold- or form-based printing technology, but that uses molds (masters) with nanoscale features. As with the printing press, the potential for mass production is clear. There are two forms of nanoimprinting: one that uses pressure to make indentations in the form of the mold on a surface, and the other, more akin to the printing press, that relies on the application of "ink" applied to the mold to stamp a pattern on a surface. Other techniques such as etching may then follow.

Nanolithography Writing on the nanoscale. From the Greek words nanos—dwarf, lithos—rock, and grapho—to write, this word literally means "small writing on rocks."

OLED or organic LED Not made of semiconductors. It is made from carbon-based molecules. That is the key science factor that leads to potentially eliminating LED's biggest drawback—size. The carbon-based molecules are much smaller.

Self-assembly In chemical solutions, self-assembly (also called Brownian assembly) results from the random motion of molecules and the affinity of their binding sites for one another. Also refers to the joining of complementary surfaces in nanomolecular interaction.

Acknowledgments

This work was supported by Deutsche Forschungsgemeinschaft (DFG, Innovationskolleg 24/A1-2313-704-P), BMBF (Laserbiodynamik 13N7515/6), and ELMINOS (AGEF). The work was also supported by the Graduiertenkolleg Physical Chemistry of Interfaces. The author acknowledges stimulating discussions with M. Grunze, T. Chassé, and F. Katzenberg. Finally, the author thanks his wife, N. Zerulla, and his research group (especially G. Isfort and M. Kölbach) for their patience.

REFERENCES

1. A. Pockels, *Nature* 43, 437 (1891).
2. A. Pockels, *Nature* 46, 418 (1892).
3. A. Pockels, *Nature* 48, 152 (1893).
4. A. Pockels, *Nature* 50, 223 (1894).
5. L. Rayleigh, *Philos. Mag.* 48, 321 (1899).
6. W. B. Hardy, *Proc. R. Soc. London A* 86, 610 (1912).
7. H. Devaux, *Smithsonian Inst. Ann. Rep.* 261 (1913).
8. I. Langmuir, *J. Am. Chem. Soc.* 39, 1848 (1917).
9. I. Langmuir, *Trans. Faraday Soc.* 15, 62 (1920).
10. K. Blodgett, *J. Am. Chem. Soc.* 57, 1007 (1935).
11. K. Blodgett, *Phys. Rev.* 51, 964 (1937).
12. W. C. Bigelow, D. L. Pickett, and W. A. Zisman, *J. Colloid Interface Sci.* 1, 513 (1946).
13. L. C. F. Blackman and M. J. S. Dewar, *J. Chem. Soc.* 162, I (1957).
14. G. L. Gaines, Jr., "Insoluble Monolayers at Liquid-Gas Interfaces." Interscience, New York, 1966.
15. A. Ulman, "An Introduction to Ultrathin Organic Films: From Langmuir-Blodgett to Self-Assembly." Academic, New York, 1988.
16. R. G. Nuzzo and D. L. Allara, *J. Am. Chem. Soc.* 105, 4481 (1983).
17. P. G. de Gennes, *Rev. Mod. Phys.* 57, 827 (1985).
18. S. Dietrich, in "Phase Transition and Critical Phenomena," (C. Domb and J. L. Lebowitz, Eds.), Vol. 12. Academic, New York, 1988.
19. C. D. Bain and G. M. Whitesides, *Angew. Chem. Int. Ed. Engl.* 28, 506 (1989).
20. F. Schreiber, *Progr. Surf. Sci.* 65, 151 (2000).
21. H. A. Biebuyck, N. B. Larsen, E. Delamarche, and B. Michel, *IBM J. Res. Dev.* 41, 159 (1997).
22. C. B. Ross, L. Sun, and R. M. Crooks, *Langmuir* 9, 632 (1993).
23. J. K. Schoer and R. M. Crooks, *Langmuir* 13, 2323 (1997).
24. S. R. Lunt, G. N. Ryba, P. G. Santangelo, and N. S. Lewis, *J. Appl. Phys.* 70, 7449 (1991).
25. Y. Gu, Z. Lin, R. A. Butera, V. S. Smentkowski, and D. H. Waldeck, *Langmuir* 11, 1849 (1995).
26. H. Sellers, A. Ulman, Y. Shnidman, and J. E. Eilers, *J. Am. Chem. Soc.* 115, 9389 (1993).
27. J. Kang and P. A. Rowntree, *Langmuir* 12, 2813 (1996).
28. D. L. Allara and R. G. Nuzzo, *Langmuir* 1, 52 (1985).
29. P. E. Laibinis, G. M. Whitesides, D. L. Allara, Y. Tao, A. N. Parikh, and R. G. Nuzzo, *J. Am. Chem. Soc.* 113, 7152 (1991).
30. R. G. Nuzzo, B. R. Zegarski, and L. H. Dubois, *J. Am. Chem. Soc.* 109, 733 (1987).
31. D. Zerulla, I. Uhlig, R. Szargan, and T. Chasse, *Surf. Sci.* 402–404, 604 (1998).
32. D. Zerulla and T. Chasse, *Langmuir* 15, 5285 (1999).
33. E. Dudzik, A. Leslie, E. O'Toole, I. T. McGovern, A. Patchett, and D. R. T. Zahn, *Appl. Surf. Sci.* 104, 101 (1996).
34. T. K. Johal, P. Finetti, V. R. Dhanak, A. W. Robinson, A. Patchett, D. R. T. Zahn, and R. McGrath, *Appl. Surf. Sci.* 104–105, 257 (1996).
35. T. Chassé, A. Chassé, H. Peisert, and P. Streubel, *Appl. Phys. A* 65, 543 (1997).
36. H. Peisert, T. Chassé, P. Streubel, A. Meisel, and R. Szargan, *J. Electron Spectrosc. Related Phenom.* 68, 321 (1994).
37. T. Chassé, H. Peisert, P. Streubel, and R. Szargan, *Surf. Sci.* 331–333, 434 (1995).
38. K. R. Finnie and R. G. Nuzzo, *Langmuir* 17, 1250 (2001).
39. K. R. Finnie, R. Haasch, and R. G. Nuzzo, *Langmuir* 17, 6968 (2001).
40. D. L. Allara, A. N. Parikh, and F. Rondelez, *Langmuir* 11, 2357 (1995).
41. K. Bierbaum and M. Grunze, *Langmuir* 11, 2143 (1995).
42. V. V. Doan, and M. J. Sailor, *Science* 256, 1791 (1992).
43. M. P. Stewart and J. M. Buriak, *Adv Mater.* 12, 859 (2000).
44. O. D. Velev and E. W. Kaler, *Adv Mater.* 12, 531 (2000).
45. S. Schuppler, S. L. Friedman, M. A. Marcus, D. L. Adler, H. Xie, F. M. Ross, Y. J. Chabal, T. D. Harris, L. E. Brus, W. Brown, E. E. Chaban, P. F. Szajowski, S. B. Christman, and P. H. Citrin, *Phys. Rev. B* 52, 4910 (1995).
46. V. Lehmann and U. Gosele, *Appl. Phys. Lett.* 58, 856 (1991).
47. J. Harper and M. J. Sailor, *Anal. Chem.* 68, 3713 (1996).
48. T. F. Harper and M. J. Sailor, *Anal. Chem.* 119, 6943 (1997).
49. K.-P. S. Dancil, D. P. Greiner, and M. J. Sailor, *J. Am. Chem. Soc.* 121, 7925 (1999).
50. [a] W. Schommers and P. von Blanckenhagen, "Structure and Dynamics of Surfaces I," Springer Topics in Current Physics, Vol. 41. Springer, Berlin, New York, Heidelberg, 1985. [b] H. Kalt, in "Optical Properties of Semiconductors," Springer Series in Solid-State Science, Vol. 120. Springer, Heidelberg, 1996.
51. N. Esser, U. Resch-Esser, M. Priestovsek, and W. Richter, *Phys. Rev. B* 53, 13257 (1996).

52. G. E. Poirer and E. D. Pylant, *Science* 272, 1145 (1996).
53. D. Zerulla and T. Chassé, *Langmuir* 18, 5392 (2002).
54. J. P. Song, N. H. Pryds, K. A. Morch, A. R. Thölen, and L. N. Christensen, *Rev. Sci. Instrum.* 64, 900 (1993).
55. K. Dickmann, F. Demming, and J. Jersch, *Rev. Sci. Instrum.* 67, 845 (1997).
56. J. A. Dagata, W. Tseng, J. Bennett, J. Schneir, and H. H. Harary, *J. Appl. Phys.* 70, 3661 (1991).
57. C. R. K. Mariann, F. K. Perkins, S. L. Brandow, T. S. Koloski, E. A. Dobisz, and J. M. Calvert, *Appl. Phys. Lett.* 63, 390 (1994).
58. K. Dickmann, F. Demming, and J. Jersch, *Rev. Sci. Instrum.* 67, 845 (1996).
59. C. A. Widrig, C. A. Alves, and M. D. Porter, *J. Am. Chem. Soc.* 113, 2805 (1991).
60. G. E. Poirer, W. P. Fitts, and J. M. White, *Langmuir* 17, 1176 (2001).
61. A. Ikai, *Surf. Sci. Rep.* 26, 261 (1996).
62. H. Neddermeyer, "Scanning Tunneling Microscopy," 1st ed. Kluwer Academic, 1993.
63. C. Bai, "Scanning Tunneling Microscopy and Its Application," 1st ed. Springer, 1994.
64. D. Zerulla, Ph.D. Dissertation, Universität Leipzig, Wilhelm-Ostwald-Institut, Germany, 1999.
65. S. Schömann and T. Chassé, *J. Vac. Sci. Technol. A* 16, 2990 (1998).
66. D. Zerulla and T. Chassé, *Chem. Phys. Lett.* 311, 8 (1999).
67. T. Chassé, D. Zerulla, and K.-H. Hallmeier, *Surf. Rev. Lett.* 6, 1179 (1999).
68. K. Bierbaum, M. Kinzler, Ch. Wöll, M. Grunze, G. Hähner, S. Heid, and F. Effenberger, *Langmuir* 11, 512 (1995).
69. J. M. Behm, K. R. Lykke, M. J. Pellin, and J. C. Hemminger, *Langmuir* 12, 2121 (1996).
70. R. Gerlach, G. Polanski, and H.-G. Rubahn, *J. Chem. Phys.* (1996).
71. H.-J. Himmel, Ch. Wöll, R. Gerlach, G. Polanski, and H.-G. Rubahn, *Langmuir* 13, 602 (1997).
72. Ch. Jung, O. Danneberger, Y. Xu, M. Buck, and M. Grunze, *Langmuir* 14, 1103 (1998).
73. D. Zerulla, N. Zerulla, and C. Ehlers (to be published).
74. J. Stöhr, NEXAFS. Springer, Heidelberg/New York, 1995.
75. D. Mayer, K.-H. Hallmeier, D. Zerulla, and R. Szargan, in "Topics in Applied Physics," (K. Wandelt, Ed.). Springer, Heidelberg, 2002.
76. M. D. Porter, T. B. Bright, D. L. Allara, and C. E. D. Chidsey, *J. Am. Chem Soc.* 109, 3559 (1987).
77. R. Hesse, T. Chassé, and R. Szargan, *Fresenius J. Anal. Chem.* 365, 48 (1999).
78. M. Wirde, U. Gelius, T. Dunbar, and D. Allara, *Nucl. Instrum. Meth. Phys. Res. B* 131, 245 (1997).
79. B. Jäger, H. Schürmann, H. U. Müller, H.-J. Himmel, M. Neumann, M. Grunze, and Ch. Wöll, *Z. Phys. Chem.* 202, 263 (1997).
80. R. C. Tiberio, H. G. Craighead, M. Lercel, T. Lau, C. W. Sheen, and D. L. Allara, *Appl. Phys Lett.* 62, 468 (1993).
81. M. J. Lercel, G. F. Redinbo, H. G. Craighead, C. W. Sheen, and D. L. Allara, *Appl. Phys Lett.* 65, 974 (1994).
82. M. J. Lercel, H. G. Craighead, A. N. Parikh, K. Seshadri, and D. L. Allara, *Appl. Phys Lett.* 68, 1504 (1996).
83. K. Siegbahn, *Nova Acta Soc. Sci. Upsaliensis* 20, 175 (1967).
84. V. I. Nefedov, "X-ray Photoelectron Spectra of Chemical Compounds; Chemistry." Moscow.
85. D. Gallet and G. Hollinger, *Appl. Phys. Lett.* 62, 982 (1992).
86. D. Rading, V. Liebing, G. Becker, H. Fuchs, and A. Benninghoven, *J. Vac. Sci. Technol. A* 16, 3449 (1998).
87. A. S. Duwez, L. M. Yu, J. Riga, J. J. Pireaux, and J. Delhalle, *Thin Solids Films* 329, 156 (1998).
88. B. Völkel, A. Gölzhäuser, H. U. Müller, C. David, and M. Grunze, *J. Vac. Sci. Technol. B* 15, 2877 (1997).
89. R. G. Nuzzo, L. H. Dubois, and D. L. Allara, *J. Am. Chem Soc.* 112, 558 (1990).
90. P. Fenter, A. Eberhardt, and P. Eisenberger, *Science* 266, 1216 (1994).
91. P. Fenter, F. Schreiber, L. Berman, G. Scoles, P. Eisenberger, and M. J. Bedzyk, *Surf. Sci.* 412–413, 213 (1998).
92. D. R. Mullins, T. Tang, X. Chen, V. Shneerson, D. K. Saldin, and W. T. Tysoe, *Surf. Sci.* 372, 193 (1997).
93. D. R. Mullins, D. R. Huntley, T. Tang, D. K. Saldin, and W. T. Tysoe, *Surf. Sci.* 380, 468 (1997).
94. B. L. Henke, J. P. Knauer, and K. J. Premaratne, *Appl. Phys.* 52, 1509 (1981).
95. M. S. Kariapper, G. F. Grom, G. J. Jackson, C. F. McConville, and D. P. Woodruff, *J. Phys. Cond. Matter* 10, 8661 (1998).
96. N. N. Greenwood and A. Earnshaw, "Chemistry of the Elements." Pergamon, Oxford, 1984.
97. K.-H. Hallmeier, D. Mayer, and R. Szargan, *J. Electron. Spectrosc. Related Phenom.* 96, 245 (1998).
98. R. F. Service, *Science* 265, 316 (1994).
99. J. Huang, D. A. Dahlgren, and J. Hemminger, *Langmuir* 10, 626 (1994).
100. J. Huang and J. Hemminger, *J. Am. Chem. Soc.* 115, 3342 (1993).
101. M. Tarlov, D. R. F. Burgess, and G. Gillen, *J. Am. Chem. Soc.* 115, 5305 (1993).
102. G. Gillen, J. Benett, M. Tarlov, and D. R. F. Burgess, *Anal. Chem.* 66, 2170 (1994).
103. K. C. Chan, T. Kim, J. K. Schoer, and R. M. Crooks, *J. Am. Chem. Soc.* 117, 5875 (1995).
104. C. D. Frisbie, E. W. Wollman, and M. S. Wrighton, *Langmuir* 11, 2653 (1995).
105. P. C. Rieke, B. J. Trarasevich, L. L. Wood, M. H. Engelhard, D. R. Baer, G. E. Fryxwell, C. M. John, D. A. Laken, and M. C. Jaehnig, *Langmuir* 10, 619 (1994).
106. A. Kumar and G. M. Whitesides, *Appl. Phys. Lett.* 63, 2002 (1993).
107. H. A. Biebuyck and G. M. Whitesides, *Langmuir* 10, 4581 (1994).
108. A. Kumar, E. Kim, and G. M. Whitesides, *Adv. Mater.* 6, 600 (1994).
109. A. Kumar, N. L. Abott, E. Kim, H. A. Biebuyck, and G. M. Whitesides, *Acc. Chem. Res.* 28, 219 (1995).
110. Y. Xia, E. Kim, X.-M. Zhao, J. A. Rogers, M. Prentiss, and G. M. Whitesides, *Science* 273, 347 (1996).
111. G. M. Whitesides and Y. Xia, *Photon. Spectra* 31, 90 (1997).
112. X.-M. Zhao, Y. Xia, and G. M. Whitesides, *Adv. Mater.* 8, 837 (1996).
113. E. Kim, Y. Xia, and G. M. Whitesides, *Nature* 376, 581 (1995).
114. E. Kim, Y. Xia, X.-M. Zhao, and G. M. Whitesides, *Adv. Mater.* 9, 651 (1997).
115. Y. Xia and G. M. Whitesides, *Angew. Chem.* 110, 568 (1998).
116. M. D. Fuerstenau, J. D. Miller, and M. C. Kuhn, in "Chemistry of Flotation," p. 27. Am. Inst. Mining Metal. Petr. Eng., New York, 1985.
117. R. Szargan, I. Uhlig, G. Wittstock, and P. Roßbach, *Int. J. Min. Process*, 51, 151 (1997).
118. A. Schaufuß, P. Roßbach, I. Uhlig, and R. Szargan, *Fresenius J. Anal. Chem.* 358, 262 (1997).
119. L. H. Dubois, B. R. Zegarski, and R. G. Nuzzo, *J. Am. Chem. Soc.* 112, 570 (1990).
120. P. Fenter, A. Eberhardt, K. S. Liang, and P. Eisenberger, *J. Chem. Phys.* 106, 1600 (1997).
121. C. W. Sheen, J. X. Shi, J. Martensson, A. N. Parikh, and D. L. Allara, *J. Am. Chem. Soc.* 114, 1514 (1992).
122. O. S. Nakagawa, S. Ashok, C. W. Sheen, J. Martensson, and D. L. Allara, *Jpn. J. Appl. Phys.* 30, 3759 (1991).
123. M. R. Linford and C. E. D. Chidsey, *J. Am. Chem. Soc.* 115, 12631 (1993).
124. D. Mayer, K. H. Hallmeier, T. Chassé, and R. Szargan, *Fresenius J. Anal. Chem.* 361 , 689 (1998).

5392 *Langmuir* **2002,** *18,* 5392−5399

Scanning Tunneling Microscopy and Spectroscopy of UHV-Deposited Dodecanethiolate Films on InP(110) Surfaces at Consecutive Doses: A Single Domain System

D. Zerulla*,† and T. Chassé‡

Physikalische Methoden für Biologie und Medizin, Heinrich-Heine-Universität Düsseldorf, Universitätsstr. 1, D-40225 Düsseldorf, Germany, and Wilhelm-Ostwald-Inst. für Physik. u. Theor. Chemie, Universität Leipzig, Linnéstr. 2, D-04103 Leipzig, Germany

Received June 4, 2001. In Final Form: January 4, 2002

The coverage and order of dodecanethiolate molecules on InP(110) surfaces is controlled via scanning tunneling microscopy (STM) investigations in dependence of the dodecanethiol dose. Starting from the clean, cleaved semiconductor surface, the STM pictures show the different states of order in the self-assembling films with molecular/atomic resolution. Additionally, scanning tunneling spectroscopy has been applied to distinguish with lateral high resolution between covered and uncovered regions on the surface. Further proof is given by (S)XPS and XPD spectra, obtained from measurements at the synchrotron storage ring BESSY and high-resolution laboratory sources, at all consecutive stages of adsorption.

1. Introduction

Alkanethiols are well-known to form self-assembling monolayers (SAMs) on metals such as gold,[1−16] silver, copper, and semiconductors.[17−20] These monolayers exhibit interesting chemical and structural properties and are therefore very promising for tailoring surface properties. The self-assembly results in a unique arrangement of the alkyl chains with a well-defined vectorial angle of the chains with respect to the surface normal. However, even on the single-crystal surfaces of the metals investigated so far, the molecular orientation regarding the azimuthal direction is not uniform. As a result of metal surface symmetry, formation of several domains of differing azimuthal molecular orientation is permitted. Here, we report for the first time on a scanning tunneling microscopy (STM) and spectroscopic analysis of self-assembling monolayers, which possess a very high degree of molecular order in both vectorial (polar) and azimuthal orientations along the crystallographic [001] direction of the semiconductor substrate. This unique feature has been observed first during X-ray absorption measurements on the carbon K edge (C K XANES (X-ray absorption near-edge structure)), which have been performed in our group in order to explore the self-assembling properties on compound semiconductor surfaces.[21−23] On the basis of these former investigations of "single-domain systems" (prepared from dilute millimolar solutions of thiols in organic solvents) with core level photoemission (XPS (X-ray photoelectron spectroscopy)), XANES, Auger electron spectroscopy (AES), and reflection/absorption infrared (RAIR) spectroscopy, we continue in this paper with a combined STM, scanning tunneling spectroscopy (STS), and soft X-ray photoelectron spectroscopy (SXPS) study of dodecanethiol films. We further extend our experiments to vacuum-deposited films in the submonolayer−monolayer region.

2. Experimental Section

Because of the active properties of the freshly cleaved InP(110) surface, all experiments (at least with submonolayer coverage) had to take place in ultrahigh vacuum (UHV). Therefore, the STM head, which has been constructed on a CF-100 flange, had to be mounted inside an UHV chamber. The latter consists of three subchambers: the FEAL system, the preparation section, and the main chamber, which are separated from each other by gate valves. The base pressure in the main and preparation chambers was 2×10^{-10} mbar using a combination of a turbo molecular/rotary pump. For the sake of low vibration, this combination could be shut down. In this case, we used a liquid nitrogen cooled Titan sublimation pump (TSP) (Varian, Italy) and an ion getter pump (HVD, Germany) instead. These were able to maintain the good vacuum conditions without generating vibrations. When the TSP was cooled with liquid nitrogen, the pressure went down to 5×10^{-11} mbar. The STM and its controller (RS4000) were manufactured by Danish Micro Engineering (DME, Denmark).

---

* Corresponding author. E-mail: zerulla@uni-duesseldorf.de.

† Heinrich-Heine-Universität Düsseldorf.

‡ Universität Leipzig.

(1) Nuzzo, R. G.; Allara, D. L. *J. Am. Chem. Soc.* **1983**, *105*, 4481.

(2) Nuzzo, R. G.; Zegarski, B. R.; Dubois, L. H. *J. Am. Chem. Soc.* **1987**, *109*, 733.

(3) Poirer, G. E.; Pylant, E. D. *Science* **1996**, *272* (5265), 1145.

(4) Kang, J.; Rowntree, P. A. *Langmuir* **1996**, *12*, 2813.

(5) Laibinis, P. E.; Whitesides, G. M.; Allara, D. L.; Tao, Y.; Parikh, A. N.; Nuzzo, R. G. *J. Am. Chem. Soc.* **1991**, *113* (19), 7152.

(6) Porter, M. D.; Bright, T. B.; Allara, D. L.; Chidsey, C. E. D. *J. Am. Chem. Soc.* **1987**, *109*, 3559.

(7) Widrig, C. A.; Alves, C. A.; Porter, M. D. *J. Am. Chem. Soc.* **1991**, *113* (8), 2805.

(8) Nuzzo, R. G.; Dubois, L. H.; Allara, D. L. *J. Am. Chem. Soc.* **1990**, *112*, 558.

(9) Gerlach, R.; Polanski, G.; Rubahn, H.-G. *J. Chem. Phys.* **1996**.

(10) Himmel, H.-J.; Wöll, Ch.; Gerlach, R.; Polanski, G.; Rubahn, H.-G. *Langmuir* **1997**, *13*, 602.

(11) Poirer, G. E.; Fitts, W. P.; White, J. M. *Langmuir* **2001**, *17*, 1176.

(12) Hansen, H. S.; Tougaard, S.; Biebuyck, H. *J. Electron Spectrosc. Relat. Phenom.* **1992**, *58*, 141.

(13) Fenter, P.; Eberhardt, A.; Liang, K. S.; Eisenberger, P. *J. Chem. Phys.* **1997**, *106* (4), 1600.

(14) Zerulla, D.; Uhlig, I.; Szargan, R.; Chassé, T. *Surf. Sci.* **1998**, *402*−*404*, 604−608.

(15) Allara, D. L.; Nuzzo, R. G. *Langmuir* **1985**, *1*, 52.

(16) Schreiber, F. *Prog. Surf. Sci.* **2000**, *65*, 151−256.

(17) Dubois, L. H.; Zegarski, B. R.; Nuzzo, R. G. *J. Am. Chem. Soc.* **1990**, *112*, 570.

(18) Lunt, S. R.; Ryba, G. N.; Santangelo, P. G.; Lewis, N. S. *J. Appl. Phys.* **1991**, *70* (12), 7449.

(19) Gu, Y.; Lin, Z.; Butera, R. A.; Smentkowski, V. S.; Waldeck, D. H. *Langmuir* **1995**, *11*, 1849−1851.

(20) Lercel, M. J.; Redinho, G. F.; Craighead, H. G.; Sheen, C. W.; Allara, D. L. *Appl. Phys. Lett.* **1994**, *65* (8), 974.

(21) Zerulla, D.; Chassé, T. *Langmuir* **1999**, *15* (16), 5285−5294.

(22) Zerulla, D.; Chassé, T. *Chem. Phys. Lett.* **1999**, *311* (1−2), 8−12.

(23) Chassé, T.; Zerulla, D.; Hallmeier, K.-H. *Surf. Rev. Lett.* **1999**, *6* (6), 1179−1186.

10.1021/la0108205 CCC: $22.00

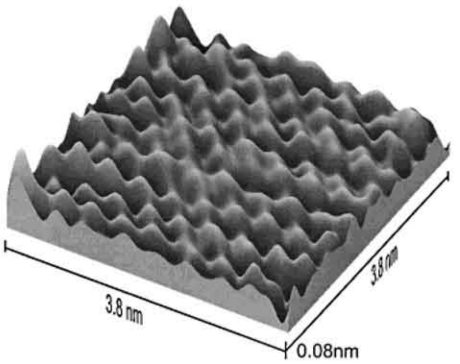

Figure 1. STM picture of freshly cleaved InP(110) ($U_T = 2.2$ V; $I_T = 1$ nA).

The tungsten tips were self-made with the help of a two-step procedure (see refs 24 and 25):

First, a straight tungsten wire with 0.35 mm diameter (Good Fellow, U.K.) has been AC-etched in contact with a 1 mmol KOH solution until a sharp tip with a radius of <100 nm appeared. Then, prior to immediate use, a second AC-etching procedure has been applied. A thin film of KOH solution was held in a loop of platinum wire (similar to a soap film), which is also used as one of the electrodes. The tungsten tip itself constitutes the second electrode and is slowly moved forward and backward through the thin KOH film by a micrometer screw. This procedure leads to very sharp (up to 10−20 nm tip radius) and uniform tip shapes. Because of additional control of the current direction of the last applied sine wave, the tips are also free from covering oxide layers.

Following this procedure, the tips were rinsed with tridest. H_2O and were directly inserted into the vacuum chamber. A self-constructed system allowed the change of not only the samples but also up to seven tips at one time, without breaking the vacuum.

The supporting X-ray photoelectron diffraction (XPD) and X-ray photoelectron spectroscopy measurements were made with an Escalab 220 iXL (Vacuum Generators VG, U.K.) spectrometer, equipped with a monochromatized Al Kα source and a computer-controlled microstage.

The dodecanethiol (Aldrich, 98%) was let into the preparation chamber by means of a sapphire-sealed leak valve (Vacuum Generators VG), which is inert to sulfur-containing species. To minimize the content of dissolved oxygen in the alkanethiol, the liquid has been degassed by several repeated pumping, purging (with N_2, 99.999%, Messer Griesheim, Germany), and freezing cycles, before passing the leak valve. The valve and its surrounding have been slightly heated (35−45 °C) to prevent condensation and physisorption of the alkanethiol molecules on the inner sealing surfaces of the leak valve.

The comparative SXPS spectra have been recorded at the BESSY synchrotron storage ring in Berlin at the undulator beamline TGM-5, using a VG Baby-Aries spectrometer.

3. Measurements

The first straightforward step in the investigation of vacuum-deposited alkanethiols on III-V semiconductors was to monitor the clean, freshly cleaved (UHV conditions) semiconductor surface itself, via STM.

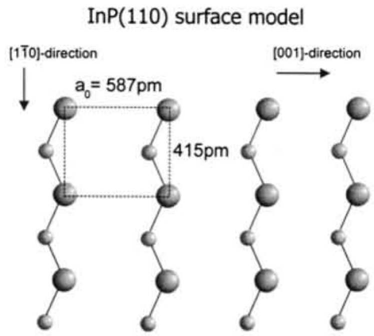

Figure 2. Model of the InP(110) surface.

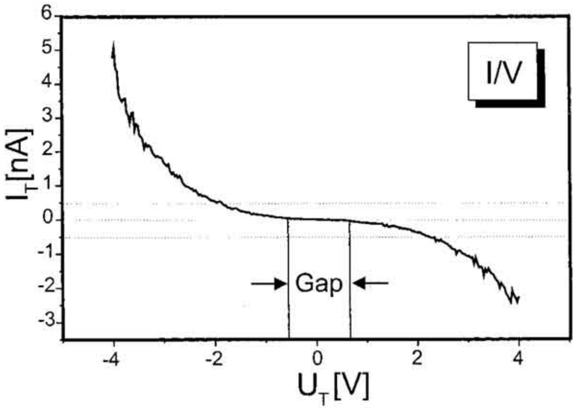

Figure 3. Locally resolved ST spectrum of the freshly cleaved InP(110) surface.

Depending on the polarity of the tip in respect to the substrate surface, the STM picture shows the positions of either the indium or the phosphorus atoms.[26−28] The surface in Figure 1 has been recorded with a positive tip, therefore showing the filled "dangling bonds" of the phosphorus atoms. The distances of the atoms have been analyzed in the [001] and [1$\bar{1}$0] directions of the surface. These measured distances of 590 and 420 pm are close to the ideal distances, 587 and 415 pm, respectively, which can be taken from the model surface in Figure 2. The differences between ideal and measured distances are well in the limit of the temperature-dependent reproducibility of the STM piezo crystals, which have been calibrated before with the help of a highly ordered pyrolytic graphite (HOPG) surface (DME, Denmark). Surface relaxation effects have an influence on the height offset of the topmost phosphorus atoms with respect to the indium atoms (I−P) but no effect on the P−P distances within the first layer.[29−32]

Further STM investigations on a larger scale show only minor distortions of the surface in the form of small steps (typical height 1−6 atoms). Typically, the surfaces are free from defects for lateral dimensions as large as 1 mm^2.

For the typical lateral scale of atomic resolved STM graphs, this in fact allows for the investigation of adsorbates on regions without any substrate defects.

STS measurements of various positions on such freshly cleaved InP(110) surfaces lead to an I/U spectrum which is shown in Figure 3. The shown spectrum is a result of 256 independently recorded spectra, which have been added to suppress random noise. The main characteristic feature of these spectra is the very good visible band gap, which is about 1.3 eV at room temperature in the case of InP. In our experiments, the line shape of the spectra was

---

(24) Dickmann, K.; Demming, F.; Jersch, J. *Rev. Sci. Instrum.* **1996**, *67* (3), 845−846.

(25) Oliva, A. I.; Romero, A.; Pena, J. L. *Rev. Sci. Instrum.* **1996**, *67* (5), 1917−1921.

(26) Ikai, A. *Surf. Sci. Rep.* **1996**, *26*, 261−332.

(27) Neddermeyer, H. *Scanning Tunneling Microscopy*, 1st ed.; Kluwer Academic Publishers: Norwell, MA, 1993.

(28) Bai, C. *Scanning Tunneling Microscopy and its Application*, 1st ed.; Springer: New York, 1994.

(29) Chassé, T.; Chassé, A.; Peisert, H.; Streubel, P. *Appl. Phys. A* **1997**, *65*, 543−549.

(30) Peisert, H.; Chassé, T.; Streubel, P.; Meisel, A.; Szargan, R. *J. Electron Spectrosc. Relat. Phenom.* **1994**, *68*, 321−328.

(31) Chassé, T.; Peisert, H.; Streubel, P.; Szargan, R. *Surf. Sci.* **1995**, *331−333*, 434−440.

(32) Schömann, S.; Chassé, T. *J. Vac. Sci. Technol., A* **1998**, *16*, 2990−2994.

independent of the exact lateral position of the STM tip, and therefore it still represents a more macroscopic feature of the semiconductor and not an atomic behavior, even if the lateral resolution in the normal image mode achieved atomic resolution.

Surface-sensitive (S)XPS studies of these cleaved surfaces, which are a proof for their cleanness, are presented elsewhere.[23,32]

After the characterization of the clean InP(110) surface, a systematic, consecutive dose-dependent treatment with dodecanethiol molecules has been applied to the semiconductor surface.

First, a dose of 1 langmuir dodecanethiol has been applied. The result of this treatment was the complete loss of resolution in the STM graphs. The reason for this behavior is probably that dodecanethiol molecules are bound via the sulfur atoms to the indium atoms.[22,23] The alkyl chains, on the other hand, only adhere loosely to the surface. Because of the sparse density of the molecules at 1 langmuir (sticking coefficient < 1), sufficient space remains between the molecules. When the STM tip scans across such a molecule, the alkyl chain is moved by the tip. Therefore, a clear STM picture could not be obtained.

Nevertheless, the adsorbed molecules can be traced with the help of XP spectroscopy. The spectra show the expected C1s/S2p intensity ratio of 12:1 (corrected with the respective sensitivity factors and the spectrometer transmission function) for dodecanethiol, while the total signal strength (e.g., C1s) of the adsorbed molecules is far below the well-known intensity expected for a typical monolayer (see Figures 7 and 8, and compare with molecules adsorbed from solutions[21]). The measured relative and absolute intensities are a proof for nonoverlapping molecules with a sparse density at the surface.

This behavior changes if a larger dose of dodecanethiol is applied. At 100 langmuir, it is possible to get a good resolved graph again. The situation is displayed in Figure 4. It shows a dense monolayer of "lying" dodecanethiol molecules. Note that the chains are not randomly distributed but mostly pointing into a crystallographic main axis (to prevent disturbances by the scanning tip and therefore misinterpretations, the main axis of the InP crystal was not chosen parallel to the picture boundaries but turned 15° counterclockwise). Figure 4a (enlarged part of Figure 4) shows the structure of the alkyl chains (all-trans conformation) which can also be resolved in some regions.

While most of the chains are pointing into the [001] direction of the substrate, upon closer inspection it can be seen that some chains point partially into other directions (see Figure 4b). This can easily be explained by the following fact: Because of the σ-bondings between the carbon atoms in the alkyl chains, turning of molecular parts around this bonding axis is permitted. While the all-trans conformation is the energetically lowest form, other conformations will occur at room temperature whose total energies are only slightly higher. Once lying on the surface at high densities, these conformations are also stabilized by the neighboring molecules within the dense package. To confirm the above thesis, it is necessary to investigate all possible geometrical variations which might occur on the surface. Assuming that the orientation of all the In−S bondings between substrate and the thiol molecules points into the [001] direction of the substrate due to the InP(110) surface (we will come to this later), the number of alternate conformations projected onto the surface is limited (at least if the permitted values of the C−C angles are low in number, because of the state of adsorption at the surface). This means that besides the pure all-trans conformation which is shown in Figure 4a, it should be possible to find a limited number of molecules in slightly differing conformations (e.g., only one turn around one bonding axis leading to a change in one angle in the carbon backbone in contrast to an all-trans conformation) and therefore differing orientation of their main axis after the deviating bond. This case is shown in Figure 4b.

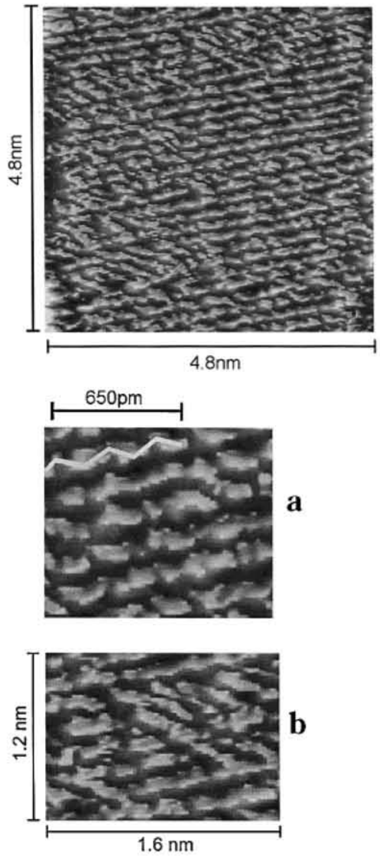

Figure 4. STM picture at 100 langmuir dodecanethiol (U_T = 2.4 V; I_T = 500 pA). (a) STM picture at 100 langmuir dodecanethiol (enlarged). The all-trans conformation of a single molecule has been graphically emphasized. (b) STM picture at 100 langmuir dodecanethiol (enlarged). The picture shows a region where some chains are misaligned.

Further geometric analysis of the STM graphs reveals that the measured bonding angles between the carbon atoms in all-trans conformation molecules are larger than 110° (about 130°−140°). First, this is a result of the slightly changed conformation of the molecules, while being physisorbed (lying) at the surface. The necessary structure to reach a minimum of total energy for a physisorbed alkyl chain (carbon in sp^3 hybridization) does not have a perfect planar carbon backbone parallel to the semiconductor surface. Second, the STM imaging mode projects this three-dimensional molecule into the two-dimensional space, resulting in pictures of molecules which seem to deviate from the octahedrally bonded situation.

A further proof that the STM graph displays lying molecules is given by angular resolved XPS measurements. Here, the ratio between the C1s and the S2p peak intensity does not change while varying the takeoff angle. Besides, the pure C1s and S2p peak intensities at a normal takeoff angle do not allow for models other than lying molecules, especially if models of higher thickness than a lying monolayer can be excluded due to the substrate (e.g., P2p or In4d) to adsorbate intensity ratio, for example, C1s (see Figures 7 and 8, step 3). If the sulfur atoms would

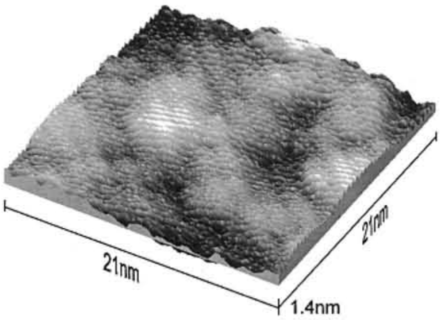

Figure 5. STM picture at 1000 langmuir dodecanethiol ($U_T = 3.8$ V; $I_T = 250$ pA).

be covered significantly by the alkyl chains, the (corrected) intensity ratio (C1s/S2p) would have to be higher than the measured ratio (≈12.2) which still displays approximately the stoichometric ratio.

Increasing the dodecanethiol dose to 1000 langmuir leads to conditions shown in Figure 5. Inspection of this STM picture reveals two different kinds of regions: the higher ones (brighter grayscales), which we interpret to consist of "standing" molecules, and the lower ones (darker grayscales), which are still formed by lying molecules as could be seen at lower doses. Note that the STM graph still shows molecular resolution simultaneously in both kinds of regions at room temperature.

To ensure that both the standing and the lying regions do indeed consist of alkyl chains, both regions have been investigated via STS. The spectra are shown in comparison with a SXPS spectrum (excited at 55 eV with synchrotron radiation), recorded from surface-bonded alkyl chains, prepared from dilute solutions of dodecanethiol (Figure 6).[21–23,33] Despite the differences in excitation, the energetic positions of the peaks are identical. Both regions can therefore be attributed to be covered with dodecanethiols. The following list of arguments can be found to support the interpretation: From the STS–SXPS comparison, one can conclude that the whole surface is covered by dodecanethiol. The average height offset of the bright and dark regions of approximately 1.0–1.4 nm (taken from STM measurements) fits into the model of lying minus standing regions, taking the length of one dodecanethiol molecule (1.84 nm) and the expected angle from the surface normal of 34° [22,23] into account. In the following, we will present additional information, derived from detailed XPS studies of the substrate (In3d, P2p) and the adsorbate (C1s, S2p), respectively.

To get additional, reliable information on the surface coverage, we performed highly resolved XPS measurements for all peaks of interest at all stages of adsorption. As an example, we provide the detailed XP spectra for step 3 (1 kLangmuir dose) in Figure 7. The intensity information was extracted from these spectra, by calculating the true peak area from an elaborate fitting procedure which uses an iterative background subtraction combined with convoluted Voigt profiles in a multipeak algorithm. The corresponding residuals are also given in each graph. The extracted intensities for all stages of adsorption are given in Figure 8. Please note that the data are normalized individually. That is, for example, the ratio between carbon and sulfur is always greater than 12. In Figure 8, the highest point (at step 4) of this ratio is normalized to 1 in order to display all graphs in the same diagram. This allows a detailed comparison between the individual intensities. A measure of the reliability of this method is given by the substrate intensities (In3d, P2p). In principle, both intensities should be identical in pairs at all points. In comparison to the magnitude of changes of the adsorbate intensities, this is true. Now, we focus on the carbon/sulfur ratio. In a first-order approximation, the intensity of both elements should rise, while more molecules are being adsorbed on the surface. The difference between both intensities in the course of adsorption is due the fact that the carbon alkyl chains are covering the binding sulfur atoms in a standing film and therefore weaken the XPS intensity of the sulfur signal. This means that the higher the C/S ratio, the more standing the ordered monolayer. Coming back to the adsorption step at 1 kLangmuir, this means that this film already shows a high degree of standing molecules, but compared to the last step (doses ≥ 10 kLangmuir) one can find that the degree of order is not at its maximum. This is exactly how we interpreted the STM graph before. The film is partially well-ordered (standing) but has also some regions which have a lower density of adsorbed molecules (lying).

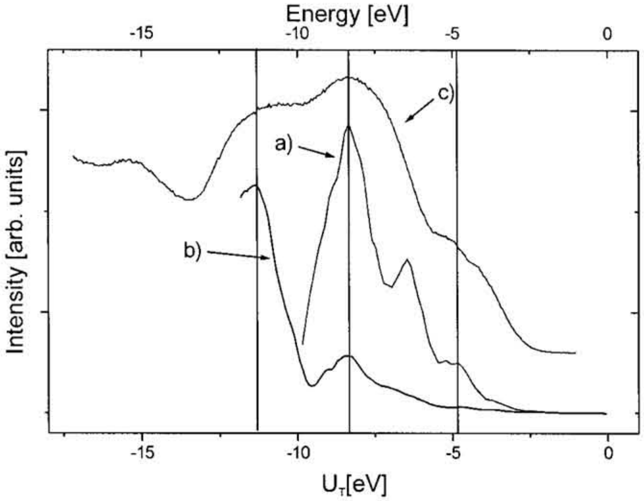

Figure 6. Locally resolved ST spectra of a DDT-covered region in comparison with a SXPS spectrum of a similar sample.

Well-ordered self-assembling monolayers, which can be compared to systems prepared from dilute solutions, are also found. The required minimum dose for a quasi faultless monolayer is between 5000 and 10 000 langmuir dodecanethiol. An example for such a system is shown in Figure 9. The SAM is prepared at 10 000 langmuir dodecanethiol on a freshly UHV-cleaved InP(110) surface. The array of standing molecules appears faultless, although at closer inspection a small deviation in brightness (≙ height) is detectable. This effect might arise from some residual stress in the SAM, which itself comes from the exceptional three-dimensional tight packing of the alkanethiol molecules in the well-ordered "van der Waals stabilized" layer.[22,23] Note that neither the grayscale nor the *z*-axis scale of Figure 9 is equivalent to that of Figure 5, but both have been adjusted for more sensitivity in height displaying. Figure 10 shows an enlarged section of the former STM graph. Even on this scale, the monolayer appears well-ordered. A small distortion of the graph can be found by comparing the resolution in the *X*- and *Y*-directions. This distortion could be caused by two reasons. First, the shape of the STM tip could be slightly asymmetric. Second, the tilted structure of the self-assembled monolayer in combination with the impact of the tip into the layer (Figure 11) could cause such an effect. Because of some further tests with this tip and the knowledge of the inner structure of the monolayer,[22,23] we

---

(33) Bierbaum, K.; Kinzler, M.; Wöll, Ch.; Grunze, M.; Hähner, G.; Heid, S.; Effenberger, F. *Langmuir* **1995**, *11*, 512–518.

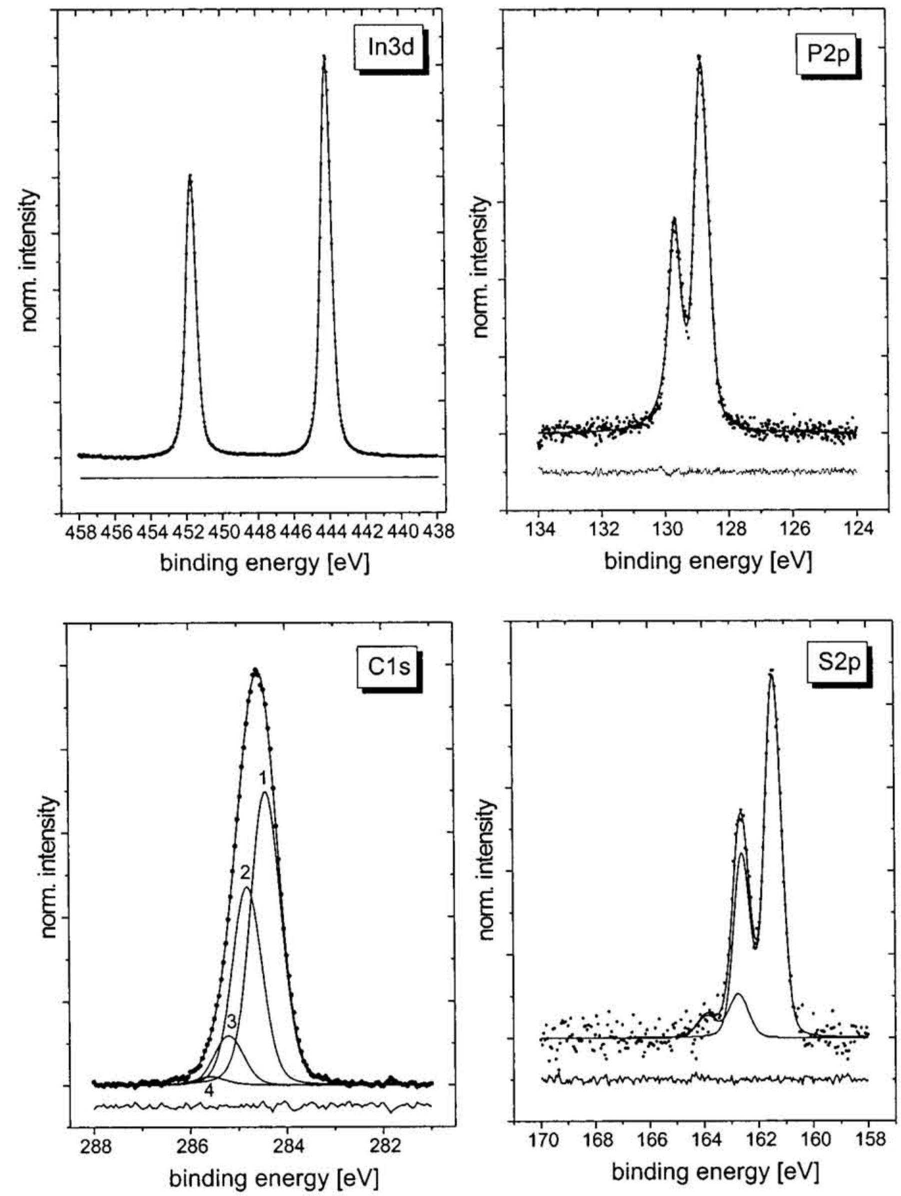

Figure 7. XPS spectra of DT on InP(110) at 1 kLangmuir: (a) In3d, (b) P2p, (c) C1s, and (d) S2p.

tend to interpret the distortion to be due to the "tilted" structure of the adsorbate and not caused by imperfections in the shape of the tip.

The STM analysis of the adsorbate system is completed by a determination of the molecular spacings. For this purpose, not only an exemplary determination on a "good fitting location" in real space has been made, but a complete two-dimensional fast Fourier transformation (FFT) (Figure 12) was done. The transformation allows us to judge the distances of all investigated molecules simultaneously and to detect superlattices and repeating distortions in one picture. Repeating structures in time (and therefore, due to the scanning, in space) are displayed as bright "spots" (accumulation points). The most prominent spots belong to the rectangular reciprocal surface unit cell of the underlying InP lattice and are highlighted via white lines for better visibility.

As far as we can judge from numerous STM graphs, the adsorbed monolayer appears faultless and well-ordered. But how can we be sure that the system under investigation is a unique, distortion-free monolayer system on larger scales? From STM measurements alone, it is practically impossible to get a positive proof of the single-domain structure. If the area under (STM) investigation is successively made larger, there will be a certain point where the necessary molecular resolution will be lost. This is especially true if superlattices and therefore domain boundaries are missing, which has to be expected for single-domain structures. To prove the single-domain structure, investigations on a macroscopic scale are necessary. For this, two different spectroscopic approaches have been chosen which are able to analyze structural aspects on macroscopic scales.

The first approach has been made by using XANES to determine the structure of the adsorbed SAMs on InP-(110) surfaces. These measurements are already published by the authors,[22,23] but because of their importance for the discussion, the results shall be summarized briefly. The sensitivity of XANES to determine the spatial orientation of the bonding axis (especially the C−C and C−H bonds at the C K edge) has been used to construct a model of the complete alkanethiol monolayer in respect to the underlying InP(110) lattice. The angular dependent (in azimuth and vectorial angle) datasets have been measured, while averaging an area (spot size) of several mm^2, hence representing a truly macroscopic feature.

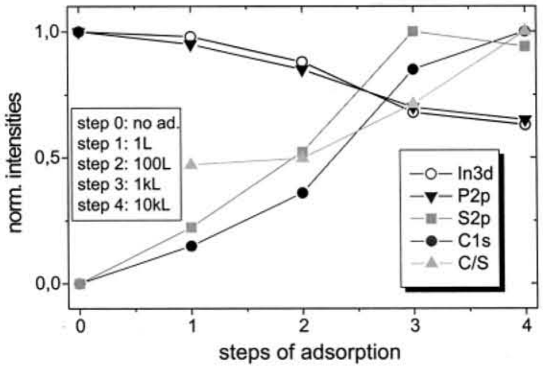

Figure 8. Comparison of the XPS intensities of adsorbate and substrate peaks and the carbon to sulfur ratio, derived from background-corrected peak areas at the different adsorption steps. Please note that all measurements have been normalized individually.

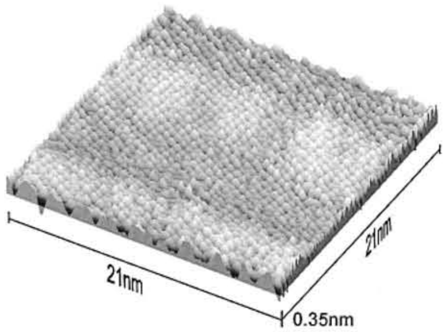

Figure 9. STM picture at 10 kLangmuir dodecanethiol (U_T = 3.8 V; I_T = 250 pA).

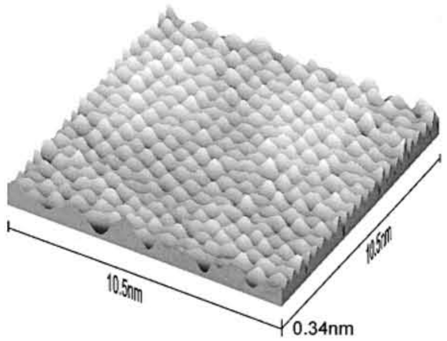

Figure 10. STM picture at 10 kLangmuir dodecanethiol (enlarged).

Although the integration of spectral features over large regions has been made, the data reveal sharp angular dependent changes. Especially, these changes are not symmetric in respect to different surface directions, which has to be expected for a oriented, single-domain system. More precisely, the following conlusions have been drawn from the XANES measurements: The angle between the surface normal and the tilted alkyl chains is 34° on InP(110) and 15° on GaP(110).[22,23] The projection of this angle onto the surface lies along the [001] axis of the substrate which has been confirmed by varying the azimuth angle parallel to the surface from 0° to 360° in 24 steps.[12,13] Within the (001) plane, the chains are only tilted to one side of the surface normal which is confirmed by varying the vectorial angle from −70° to +70° from the normal in more than 30 steps.[22,23]

From SXPS measurents which have been tuned for maximum surface sensitivity, it additionally has been proved that the chemical binding of SAM and substrate takes place between the thiol sulfur and the indium, while the hydrogen atoms which are deprotonated in the binding process are connected to the phosphorus atoms.[32]

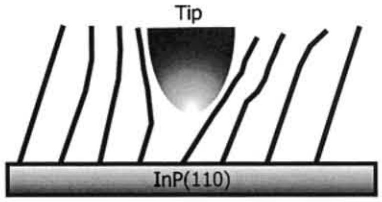

Figure 11. Model of the dodecanethiol−InP(110) system while measured by STM.

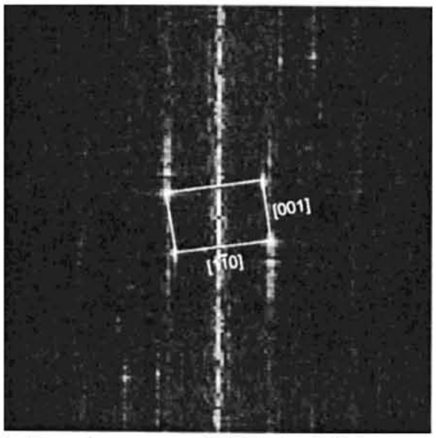

Figure 12. Two-dimensional FFT of a STM measurement of a completely DDT-covered InP(110) surface.

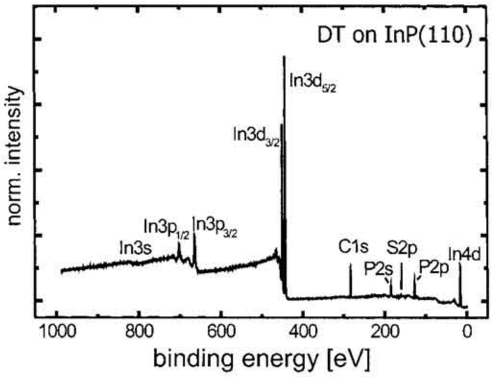

Figure 13. Survey spectrum of DT on InP(110) at doses ≥ 10 kLangmuir.

The set of XPS intensities in Figure 8 also supports the thesis of a well-ordered system. The C/S ratio is at its maximum, while the corresponding substrate intensities are at their minimum.

To investigate the cleanness of the self-assembled system, we present an XPS survey spectrum (see Figure 13). Only peaks which are related to the substrate (In, P) or the adsorbate (C, S) are present. No oxygen or other contaminants are detectable which is proof of a good surface preparation.

We are now ready to sketch a complete model of the adsorbate−substrate system. However, to eliminate all possible objections against our conclusions we will further prove the exceptional order of the SAMs by using XPD on exactly the same UHV-adsorbed dodecanethiol film (10 kLangmuir) we formerly investigated by STM. For that, we made two sets of angular dependent measurements at room temperature on spot sizes of several mm^2. The first one, with angular variations within the (001) plane, shows no significant deviations in intensity. But the second set (consisting of two independent series) which is made in the (1$\bar{1}$0) plane shows a clear peak at 34° but not at −34°

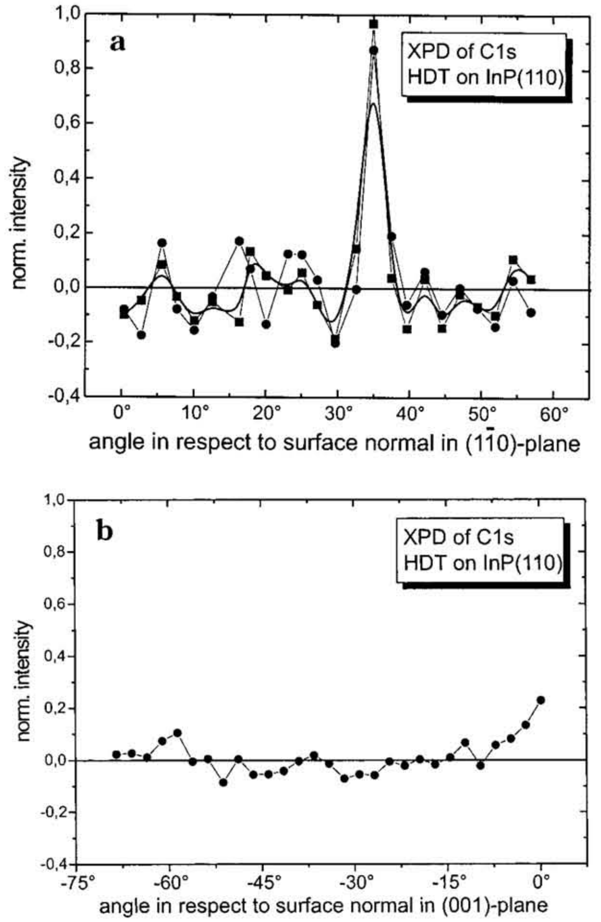

Figure 14. XPD experiment at the energy of the C1s peak (a) along the (1$\bar{1}$0) plane and (b) along the (00$\bar{1}$) plane of the InP lattice.

from normal (see Figure 14). This peak comes from the so-called "channeling" of the photoelectrons along the alkyl chains and therefore describes the orientation of the chains. Please note two important additional pieces of information which can be derived from these measurements: first, the peak is not symmetric in respect to the surface normal, and second, the peak is absent in the perpendicular plane. This again allows only one conclusion: the adsorbed monolayer is a single-domain system. Furthermore, from our analysis one may conclude that fully assembled monolayers, prepared from solutions, and UHV-adsorbed monolayers at high doses (> 10 kLangmuir) do form the same kind of structure on InP(110) surfaces. To complete the model of the spatial geometry of the adsorbate–substrate system, we are in need of the exact orientation of the substrate lattice in respect to the adsorbate. Having the exact orientation in space of the alkyl chains, the only missing parameter is the orientation of the substrate. From the previously shown XPD measurements on preoriented InP single crystals, it is clear that the alkyl chains lie in the (1$\bar{1}$0) plane. The symmetry properties of the semiconductor lattice allow the further determination of "tilt direction" in respect to sequence and spacings of the non-axial-symmetric substrate lattice in the denoted plane. Hence, a second set of XPD measurements has been made along the (1$\bar{1}$0) plane. To investigate the orientation of the substrate and not the adsorbate, the P2p peak instead of the C1s peak was chosen. The result of this experiment is depicted in Figure 15. Because of the unequivocal result, an interpretation using simple first-order scattering is sufficient. The matching of the first-order scattering model and the XPD peaks is illustrated in Figure 16. Taking all ascertained data from the measurements, we can now complete the structure of the single-domain adsorbate–substrate system. The resulting model is shown in Figure 17.

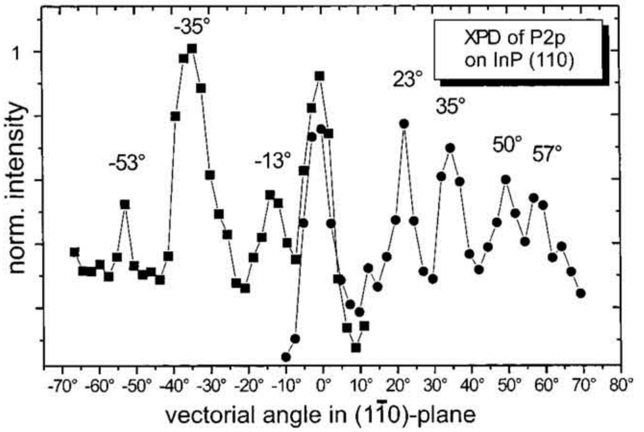

Figure 15. XPD experiment at the energy of the P2p peak along the (1$\bar{1}$0) plane of the InP lattice.

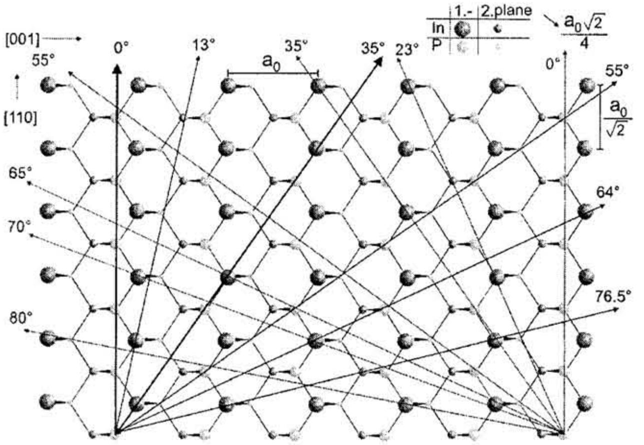

Figure 16. Illustration of the first-order scattering within the (1$\bar{1}$0) plane.

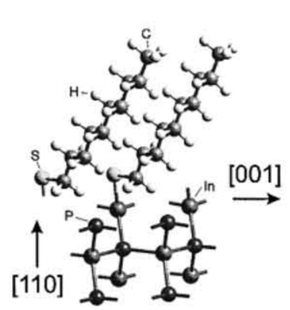

Figure 17. Model of the adsorbate–substrate system.

4. Discussion

The STM/STS results lead to further insights into the behavior of self-assembling monolayers on III-V(110) surfaces. From the preceding spectroscopic investigations,[21–23] which were carried out with alkanethiols adsorbed from solutions, it was clear that the organic films build up a very highly ordered and dense layer on large scales. The data derived from these spectroscopic measurements include the molecular tilt angle of 34° (InP(110)) and 15° (GaP(110)) from the surface normal into the [001] direction of the substrate.

An explanation for this behavior can be given solely by geometrical considerations. The rectangular surface unit cell of this zinc blende type substrate is characterized by In−In (P−P) spacings along the [001] and [1$\bar{1}$0] surface directions of 587 and 415 pm, respectively. The surface indium and phosphorus atoms (In−P bond length of 254 pm) are linked to form In−P zigzag chains within the InP(110) surface plane, which extend along the [1$\bar{1}$0] direction. Thus, following structural arguments regarding the space requirements of the alkyl chains and their well-known tendency to form dense structures, a tilt of the alkyl chains toward [001] is indeed much more likely than toward [1$\bar{1}$0]. These simple arguments agree very well with our above-mentioned observations regarding the tilt direction. Furthermore, a dependence of the tilt angle on the lateral distance of the sulfur−substrate bonding sites on the surface and thus on the substrate lattice constant had to be expected. In fact, we observed such a trend by investigating thiol adsorption on different semiconductor surfaces.[21−23] Besides this purely geometrical consideration, we have to be aware of the structural inequivalence of the two opposite [001] surface directions due to asymmetry of the In−P zigzag chains, which exhibit an indium and a phosphorus side. This structural asymmetry is also known to be responsible for the opposite spatial orientations of the empty and filled dangling bond orbitals of the surface indium and phosphorus atoms, respectively. Hence, it is reasonable to suggest that the experimentally observed preference of just one orientation of the alkyl chain has to be attributed to the orientation of these dangling bonds, that is, to the empty indium dangling bonds, which was proved by SXPS measurements.[23] Thus, structure and bonding constraints evidently force the adsorbed monolayer to adopt a uniquely well-defined structure, which lets us propose the existence of single domains of the monolayer on InP(110), only limited by high cleavage steps or other large defects of the cleaved substrate surface.

One drawback of the preceding pure spectroscopic investigations[21−23] is that they are bound to more integral features of the molecular behavior. From the sharp contrast in angular dependent spectroscopy, it is evident that the whole layer under investigation is highly ordered and oriented into a specific direction, but not that all single molecules follow such a preorientation. This is only possible by using a microscopic technique (e.g., STM).

A second drawback of the previous measurements from solutions[14,21−23] is the inherent difficulty of studying a self-assembling process with UHV-dependent techniques. In fact, that was possible (e.g., by interrupting the process) but had a lack of reproducibility. Here, these problems were bypassed via UHV-depositing of the alkanethiols. Additionally, it was possible to shed more light onto the role of solvent molecules in the mechanism of self-assembly and the necessary doses.

From the measurements with low doses, it is obvious that the preorientation of the alkyl chains, pointing toward the crystallographic [001] axis of the substrate, is induced by the empty (In) dangling bonds on the surface, while the tilt angle itself is a result of the dense package and the three-dimensional space requirements of the alkyl chains at higher doses.

Furthermore, all investigated regions at doses higher than 10 kLangmuir are free from defects. Considering all of the previous spectroscopic investigations, it is justified to use the term "single domain" to describe the alkanethiol monolayers.

The different stages of adsorption also give an explanation for the comparably high doses needed to get a densely packed layer despite the high reactivity and therefore high sticking coefficient of the surface. The reason for the requirement of higher doses is that the lying molecules on the semiconductor surface hinder the contact between new incoming molecules and the substrate surface itself. This is also the main reason for the differences in adsorption kinetics in comparison to adsorptions from solutions. There, the alkanethiols are expected to be kept afloat by the surrounding solvent molecules and that is why they do not block the surface at low coverages.

Summarizing the recent results for UHV deposition, four main phases of adsorption on InP(110) were found:

First, at doses of <10 langmuir the surface is only sparsely covered, still permitting the alkyl chains to move "sideways" on the surface; therefore, no stable STM image was presented. Second, approximately at 10 langmuir, a dense layer consisting of lying molecules is formed. The contact between the alkyl chains is stabilizing enough to give good resolution even at room temperature. Third, at doses of 1 kLangmuir, parts of the monolayer start to stand up. This is done neither statistically nor individually but in well-defined domains, while other regions are still flat on the surface. A comparison between the height of the standing and the lying molecules in the same graph permits us to deduce these differences precisely. From that, we can learn how deeply the tip penetrates the organic layer. From other papers, concerned with the behavior of tip−surface interactions on organic films, it is well-known that the tip might intrude into the organic layer while scanning.[34−36] This behavior is also to be expected for the STM parameters used here in connection with the insulating properties of the adsorbate system under investigation (see Experimental Section). Further proof is given by the height information of the different regions in Figure 5. The average height difference of the standing and the lying regimes is about 0.8 nm. (Please note that the given *z*-axis in the graph denotes the maximum distance between the highest and the lowest point, and therefore the average distance between neighboring regions is significantly lower.) If the tip would not intrude into the layer, this distance would be about 1.5 nm (the height of a 34° tilted dodecanethiol monolayer) minus the height of a lying molecule, which should be near 0.2 nm. The result of 1.3 nm is significantly higher than the measured value of 0.8 nm; therefore, the tip has to intrude about 0.5 nm into the layer as is depicted in Figure 11.

In the last stage (dose > 10 kLangmuir), a macroscopic single-domain monolayer covers the semiconductor, which is virtually free from defects. All molecules have the well-defined tilt angle onto the [001] direction of the InP(110) surface. The chain−chain distances and therefore the tilt angle reflect the lattice properties of the underlying semiconductor, which was additionally proved by a FFT analysis of the STM picture and locally resolved tunneling spectra.

Acknowledgment. The work was supported by the Deutsche Forschungsgemeinschaft (Innovationskolleg 24/A1-2313-704-P and Graduiertenkolleg Physical Chemistry of Interfaces) and by the BMBF (05SE8OLA). Many thanks to Diana Vilchez and Philipp Lilie for correcting the manuscript.

LA0108205

---

[34] Behm, J. M.; Lykke, K. R.; Pellin, M. J.; Hemminger, J. C. *Langmuir* **1996**, *12* (8), 2121−2124.

[35] Dagata, J. A.; Tseng, W.; Bennett, J.; Schneir, J.; Harary, H. H. *J. Appl. Phys.* **1991**, *70* (7), 3661−3665.

[36] Ross, C. B.; Sun, L.; Crooks, R. M. *Langmuir* **1993**, *9* (3), 632−636.

SXPS and XANES Studies of Interface Reactions of Organic Molecules on Sulfide Semiconductors

Dirk Mayer, Karl Heinz Hallmeier, Dominic Zerulla, and Rüdiger Szargan

Universität Leipzig, Wilhelm-Ostwald-Institut für Physikalische und Theoretische
Chemie, Linnéstr. 2, 04103 Leipzig, Germany
`szargan,khall@rz.uni-leipzig.de`

Abstract. The interaction of the organic heterocycle 2-mercaptobenzothiazole (MBT) with CdS(10$\bar{1}$0) surfaces was investigated using SXPS and NK XANES spectra excited with synchrotron radiation. The molecules were found to be chemisorbed after deprotonation at the nitrogen atom. Angular dependent NK XANES measurements of the adsorbate complex indicated an upright and tilted orientation of the MBT molecular planes of the adsorbed MBT molecules in the [$\bar{1}2\bar{1}0$] direction of the crystal. In consequence of an interface reaction step an overlayer of the disulfide bis-(2-benzothiazolyl)disulfide (BBTD) was detected. This second reaction step was found to be induced by photoelectrical generation of electron–hole pairs in the semiconductor. A proposed reaction model includes the transport of the charge carriers to the semiconductor surface and subsequent charge transfer across the interface. The model was verified by adsorption experiments on differently doped semiconductor crystals which resulted in distinct differences in adsorbate composition.

1 Introduction

The controlled chemical and physical manipulation of organic adsorbates on sulfide surfaces in solutions may further develop the separation of natural complex sulfide mixtures by froth flotation and may create new applications in catalysis and sensor and solar techniques.

Much of the previous adsorption work deals with the bonding of thiolates and related compounds forming more or less self-assembled monolayers [1,2,3,4,5,6,7,8,9,10,11]. The adsorption of heterocyclic thiolate compounds introducing π-systems and specific functional groups into the molecular assembly of the adsorbate modifying also the redox behaviour of the system was investigated only recently [12,13,14]. With increasing progress in direct characterization of the solid/electrolyte interface by scanning microscopies (STM, AFM, SECM), by FTIR and electroanalytical in situ techniques, also interest in ex situ investigation of the chemical states of particular atoms as well as their in-depth distribution above and below the interface by means of electron [15,16,17] and X-ray absorption spectroscopies [18,19] is rising.

K. Wandelt, S. Thurgate (Eds.): Solid–Liquid Interfaces, Topics Appl. Phys. **85**, 97–112 (2003)

This chapter presents new results on the adsorption of 2-mercaptobenzothiazole (MBT=Hmbt) on CdS$(10\bar{1}0)$. The investigation focuses on chemical binding, molecular orientation and oxidation of the adsorbate applying standard models of photoelectron attenuation and chemical shift of the core electron spectra (XPS) as well as the angle dependence of the X-ray absorption near edge structures (XANES). Highly resolving and surface sensitive techniques using monochromatized synchrotron radiation and sophisticated fitting procedures for decomposing the complex S $2p$ photoelectron spectra were used to separate the different spectral components of the adsorbate and the substrate. The influence of temperature and light intensity on the interface reaction rates is pointed out in order to elucidate the possibility for controlling and engineering surface properties by means of thermal and photoelectric effects.

2 Experimental

Photoelectron spectra were excited with tunable synchrotron radiation from BESSY (Berlin), the monochromator PM-5 and the HIRES photoelectron spectrometer. The XP-spectra were fitted with the peak-fitting program "Unifit for Windows" [20] using Gaussian–Lorentzian peak shape deconvolution. XANES spectra were derived from partial or total electron yield recorded with the HE-TGM 2 monochromator applying different retarding potentials in order to enhance the surface sensitivity of the measurements.

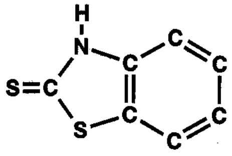

MBT=Hmbt

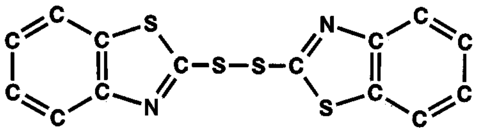

BBTD

Adsorption experiments were carried out using commercial lowly (10^8 Ωcm) and highly (1–10 Ωcm) doped CdS$(10\bar{1})$ wafers (Crystal GmbH, Berlin Germany). 2-mercaptobenzothiazole (MBT) and the oxidation product disulfide bis-(2-benzothiazolyl)disulfide (BBTD) were purchased from Aldrich Chemicals (Steinheim, Germany) in 98 % purity. The interface reactions were performed at clean and preoxidized crystal surfaces in aqueous 10^{-5} M and 10^{-4} M MBT solutions under nitrogen flux for different durations of reaction and temperatures. Because of the low solubility of the MBT in water addition of 5 % v/v methanol was necessary. After adsorption the sample was rinsed by a methanol/water (5 % v/v) solution and dried in a nitrogen flow. The CdS surfaces were oxidized by ozone produced in air by illuminating with UV light of a low-pressure mercury lamp. Elemental sulfur was deposited by etching the crystals in a 5 ‰ v/v Br_2/methanol solution.

3 Results and Discussion

The molecule of the chelating agent 2-mercaptobenzothiazole contains three reactive centers and exhibits a special affinity to metal atoms of different chalcogenide crystals [14,19].

3.1 Chemical Composition of the Adsorbate

The S 2*p* photoelectron spectra of the adsorbate system are composed by four components (Fig. 1) resulting from the substrate sulfur S^1 and two sulfur atoms S^2 and S^3 of the MBT.

The component S^2 with a binding energy of 162.9 eV can be attributed to the exocyclic sulfur atom of the chemisorbed mbt^- anion. The S 2*p* energy

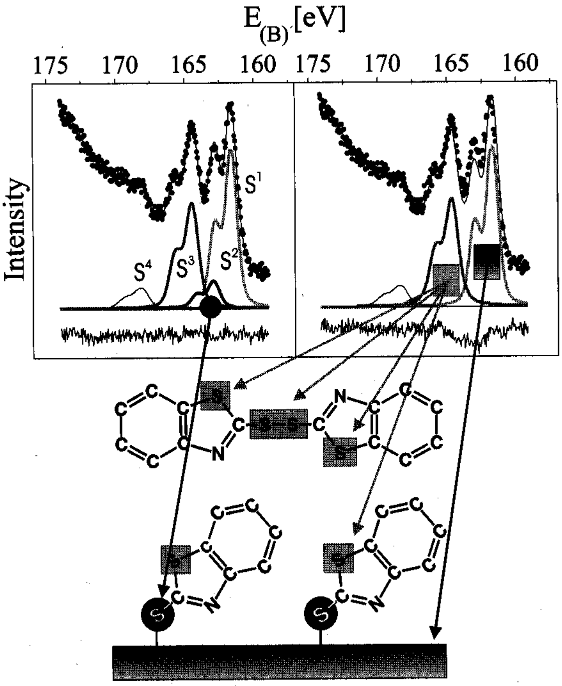

Fig. 1. S 2*p* photoelectron spectra of CdS(10$\bar{1}$0) after 10 min reaction time in 10^{-5}M MBT solution

of this atom is 0.8 eV shifted to higher energies with respect to the exocyclic sulfur of the pure MBT reflecting electronic charge donation from the sulfur to the cadmium atom at the semiconductor surface. The endocyclic sulfur atom of the MBT molecule should contribute to the S 2*p* signal S^3 in accord to the 1:1 atomic ratio. This component S^3, however, is much more intensive pointing at additional sulfur species containing (–S–) or (–S–S–) groups.

Therefore we conclude that bis-(2-benzothiazolyl)disulfide was formed by oxidation/dimerization. The four sulfur atoms from two (–S–) and one (–S–S–) groups (see above) giving only slightly shifted S 2*p* signals should contribute to the same spectral component S^3. Comparing the S 2*p* binding energies with results of the MBT adsorption on PbS (galena) and FeS_2 (pyrite) shows nearly the same energies for the S^3 components and distinct differences for S^2 [14,19]. Otherwise the distances between the binding energies of S^1 and S^2 differ just weakly by less than 0.3 eV for all three adsorbate systems. One may conclude the atomic potential at the exocyclic sulfur to be determined by the bonding interaction with the substrate:

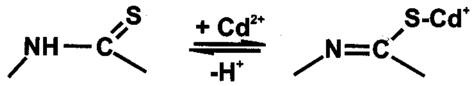

(MBT=Hmbt) (Cd-mbt)

In contrast, the comparable energies for the S^3 components of the adsorbate system and the pure MBT indicate the absence of any interaction between the endocyclic sulfur and the substrates. The doublet S^4 at 168 eV is due to a very small fraction of SO_4^{2-} remained after ex situ preparation of the CdS wafer with UV/ozone and rinsing the soluble sulfate by water.

The chemisorption of the MBT molecule at the surface via the thiolate group is accompanied by a deprotonation of the nitrogen atom as indicated above. This deprotonation should strongly influence the N 1*s* and NK XANES features. Thus the N 1*s* spectra (Fig. 2) exhibit a low-energy signal at about 399 eV created by the sp^2 hybridized nitrogen atom (–N=) arising from the formation of a π bond between the nitrogen and the adjacent carbon atom as a consequence of the deprotonation. This π bond is indicated also by the NK XANES features which exhibit characteristic sp^2 preabsorption structures (see below).

The intensity of the (–N=) component rises with increasing MBT concentration due to increasing amount of reaction products. The additional component (–$\underline{\text{N}}$H–) at 400.6 eV may originate from ubiquitous impurities in the atmosphere as a result of the ex situ preparation.

The NK XANES of the adsorbate resulting from the interaction between a 10^{-4} M MBT solution and a CdS wafer is similar to the spectrum of the $Cd(mbt)_2$ complex (Fig. 3) and clearly shifted with respect to the reference MBT because of the deprotonation.

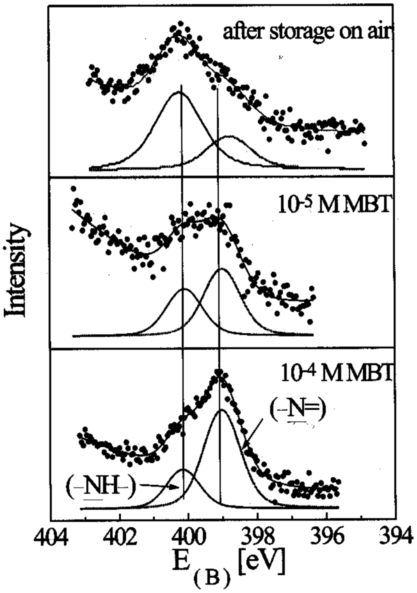

Fig. 2. N 1s spectra of CdS(10$\bar{1}$0) after 10 min reaction time in 10^{-4}M and 10^{-5}M MBT solution

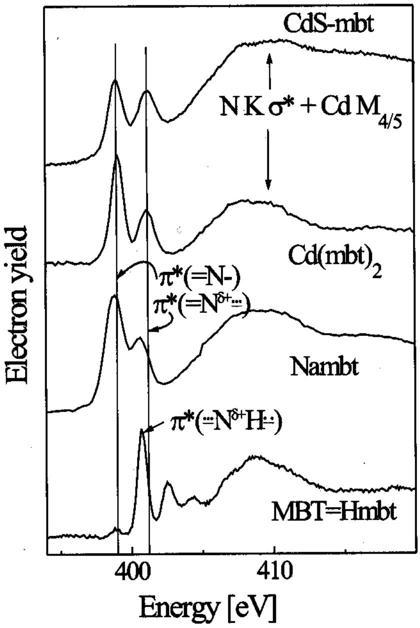

Fig. 3. NK XANES of Hmbt, Nambt and Cd(mbt)$_2$ in comparison with the spectrum of CdS(10$\bar{1}$0) after 10 min reaction time in 10^{-4} MBT solution

Two π resonances appear arising from $1\,\mathrm{s}^{-1}2p\pi^*$ excitations at (–N=C–S) groups of the thiolate mbt$^-$. These characteristic resonances occur in molecules with (–N=C–) groups in the bridging position with conjugated π electrons and can be understood as transitions of N $1s$ electrons into two different antibonding $2p\pi^*$ states [18,19]. The splitting of the π resonances arises from conjugation effects as confirmed by Hartree–Fock calculations of unoccupied states in benzalaniline using the $Z+1$ approximation for the excited atom [21]. A high energy σ resonance above 408 eV can be attributed to a $1\,\mathrm{s}^{-1}\sigma^*(2p)$ excited state located at the nitrogen atom.

3.2 Orientation of the Adsorbed Molecules

The orientation of the molecules on the surface is determined by bonding interactions between the molecule and the surface, by intermolecular interactions and by the dimensions of the molecules. By rotating the adsorbed mbt$^-$ anion around the Cd–S and S–C bonds and varying simultanously the Cd–S–C angle nearly every molecular orientation can be obtained (Fig. 4, left).

One MBT molecule oriented in the $[\bar{1}2\bar{1}0]$ direction completely occupies two Cd sites. In the [0001] direction one molecule completely occupies one Cd atom and partially a second one. By rotating the molecule out of this orientation the second Cd atom becomes accessible for the adsorption of an additional molecule (see Fig. 4, right).

Such rotation can be caused by intermolecular interactions between adjacent molecules if the substrate dominated distance a between the molecular planes is larger than their van der Waals radii. The resulting effective molecular distance c is given by $\cos\alpha = c/a_{\mathrm{x}}$.

The orientation of molecules with respect to a particular crystal direction can be determined by angle-dependent K XANES measurements varying the angles between the edge or surface normal of the crystal with respect to the polarization direction $\overline{\boldsymbol{E}}$ of the exciting synchrotron radiation. For this

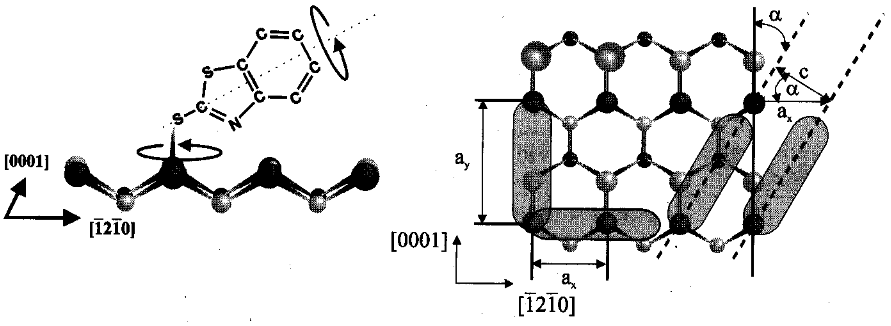

Fig. 4. Models of the Cd-mbt complex on the CdS(10$\bar{1}$0) surface

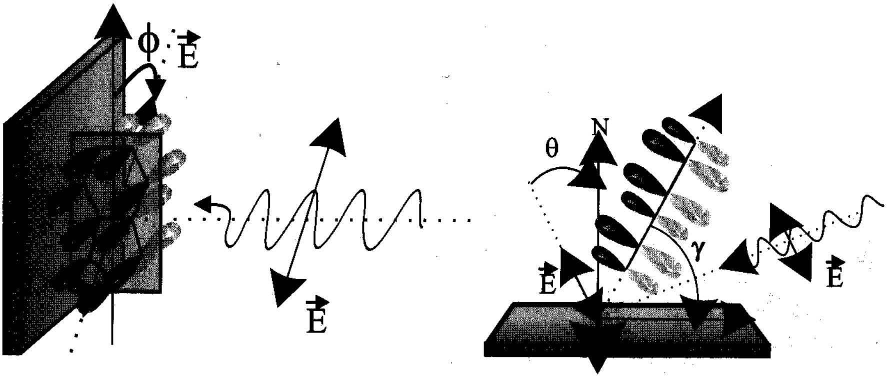

Fig. 5. Azimuthal (*left*) and polar (*right*) orientation of the molecular plane of MBT on the CdS(10$\bar{1}$0) surface with respect of the polarization vector $\vec{E}$ of the exciting radiation

aim the azimuthal angle ϕ between a crystal edge and the direction of $\vec{E}$ is changed by rotating the sample around the surface normal (Fig. 5, left).

The resulting resonance intensities at different azimuthal angles depend on the position of the respective $2p\pi$ molecular orbitals. The maximal transition moment and absorption cross-section is expected to have equal direction to the electric field vector of the exciting radiation $\vec{E}$ and the $p\pi^*$ orbital. Figure 6 shows the azimuthal angle dependence of the NK XANES of the adsorbate sytem CdS-mbt with the angles 90°, and 0° indicating the $\vec{E}$-direction along the [0001] and [$\bar{1}2\bar{1}0$] directions respectively. The normalized intensities of the first $2p\pi^*$ resonances with respect to the σ^* resonance are shown in the polar diagram giving a maximum at 90° and a minimum at 0°.

Since antibonding $2p\pi^*$ states are oriented perpendicularly with respect to the σ frame of the molecular plane, the molecular plane is directed in the [$\bar{1}2\bar{1}0$] direction. Thus every molecule occupies two Cd atoms at the surface. This adsorbate configuration, only slightly deviating from the [$\bar{1}2\bar{1}0$] direction, was predicted by DFT calculations giving a minimum of total energy including bonding interactions between the nitrogen atoms of the mbt$^-$ and Cd surface sites (see Fig. 4, left) [22].

The NK XANES exhibits nearly the same resonance intensities after rotating the sample by about 180° (Fig. 6, middle and lower part) indicating the conservation of the mirror plane of the molecule during the core excitation.

After determination of the azimuthal orientation of the adsorbed molecule also the determination of the tilt angle γ of the molecular plane with respect to the surface is possible. For this aim the polar angle θ between the surface normal N of the crystal and the direction of $\vec{E}$ is changed by tilting the sample relative to the beam direction (Fig. 5, right). Comparing the experimental intensity ratios at the π resonance at normal ($\theta = 90°$) and tilted incidence with theoretical curves gives the tilt angle of the adsorbed molecule [18].

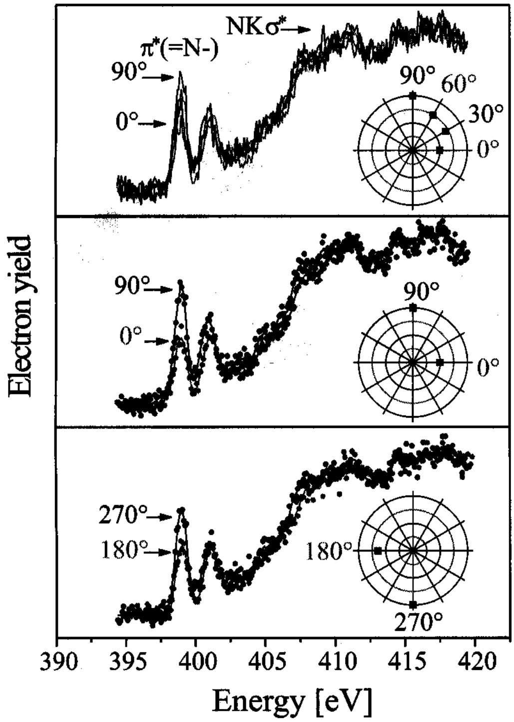

Fig. 6. Variation of the NK XANES of Cd-mbt on CdS(10$\bar{1}$0) with varying azimuthal angle ϕ

Figures 7 and 8 show the experimental polar angle dependence of CK and NK XANES, respectively, of the adsorbate system CdS-mbt. The π resonance in the preabsorption region is stronger at normal X-ray incidence with a field vector $\overline{\boldsymbol{E}}$ giving a large projection in the direction of the π^* orbital of an almost upright standing molecule.

The decreasing intensity in the π^* region with decreasing angle of incidence θ gives an indication for a tilted orientation of the molecular planes of the adsorbed molecules relative to the crystal surface. Analyzing the intensity ratios comparing to that predicted by theory [18] a tilt angle of $\gamma = 63^\circ \pm 5^\circ$ between the molecular plane and the surface was obtained. Such an upright adsorbate constitution in the $[\bar{1}2\bar{1}0]$ direction proves the assumption of a bidentate coordination of MBT with the exocyclic sulfur and the nitrogen of MBT to two adjacent Cd atoms in the CdS surface, as predicted by DFT calculations [22].

3.3 Thermal Activation of the Adsorption

Treating the CdS surface with a 10^{-4} M MBT solution a strong influence of the temperature on the absorption rate was found (Fig. 8). For a more

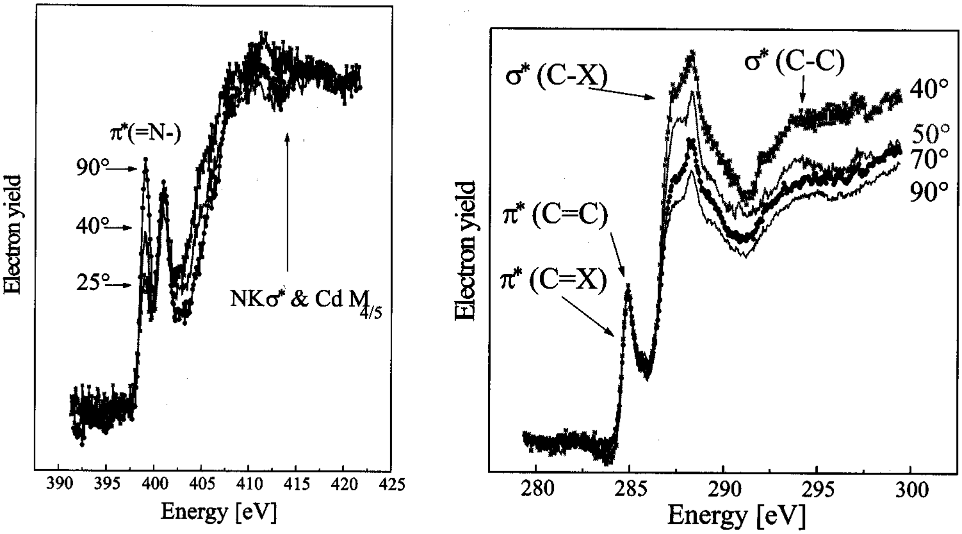

Fig. 7. Variation of NK XANES *(left)* and CK XANES *(right)* of Cd-mbt on CdS(10$\bar{1}$0) with varying polar angle θ

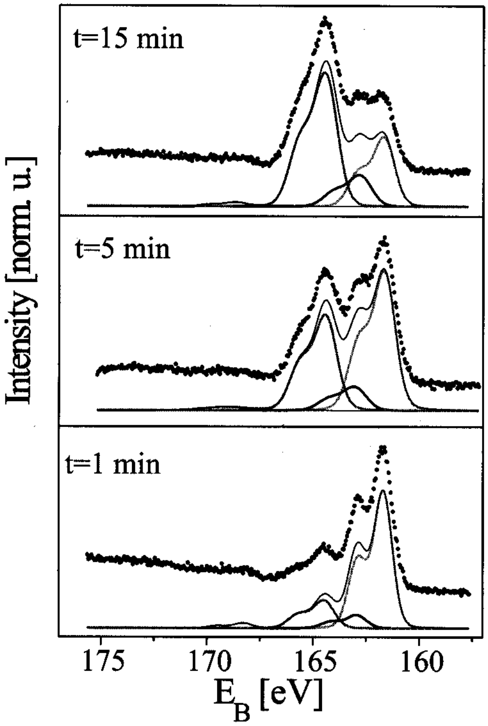

Fig. 8. S 2p spectra of CdS(10$\bar{1}$0) after different reaction times in 10^{-5} M MBT solution at 45 °C

detailed kinetic interpretation of the absorption (k_a) and oxidation (k_b) processes

$$\begin{aligned}\mathrm{Hmbt} + [\mathrm{Cd}^+]_{\mathrm{CdS}} &\xrightarrow{k_a} [\mathrm{Cd-mbt}]_{\mathrm{CdS}} + \mathrm{H}^+ \\ &\xrightarrow{k_b} (1/2)\mathrm{BBTD} + [\mathrm{Cd}^+]_{\mathrm{CdS}} + (1/2)\mathrm{H}_2 \qquad (1)\end{aligned}$$

the S $2p$ intensity ratios of S^1, S^2 and S^3 components have been used to calculate the fractions of the (–S–) and (–S–S–) chemical states of the BBTD and the (–S–) and ($-S^-$) states of the adsorbate Cd-mbt [23] presented in Fig. 9 in the form of fractions of a monolayer coverage. Estimating roughly a zero reaction order for the starting period with approximately constant numbers of free surface sites a linear approximation of the growing coverage with time seems meaningful giving rate constants of $k_a = 0.051/\mathrm{min}(25\,°\mathrm{C})$ and $0.224/\mathrm{min}(45\,°\mathrm{C})$. From the ratio of these rate constants an activation barrier $E_A = 58.3\,\mathrm{kJ/mol}$ was obtained. The thermal activation of MBT adsorption also controls the generation of the oxidation product BBTD (see Fig. 10, upper part) if photon induced electronic excitations in the semiconducting CdS substrate provides enough free energy for surpassing the energy barrier.

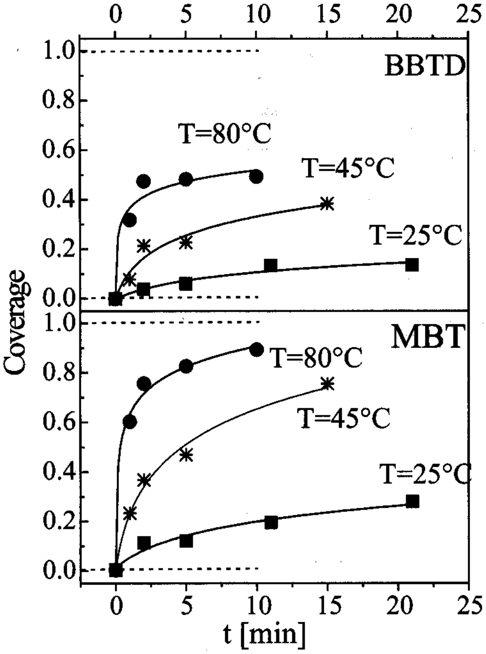

Fig. 9. Variation of the concentration of different sulfur bonding states of the MBT and BBTD molecules on CdS(10$\bar{1}$0) depending on the reaction time in 10^{-4} M MBT solution at different temperatures

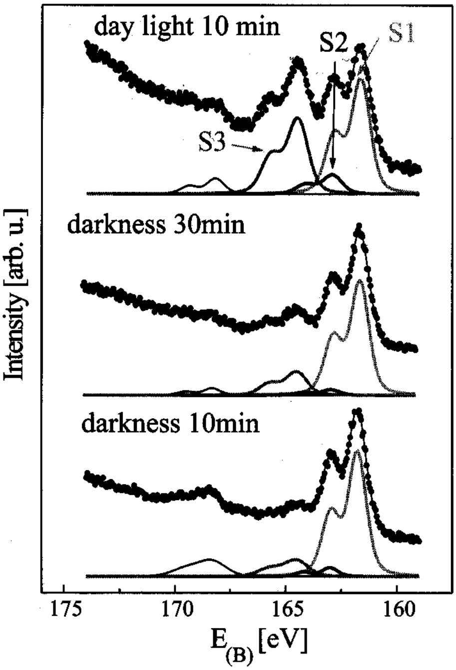

Fig. 10. S 2*p* spectra of CdS(10$\bar{1}$0) after reaction in 10^{-5} M MBT solution indicating the influence of daylight on the reaction rate

3.4 Photooxidation of the Adsorbate

The semiconductor CdS with a direct band gap of 2.4 eV absorbs light in the visible spectral range. This process may influence the chemical reactions at the semiconductor/electrolyte interface. This effect is clearly indicated comparing the S 2*p* spectra of Fig. 10 reflecting the adsorbate composition on CdS samples treated at daylight and darkness with a solution of MBT at room temperature. In contrast to the treatment in darkness the investigation of illuminated samples gave a high contribution of (–S–S–) adsorbate S^3 signals. Obviously the free energy of the dimerization/oxidation by water reduction known from the standard redox potentials giving a barrier of 0.615 eV (see Fig. 11) is provided by photon induced electronic excitation of the CdS substrate.

The reaction model in Fig. 12 based on a charge transfer model developed by *Gerischer* [24] includes possible steps of the photodimerization reaction in the bulk substrate, at the surface, in the ad-layer and in solution.

In the left part of the diagram the formation and recombination of electron-hole pairs after absorption of light are presented. Trapping in band gap states and transfer of arriving charge carriers across the surface is indicated in the middle part of the figure. The adsorbed MBT with a redox potential

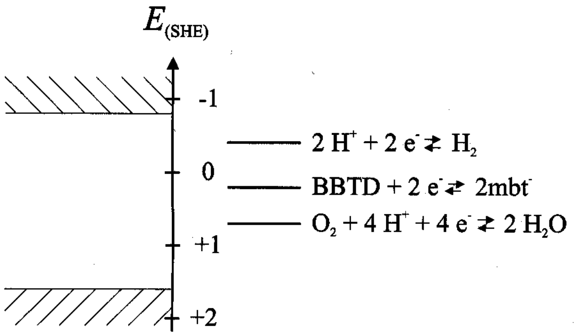

Fig. 11. Redox potentials for MBT, oxygen and water scaled schematically with the band edges of CdS

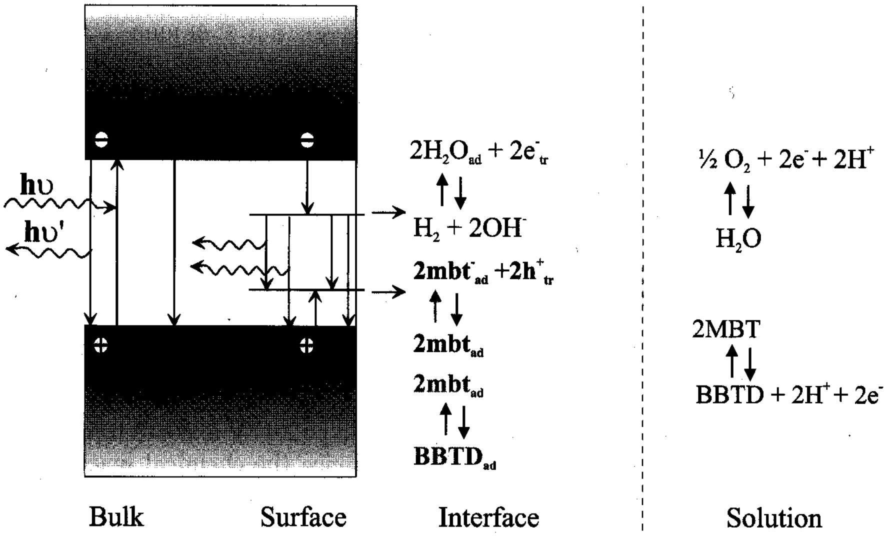

Fig. 12. Reaction model for the oxidation of MBT in the adsorbate system CdS/MBT: photon induced electronic excitation and recombination processes in the CdS substrate and charge transfer across the surface (*left*); water reduction, MBT oxidation and dimerization in the ad-layer (*middle*) and in bulk solution (*right*)

of 0.205 V (SHE) for a 10^{-4}M MBT solution at pH 7 provides hole acceptor states well above the valence band edge at 1.6 eV. The hole transfer initiates the dimerization giving BBTD. The reduction of water might be considered as corresponding redox process for maintaining the charge carrier balance. The redox potential of water at pH 7 amounts −0.41 V well below the conduction band edge at −0.8 V [25] enabling electron transfer across the surface. Formation of hydrogen has also been confirmed during charge transfer reactions with a set of organic compounds on colloidal CdS and ZnS [26].

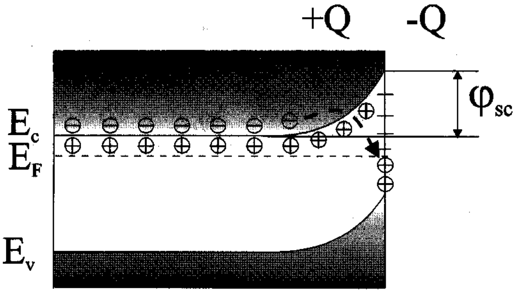

Fig. 13. Model of the space-charge region with the potential barrier φ_{sc} at the semiconductor surface

In order to minimize the influence of adsorbed O_2 on the oxidation the solutions were saturated with nitrogen. Nevertheless oxygen reduction may contribute weakly to the BBTD production because a small increase with time of the S $2p$ S^3 signal containing the (–S–S–) group after treatment of the sample in darkness has been detected (see Fig. 10).

The number of charge carriers and the charge transfer rate across the surface determining the oxidation rate is controlled by the band edge position close to the surface. In contrast to the simplified band pattern presented above, the majority carrier migration from the bulk to unoccupied states at the surface generates a dipole layer accompanied by an upbending of the bands and a depletion of electrons in the near-surface region of the n-type CdS (Fig. 13).

The resulting surface barrier φ_{sc} may restrict or even prevent the transport of charge carriers to the surface. Photon ($h\nu > E_g$) generated electron hole pairs separated by the electric field of the space charge region give minority carriers (holes) at the surface ready for the oxidation of the adsorbed mbt^- donor. In contrast to this branch of the charge transfer the electrons have to pass the surface barrier before arriving at the adsorbed acceptor molecules preferentially by tunneling. The probability of this process increases with decreasing φ_{sc} and x_0. The decrease of φ_{sc} by photon induced electron excitation explains the strong increase of the Cd-mbt oxidation rate during illuminating with daylight.

The interpretation of the daylight effect is confirmed by comparing the adsorbate oxidation rate on highly and lowly doped n-CdS. The S $2p$ spectra show a distinctly higher intensity of the component S^3 from BBTD for the highly doped CdS (Fig. 14). Obviously a higher charge transfer rate occurs in the semiconductor with the larger number N of ionized donors. This phenomenon can be understood taking into account the dependence of the depletion extension region being $x_0^2 \sim 1/N$ explaining the higher tunneling probability for the higher dopant concentration.

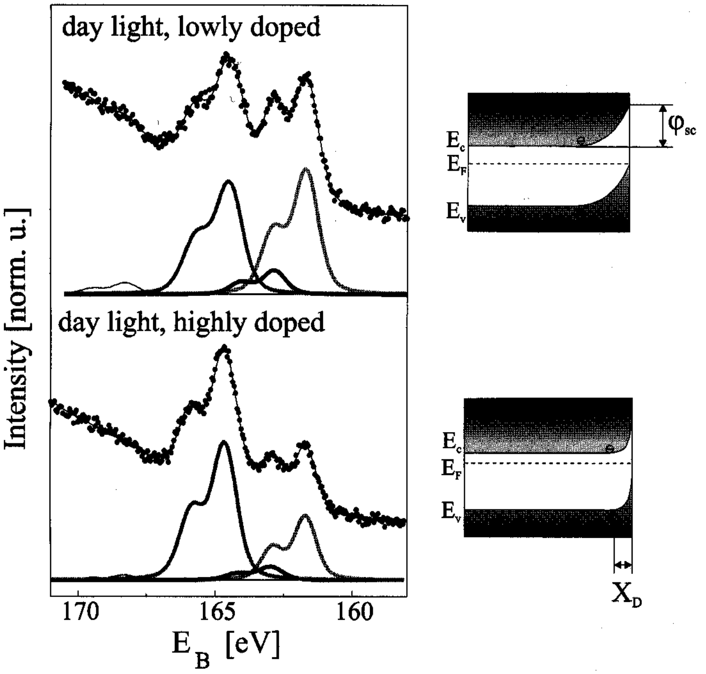

Fig. 14. S 2*p* spectra of MBT adsorbate demonstrating the influence of doping on the photon induced oxidation of MBT adsorbate on CdS from 10 min treatment in 10^{-4}M MBT solution at 25 °C

4 Conclusions

The reaction of MBT with the n-typ CdS($10\bar{1}0$) surface gives a layer containing a Cd-mbt adsorbate complex and bis(2-benzothiazolyl)disulfide (BBTD). The MBT molecules are chemisorbed via the thiolate group accompanied by a deprotonation of the nitrogen atom. In consequence of a second interface reaction step the disulfide bis-(2-benzothiazolyl)disulfide (BBTD) is formed.

Angular dependent NK XANES measurements of the adsorbate complex indicate an orientation of the molecular planes in the [$\bar{1}2\bar{1}0$] direction of the crystal and a tilted orientation of upright standing molecules confirming the bidentate coordination via the exocyclic sulfur and the nitrogen of MBT to two adjacent Cd atoms in the CdS surface. As a result of temperature dependent adsorption experiments an activation barrier of 58.3 kJ/ mol was obtained.

Photon induced electron–hole pair generation influences the oxidation of the Cd–mbt adsorbate at the solid/electrolyte interface causing a strong increase of the electron transfer rate across the surface when illuminating the sample by daylight. The thermal activated chemisorption of MBT in the chemisorption/oxidation/dimerization sequence becomes rate controlling during daylight exposition increasing the BBTD coverage rate.

The proposed model is supported by the investigation of lowly and highly doped CdS samples indicating an increased amount of the disulfide species in the latter case. Obviously reactions at the interface predominate in comparison to redox processes in the solution.

Acknowledgements

This work was supported by BMBF contract No. 05 625 OLA5. The authors are grateful to the BESSY staff, especially Dr. W. Braun, Dr. Ch. Jung, C. Hellwig and M. Mast.

References

1. A. Ulman: *An Introduction to Ultrathin Organic Films: from Langmuir-Blodgett to Self-Assembly* (Academic Press, New York 1991)
2. L. H. Dubois, B. R. Zegarski, R. G. Nuzzo: J. Am. Chem. Soc. **112**, 570 (1990)
3. D. Zerulla, I. Uhlig, R. Szargan, T. Chassé: Surf. Sci. **402–404**, 604 (1998)
4. R. Szargan, S. Karthe, E. Suoninen: Appl. Surf. Sci. **55**, 227 (1992)
5. J. Mielczarsky, E. Suoninen: Surf. Interface Anal. **6**, 34 (1984)
6. A. N. Buckley, R. Woods: Int. J. Miner. Process. **28**, 301 (1990)
7. I. Persson: J. Coord. Chem. **32**, 261 (1994)
8. M. D. Porter, T. B. Bright, D. L. Allara, C. E. D. Chidsey: J. Am. Chem. Soc. **109**, 3559 (1987)
9. J. Hautman, M. L. Klein: J. Chem. Phys. **91**, 4994 (1989)
10. M. Grunze: Phys. Scr. B **149**, 711 (1993)
11. P. Harder, M. Grunze, R. Dahint, G. M. Whitesides, P. E. Laibinis: J. Phys. Chem. B **102**, 426 (1998)
12. E. Umbach, K. Glockler, M. Sokolowski: Surf. Sci. **404**, 20 (1998)
13. C. M. Whelan, M. R. Smith, C. J. Barnes, N. M. D. Brown, C. A. Anderson: Appl. Surf. Sci. **134**, 144 (1998)
14. A. Schaufuß, P. Roßbach, I. Uhlig, R. Szargan: Fresenius J. Anal. Chem. **358**, 262 (1997)
15. K. Siegbahn, C. Nordling, A. Fahlmann: *ESCA: Atomic, Molecular and Solid State Structure by Means of Electron Spectroscopy* (Almqvist Wiksell, Uppsala 1967)
16. C. R. Brundle, A. D. Baker (Eds): *Electron Spectroscopy: Theory, Techniques, and Applications*, Vol. 1 (Academic Press, London 1977)
17. D. Briggs, M. P. Seah (Eds): *Practical Surface Analysis*, Vol. 1, *Auger and X-ray Photoelectron Spectroscopy* (Salle Sauerländer, Frankfurt 1990)
18. J. Stöhr: *NEXAFS Spectroscopy*, Springer Ser. Surf. Sci. **25** (Springer, Berlin, Heidelberg 1992)
19. K. H. Hallmeier, D. Mayer, R. Szargan: J. Electron Spectrosc. **96**, 245 (1998)
20. R. Hesse, T. Chassé, R. Szargan: Fresenius J. Anal. Chem. **365**, 48 (1999)
21. C. Hennig, K.-H. Hallmeier, I. Uhlig, S. Irle, W. H. E. Schwarz, C. Jung, C. Hellwig, A. Bach, M. Möbius, L. Beyer, R. Szargan: BESSY-Jahresbericht, 172 (1993)

22. D. Mayer, K. H. Hallmeier, B. Flemmig, J. Reinhold, R. Szargan: BESSY-Jahresbericht 341 (1998)
23. D. Mayer: Adsorbatanalyse an chemisch modifizierten Cadmiumsulfidoberflächen. Thesis, Universität Leipzig (1999)
24. H. Gerischer: Z. Phys. Chem. N. F. **27**, 48 (1961)
25. J. R. White, A. J. Bard: J. Phys. Chem. **89**, 1947 (1985)
26. J. Kisch: J. Prakt. Chem. **336**, 635 (1994)

Review

Between Physics and Biology – A Review of Light Matter Interactions on the Nanoscale as Probes in Biological Applications

Martin Pfannmöller and Dominic Zerulla

Institute of Pharmacy and Molecular Biotechnology, University of Heidelberg, Germany

School of Physics, UCD University College Dublin, Ireland

Abstract

Microscopy and spectroscopy as the classical techniques to investigate biological mechanisms have dramatically changed their paradigms in recent years. Their applications have advanced into areas with resolutions under the diffraction limit. New techniques have emerged based on well-known physical phenomena, such as Raman scattering, the creation of surface plasmons or scattering of nanometer sized metal particles. These phenomena predict to open new fields into the study of biological molecules, their properties and interactions. This work reviews the basic theoretical background and progress, which has been obtained for the understanding of interactions of light with particles on the nanometer scale.

Contents

1 Introduction

Biology does not state any laws of complex cellular systems, for example how the level of gene expression influences the fate of a cell or an organism and vice versa, nor does it quantatively describe how a protein is mediated into its final functional state. Yet biological research reveals to an ever increasing extent that there is a highly complicated network. The more pathways, the more genes connected to diseases and the more macromolecular interaction patterns are found, the more complex this network gets. A goal of the biological physicist is the characterization of the behaviour of biological systems. However, to create and validate theories, which try to simulate such a complex system as a cell and all its molecular components, *in situ* or *in vivo* studies of live objects are necessary.

The continuous improvement of fluorophores has led to applications of single molecule imaging (SMI) through fluorescence (Sako, 2006). Still the diffraction limit, which has so far bound the attainable spatial resolution to ≈ 250 nm (de Lange et al., 2001), prevents a further increase of measurable particle densities by conventional light microscopy.

Several techniques, originally associated with surface science and inorganic spectroscopy, have proven to be useful in combination with biological applications. The creation of resonant surface plasmons (SPs), especially in combination with the unique properties of metal nanoparticles (NPs) and nanostructures, enhances fluorescence (FS) and Raman spectroscopy (RS) and has excited the scientific community. The principles of these techniques are well described, however, there is an inscrutable amount of information in the literatur about possible applications. This work therefore intends to review several achievements that have been made in the last decade in the fields of imaging and spectroscopy coupled to the excitation of SPs. Furthermore, we will investigate in which way that opens new possibilities to observe biomolecules beyond the diffraction limit. After basic theoretical introductions to Raman scattering, surface plasmon resonance (SPR) and the surface enhancement by metal NPs, it is shown how these properties give rise to new measurement methods, e.g. enhanced fluorescence (SPCE) (Lakowicz, 2006), single particle detection (Kneipp et al., 1998) or characterization of biological compounds (Kneipp et al., 2002).

It was already predicted by Wessel in 1985 (Wessel, 1985) that the establishment of surface enhanced optical techniques will provide a lateral resolution of down to 1 nm. It is therefore worthwile to look at current developments and what they predict for the future of biological research.

2 Theoretical background

2.1 Surface plasmon resonance

The conduction electrons in a metal can be regarded as a quasi-free electron plasma. Either incident charged particles or incident photons are therefore able to induce oscillations of charge densities at an interface between the metal and a dielectric, or in general at the interface of two media with dielectric constants of opposite signs (Otto, 1968; Kretschmann and Raether, 1968; Homola et al., 1999). For small deflections a linear dependance according to

$$\vec{P} = \varepsilon_0 \chi \vec{E}$$

describes the relation between the disturbance $\vec{E}$ (the electric field) and the reaction $\vec{P}$, which is the polarisation induced at the interface of the metal. In this equation ε_0 is the dielectric constant in vacuum and χ the electric susceptibility, a material constant, which is dependent on the frequency ω.

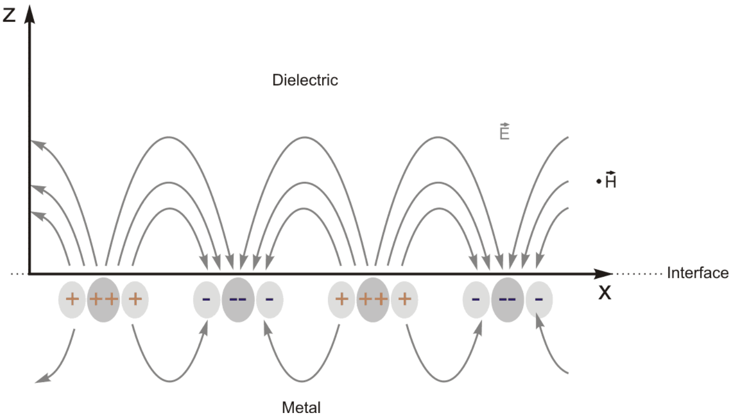

Figure 1: Illustration of the charge-density oscillation and the corresponding electric field at the interface between a metal and a dielectric medium. The varying density of the field lines indicate that the field declines much faster into the metal than into the dielectric (Revised from Willets and Van Duyne, 2007).

As illustrated in Fig. 1, the induced SP can be regarded as a propagating surface plasmon wave (SPW) at the interface ot the two media. An SPW is a longitudinal electric or transversal magnetic polarized wave, i.e. the vector of the magnetic field is perpendicular to the wave vector $\vec{k}$ and parallel to the plane of the interface. The field distribution of SPWs can be derived by solving Maxwell's equations for light propagating in matter and using boundary conditions for wave equations that must describe a wave at the interface of two media. This yields the frequency-dependency of the wave vector $\vec{k}_{SP}$, i.e. the dispersion relation for SPs (Sambles et al., 1991),

$$\vec{k}_{SP} = \vec{k}_0 \sqrt{\frac{\epsilon_m \epsilon_d}{\epsilon_m + \epsilon_d}} \tag{1}$$

where $\vec{k}_0 = \omega/c$ denotes the wave vector in free space, and ϵ_m and ϵ_d the dielectric functions of the metal and the dielectric, respectively.

As the wave propagates along the surface, the electric field perpendicular to the wave vector decays exponentially into the surrounding media. The field is said to be evanescent and decreases more rapidly on the metal side (see Fig. 1) where the decay length is dependent on the skin depth. Several conditions have to be fulfilled for Eq. 1 to describe an SPW. The real part of ϵ_m has to be negative and its absolute value smaller than ϵ_d (refer to Sambles et al., 1991, for a comprehensive derivation of constrains regarding the excitation of an SPW). This is true for various metals, such as aluminium, silver or gold, although silver and gold are most commonly used (Homola et al., 1999).

Excitation of SPWs

Examining Eq. 1 for $\vec{k}_{SP} \rightarrow 0$ and $\vec{k}_{SP} \rightarrow \infty$ reveals that the dispersion relation is approximately linear and near to that of light in free space for small $\vec{k}_{SP}$ but converges to a limit for large $\vec{k}_{SP}$, where the value of ϵ_m is the negative equal of ϵ_d. As seen in Fig. 2, where the frequency is plotted against the $\vec{k}$-component parallel to the interface in the direction of propagation, the momentum of the SPW propagation is always higher than that of the light line. An example calculation of Eq. 1 for a silver-air interface and the red part of the visible spectrum yields a value for $\vec{k}_{SP}$ that is approximately 1.03 times higher than $\vec{k}_0$ (Barnes et al., 2003).

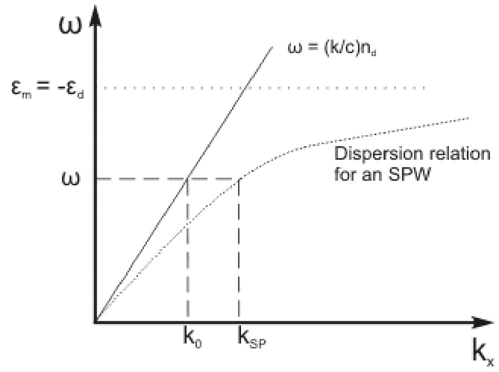

Figure 2: Frequency in relation to the component of the k-vectors in the direction of propagation of light in free space and of an hypothetically excited SPW. As both curves never intersect and thus the momenta do not match for any frequency, no SPW can be excited by light that is incident on metal from air.

This finding implies that excitation of an SPW is not possible at the smooth boundary between metal and air when light is incident through free space. Besides using rough surfaces, three common techniques for surfaces provide the necessary enhancement of the light propagation vector:

i) If light is directed through a medium with higher refractive index n_g, the phase velocity is reduced to c/n_g, where c is the velocity of light in vacuum. The slope of the light line in the dispersion diagram of Fig. 2 therefore decreases. Both curves now intersect, i.e. there is a frequency where the propagation constants match. Hence incident light with that resonance frequency can excite an SPW at the interface. In 1968 Otto suggested a configuration using a prism (Otto, 1968). In this setup light is totally reflected at the glass air interface. The evanescent field at this boundary is able to penetrate a small air gap and to induce an SP in a metal layer at the other end of the gap. However, this gap has to be held constant and very small. In the same year Kretschmann and Raether (Kretschmann and Raether, 1968) introduced a similar configuration (Fig. 3a). Here a thin metal layer is attached to the outer side of the prism. The evanescent field of the total reflected light excites an SPW at the interface between the metal and air or dielectric on the opposite side. This simplifies the setup and opens the door to probe analytes as the outer metal dielectric interface is freely accessible, which is why this configuration is most commonly used today.

ii) Another configuration, which is presented in Fig. 3b, utilizes a diffraction grating taking advantage of the fact that the wave vector component of the diffracted light parallel to the surface is increased. This effect was first observed by Wood but correctly explained by Ritchie more than half a century later (Wood, 1902; Ritchie et al., 1957). To match the wave vectors of incident light and the SPW, the periodicity of the grating has to be changed.

iii) Furthermore a waveguide can be used to couple a wave mode into the system with a small metal layer on top of the guide (Fig. 3c). The process of excitation of an SPW is similar to the prism-coupled configuration. The evanescent field of the guided wave penetrates the metal layer and excites a surface plasmon at the other side facing a dielectric.

Sensing optical properties of the surrounding medium

Due to the unique characteristics of SPWs, surface plasmon resonance as a technique has been used for numerous chemical and biological applications. The near-field of a localised

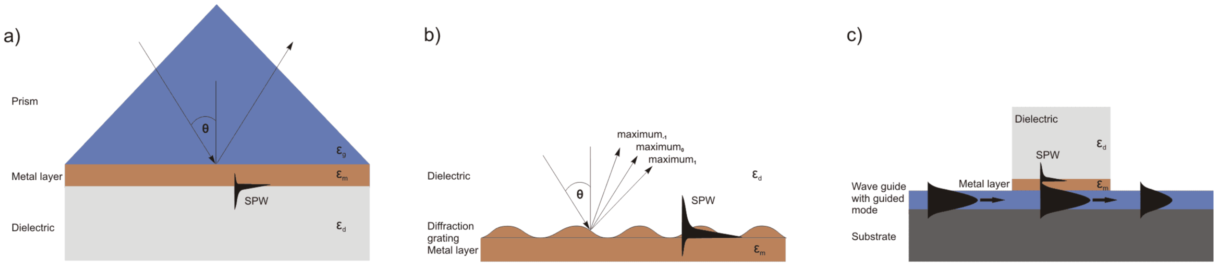

Figure 3: Three possible configurations used to create an SPW. a) Kretschmann configuration with prism-coupled excitation. b) SPW produced by momentum enhanced diffracted waves on a diffraction grating. c) Incident light coupled in through a wave guide. In a and c an evanescent beam penetrates a thin metal layer and excites an SP at the metal–dielectric interface.

SP is strongly enhanced in the dielectric. That is why the wave vector is dependent on the material in the vicinity of the surface. Different amounts of bound compounds cause a change in the local refractive index in the near-field. By measuring the properties of outgoing light such as angular dependent intensity and polarisation, shifts in the SPR properties and therefore in the refractive index sensitively indicate changes in the corresponding surface near concentration of the molecular species of interest. There is a variety of sensor configurations. This work does not intend to comprehensively treat corresponding setups and characteristics. The reader may be referred to two excellent reviews covering recent findings of the last ten years in sensor technology and applications (Homola et al., 1999; Homola, 2003). Sensors are generally classified according to their type of modulation (e.g. angle, intensity, wavelength, phase and polarisation). Fig. 4 shows results from example measurements. When the angle of incident light with constant frequency is changed over a certain range there is one angle where resonance occurs. Here the x-components of the wave vectors match. In this case the reflected light amplitude has a minimum (see Fig. 4a) because energy can effectively be transferred to the resonant SP. A change in refractive index in the near-field causes a predictable shift (and vice versa) in the angle at which the SP resonance occurs. However, please note that the minimum reflectivity does not precisely indicate the maximum SP excitation but is only near to that. This is due to the nature of the minimum which is given by the destructive interference between the normally reflected light and the the phase shifted SP re-emission. Similarly, phase alterations with respect to incident angle can be recorded (Fig. 4a). When wavelength modulation at constant incident angle is used, the wavelength is measured at which the minimal reflectivity, i.e. the strongest coupling, occurs (Fig. 4b).

2.2 The Raman effect

In 1928 Chandrasekhara Venkata Raman discovered the effect that light scattered by molecules may contain fractions with longer or smaller wavelengths than that of the inci-

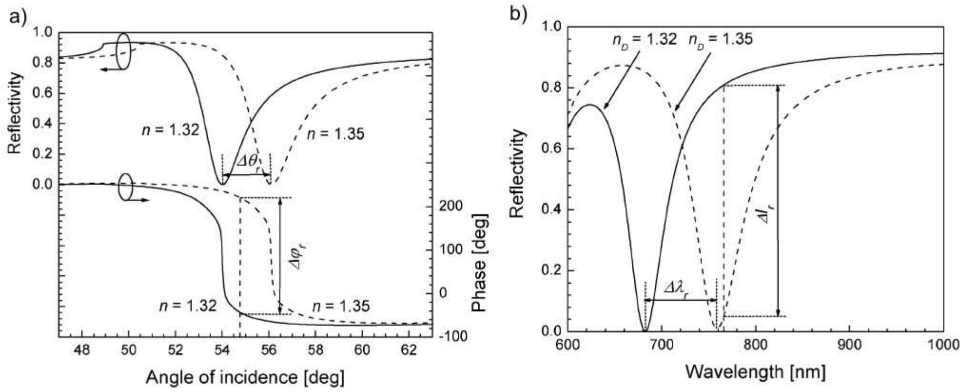

Figure 4: Examples of responses of an SPR setup with Kretschmann configuration (50 nm gold layer) to different types of modulation for two refractive indices. a: Reflectivity and phase for different angles of incident and constant wavelength (682 nm). b: Reflectivity for different wavelenghts and constant incident angle (52°).. (Homola, 2003).

dent light. In the majority of cases light is elastically scattered. This so-called Rayleigh scattering produces light, which is re-emitted isotropically at the same frequency. However, when the molecule ends in another vibrational or rotational state than before the scattering, the energy of the emitted photon is shifted of an amount equal to the energy difference between these two states. When the end state is higher than the initial state the light's frequency is decreased (Stokes' line). If in contrast the excitation occurs from a higher vibrational or rotational level compared to the end level, a shift towards larger frequencies occurs (anti-Stokes' line). As there are unique discret energy levels for every molecule, an analysis of the Raman spectrum is a fingerprint of, and provides information about, the states and the shape of molecules (for an introduction to the interpretation of Raman spectra refer to Smith and Dent, 2005). The Raman effect underlies a scattering process. That is why monochromatic light from near-infrared (NIR), visible or ultraviolett (UV) sources can be used as incident radiation (Hanlon et al., 2000). The option to use UV or NIR light renders this technique very useful for Raman active compounds with respect to keeping the fluorescence background as low as possible. Fig. 5a presents a comparison of the processes involved in fluorescence and Raman Stokes' scattering for UV, visible, and NIR light excitation. In fact, for the first two, resonant excitation is illustrated: i.e. the molecule is excited into a higher electronic state and returns into the electronic ground state through fluorescence or Raman scattering. The difference between the fluorescent and the scattered photon however is typically much higher for UV light than for visible light. Thus fluorescence induced by UV light can sometimes be better separated from the Raman light than that induced by visible light. In the third case in Fig. 5a the energy of near infra-red light is not sufficient for a transition into a higher electronic state. The incident light is inelastically scattered by means of a transition between the ground vibrational and a virtual state and back to a higher vibrational state. Consequently, fluorescence can not occur as there is no absorption of the incident photon.

Anti-Stokes' Raman scattering is only observed when the molecule is in a higher vibrational state prior to interactions with incident light. This is shown in Fig. 5b together with normal Rayleigh scattering. The illustration makes clear that the difference $\Delta\nu$ between the incident and scattered light of Stokes' lines equals the exact negative value of anti-Stokes' lines of the corresponding transitions. Further noticable is the fact that Rayleigh scattering is much more intense so that amounts of Raman scattered light sufficient for modern spectroscopy are only obtained with incident narrow bandwidth laser light.

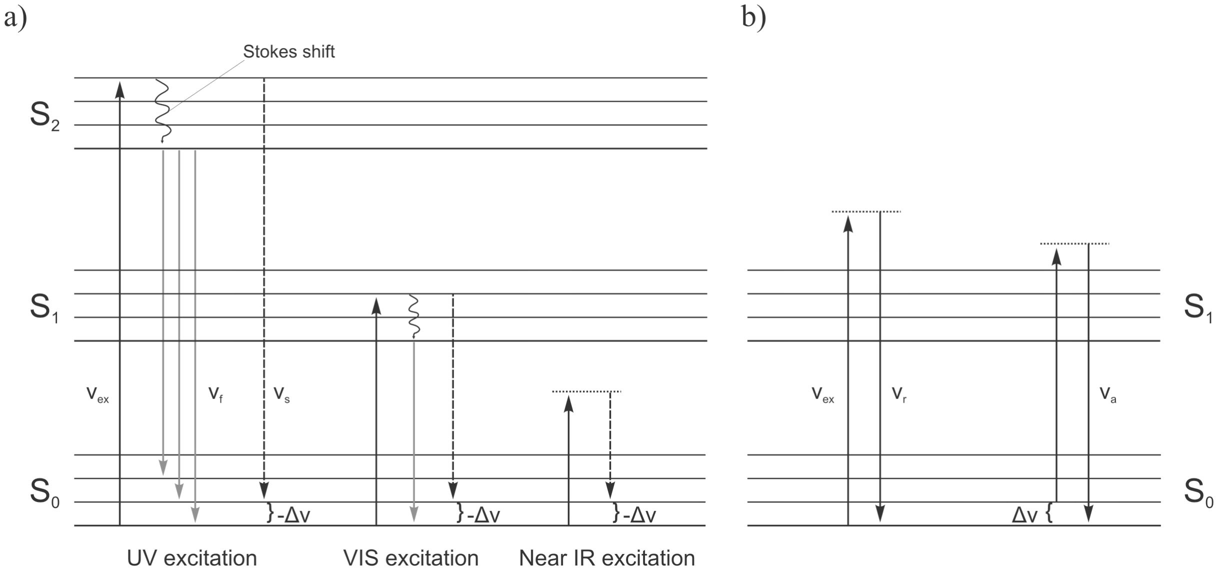

Figure 5: Schematic of intramolecular electronic and vibrational transitions explaining fluorescence as well as Rayleigh and Raman scattering. a) Fluorescence (dottet arrows) and Raman scattering (dashed arrows) for different incident wavelengths corresponding to UV, visible and near-IR light. Note that when incident light is used whose energy does not suit the energy difference between electronic transitions, only scattering, no fluorescence, is observed as an essential non-absorbing interaction. b) Illustration of both the difference between Stokes' and anti-Stokes' scattering as well as between Raman and Rayleigh scattering. The latter is connected to full elastic interactions and occurs much more frequently than Raman scattering, which produces a positive or negative shift in wavelength ($-\Delta\nu$ or $\Delta\nu$ respectively).

An introductive treatment of rotational and vibrational Raman spectra according to possible quantum states is covered elsewhere (Banwell and McCash, 1994). For the sake of simplicity only the classical explanation of the conditions under which Raman scattering occurs is shown here. As mentioned above, the polarisation of a material is dependant on the susceptibility χ, which is in the general case a tensor. Similarly the polarisation of a molecule may be written as,

$$\vec{P} = \alpha \vec{E}$$

where α is the polarisability tensor of the molecule. In the approximation of a molecule with a radius much smaller than the incident light wave, the electric field vector around the molecule can be regarded as constant. This induces a displacement of the electron bond and thus with an electric dipole moment. The electrons oscillate at the frequency of the disturbance and emit radiation with exactly the same frequency, which is explained by Rayleigh scattering. If a change of the vibrational or rotational state is connected to a change in the polarisability, there will be superimposed oscillations of these internal motions. An alternating polarisability is the prerequisite for a compound to be Raman active as it is able to get into a higher or lower state by means of scattering. Note that this rule is contrasted to that for IR or microwave excitation where in order for a molecule to be active, the vibration or rotation must induce a change in the dipole moment. However, this review focusses on biological applications. Most biomolecules are rather complex so that it can generally be expected that they are both IR and Raman active.

2.3 Surface-enhanced Raman spectroscopy

In 1974 Fleischman et al. discovered that an intense Raman scattering is observed when analysing pyridine adsorbed on roughened silver electrodes (Fleischman et al., 1974). However they did not recognise it as an enhancement. Hence the determination of characteristics and approaches to a theoretical description of this effect have been subject to studies in the following decades. It has been found to be an enhancement of the Raman spectroscopic lines of a compound adsorbed on metal surfaces, which preferentially consists of multiple, microscopic domains (Moskovits, 1985). Over the years many theories have been developed in need to explain the underlying principles of this phenomenon, which is referred to as Surface-enhanced Raman scattering (SERS). Many reviews on this topic can be found troughout the published literature (see for example Kneipp et al., 2002; Campion and Kambhampati, 1998; Otto et al., 1992; Moskovits, 1985). New calculations and experimental findings in the mid-nineteees resulted in measured Raman cross sections of $10^{-17} - 10^{-16}$ cm^2/molecule for SERS which is large in comparison to normal non-resonant RS (Kneipp et al., 1996) . These figures have proven to be realistic for special shapes of enhancing metal objects. Two different effects are understood to contribute to the enhancement, electromagnetic field enhancement and chemical enhancement (first-layer effect). Basic explanations of these ideas are addressed in the following paragraph. However it should be noted at this stage that a complete, system independent theory on SERS is still missing.

Enhancement factors

SPs can also be excited on very small objects such as spheres, general spheroids or objects of arbitrary shapes. See Fig. 6) for an illustration of SP oscillations on a nano sphere. As explained in the preceding section, the near-field in the vicinity of the object is effected and in turn effects compounds nearby, especially molecules which are bound to the surface. For spheres with a radius–wavelength ratio smaller than 0.05 (Kneipp et al., 2002), in the electrostatic approximation, the field amplitudes of the incident laser light can be added to the polarisation field of the particle (Bouhelier, 2006),

$$\alpha = 4\pi r^3 \frac{\epsilon_m - \epsilon_d}{\epsilon_m + 2\epsilon_d} \tag{2}$$

where α denotes the polarisability of the sphere, r the radius, and ϵ_m and ϵ_d the dielectric functions of the sphere and the surrounding dielectric, respectively. The resultant combined field E_r can be written as

$$E_r = E_0 \frac{3\epsilon_d}{\epsilon_m + 2\epsilon_d} \tag{3}$$

where E_0 is the field amplitude without the particle. Both equations 2 and 3 reach a maximum when $\epsilon_m = -2\epsilon_d$. In accordance with that the imaginary part of ϵ_m has to be equal to zero. The imaginary part of the dielectric function of nobel metals is sufficiently small in order to show a clear maximum. In this case a strong near-field in the vicinity of the particle can be obtained. According to rough approximations (Campion and Kambhampati, 1998) the enhancement scales with $\approx E^4$, which leads to high yields of RS of molecules bound to the surface. For objects other than spheres, calculations become more complicated. For ellipsoidal particles, for example, there are separate resonance conditions for every principle axis. In general, electromagnetic field enhancement strongly depends on the composition, size and shape of the object. New models have been introduced to describe the field distribution and corresponding enhancements for arbitrary shaped metal objects. The reader is referred to a recently published article, which reviews these methods (Bouhelier, 2006). Therefore the second part of this work mainly deals with achievements and applications regarding spherical particles.

Electromagnetic factors do not alone account for observed enhancements. It is generally accepted that chemical or electronic effects contribute to the enhancement by a factor of $\approx 10 - 100$ (Kambhampati et al., 1998) and is also referred to as first-layer effect because molecules have to be in direct contact with the metal. Several mechanisms are regarded as possible origins of chemical enhancement. A possible mechanism involves an electronic coupling between metal and bound compounds, which leads to a higher cross

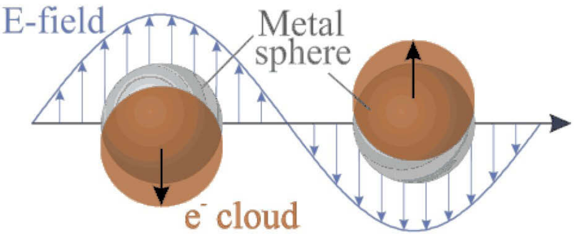

Figure 6: Illustration of an SP oscillation of a sphere for the approximation that the radius is much smaller than the wavelength (Revised from Willets and Van Duyne, 2007).

section (Kneipp et al., 2002). Another process is due to the broadening of molecular orbitals adsorbed to the metal or to the creation of new electronic transition (charge transfer) between the compound and the metal (Campion and Kambhampati, 1998; Kambhampati et al., 1998; Otto et al., 1992). Charge transfer effects lead to an increasing number of resonant conditions that are connected to increased Raman scattering. Note that because of newly created or broadened transitions, characteristic Raman lines can be shifted towards different frequencies. Moreover line widths can change or new lines can appear due to new selective resonant effects. Nevertheless, under similar conditions specific fingerprints are generally observed for single molecules.

2.4 Metal nanoparticles and the near-field

Scattering properties

An SP that is induced by monochromatic light in metal nanoparticles (NPs) is characterised as an oscillation of the electron cloud. Thus with the presence of moving charges the particle itself re-radiates light of the same frequency. Due to the connection to SPs this type of scattering is called plasmon scatter. For objects at subwavelength sizes, again quasistatic approximations of the Rayleigh regime can be applied. The scattered intensity for a particle is given by (Yguerabide and Yguerabide, 1998a)

$$I = \frac{16\pi^4 a^6 n_d^4 I_0}{r^2 \lambda_0^4} \left| \frac{m^2 - 1}{m^2 + 2} \right|^2 \sin^2(\alpha) \tag{4}$$

where I and I_0 denote the scattered and incident intensity, respectively, r the distance between the particle and the location of the detector, a the radius of the sphere, n_d the refractive index of the surrounding medium, λ_0 the incident wavelength, α the angle between the detection direction and the direction of the incident polarization, and m the ratio of the complex refractive index of the bulk metal and n_d. The ratio m is thereby dependant on the wavelength. By applying a monochromatic light source only scattered light of the same frequency can be detected. Subsequent measurements are based on the determination of shifts in angle or polarisation dependency of the scattered light or in absorption. These optical characteristics change, for example, when compounds bind to the particle or when particles congregate upon certain interactions. Theories and applications for such measurements were reviewed recently (Aslan et al., 2005).

Scattered light by small particles that are illuminated with polychromatic light however displays a clear spectral distribution. As pictured in Fig. 7 the scattering cross section C_{sca}, which is a measure of the total scattered light in all directions, varies with increasing wavelength. It can be seen for the nobal metals silver and gold that there is a resonance wavelength, i.e. a maximum for C_{sca} in a narrow region of the spectrum (Yguerabide and Yguerabide, 1998a). Thus a gold or silver particle scatters a narrow band of incident polychromatic light at much higher intensities than other parts of the incident spectrum. This behaviour allows the application of NPs as reporters for detection even in simple optical microscopy. The brightness of an NP with 100 nm in diameter is equivalent to $\approx$ 100000 fluorescein molecules (Schultz, 2003), thereby providing a detection source without the drawbacks of fluorescent imaging such as photobleaching, autofluorescence background or the need of intense light strongly interacting with the medium. The scattered light intensity distribution of three differently sized particles can be seen in Fig. 8. The different sizes are clearly distinguishable by different resonance wavelengths, albeit still in the visible region.

The shift in resonance wavelength, however, can not be explained by means of Rayleigh approximation. Resonance condition according to Eq. 4 occurs when the term $m^2 + 2$ in the denominator tends to zero. This term is dependant merely on the real and imaginary parts of the refractive indices. There is no size dependance. Thus the intensity peak increases with the sixth power of the radius but does not shift. Light scattered by larger particles is described by Mie's theory (Mie, 1908). Superpositions, i.e. dipol, quadrupol and higher order oscillations have to be taken into account because the particle no longer homogeneously feels the same phase of the incident electromagnetic wave. Mie scattering spectroscopy is originally based on the formal solution to the scattering of light by a homogeneous sphere published by Gustav Mie in 1908. Briefly, the mathematical derivation begins with Maxwell's equations and the necessary boundary conditions, which are then transformed into spherical polar coordinates with a solution of the wave vector equation emerging. The coefficients for scattering arise and the theory is extended to the far-field solution based in a plane constructed from the incident and scattered waves. Finally, the measurable quantities, namely Stokes parameters, and the formulation of the phase matrix can be found. A comprehensive outline of the theory can be found in Liou (1977). The final phase matrix for scattering by a homogeneous sphere is provided below.

$$\mathbf{P} = \begin{bmatrix} P_{11} & P_{12} & 0 & 0 \\ P_{12} & P_{11} & 0 & 0 \\ 0 & 0 & P_{33} & -P_{34} \\ 0 & 0 & P_{34} & P_{33} \end{bmatrix} \tag{5}$$

where

$$P_{11} = \frac{4\pi}{2k^2\sigma_{sca}}(i_1(\theta) + i_2(\theta)), \tag{6}$$

$$P_{12} = \frac{4\pi}{2k^2\sigma_{sca}}(i_1(\theta) - i_2(\theta)), \tag{7}$$

$$P_{33} = \frac{4\pi}{2k^2\sigma_{sca}}(i_3(\theta) + i_4(\theta)), \tag{8}$$

$$P_{12} = \frac{4\pi}{2k^2\sigma_{sca}}(i_3(\theta) - i_4(\theta)). \tag{9}$$

Here k is the wave vector, σ_{sca} is the scattering cross section, θ is the scattering angle and i_j (j=1, 2, 3, 4) are the intensity functions.
One of the consequences is that the intensity pattern vs. wavelength shifts as seen in Fig. 8. A compact introduction to the derivation of the Mie theory can be found elsewhere (Yguerabide and Yguerabide, 1998a). Theoretical calculations and advanced spectroscopic investigations on non-spherical nanoparticles can be found in (Sönnichsen et al., 2002, 2005; Grigorenko et al., 2006; Doyle et al., 2007). There is also a review of recent approaches that try to extend it to arbitrarily shaped objects (Kelly et al., 2003).

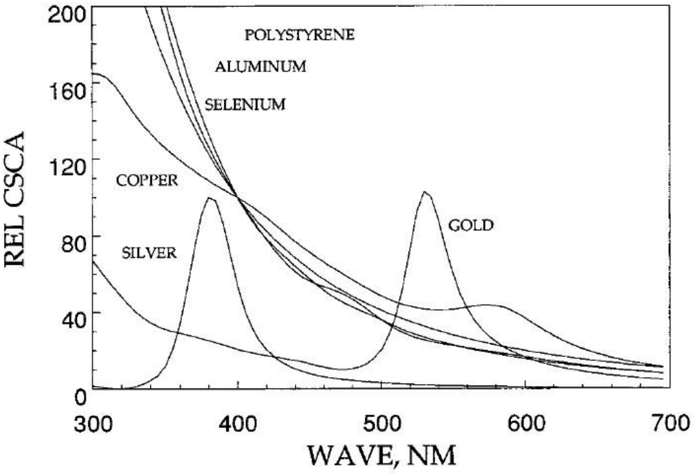

Figure 7: Scattering cross sections C_{sca} vs. wavelength λ for several metal and polysterene particles with diameters within the Rayleigh limit. Calculations were done for water ($n_d = 1.33$) (Yguerabide and Yguerabide, 1998a).

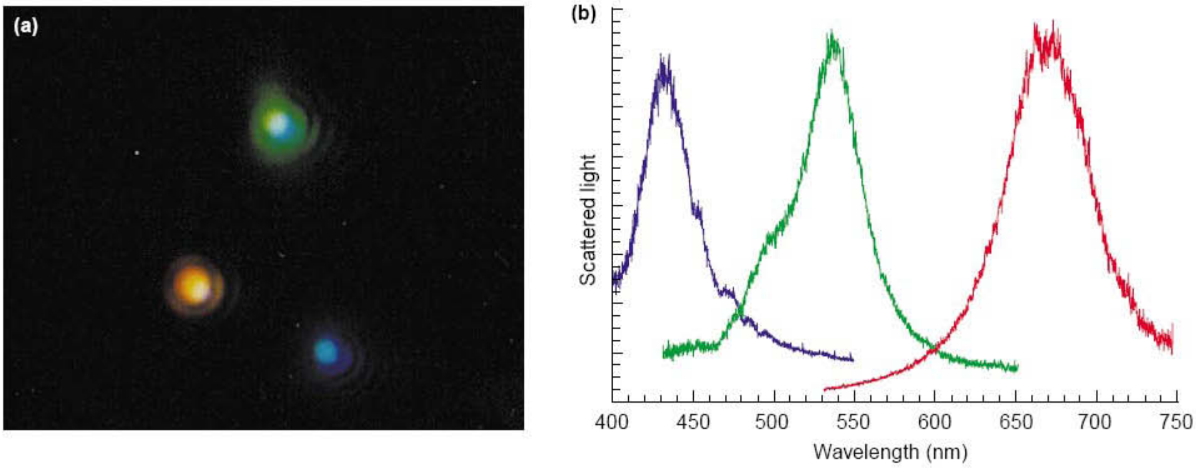

Figure 8: Illustration of the resonance peak of scattered light by particles of three different sizes. a: The resonance colour of a polychromatic light source is highly scattered by subwavelength sized particles so that they can be detected and distinguished in a normal colour photograph. The distance of the particles is $\approx 4\ \mu$m so that scattered light can be regarded as not influencing the behaviour of other particles. b: Graphs of the scattered light intensities as a function of wavelength (Schultz et al., 2000).

Complex Nanoparticles and their Synthesis

Silver and especially gold particles are open to distinct functionalisation by surface chemistry and are at the same time well suited for use in biological systems due to their inertness. A problem that has to be solved is the realisation of synthesising particle populations of homogeneous size and monodispersity. There have been a variety of approaches for the production of NPs; among them are electrochemical methods, gas phase condensation and solution phase chemical methods (Daniel and Astruc, 2004). The most prominent technique so far has been citrate reduction, which can produce NPs of $12 - 20$ nm in size with a standard deviation of $\approx 10 - 16\%$ (Frens, 1973). To produce smaller particles of $1 - 3$ nm size, a method was developed involving borohydride reduction in the presence of an alkanethiol capping agent (Brust et al., 1994). Uniform size distributions within populations of larger particles had not been obtained until relatively recently. Several published reports describe size controlled syntheses by seeding growth for NPs of $5 - 40$ nm (Jana et al., 2001a,b) and even up to 100 nm in diameter (Brown et al., 2000). Both authors suggest the use of preformed small NPs and subsequent reduction of Au^{3+} on these supports, whereas repetitive seeding is necessary in order to yield monodispersed, uniformly grown spheres.

However, apart from spherical nanoparticles a whole zoo of different shaped nanoobjects have been created. Their advantage is either higher electromagnetic near fields, better focus of EM fields, higher sensitivity of their SPR against molecular adsorption and shift of resonance wavelenghts into more appropriate regions. The preferable spectral range used for biological samples is IR light because of the low absorption by molecules within the optical path. As particle shape and composition have a strong influence on the scattering and absorption properties of NPs, much research has gone into the determination of differently composed and shaped objects. It has been shown that the resonance peak shifts to the red end of the visible spectrum when corresponding spheres, stars, pentagons, triangles and bowties are compared (see Fig. 9a) (Mock et al., 2002; Nehl et al., 2004, 2006; Hao et al., 2007; Fromm et al., 2004). The preparation of nanoprisms has recently been reported (Sun and Xia, 2003; Jin et al., 2001) as well as the unique properties of nanorods (Murphy et al., 2005; Link and El-Sayed, 1999; Sönnichsen et al., 2002, 2005; Wang et al., 2006), where two plasmon resonance bands can be observed, one longitudinal and one transverse band along the long axis and the short axis respectively. Structures like nanorods or wires can have further enhanced electric fields at the tips, which is referred to as the lightning-rod effect (Bouhelier, 2006; Imura et al., 2004; Kelly et al., 2003). A further promising approach uses nanoshells where a 40 − 250 nm sized dielectric sphere (for example silica) is coated with a thin metal layer of 10 − 30 nm in diameter (Jackson and Halas, 2001; Oldenburg et al., 1998). Depending on the core–shell radius ratio the resonance peak is shifted from visible to IR spectrum as Fig. 9b shows. According to a report by Oldenburg et al., by varying the relative sizes and composition the peak is predicted to shift across the spectrum to up to 2.2 μm (Oldenburg et al., 1999).

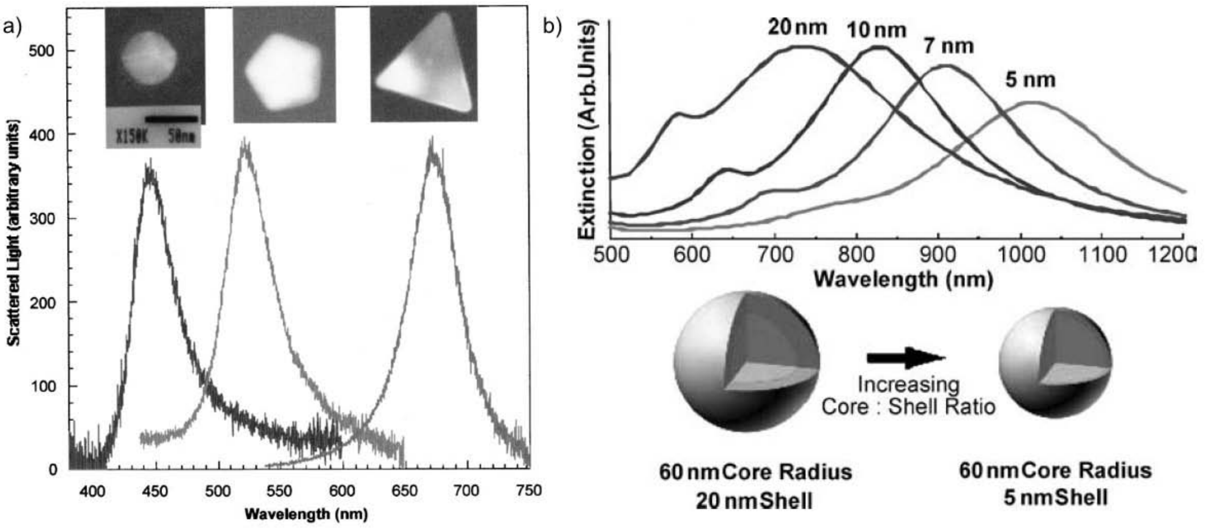

Figure 9: Dependence of the plasmon resonance peak on particle structural properties. a: Red shift in the spectra of silver NPs of different shapes. (Mock et al., 2002) b: Effect of increasing the core-shell ratio of nanoshells (60 nm core radius with decreasing gold shell radii of 20,10,7 and 5 nm). The large red shift illustrates the dramatic responses to subtle changes in the composition of a NP (Hirsch et al., 2006).

2.5 Optical Scanning Near-field Techniques

The ability to view and study samples under high magnification is enourmously important in many disciplines such as materials research, the biological sciences and the medical sciences. Conventionally, optical techniques haver been most widely used for these purposes given their long historical development, noninvasiveness, ease of use and relatively low cost. However, resolutions obtainable in conventional far-field microscopy are limited to the diffraction limit of $\approx \lambda/2.3$. In 1984 Pohl, Denk and Lanz have demonstrated that subwavelength resolution optical image recording was possible by moving an illuminated, narrow subwavelength aperture along a test object equipped with fine-line structures(D.W. et al., 1984). Details of 25-nm size could be recognized using 488-nm radiation. The result indicated a resolving power of at least $\lambda/20$. This so-called scanning near field microscope SNOM (also called NSOM) uses the ability of light to go through an sub wavelength aperture albeit with an exponential loss in intensity. For the greater detail please refer to Robert Dunn's excellent review on this matter (Dunn, 1999). However, in order to use SNOM techniques the shear force on the used fibre tips must be controlled. Otherwise the changes in signal through this shear mechanism might be stronger than the actual desired optical signals (Brunner et al., 1997). The exponential loss of intensity at the subwavelength aperture has led to new developments which circumvent the problem by omitting the aperture (apertureless scanning nearfield microscopy ASNOM). Known techniques place a metallic tip into the near field of the scanned sample which is illuminated directly by a laser beam. Either the scattered light from this tip is recorded or a surface plasmon polariton is excited at the tip which exhibits its own strong near field which can be used e.g. for Raman scattering (Tip enhaced Raman Scattering, TERS) (Stöckle et al., 2000; Anderson, 2000).

3 Plasmon resonance and biological applications

There has been a dramatic increase of research articles dealing with phenomena of plasmon resonance. Thus, further research went into the study of the statistics of scientific publications in this field. In 2004, for example, following an exponential growth, the number of published articles about silver and gold NPs alone is said to have reached more than 5000 (Eustis and El-Sayed, 2006, who give a comprehensive overview of recent reviews across the field).

In light of this unobservable amount, this work does not claim to be exhaustive. It is nevertheless intended to show some of the current developments important for biological applications, such as well established assays of "normal" SPR, the emergence of new bioassays exploiting the scattering properties of NPs, as well as the promising effects of surface enhancements on metal surfaces and the successive improvements to fluorescence microscopy and RS.

3.1 Conventional biosensors for flat surfaces

SPR sensors have proven to be useful in a variety of detection systems, where the underlying principle is the change of refractive index in the near field of excited SPs due to molecule binding or adsorption. Applications are hence restricted to the measurement of quantitative events, such as increase in the amount of bound analytes. The obtainable lateral resolution parallel to the surface is dependant on the decay length of the SP, which is 19 μm for silver and 3 μm for gold at a wavelength of 630 nm (Homola et al., 1999). Since the introduction of a commercial biosensor in 1990 (Pharmacia Biosensor, BIAcore), the use of SPR as a sensing device has been widely spread. Biological applications can be found in three major fields: (i) kinetic studies of biomolecular interactions at the surface, (ii) interaction assays i.e. probing binding events between molecules such as DNA, proteins and even viruses or bacteria, and (iii) monitoring interaction of molecules within and with lipid layers and self assembled monolayers (SAMs) (McDonnell, 2001; Green et al., 2000; Silin and Plant, 1997; Zerulla et al., 2003).

Detection from bulk medium

In spite of the low lateral resolution SPR has been used to image cell-substrate contacts and cell movements (Giebel et al., 1999). Here the metal layer was composed of aluminium, with a SP decay length of below 1 μm. The microscopic image was combined with the high vertical resolution to image the type of contacts and to track cell movements. Different reflectivity curves for different points across the contact area thereby reflect the cell–substrate distance and thus whether a very close and tight (focal) or loose contact was observed.

More prominent applications are interaction analyses as well as studies of adsorption kinetics of molecules. The first biosensing experiments were conducted in 1983, where SPR was proposed to be suitable to be used as an immunosensing technique (Liedberg et al., 1995, 1983). An immunoglobulin was reported to be spontaneously adsorbed on a silver metal layer. Upon addition of an antibody analyte, a change in reflection intensity was recorded due to binding of the antibody to the bound immunoglobulin. A small flow cell volume made it possible to detect the very low analyte concentration. These initial experiments have improved and are used in a variety of assay systems, based on selective interaction analyses. Masses and consequently analyte concentrations can be determined by dynamic monitoring of direct binding to immobilised target molecules (Fig. 10a), sandwich assays with the addition of second antibodies (Fig. 10b) or inhibition assays (Fig. 10c). The possible versatility of SPR devices can be utilised to sense for example contaminations, toxic substances, drug targets in many areas of industry, health care and research. Comprehensive reviews exist for all mentioned research fields (Homola, 2003; van Regenmortel et al., 1998). In these applications the kinetic constants of target molecules can be calculated due to the possibility of dynamic observation such as effects on the plasmon resonance. Thereby, interaction analyses and calculations of binding constants are not restricted to immunosensing or small molecules.

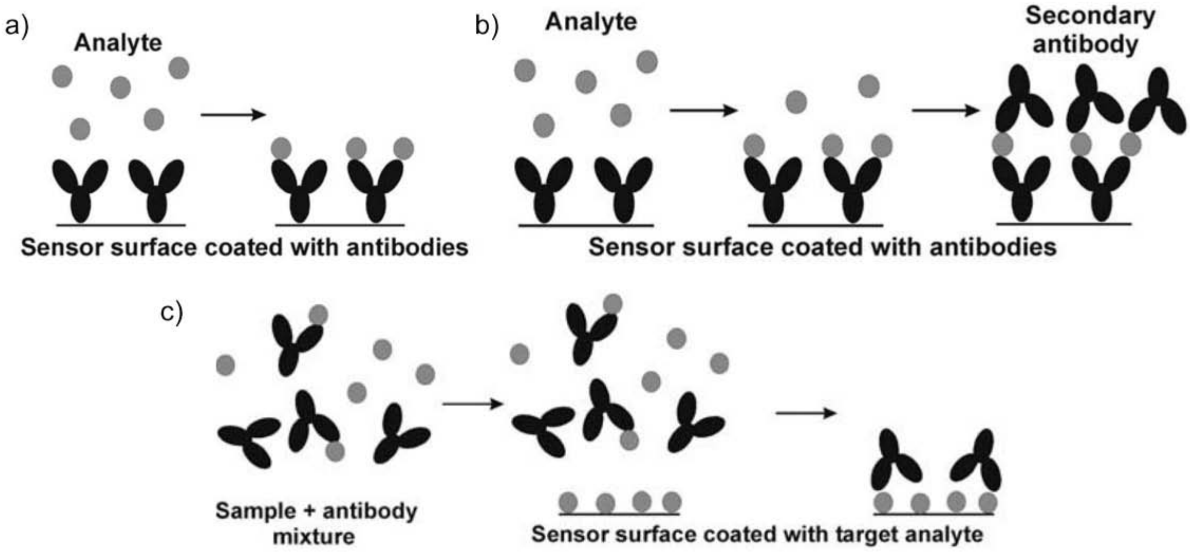

Figure 10: Common types of assays using antibody recognition with SPR. a) Direct binding. Antibodies are adsorbed on the surface and specifically bind analytes from bulk medium. b) Sandwich assay. Secondary antibodes bind to the first antibody-analyte complex to increase the sensed material per bound molecule of analyte. c) Indirect (competitive) binding assay. Solution with analyte and antibody is added to analyte coated surface. Antibodies that have free binding sites adsorb to the surface (Homola, 2003).

DNA–protein interactions are widely described (Majka and Speck, 2007). In this case DNA molecules are bound to the surface and protein binding is monitored, for example potential DNA-binding drugs (Lin et al., 2005). Even the detection of blood plasma coagulation (Vikinge et al., 2000), viral (Boltovets and Nesterova, 2006; Amano and Cheng, 2005; Dubs et al., 1992) as well as bacterial (Perkins and Squirrell, 2000) targets have been reported providing evidence that SPR can be useful for fast detection of contents and characteristics of blood or environmental samples. The potential is further increased through the development of mobile devices relying upon miniaturised sensors (Soelberg et al., 2005) and the use of fibre optics (see Homola, 2003), and consequently the manufacturing of devices with multi-channel detection units (Homola et al., 2005).

Mono- and bilayers

It is the dynamic monitoring of kinetic binding parameters that attracts the focus of a vast amount of researchers to SPR, namely within the fields of food analysis, proteomics, immunogenicity and drug research (Karlsson, 2004). Many important interactions however take place in cell membranes. Membrane proteins show unique behaviour and properties only when incorporated within a membrane. It is therefore necessary to mimic native conditions in *in vitro* studies as much as possible. Many membrane models such as supported monolayers (Fig. 11a) or bilayers, tethered lipid membranes (Fig. 11b), or liposomic monolayers (Fig. 11c-f) have been developed and also proven to be useful with SPR setups (Mozsolits et al., 2003). In these cases SPR spectra can be evaluated by applying thin-film theory based on Maxwell's equations (Salamon et al., 1997a,b). Here membranes as well as incorporated and peripheral bound proteins used as analytes are expressed in terms of different layers with respective values of refractive indexes, extinction coefficients and thicknesses (see Fig. 12a). These are determined by fitting model equations to the obtained spectra. It was also shown that a dielectric layer such as SiO_2 on top of the metal layer can be used to couple both p- and s-polarised light with two distinct SP excitations (Salamon and Tollin, 2001). This so called coupled plasmon-waveguide resonance is used to get information about anisotropic characteristics of the analysed layer due to structural changes (Salamon et al., 1999), for example light induced binding of the G-protein transducin to the photoreceptor rhodopsin (see Fig. 12b). Rhodopsin was already studied earlier (Heyse et al., 1998). In addition, binding events of other G-protein coupled receptors have been monitored by SPR (Alves et al., 2005; Stenlund et al., 2003). Mozsolits et al. explored and reviewed peptide–membrane binding characteristics on supported layers (Mozsolits and Aguilar, 2002; Mozsolits et al., 2001). The possibility to study the kinetics of peptide interactions, for example anti-microbial peptides like melittin, with membranes makes SPR a very important tool in the search for antibacterial drugs. Other authors used liposomes to measure the affinity of potential drug compounds to membranes (Beseničar et al., 2006; Frostell-Karlsson et al., 2005; Abdiche and Myszka, 2004). Riesner, Otto and Zerulla suggested to use surface plasmon enhanced Raman scattering to monitor conformational changes of prion proteins embedded in membranes (Zerulla et al., 2003). Apart from rapid drug screenings, the determination of the stability of drug–membrane connections can also be used to develop new methods for drug targeting via liposomes. Furthermore SPR has been combined with consecutive methods, such as surface plasmon enhanced fluorescence spectroscopy ((Lakowicz, 2006)) in order to improve tracking of molecules within membranes (Wiltschi et al., 2006), mass spectrometry to identify structural features of incorporated proteins (Nedelkov and Nelson, 2003), or monitoring of high density layers of channel-forming proteins, which would increase the response to ion concentration or ligand binding (Terrettaz et al., 2002).

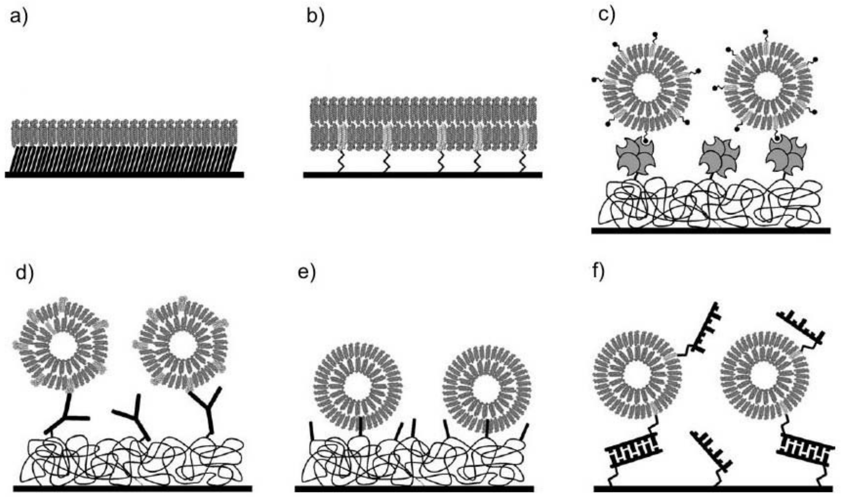

Figure 11: Various membrane models used to measure protein–membrane interactions with SPR. a: Supported lipid monolayers. b: Tethered lipid bilayers. c: Coating with liposomes, immobilised through biotin-avidin binding. d: Coating with liposomes, immobilised by binding of incorporated lipopolysaccharides to antibodies attached to the surface. e: Coating with liposomes, immobilised by protruding lipophilic groups covalently bound to the surface. f: Coating with liposomes, immobilised by hybridisation of DNA strands, of which one is bound to the surface and one to a derivatised liposome (Beseničar et al., 2006).

3.2 Detection of light scattered by nanoparticles

NPs are not only used for imaging purposes but also for prospective medical and research applications, for example targeted drug release through heating or as contrast agents and in cell sorting arrays due to their magnetic properties (Sharma et al., 2006; Sonvico et al., 2005). Microscopic techniques could have been improved using the special scattering properties of NPs. As NPs display a unique color when illuminated by white light which has been explained in a previous section of this review. Possible shifts in intensity and in bandwidth pattern of the scattered light are exploited in different ways. First, the absorption peak shift can be measured upon binding of biomolecules to the NP surface. The Optical properties are subject to the amount of bound material. Proofs of principle are provided in several articles (Nath and Chilkoti, 2002; Eck et al., 2001; Englebienne, 1998). Second, biomolecules can be labeled by NPs and directly tracked on a level of single molecule imaging (Yguerabide and Yguerabide, 2001, 1998b), or used as a probe for specific cells. The latter effect has been utilised to monitor disruption of bacteria by potential antimicrobial drugs (Kyriacou et al., 2004) and specific binding of antibody-labeled NPs to cancerous cells (El-Sayed et al., 2005; Sokolov et al., 2003). El-Sayed et al.

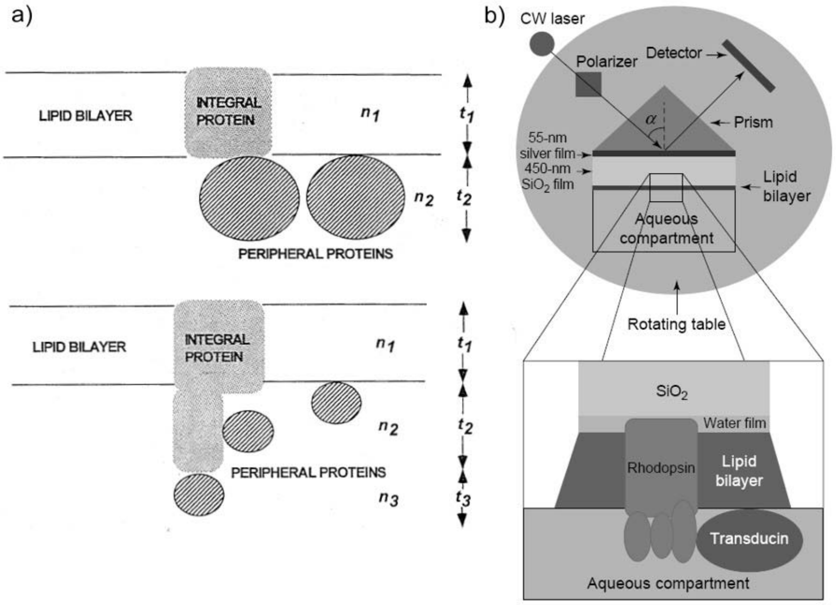

Figure 12: Illustration of thin-layer model to analyse SPR spectra of surfaces coated with different layers of lipids and proteins. a: Difference of integral membrane and peripheral proteins. Supported membranes and each possible analyte consitute a separate layer with optical parameters evaluated with the theoretical model. (Salamon et al., 1997b) b: Configuration of a coupled plasmon-waveguide resonance setup. A second layer of dielectric (in this case SiO_2) is put on top of the metal layer. It couples s-polarised light to the excitation of a second distinct SP, which makes it possible to determine structural changes du to transducin binding to rhodopsin (Salamon et al., 1999).

used NPs conjugated with anti-epidermial growth factor receptor antibodies and could show by imaging with a conventional light microscope that labeled NPs specifically bind to the outer side of oral cancer cells (Fig. 13). A third kind of approach is similar to the second. It consists of detecting target molecules but mostly uses the shift of peak intensities due to coagulation of NPs upon specific binding with conjugated molecules, with the optical properties and melting conditions being described elsewhere (Niemeyer, 2001; Jin et al., 2001). In regard to possible applications it has led to new DNA detection assays.

New microarray and DNA mismatch detection methods

Microarrays have been employed to analyse protein levels, cells and a variety of other biomolecules (Stears et al., 2003). The most important application has been the study of gene expression levels in cells of certain tissues or organisms. For this, an array of DNA oligomers is spotted onto a slide with each molecule complementary to a part of a target gene. For the conventional microarray setup, mRNA has to be reversely transcribed into copy DNA. The products must be conjugated to probe molecules, mostly fluorescent dyes. A set of control and sample DNA, both linked to two different dyes, is then added to the array of complementary DNA strands. Subsequently this array has to be read out in a

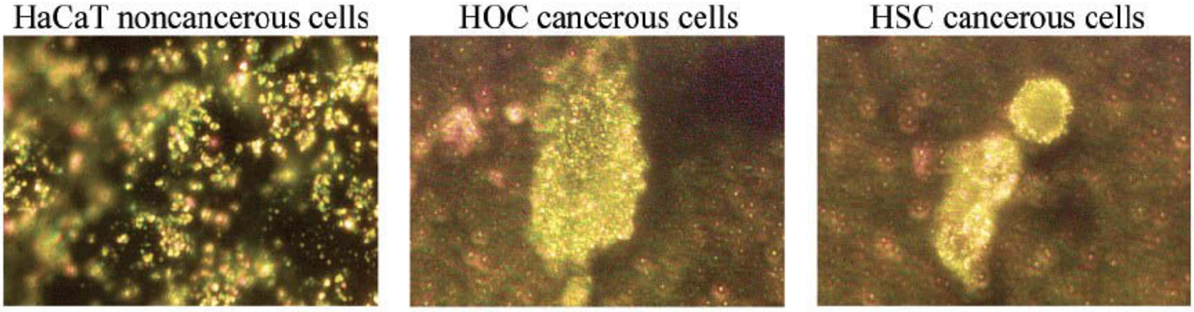

Figure 13: Different binding of antibody-labeled NPs to the epidermial growth factor receptor of one noncancerous (HaCaT) and two cancerous cell lines (HOC and HSC). One can clearly distinguish between the benign and malignant cells. Conjugated NPs bind specifically to the antigen of the target receptor, which is more abundantly expressed in cancer cells (El-Sayed et al., 2005).

laser scanner. Depending on which type of DNA is more abundant for one gene, more molecules of this type bind in the corresponding spot. The conjugated dye of this type of DNA is then seen over the dye of the other type.

This extensive procedure is very complex and special scanners have to be used in a time consuming process to detect DNA hybridisation. Moreover it is dependant on fluorescence with the drawback of possible photo bleaching. NPs offer another method of detecting specific DNA binding. DNA oligomers can be be linked to NPs by adding a thiol group, which goes into a stable covalent bond with gold. Binding was even further stabilised by introducing multiple thiol anchors (Li et al., 2002). It has been documented that these single complexes can bind to immobilised complementary DNA and detected by scattered light of the NPs with white light illumination (see Fig. 14a). Several authors have illustrated that very specific binding occurs (Köhler et al., 2001; Reichert et al., 2000). Other groups used nucleotide targets to link particle conjugates to colloid assemblies (Thaxton et al., 2006; Taton et al., 2000). As illustrated in Fig. 14b the resonance peak of the scattered light undergoes a red-shift. This shift can be detected in response to a very low amount of oligonucleotides of ≈ 10 fmol (Elghanian et al., 1997), which makes it a more sensitive technique than conventional fluorescent labeling (Bao et al., 2002). Furthermore all groups have demonstrated that melting of NP colloids occurs in a very low temperature range (see Fig. 14b). Thus, hybridisation can be controlled very precisely by adjusting the temperature. Beyond that, the melting conditions are subject to perfect binding, i.e. a single mismatch can cause the melting temperature to decrease significantly. NPs therefore promise to be useful in detection of selective detection of sequence differences such as single nucleotide polymorphisms (Storhoff et al., 1998).

Microarrays of NP linked DNA molecules can be read out without fluorescent labeling using a flatbed scanner or a setup with a conventional microscope. Furthermore NPs are more photostable than fluorescent dyes. Another group (Chen et al., 2005) combined

SPR to phase-shift interferometry and further improved the resolution and possible high-troughput screenings.

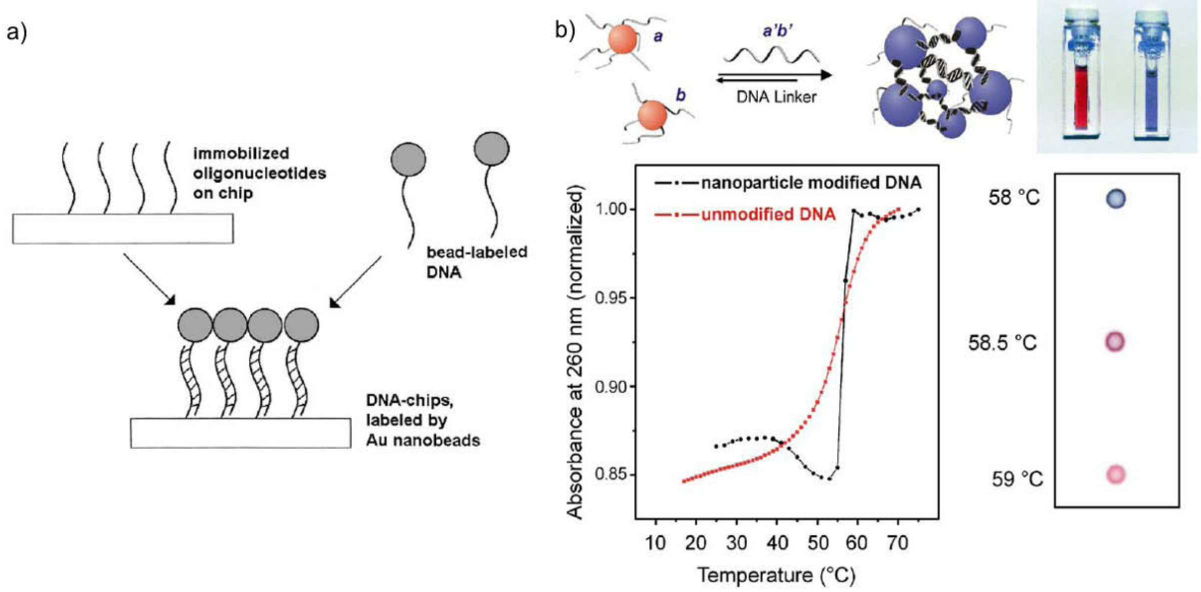

Figure 14: Possible detection of target DNA molecules by binding to NPs linked to probe DNA. a) Simple hybridisation of NP conjugates to surface bound target DNA. Hybridisation events are then detected due to scattered light by bound particles (Köhler et al., 2001). b) Assembly to NP colloids. Target DNA serves as a linker between complementary strands that are linked to the NPs. SPWs are coupled within this assembly, which alters the optical properties, and a red-shift of resonance peak is observed. The stability is very sensitive to temperature changes near the melting temperature (Thaxton et al., 2006).

3.3 Effects on molecules in close proximity to metals

Apart from direct measurements of NP scattered light, SP excitation is used to couple different probing mechanisms. The near-field of SPs in the vicinity of metal surfaces can substantially enhance the efficiency of electronical or vibrational transitions. The first is used for surface-enhanced fluorescence (SEF) and the latter for surface-enhanced Raman spectroscopy (SERS). There is a detailed theoretical understanding of both mechanisms. Recent publications report on new techniques to improve single molecule detection. Kühn et al. suggest to place a NP near a fluorescent molecule with a scanning probe cantilever tip (Kühn et al., 2006) whereas Enderlein used calculations for metal nanocavities with a fluorophore inside (Enderlein, 2002a,b). Both approaches predict an increase in fluorescent brightness by one order of magnitude. For single molecule SERS, taking only electromagnetic enhancement into acount, it was shown that a very high field enhancement of the order of 10^{11} is necessary (Xu et al., 2000). Such high enhancement is achieved within so-called “hot spots”, which are small areas between particle aggregates where coupling of SP excitation occurs. Le Ru et al. presented ways of how to analyse the phenomenology

of single molecule SERS and discussed ways of how to overcome the problem to attain presence of a single molecule within a hot spot (Le Ru et al., 2006).
Nanostructured surfaces are another possibility to tailor the EM near-field of surface plasmons. Recent developments have shown that complex structures can be created on surfaces by chemical self-assemling techniques and different types of lithographie (E-beam, scanning probe, X-rays). Ebbesen et al. have reported extraordinary, surface plasmon supported transmission through nanoholes and nanoslits (Barnes et al., 2003; Ebbesen et al., 1998; Lezec et al., 2002). An entirely different approach is the tailoring of SP properties such as group velocity, dispersion and localisation by using a tuneable, adaptive surface. Here the nanostructured surface is made from metallic nanowires, embedded onto a stretchable polymer which allows for rapid changes of the periodicity of the system (Rehwald et al., 2007).

However, benefits of near-field enhancement are not restricted to single molecule detection. More general effects on fluorescence and RS as well as interesting benefits are widely discussed, which are shortly reviewed in the following two paragraphs.

Enhanced fluorescence

Much of the recent work on SEF has been carried out by Geddes, Lakowicz et al. (Geddes and Lakowicz, 2002; Geddes et al., 2004; Lakowicz, 2006, 2005, 2004, 2001). Theoretical derivations as well as proposed and conducted experiments are comprehensively reviewed in these articles. Possible interactions of fluorophores with a metal surface are summarised in Fig. 15a. Several possibilities of excitation and emission processes exist. First, a fluorophore can be excited by direct absorption of incident photons. Second, in close proximity to the metal on the side of the excited SP (for example using a glass prism in the Kretschmann configuration) the fluorescent molecule can interact with the near-field of the plasmon or with a photon emitted by the plasmon. Finally, the concentrated field near a NP or flat metal surface could cause energy transfer to the fluorophore. It was shown recently that this is indeed the case (Lakowicz, 2004; Isfort et al., 2006a,b). Above that, it was not clear whether the detected red-shifted light was coming through an entirely coherent process or whether it was generated in a two step process where a first SPP excitation has excited the fluorophore. The fluorecent photons from that process have triggered a second SPP process which emits back to the excitation side under changed SP conditions. However, the observation of hollow emission cones (see Fig. 15b) led to the assumption that light is detected via plasmon excitation that itself radiates light into the substrate, which is called surface plasmon-coupled emission (SPCE) (Lakowicz, 2006). Thus, fluorescent light is not isotropically detected. Excitation of an SP must satisfy the condition of wave vector matching. Thus the angle of the cone to the surface normal is found to be wavelength dependant, i.e. is shifted in relation to the angle of the incident light. Light from fluorophores of different wavelengths can therefore be distinguished by different angles of the cone, which could lead to more sensitive detection methods. The most important parameter for the observation of this effect however is the distance between the surface and fluorescent molecules (Geddes and Lakowicz, 2002; Geddes et al., 2004). Within a range of 5 nm distance non-radiative quenching by the metal predominantly causes transition to the ground state. Energy transfer for SP excitation occurs from a further distance. It is dependant on the presence of the fluorophore within the evanescent field and on the efficiency of coupling.

Several advantages over conventional fluorescence have been predicted. According to Lakowicz ultrabight probes with an 1000-fold increase of fluorescent intensity might be possible (Lakowicz, 2006). Such an increase would be due to two effects (Enderlein, 2002b). First, the presence of a very strong field leads to more excitation transitions and hence to higher brightness. Second, the lifetime of an SP is much lower than that of the excited electronical state of the fluorophore. Energy transfer to the metal and subsequent reemission therefore occurs much faster, which results in an increase of the fluorescent decay rate. One molecule can be excited more often within a certain time interval. Above that the latter effect therefore decreases photobleaching.

In spite of the comprehensive theoretical understanding of SEF not too many experimental results have been presented so far. Fluorescein-labeled oligonucleotides (Zhang et al., 2005) and a phenyl-phenanthridine dye (Zhang and Lakowicz, 2005) on silver NPs were examined in exemplary experiments. The enhancements were found to be only two-fold and three-fold respectively. One of the first applications of SEF was conducted for the study of muscle (Borejdo et al., 2006). It was successfully shown that SPCE was of the order of one magnitude higher than normal fluorescent emission. A further interesting approach was described in 2006 (Kasry and Knoll, 2006). It was suggested and experimentally shown with labelled antibodies that long range surface plasmons can be created. SPs were excited on both sides of a thin metal layer. The overlap of their fields resulted in two new coupled modes, one short range and one long range mode. The latter penetrates much further into the substrate thereby increasing the depth of detectable enhanced fluoroescence.

Raman spectroscopy and SERS

Biological molecules such as proteins, DNA and lipids show characteristic Raman spectra. It has been demonstrated that it is possible to use fingerprint spectra to distinguish between healthy and diseased animal or human tissue. Such analyses are mostly based on quantitative determination of molecule types in different tissues (Mahadevan-

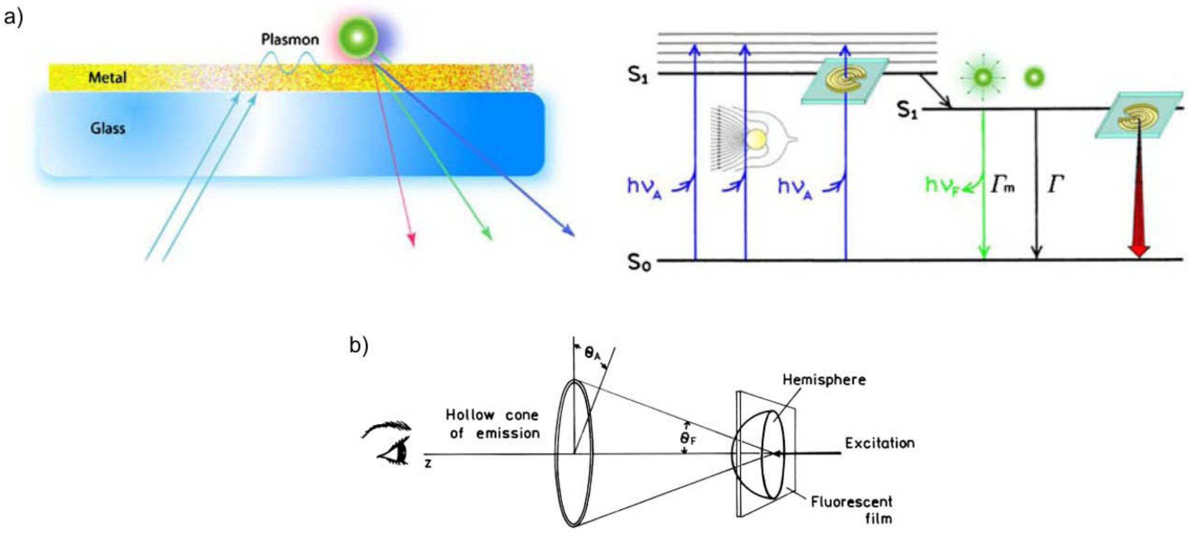

Figure 15: The suggested model of surface enhanced fluorescence. a) Fluorophores in close proximity to a metal surface and an SP are excited by energy transfer from the near-field. Transition to the ground state can occur via "normal" decay Γ or via a second coupling, i.e. excitation of a SP and reemission into the substrate with a much faster decay rate Γ_m. The latter process must satisfy the condition of wave vector matching, which leads to the emission of a hollow cone. The angle of the cone is therefore dependent on the magnitude of the red-shift of fluorescent light. (Lakowicz, 2006) b) Illustration of the surface plasmon-coupled cone (Lakowicz, 2004).

Jansen and Richards-Kortum, 1996). For possible applications in this field non-enhanced Raman spectroscopy is used. The reader is therefore referred to other reviews that exhaustively discuss clinical implementation of RS in general (Choo-Smith et al., 2002), studies of protein, DNA as well as lipid alterations and connected shifts of Raman spectra (Mahadevan-Jansen and Richards-Kortum, 1996), the combination of RS with optical tweezers to selectively identify viral particles (Lambert et al., 2006), and improved techniques for *in vivo* detection of diseased cells such as malignant or pre-malignant tissue via fiber optic probes. However, before we start to discuss SERS and its impact on biological or clinical applications the reader should note that besides SERS additional signal enhancement techniques are available in form of Resonance Raman spectroscopy (RRS). In RRS the excitation wavelength is tuned to match the optical absorption of the molecular group of interest. This enhances the cross section of the Raman process several order of magnitude and has been used by T. Spiro et al. and G. Thomas et al. to investigate complex proteins (Spiro, 1988; Spiro and Strekas, 1972; Benevides et al., 1996). In order to investigate the conformation of proteins the exciting laser source needs to emit into the chemical groups near the peptide bounds. Their absorption lies in the ultraviolett region between 190 nm an 220 nm. S. Asher et al. have used this technique to determine the secondary structural content of polypeptides and have shown that for such systems the average secondary structure can be investigated (Mikhonin et al., 2006,?; Asher, 2001;

Chi et al., 1998).
The implementation of SERS for *in vivo* measurements is still in its infancy as possible procedures are subject to extensive preparation steps such as adsorbing sample molecules to metallic objects. Stuart et al. implanted a glucose sensor with an optical path into a rat (Stuart et al., 2006). The sensor consisted of a flat gold surface functionalised with a mixed alkanethiol SAM. Glucose can partition in to and out of the SAM. SERS spectra of glucose are analysed to determine the blood glucose concentration of the rat.

There are however numerous approaches for fundamental studies and detection arrays, which have already been discussed (Willets and Van Duyne, 2007; Talley et al., 2004). SERS was for example used to detect the amount of redox enzymes in the outer membrane of a gram negative bacterium (Biju et al., 2007). Occurences of nanoscale domains were monitored with the help of distinctive Raman spectra determined for small focus areas. Together with topographic information from AFM data this technique promises to be informative for the study of mechanisms for the respiratory chain. Another group proved that membrane molecules of *E. coli* serve as nucleation centers for silver colloids (Efrima and Bronk, 1998). The silver coating was enough to enhance the Raman signal in order to obtain main bands specific for proteins and membrane molecules. Sengupta et al. pointed out that recording Raman fingerprints of bacteria can be used as a feasible technique for the detection of possible pathogens from samples with a concentration of down to $\approx 10^3$ cfu/ml (Sengupta et al., 2006).

Not only are membrane molecules in the focus of interest but membranes are also used as a model barrier to determine diffusion constants of potential drugs. Wood et al. examplarily measured the diffusion of pyridine through a Silastic membrane by placing silver NP colloids on the other side of the membrane (Wood et al., 1997). The most promising results have been obtained for experiments with DNA molecules. DNA can be connected to a variety of fluorescent dye molecules exhibiting Raman activity. Possible dyes for resonance Raman spectra, i.e. SERRS experiments are described (Graham et al., 2006; Faulds et al., 2005). Recently the same authors demonstrated that simultaneous binding of DNA probes labeled with five different dyes to target DNA can be monitored via dual-wavelength excitation (Faulds et al., 2007). Distinctive Raman shifts for the dyes were quantitatively evaluated in these experiments in which resonance excitation was used. So called multiplexed analysis was also conducted with ‘normal’ SERS (Cao et al., 2002). Labeled DNA oligomers were coupled to 13 nm gold NPs and added to a system of target DNA bound to a silver layer (Fig. 16a). The diameter of the NPs was to small to give strong enough scattering or Raman enhancing. Only in close proximity to the silver surface, i.e. upon hybridisation, could binding within spots as well as Raman signals of the dye be detected by a flatbed scanner or by single laser excitation respectively (Fig. 16b). Subsequently, six different probe DNA oligomers of various viruses were labeled with six different dyes showing distinctive Raman spectra (Fig. 16c). In several experiments mixtures of all probes were added to chips with all or systematically removed targets. In (Fig. 16d) the results are presented. No false-positives or false-negatives were observed and bound probe DNA was explicitly identified by analysis of the obtained Raman spectra. According to the authors, the unoptimised detection limit was 20 fM. Combined with competitive binding and processing of a single Raman spectrum this methode promises to dramatically improve microarray analyses. In another approach, SERS was used to specifically detect viral DNA with a complementary, labeled hairpin structure coupled to a silver NP (Wabuyele and Vo-Dinh, 2005). The label is in close proximity of the metal surface when the hairpin structure is intact. When complementary, viral DNA is present, the target hairpin changes to a straight conformation and the signal is diminished (Fig. 17). Finally, Kneipp et al. proved that single DNA base molecules can be detected when bound to silver NPs (Kneipp et al., 1998). Further developments of this approach could lead to a new sequencing strategy where single cleaved nucleotides could be instantly detected, e.g. within a flowing stream of colloidal solution.

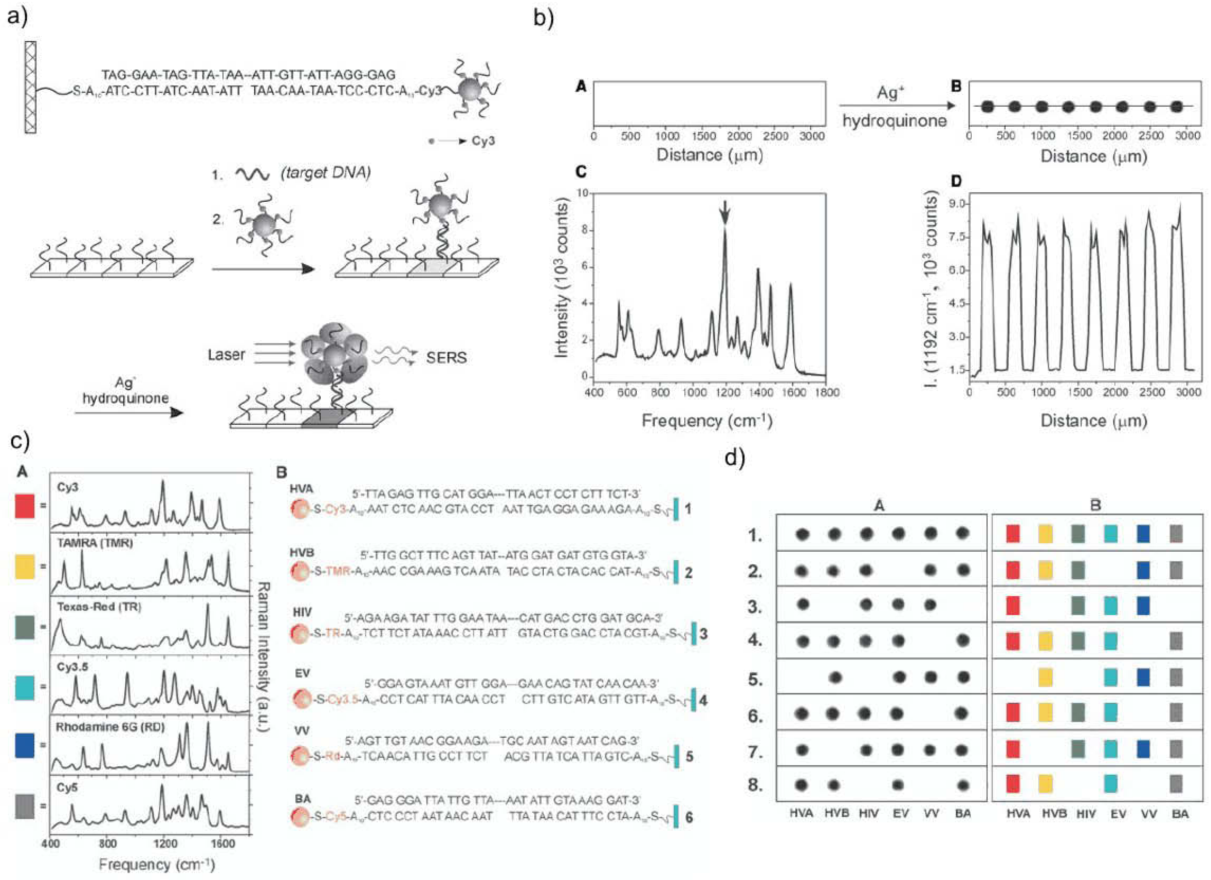

Figure 16: Detection of labeled DNA with SERS. a: Sandwich assay with NP mediated binding of probe to target DNA. The latter is bound to a silver surface, which is responsible for enhancement of the Raman signal. b: Scattered incident and Raman light are only detectable when dyes are in close proximity of the silver surface, i.e. when hybridisation occurs. c: Six different dyes were used and are distinguishable due to their different Raman spectra. d: No false-positives or false-negatives were observed in experiments with various target DNA sequences. Distinctive labels and consequently DNA molecules were detected by analysing the Raman signals, which is shown in the colour encoded table (Cao et al., 2002).

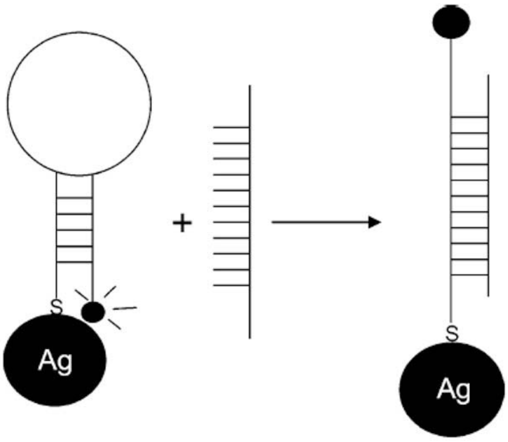

Figure 17: Illustration of the detection of viral DNA. A complimentary hairpin DNA strand is coupled to a metal NP and labeled with a Raman active dye. In case probe DNA is present it binds to the hairpin structure. This causes a breakup and stretching of the hairpin. The dye is not in close proximity anymore, which is why the Raman signal diminishes due to less enhancement (Wabuyele and Vo-Dinh, 2005).

4 Towards future applications with two-photon processes

During the last decade multiphoton spectroscopy has gained a lot of attention due to its unique advantages for studying living systems. Although as a nonlinear process a high power excitation laser (typically in the femrosecond range) is involved, multiphoton fluorescence has been extensively used (So et al., 2000; Mertz et al., 1995). As two photons are absorbed simultaneously, near-IR light can be used for excitation in the visible or even UV range, which causes much less photodamage. Furthermore the laser power is only high enough in a very small focal volume so that photobleaching is depleted and image contrast increased. Only molecules in the focus area are excited and recorded. It is however still necessary for multiphoton fluorescence to introduce dye molecules to the examined system or to bind target compounds to fluorescent probes. Dyes can have effects on the properties of the system, or even produce or degrade to toxic substances and can therefore cause photodamage.

Here too, surface plasmon enhanced techniques have been proposed to be used to intensify fluorescence (Kano and Kawate, 1996). Alternatively, there have been approaches to circumvent the need to alter native composition and at the same time take advantage of multiphoton excitation processes. Hyper-Raman and anti-Stokes scattering have been described nearly as early as conventional RS (compare Smith and Dent, 2005). Due to recent advancements in laser technology, both techniques have been brought into focus again for applications in biology.

4.1 Hyper-Raman and anti-Stokes scattering

Techniques for imaging vibrational states like IR spectroscopy and RS are possibilities to use intrinsic emission properties of sample compounds. However, the resolution of the former is limited by the long wavelength of utilised light. In the absence of additional enhancement techniques in order to gain strong Raman signals high laser power is necessary, or compounds have to be bound or brought into close proximity of metal surfaces. In normal Raman spectra anti-Stokes lines can be identified but these signals are usually very weak as higher vibrational levels are not sufficiently occupied and overlied by fluorescence background. Coherent anti-Stokes scattering (CARS) is a technique that creates stronger anti-Stokes signals and has proven to be useful for imaging purposes. CARS is a four-wave mixing nonlinear process (for excellent reviews on the theory and instrumentation see Rodriguez et al., 2006; Cheng and Xie, 2004; Holtom et al., 2001), which is why it exhibits all advantages of multiphoton imaging. Moreover stimulated emission is involved in the creation of anti-Stokes radiation. Thus, CARS signals are anisotropically emitted and enhanced by resonant emission events. This method was first applied for sectioned imaging of live cells in 1999 (Zumbusch et al., 1999). Since then it has been shown that the vibration of aliphatic C-H bonds give rise to CARS signals strong enough to image compartments and cells by its surrounding membranes. CARS of liposomes (Cheng and Xie, 2004; Nan et al., 2003), axonal myelin (Wang et al., 2005) and expansion of cells in a collagen matrix (Kaufman et al., 2005) have been observed. In Fig. 18a-d CARS images of different sections of mouse fibroblast cells are presented. Membranes of the nucleus and mitochondria are distinguishable from the cytoplasm. The mitochondria were labeled with a fluorescenct dye and it was shown that compared to a simultaneously taken CARS image (Fig. 18e-f) similar structures are resolved. Other CARS techniques have been applied. Cheng et al. used only epi-detected, backscattered radiation (E-CARS) to reduce contributions of solvents (Cheng et al., 2001). Less abundant small objects with weak signals can be detected with this method as radiation from solvents and molecules in excessive amounts interacts over a long range and therefore is predominantly emitted forwards. In multiplex CARS the broadened bandwidth of ultra-short laser pulses was used to detect multiple Raman spectral lines (Wurpel et al., 2005).

In 1988 pyridine was shown to give a hyper-Raman signal (Golab et al., 1988). In hyper-Raman scattering, Raman spectra are recorded but excitation occurs via two-photon absorption. The cross-section is of 35 orders of magnitude smaller than for normal Raman scattering. It is discussed that surface enhancement has a much greater effect on hyper-Raman signals due to non-linear responses, which is why it is suggested to be used as another multiphoton technique for biological imaging (Kneipp et al., 2006).

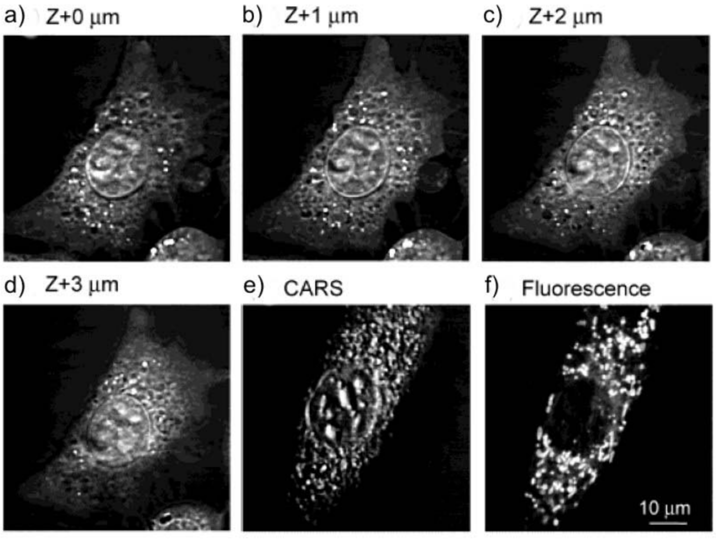

Figure 18: CARS images of fibroblast cells revealing structures surrounded by membranes. The incident wavelength was adjusted so that aliphatic C-H bonds are excited. a-d: Images of different depths. e-f: CARS image compared to same section recorded with fluorescence labeled mitochondria (Cheng and Xie, 2004).

5 Conclusions

This review has summarised recent developments in scattering and spectroscopic techniques using excitation of SPs on metal surfaces and the effects of their electromagnetic near-field on molecules in the vicinity. Raman scattering, Mie scattering and fluorescence are well-described phenomena and have been extensively used over the last several decades. Light scattering theory of NPs is extended to determine compounds bound to the surface by detecting scattered light in the visible range. Raman and fluorescence signals are dramatically enhanced near an excited SP. Such strong responses have been proven to be useful to decrease detection limits and increase resolution of analyte detection. There is strong evidence for NPs to be the next-generation labeling technique for bio-diagnostic research. Enhancement effects and narrow bandwidths of spectroscopic fingerprints will replace elaborate preparation methods of today's approaches for measuring single molecules such as DNA and proteins up to larger objects like viruses and bacteria. Thus, nanophysical techniques will considerably influence biological applications for diagnosis and fundamental research.

References

Abdiche, Y. N. and D. G. Myszka (2004). Probing the mechanism of drug/lipid membrane interactions using biocore. *Analyt. Biochem. 328*, 233–243.

Alves, I. D., C. K. Park, and V. J. Hruby (2005). Plasmon resonance methods in gpcr signaling and other membrane events. *Curr. Protein Pept. Sci. 6*(4), 293–312.

Amano, Y. and Q. Cheng (2005). Detection of influenza virus: traditional approaches and development of biosensors. *Anal. Bioanal. Chem. 381*, 156–164.

Anderson, M. (2000). Locally enhanced raman spectroscopy with an atomic force microscope. *Appl. Phys. Lett. 76*, 3130.

Asher, S. (2001). Uv resonance raman spectroscopy. *John Wiley, New York 1*, 557–1571.

Aslan, K., J. R. Lakowicz, and C. D. Geddes (2005). Plasmon light scattering in biology and medicine: new sensing approaches, visions and perspectives. *Curr. Op. Chem. Biol. 9*, 538–544.

Banwell, C. N. and E. M. McCash (1994). *Fundamentals of molecular spectroscopy.* Cambridge: McGraw-Hill Publishing.

Bao, P., A. G. Frutos, C. Greef, J. Lahiri, U. Müller, T. C. Peterson, L. Warden, and X. Xie (2002). High-sensitivity detection of dna hybridization on microarrays using resonance light scattering. *Anal. Chem. 74*(8), 1792–1797.

Barnes, W. L., A. Dereux, and T. W. Ebbesen (2003). Surface plasmon subwavelength optics. *Nature 424*, 824–830.

Benevides, J., T. Terwilliger, S. Vohník, and G. Thomas (1996). Raman spectroscopy of the ff gene v protein and complexes with poly(da): Nonspecific dna recognition and binding. *Biochemistry 35*(29), 9603.

Beseničar, M., P. Maček, J. H. Lakey, and G. Anderluh (2006). Surface plasmon resonance in protein–membrane interactions. *Chem. Phys. Lip. 141*, 169–178.

Biju, V., D. Pan, Y. A. Gorby, J. Fredrickson, J. McLean, D. Saffarini, and H. P. Lu (2007). Combined spectroscopic and topographic characterization of nanoscale domains and their distibutions of a redox protein on bacterial cell surfaces. *Langmuir 23*(3), 1333–1338.

Boltovets, P. M. and N. V. Nesterova (2006). Use of the surface plasmon resonance method for the virological investigations. *Mikrobiol. Z. 68*(3), 86–98.

Borejdo, J., Z. Gryczynski, N. Calander, P. Muthu, and I. Gryczynski (2006). Application of surface plasmon coupled emission to study of muscle. *Biophys. J. 91*(7), 2626–2635.

Bouhelier, A. (2006). Field-enhanced scanning near-field optical microscopy. *Microsc. Res. Tech. 69*, 563–579.

Brown, K. R., D. G. Walter, and M. J. Natan (2000). Seeding of colloidal au nanoparticle solutions. 2. improved control of particle size and shape. *Chem. Mater. 12*(2), 306–313.

Brunner, R., A. Bietsch, O. Hollricher, and O. Marti (1997). Distance control in near-field optical microscopy with piezoelectrical shear-force detection suitable for imaging in liquids. *Rev. Sci. Instrum. 68*(4), 1769–1772.

Brust, M., M. Walker, D. Bethel, D. J. Schiffrin, and R. Whyman (1994). Synthesis of thiol-derivatised gold nanoparticles in a two-phase liquid-liquid system. *J. Chem. Soc., Chem. Commun. 1*, 801–803.

Campion, A. and P. Kambhampati (1998). Surface-enhanced raman scattering. *Chem. Soc. Rev. 27*, 241–250.

Cao, Y. C., R. Jin, and C. A. Mirkin (2002). Nanoparticles with raman spectroscopic fingerprints for dna and rna detection. *Science 297*, 1536–1540.

Chen, S.-J., Y.-D. Su, F.-M. Hsiu, C.-Y. Tsou, and Y.-K. Chen (2005). Surface plasmon resonance phase-shift interferometry: Real-time dna microarray hybridization analysis. *J. Biomed. Opt. 10*(3), 1–6.

Cheng, J.-X., A. Volkmer, L. D. Book, and X. S. Xie (2001). An epi-detected coherent anti-sokes raman scattering (E-CARS) microscope with high spectral resolution and high sensitivity. *J. Phys. Chem. B 105*(7), 1277–1280.

Cheng, J.-X. and X. S. Xie (2004). Coherent anti-stokes raman scattering microscopy: Instrumentation, theory, and applications. *J. Phys. Chem. B 108*(3), 827–840.

Chi, Z., X. Chen, J. Holtz, and S. Asher (1998). Uv resonance raman selective amide vibrational enhancement: Quantitative methodology for determining protein secondary structure. *Biochemistry 37*, 2854–2864.

Choo-Smith, L.-P., H. G. M. Edwards, H. P. Endtz, J. M. Kros, F. Heule, H. Barr, J. S. Robinson, H. A. Bruining, and G. J. Puppels (2002). Medical applications of raman spectroscopy: from proof of principle to clinical implementation. *Biopolymers 67*, 1–9.

Daniel, M.-C. and D. Astruc (2004). Gold nanoparticles: Assembly, supramolecular chemistry, quantum-size-related properties, and applications toward biology, catalysis and nanotechnology. *Chem. Rev. 104*(1), 293–346.

de Lange, F., A. Cambi, R. Huijbens, B. de Bakker, W. Rensen, W. Garcia-Parajo, N. van Hulst, and C. G. Figdor (2001). Cell biology beyond the diffraction limit: near-field scanning optical microscopy. *J. Cell Science 114*(23), 4153–4160.

Doyle, G., B. Ashall, M. Galvin, M. Berndt, S. Crosbie, and D. Zerulla (2007). Mie scattering and surface plasmon based spectroscopy for the detection of nanoparticle-protein interactions. *Appl. Phys. in print.*

Dubs, M. C., D. Altschuh, and M. H. van Regenmortal (1992). Mapping of viral epitopes with conformationally specific monoclonal antibodies using biosensor technology. *J. Chromatogr. 597*(1-2), 391–396.

Dunn, R. (1999). Near-field scanning optical microscopy. *Chem. Rev. 99*(10), 2891–2927.

D.W., P., W. Denk, and M. Lanz (1984). Optical stethoscopy - image recording with resolution lambda/20. *Appl. Phys. Lett. 44*(7), 651–653.

Ebbesen, T., H. Lezec, H. Ghaemi, and P. Thio, T.and Wolff (1998). Extraordinary optical transmission through sub-wavelength hole arrays. *Nature 391*, 667–669.

Eck, D., C. A. Helm, N. J. Wagner, and K. A. Vaynberg (2001). Plasmon resonance measurements of the adsorption and adsorption kinetics of a biopolymer onto gold nanocolloids. *Langmuir 16*(4), 957–960.

Efrima, S. and B. V. Bronk (1998). Silver colloids impregnating or coating bacteria. *J. Phys. Chem. B 102*(31), 5947–5950.

El-Sayed, I. H., X. Huang, and M. A. El-Sayed (2005). Surface plasmon resonance scattering and absorption of anti-egfr antibody conjugated gold nanoparticles in cancer diagnostics: applications in oral cancer. *Nano Lett. 5*(5), 829–834.

Elghanian, R., J. J. Storhoff, R. C. Mucic, R. L. Letsinger, and C. A. Mirkin (1997). Selective colorimetric detection of polynucleotides based on the distance-dependent optical properties of gold nanoparticles. *Science 277*, 1078–1081.

Enderlein, J. (2002a). Spectral properties of a fluorescing molecule within a sperical metallic nanocavity. *Phys. Chem. Chem. Phys. 4*, 2780–2786.

Enderlein, J. (2002b). Theoretical study of single molecule fluorescence in a metallic nanocavity. *Appl. Phys. Lett. 80*(2), 315–317.

Englebienne, P. (1998). Use of colloidal gold surface plasmon resonance peak shift to infer affinity constants from the interactions between protein antigens and antibodies specific for single or multiple epitopes. *Analyst 123*, 1599–1603.

Eustis, S. and M. A. El-Sayed (2006). Why gold nanoparticles are more precious than pretty gold: Noble metal surface plasmon resonance and its enhancement of the radiative and nonradiative properties of nancrystals of different shapes. *Chem. Soc. Rev. 35*, 209–217.

Faulds, K., F. McKenzie, W. E. Smith, and D. Graham (2007). Quantitative simultaneous multianalyte detection of dna by dual-wavelength surface-enhanced resonance raman scattering. *Angew. Chem. Int. Ed. 46*, 1–4.

Faulds, K., W. E. Smith, and D. Graham (2005). Dna detection by surface enhanced resonance raman scattering (serrs). *Analyst 130*, 1125–1131.

Fleischman, M., P. J. Hendra, and A. J. McQuillan (1974). Raman spectra of pyridine adsorbed at a silver electrode. *Chem. Phys. Lett. 26*(2), 163–166.

Frens, G. (1973). Controlled nucleation for the regulation of particle size in monodisperse gold suspensions. *Nature 241*, 20–23.

Fromm, D. P., A. Sundaramurthy, P. J. Schuck, G. Kino, and W. E. Moerner (2004). Gap-dependent optical coupling of single "bowtie" nanoantennas resonant in the visible. *Nano Lett. 4*, 957–961.

Frostell-Karlsson, A., H. Widegren, C. E. Green, M. D. Hämäläinen, L. Westerlund, R. Karlsson, K. Fenner, and H. van de Waterbreemd (2005). Biosensor analysis of interaction between drug compounds and liposomes of different properties; a two-dimensional characterization tool for estimation of membrane absorption. *J. Pharmaceut. Sci. 94*(1), 25–37.

Geddes, C. D., I. Gryczynski, J. Malicka, Z. Gryczynski, and J. R. Lakowicz (2004). Directional surface plasmon coupled emission. *J. Fluoresc. 14*(1), 119–123.

Geddes, C. D. and J. R. Lakowicz (2002). Metal-enhanced fluorescence. *J. Fluoresc. 12*(2), 121–129.

Giebel, K.-F., C. Bechinger, S. Herminghaus, M. Riedel, P. Leiderer, U. Weiland, and M. Bastmeyer (1999). Imaging of cell/substrate contacts of living cells with surface plasmon resonance microscopy. *Biophys. J. 75*, 509–516.

Golab, J. T., J. R. Sprague, K. T. Carron, G. C. Schatz, and R. P. van Duyne (1988). A surface enhanced hyper-raman scattering study of pyridinge adsorbed onto silver: Experiment and theory. *J. Chem. Phys. 88*(12), 7942–7951.

Graham, D., K. Faulds, and W. E. Smith (2006). Biosensing using silver nanoparticles and surface enhanced resonance raman scattering. *Chem. Commun.*, 4363–4371.

Green, R. J., R. A. Frazier, K. M. Shakesheff, M. C. Davies, C. J. Roberts, and S. J. B. Tendler (2000). Surface plasmon resonance analysis of dynamic biological interactions with biomaterials. *Biomat. 21*, 1823–1835.

Grigorenko, I., S. Haas, and A. Levi (2006). Electromagnetic response of broken-symmetry nanoscale clusters. *Phys. Rev. Lett. 97*, 036806.

Hanlon, E. B., R. Manoharan, T.-W. Koo, K. E. Schafer, J. T. Motz, M. Fitzmaurice, J. R. Kramer, I. Itzkan, R. R. Dasari, and M. S. Feld (2000). Prospect for in vivo raman spectroscopy. *Phys. Med. Biol. 45*, R1–R59.

Hao, F., C. L. Nehl, J. H. Hafner, and P. Nordlander (2007). Plasmon resonances of a gold nanostar. *Nano Lett. 7*, 729–732.

Heyse, S., O. P. Ernst, Z. Dienes, K. P. Hofmann, and H. Vogel (1998). Incorporation of rhodopsin in laterally structured supported membranes: observation of transducin activation with spatially and time-resolved surface plasmon resonance. *Biochem. 37*(2), 507–522.

Hirsch, L. R., A. M. Gobin, A. R. Lowery, F. Tam, R. A. Drezek, N. J. Halas, and J. L. West (2006). Metal nanoshells. *Ann. Biomed. Eng. 34*(1), 15–22.

Holtom, G. R., B. D. Thrall, B.-Y. Chin, H. S. Wiley, and S. D. Colson (2001). Achieving molecular selectivity in imaging using multiphoton raman spectroscopy techniques. *Traffic 1*, 781–788.

Homola, J. (2003). Present and future of surface plasmon resonance biosensors. *Anal. Bioanal. Chem. 377*, 528–539.

Homola, J., H. Vaisocherová, J. Dostálek, and M. Piliarik (2005). Multi-analyte surface plasmon resonance biosensing. *Methods 37*, 26–36.

Homola, J., S. S. Yee, and G. Gauglitz (1999). Surface plasmon resonance sensors: review. *Sensors and Acuators B 54*, 3–15.

Imura, K., T. Nagahara, and H. Okamoto (2004). Plasmon mode imaging of single gold nanorods. *J. Am. Chem. Soc 126*, 12730–12731.

Isfort, G., K. Schierbaum, and Z. D. (2006a). Causality of surface plasmon polariton emission processes. *Phys. Rev. B 73*, 033408.

Isfort, G., K. Schierbaum, and Z. D. (2006b). Polarization dependence of surface plasmon polariton emission. *Phys. Rev. B 74*, 033404.

Jackson, J. B. and N. J. Halas (2001). Silver nanoshells: Variations in morphologies and optical properties. *J. Phys. Chem. B 105*(14), 2743–2746.

Jana, N. R., L. Gearheart, and C. J. Murphy (2001a). Evidence for seed-mediated nucleation in the chemical reduction of gold salts to gold nanoparticles. *Chem. Mater. 13*(7), 2313–2322.

Jana, N. R., L. Gearheart, and C. J. Murphy (2001b). Seeding growth for size control of 5–40 nm diameter gold nanoparticles. *Langmuir 17*(22), 6782–6786.

Jin, R., Y. Cao, C. A. Mirkin, K. L. Kelly, G. C. Schatz, and J. G. Zheng (2001). Photoinduced conversion of silver nanospheres to nanoprisms. *Science 294*, 1901–1903.

Kambhampati, P., C. M. Child, M. C. Foster, and A. Campion (1998). On the chemical mechanism of surface enhanced raman scattering: Experiment and theory. *J. Chem. Phys. 108*(12), 5013–5026.

Kano, H. and S. Kawate (1996). Two-photon-excited fluorescence enhanced by a surface plasmon. *Optics Lett. 21*(22), 1848–1850.

Karlsson, R. (2004). Spr for molecular interaction analysis: a review of emerging application areas. *J. Mol. Recognit. 17*, 151–161.

Kasry, A. and W. Knoll (2006). Long range surface plasmon fluorescence spectroscopy. *Appl. Phys. Lett. 89*, 1–3.

Kaufman, L. J., C. P. Brangwynne, K. E. Kasza, E. Filippidi, V. D. Gordon, T. S. Deisboeck, and D. A. Weitz (2005). Glioma expansion in collagin i matrices: Analyzing collagen concentration-dependent growth and motility patterns. *Biophys. J. 89*, 635–650.

Kelly, K. L., E. Coronado, L. L. Zhao, and G. C. Schatz (2003). The optical properties of metal nanoparticles: the influence of size, shape, and dielectric environment. *J. Phys. Chem. B 107*(3), 668–677.

Köhler, J. M., A. Csáki, J. Reichert, R. Möller, W. Straube, and W. Fritzsche (2001). Selective labeling of oligonucliotide monolayers by metallic nanobeads for fast optical readout of dna-chips. *Sens. Act. B 76*, 166–172.

Kühn, S., U. Håkanson, L. Rogobete, and V. Sandoghdar (2006). On-command enhancement of single molecule fluoresscence using a gold nanoparticle as an optical nano-antenna. arXiv:cond-mat/0604474.

Kneipp, J., H. Kneipp, and K. Kneipp (2006). Two-photon vibrational spectroscopy for biosciences based on surface-enhanced hyper-raman scattering. *PNAS 103*(46), 17149–17153.

Kneipp, K., H. Kneipp, I. Itzkan, R. R. Dasari, and M. S. Feld (2002). Surface-enhanced raman scattering and biophysics. *J. Phys.: Condens. Matter 14*, R597–R624.

Kneipp, K., H. Kneipp, B. Kartha, R. Manoharan, G. Deinum, I. Itzkan, R. R. Dasari, and M. S. Feld (1998). Detection and identification of a single dna base molecule using surface-enhanced raman scattering (sers). *Phys. Rev. E 57*(6), R6281–R6284.

Kneipp, K., Y. Wang, H. Kneipp, I. Itzkan, R. R. Dasari, and M. S. Feld (1996). Population pumping of excited vibrational states by spontaneous surface-enhanced raman scattering. *Phys. Rev. Lett. 76*(14), 2444–2447.

Kretschmann, E. and H. Raether (1968). Radiative decay of non-radiative surface plasmons excited by light. *Z. Naturforsch. 23A*, 2135–2136.

Kyriacou, S. V., W. J. Brownlow, and X.-H. N. Xu (2004). Using nanoparticle optics assay for direct observation of the function of antimicrobial agents in single live bacterial cells. *Biochem. 43*(1), 140–147.

Lakowicz, J. R. (2001). Radiative decay engineering: biophysical and biomedical applications. *Anal. Biochem. 298*, 1–24.

Lakowicz, J. R. (2004). Radiative decay engineering 3: Surface plasmon-coupled directional emission. *Anal. Biochem. 324*, 153–169.

Lakowicz, J. R. (2005). Radiative decay engineering 5: metal-enhanced fluorescence and plasmon emission. *Anal. Biochem. 337*, 171–194.

Lakowicz, J. R. (2006). Plasmonics in biology and plasmon-controled fluorescence. *Plasmonics 1*, 5–33.

Lambert, P. J., A. G. Whitman, O. F. Dyson, and S. M. Akula (2006). Raman spectroscopy: the gateway into tomorrow's virology. *Virology J. 3*(51).

Le Ru, E. C., P. G. Etchegoin, and M. Meyer (2006). Enhancement factor distribution around a single surface-enhanced raman scattering hot spot and its relation to single molecule detection. *J. Chem. Phys. 125*, 204701.

Lezec, H. J., A. Degiron, E. Devaux, R. A. Linke, L. Martin-Moreno, F. J. Garcia-Vidal, and T. W. Ebbesen (2002). Beaming light from a subwavelength aperture. *Science 297*, 820–822.

Li, Z., R. Jin, C. A. Mirkin, and R. L. Letsinger (2002). Multiple thiol-anchor capped dna-gold nanoparticle conjugates. *Nucleic Acids Res. 30*(7), 1558–1562.

Liedberg, B., C. Nylander, and I. Lundström (1983). Surface plasmon resonance for gas detection and biosensing. *Sens. Act. 4*, 299–304.

Liedberg, B., C. Nylander, and I. Lundström (1995). Biosensing with surface plasmon resonance – how it all started. *Biosens. Bioelectr. 10*, i–ix.

Lin, L.-P., L.-S. Huang, C.-W. Lin, C.-K. Lee, J.-L. Chen, S.-M. Hsu, and S. Lin (2005). Determination of binding constant of dna-binding drug to target dna by surface plasmon resonance biosensor technology. *Curr. Drug. Tar. - Imm., End. Met. Dis. 5*(1), 61–72.

Link, S. and M. A. El-Sayed (1999). Spectral properties and relaxation dynamics of surface plasmon electronic oscillations in gold and silver nanodots and nanorods. *J. Phys. Chem. B 103*(40), 8410–8426.

Liou, K. (1977). *Applied Mathematics and Computation 3*, 331–358.

Mahadevan-Jansen, A. and R. Richards-Kortum (1996). Raman spectroscopy for the detection of cancers and precancers. *J. Biomed. Optics 1*(1), 31–70.

Majka, J. and C. Speck (2007). Analysis of protein–dna interactions using surface plasmon resonance. *Adv. Biochem. Engin./Biotechnol. 104*, 13–36.

McDonnell, J. M. (2001). Surface plasmon resonance: towards an understanding of the mechanism of biological molecular recognition. *Curr. Op. Chem. Biol. 5*, 572–577.

Mertz, J., C. Xu, and W. W. Webb (1995). Single-molecule detection by two-photon-excited fluorescence. *Optics Lett. 20*(24), 2532–2534.

Mie, G. (1908). Contribution to the optics of suspended media, specifically colloidal metal suspensions. *Ann. Phys. 25*, 377–445.

Mikhonin, A. V., Z. Ahmed, A. Ianoul, and S. Asher (2006). Assignments and conformational dependencies of the amide iii peptide backbone uv resonance raman bands. *J. Phys. Chem. B 108*, 19020–19028.

Mikhonin, A. V., S. Bykov, N. Myshakina, and S. Asher (2006). Peptide secondary structure folding reaction coordinate: Correlation between uv raman amide iii frequency, y ramachandran angle, and hydrogen bonding. *J. Phys. Chem. B 110*(4), 1928–1943.

Mock, J. J., M. Barbic, D. R. Smith, D. A. Schultz, and S. Schultz (2002). Shape effects in plasmon resonance of individual colloidal silver nanoparticles. *J. Chem. Phys. 116*(15), 6755–6759.

Moskovits, M. (1985). Surface-enhanced spectroscopy. *Rev. Mod. Phys. 57*(3), 783–826.

Mozsolits, H. and M.-I. Aguilar (2002). Surface plasmon resonance spectroscopy: an emerging tool for the study of peptide-membrane interactions. *Biopol. 66*, 3–18.

Mozsolits, H., W. G. Thomas, and M.-I. Aguilar (2003). Surface plasmon resonance spectroscopy in the study of membrane-mediated cell signalling. *J. Pept. Sci. 9*, 77–89.

Mozsolits, H., H.-J. Wirth, J. Werkmeister, and M.-I. Aguilar (2001). Analysis of antimicrobial peptide interactions with hybrid bilayer membrane systems using surface plasmon resonance. *Biochim. Biophys. Act. 1512*, 64–76.

Murphy, C. J., T. K. Sau, A. M. Gole, C. J. Orendorff, J. Gao, L. Gou, S. E. Hunyadi, and T. Li (2005). Anisotropic metal nanoparticles: Synthesis, assembly, and optical applications. *J. Phys. Chem. B 109*(29), 13857–13870.

Nan, X., J.-X. Cheng, and X. S. Xie (2003). Vibrational imaging of lipid droplets in live fibroblast cells with coherent anti-stokes raman scattering microscopy. *J. Lip. Res. 44*, 2202–2208.

Nath, N. and A. Chilkoti (2002). A colorimetric gold nanoparticle sensor to interrogate biomolecular interaction sin real time on a surface. *Anal. Chem. 74*(3), 504–509.

Nedelkov, D. and R. W. Nelson (2003). Surface plasmon resonance mass spectrometry: recent progress and outlooks. *Trends Biotechn. 21*(7), 301–305.

Nehl, C. L., N. K. Grady, G. P. Goodrich, F. Tam, N. J. Halas, and J. H. Hafner (2004). Scattering spectra of single gold nanoshells. *Nano Lett. 4*(12), 2355–2359.

Nehl, C. L., H. Liao, and J. H. Hafner (2006). Optical properties of star-shaped gold nanoparticles. *Nano Lett. 6*(4), 683–688.

Niemeyer, C. M. (2001). Nanoparticles, proteins, and nucleic acids: biotechnology meets materials science. *Angew. Chem. Int. Ed. 40*, 4128–4158.

Oldenburg, S. J., R. D. Averitt, S. L. Westscott, and N. J. Halas (1998). Nanoengineering of optical resonances. *Chem. Phys. Lett. 288*, 243–247.

Oldenburg, S. J., J. B. Jackson, S. L. Westscott, and N. J. Halas (1999). Infrared extinction properties of gold nanoshells. *Appl. Phys. Lett. 75*(119), 2897–2899.

Otto, A. (1968). Excitation of surface plasma waves in silver by the method of frustrated total reflection. *Z. Physik 216*, 398–410.

Otto, A., I. Mrozek, H. Grabhorn, and W. Akemann (1992). Surface-enhanced raman scattering. *J. Phys.: Condens. Matter 4*, 1143–1212.

Perkins, E. A. and D. J. Squirrell (2000). Development of instrumentation to allow the detection of microorganisms using light scattering in combination with surface plasmon resonance. *Biosens. Bioelectr. 14*, 853–859.

Rehwald, S., M. Berndt, F. Katzenberg, S. Schwieger, E. Runge, K. Schierbaum, and D. Zerulla (2007). Tunable metallic mesoscale ribbons: A new degree of freedom in plasmonics. *Phys Rev. B submitted.*

Reichert, J., A. Csáki, J. M. Köhler, and W. Fritzsche (2000). Chip-based optical detection of dna hyridization by means of nanobead labeling. *Anal. Chem. 72*(24), 6025–6029.

Ritchie, R. H., E. T. Arakawa, J. J. Cowan, and R. N. Hamm (1957). Surface-plasmon resonance effect in grating diffraction. *Phys. Rev. Lett. 21*(22), 1530–1533.

Rodriguez, L. G., S. J. Lockett, and G. R. Holtom (2006). Coherent anti-stokes raman scattering microscopy: A biological review. *Cytomet. Part A 69A*, 779–791.

Sako, Y. (Epub 2006). Imaging single molecules in living cells for systems biology. *Mol. Sys. Biol. 2*(56), 1–6.

Salamon, Z., M. F. Brown, and G. Tollin (1999). Plasmon resonance spectroscopy: probing molecular interactions within membranes. *TIBS 20*, 213–219.

Salamon, Z., H. A. Macleod, and G. Tollin (1997a). Surface plasmon resonance spectroscopy as a tool for investigating the biochemical and biophysical properties of membrane protein systems. i: Theoretical principles. *Biochim. Biophys. Act. 1331*, 117–129.

Salamon, Z., H. A. Macleod, and G. Tollin (1997b). Surface plasmon resonance spectroscopy as a tool for investigating the biochemical and biophysical properties of membrane protein systems. ii: Applications to biological systems. *Biochim. Biophys. Act. 1331*, 131–152.

Salamon, Z. and G. Tollin (2001). Optical anisotropy in lipid bilayer membranes: coupled plasmon-waveguide resonance measurements of molecular orientation, polarizability, and shape. *Biophys. J. 80*(3), 1557–1567.

Sambles, J. R., G. W. Bradbery, and F. Z. Yang (1991). Optical-excitation of surface-plasmons: an introduction. *Contemp. Phys. 32*, 173–183.

Schultz, D. A. (2003). Plasmon resonant particles for biological detection. *Curr. Op. Biotech. 14*, 13–22.

Schultz, S., D. R. Smith, J. J. Mock, and D. A. Schultz (2000). Single-target molecule detection with nonbleaching multicolor optical immunolabels. *PNAS 97*, 996–1001.

Sengupta, A., M. Mujacic, and E. J. Davis (2006). Detection of bacteria by surface-enhanced raman spectroscopy. *Anal. Bioanal. Chem. 386*, 1379–1386.

Sharma, P., S. Brown, G. Walter, S. Santra, and B. Moudgil (2006). Nanoparticles for bioimaging. *Adv. Colloid Interface Sci. 123–126*, 471–485.

Silin, V. and A. Plant (1997). Biotechnological applications of surface plasmon resonance. *TIBTECH 15*, 353–359.

Smith, E. and G. Dent (2005). *Modern Raman Spectroscopy - A Practical Approach.* West Sussex: Wiley.

Sönnichsen, C., B. M. Reinhard, J. Liphardt, and A. P. Alivisatos (2005). A molecular ruler based on plasmon coupling of single gold and silver nanoparticles. *Nat. Biotechnol. 23*(6), 741–745.

So, P. T. C., C. Y. Dong, B. R. Masters, and K. M. Berland (2000). Two-photon excitation fluorescence microscopy. *Annu. Rev. Biomed. Eng. 2*, 399–429.

Soelberg, S. D., T. Chinowsky, G. Geiss, C. B. Spinelli, R. Stevens, S. Near, P. Kauffman, S. Yee, and C. E. Furlong (2005). A portable surface plasmon resonance sensor system for real-time monitoring of small to large analytes. *J. Ind. Microbiol. Biotechnol. 32*, 669–674.

Sokolov, K., M. Follen, J. Aaron, I. Pavlova, A. Malpica, R. Lotan, and R. Richards-Kortum (2003). Real-time vital optical imaging of precancer using anti-epidermal growth factor receptor antibodies conjugated to gold nanoparticles. *Cancer Res. 63*, 1999–2004.

Sönnichsen, C., T. Franzl, T. Wilk, G. von Plessen, J. Feldmann, O. Wilson, and P. Mulvaney (2002). Drastic reduction of plasmon damping in gold nanorods. *Phys. Rev. Lett. 88*, 077402.

Sonvico, F., C. Dubernet, P. Colombo, and P. Couvreur (2005). Metallic colloid nanotechnology, applications in diagnosis and therapeutics. *Curr. Pharm. Des. 11*(16), 2091–2105.

Spiro, T. G. (1988). Biological applications of raman spectroscopy. *Wiley, New York I-III*, 1.

Spiro, T. G. and C. Strekas (1972). Resonance raman spectra of hemoglobin and cytochrome c: Inverse polarization and vibronic scattering. *Proc. Natl. Acad. Sci. USA 69I*, 2622.

Stears, R. L., T. Martinsky, and M. Schena (2003). Trends in microarray analysis. *Nature Medicine 9*(1), 140–145.

Stenlund, P., G. J. Babcock, J. Sodrosko, and D. G. Myszka (2003). Capture and reconstituion of g protein-coupled receptors on a biosensor surface. *Analyt. Biochem. 316*, 243–250.

Stöckle, R., Y. Doug Suh, V. Deckert, and R. Zenobi (2000). Nanoscale chemical analysis by tip-enhanced raman spectroscopy. *Chem. Phys. Lett. 318*, 131.

Storhoff, J. J., R. Elghanian, R. C. Mucic, C. A. Mirkin, and R. L. Letsinger (1998). One-pot colorimetric differentiation of polynucleotides with single base imperfections using gold nanoparticle probes. *J. Am. Chem. Soc. 120*(9), 1959–1964.

Stuart, D. A., J. M. Yuen, N. Shah, O. Lyandres, C. R. Yonzon, M. R. Glucksberg, J. T. Walsh, and R. P. Van Duyne (2006). In vivo glucose measurement by surface-enhanced raman spectroscopy. *Anal. Chem. 78*(20), 7211–7215.

Sun, Y. and Y. Xia (2003). Triangular nanoplates of silver: Synthesis, characterization, and use as sacrificial templates for generating triangular nanorings of gold. *Adv. Mater. 15*(9), 695–699.

Talley, C. E., T. R. Huser, C. W. Hollars, L. Jusinski, T. Laurence, and S. M. Lane (2004, 9). Nanoparticle based surface-enhanced raman spectroscopy. NATO Advanced Study Institute: Biophotonics, Ottawa, Canada.

Taton, T. A., C. A. Mirkin, and R. L. Letsinger (2000). Scanometric dna array detection with nanoparticle probes. *Science 289*, 1757–1760.

Terrettaz, S., W.-P. Ulrich, H. Vogel, Q. Hong, L. G. Dover, and J. H. Lakey (2002). Stable self-assembly of a protein engineering scaffold on gold surfaces. *Prot. Sci. 11*, 1917–1925.

Thaxton, C. S., D. G. Georganopoulou, and C. A. Mirkin (2006). Gold nanoparticle probes for the detection of nucleic acid targets. *Clin. Chim. Acta 363*, 120–126.

van Regenmortel, M. H. V., D. Altschuh, J. Chatellier, and L. Christensen (1998). Measurement of antigen–antibody interactions with biosensors. *J. Mol. Rec. 11*, 163–167.

Vikinge, T. P., K. M. Hansson, J. Benesch, K. Johansen, M. Ranby, T. L. Lindahl, B. Liedberg, I. Lundström, and P. Tengvall (2000). Blood plasma coagulation studieed by surface plasmon resonance. *J. Biomed. Opt. 5*(1), 51–55.

Wabuyele, M. B. and T. Vo-Dinh (2005). Detection of human immunodeficiency virus type 1 dna sequence using plasmonics nanoprobes. *Anal. Chem. 77*(23), 7810–7815.

Wang, H., D. Brandl, F. Le, P. Nordlander, and N. Halas (2006). Nanorice: A hybrid plasmonic nanostructure. *Nano Lett. 6*, 827–832.

Wang, H., Y. Fu, P. Zickmund, R. Shi, and J.-X. Cheng (2005). Coherent anti-stokes raman scattering imaging of axonal myelin in live spinal tissues. *Biophys. J. 89*, 581–591.

Wessel, J. (1985). Surface-enhanced optical microscopy. *J. Opt. Soc. Am. B 2*(9), 1538–1541.

Willets, K. A. and R. P. Van Duyne (2007). Localized surface plasmon resonance spectroscopy and sensing. *Ann. Rev. Phys. Chem. 58*, 267–297.

Wiltschi, B., W. Knoll, and E.-K. Sinner (2006). Binding assays with artificial tethered membranes using surface plasmon resonance. *Methods 39*, 134–146.

Wood, E., C. Sutton, A. E. Beezer, J. A. Creighton, A. F. Davis, and J. C. Mitchell (1997). Surface enhanced raman scattering (sers) study of membrane transport processes. *Int. J. Pharm. 154*, 115–118.

Wood, R. W. (1902). On a remarkable case of uneven distribution of light in a diffraction grating spectrum. *Proc. R. Soc. London A18*, 269.

Wurpel, G. W. H., H. A. Rinia, and M. Müller (2005). Imaging orientational order and lipid density in multilamellar vesicles with multiplex cars microscopy. *J. Microsc. 218*(1), 37–45.

Xu, H., J. Aizpurua, M. Käll, and P. Apell (2000). Electromagnetic contributions to single-molecule sensitivity in surface-enhanced raman scattering. *Phys. Rev. E 62*(3), 4318–4324.

Yguerabide, J. and E. Yguerabide (1998a). Lighter-scattering submicroscopic particles as highly fluorescenct analogs and their use as tracer labels in clinical and biological applicaionts: I. theory. *Analyt. Biochem. 262*, 137–156.

Yguerabide, J. and E. Yguerabide (1998b). Lighter-scattering submicroscopic particles as highly fluorescenct analogs and their use as tracer labels in clinical and biological applicaionts: I. theory. *Analyt. Biochem. 262*, 157–176.

Yguerabide, J. and E. Yguerabide (2001). Resonance light scattering particles as ultrasensitive labels for detection of analytes in a wide range of applications. *J. of Cellular Biochem. Suppl. 37*, 71–81.

Zerulla, D., G. Isfort, M. Kolbach, A. Otto, and K. Schierbaum (2003). Sensing molecular properties by atr-spp raman spectroscopy on electrochemically structured sensor chips. *Electrochim. Acta 48*(20), 2943–2947.

Zhang, J. and J. R. Lakowicz (2005). Enhanced luminescence of phenyl-phenanthridine dye on aggregated small silver nanoparticles. *J. Phys. Chem. B 109*(18), 8701–8706.

Zhang, J., J. Malicka, I. Gryczynski, and J. R. Lakowicz (2005). Surface-enhanced fluorescence of fluorescein-labeled oligonucleotides capped on silver nanoparticles. *J. Phys. Chem. B 109*(16), 7643–7648.

Zumbusch, A., G. R. Holtom, and X. S. Xie (1999). Three-dimensional vibrational imaging by coherent anti-stokes raman scattering. *Phys. Rev. Lett. 82*(20), 4142–4145.

PHYSICAL REVIEW B **73**, 033408 (2006)

Causality of surface plasmon polariton emission processes

G. Isfort and K. Schierbaum
Heinrich-Heine Universität Düsseldorf, Institut für Physik der kondensierten Materie, Abteilung für Materialwissenschaft, Germany

D. Zerulla*
University College Dublin, UCD, Physics, Belfield, Dublin 4, Ireland

(Received 17 November 2005; published 26 January 2006)

Fundamental physical quantum phenomena, such as surface plasmon polaritons (SPP's), require specific conditions as described in their dispersion relation for excitation by photons. These conditions exactly define the **k** vector of the incident photons as well as the elastically reemitted, outbound photons that follow from the decay of the plasmon. Our conclusion demonstrates that these requisites are indeed fulfilled even on the introduction of an inelastic, wavelength-shifting process like fluorescence emission to the system. Such a process is established by placing fluorescent molecules into the strong evanescent field of the SPP. The analysis of the outbound photons shows an angular behavior, which can only be explained if the fluorescent photons also satisfy SPP conditions. This behavior enables the development of a model for the chronology and causality of surface plasmon polariton deexcitation mechanisms.

DOI: 10.1103/PhysRevB.73.033408 PACS number(s): 73.20.Mf, 78.66.−w, 42.82.Gw

I. INTRODUCTION

Surface plasmon polaritons (SPP's) play an important role in a multitude of applications such as surface-enhanced Raman scattering (SERS) and surface plasmon resonance (SPR).[1,2] It is therefore expected that a fundamental understanding of the mechanisms and chronology of SPP excitations and deexcitations will unlock novel perspectives and methodologies—e.g., ultrasensitive detectors required for biotechnology.[3,4] The dispersion relation of SPP's dictates the conditions under which they are excited. Specifically, their excitation is not possible by direct irradiation of photons on the thin metal film but requires special optical configurations, such as those initially proposed by Raether and Kretschmann[5] and Otto.[6] Their common property is that the photons approach from an optically denser medium, before impinging on the metal in an attenuated total reflection (ATR) setup.[5,6] In this paper we will exclusively use the Kretschmann configuration (see Fig. 1). For SPP's excited at thin, smooth metal surfaces, the excitation of an SPP according to its dispersion relation is given by the equation (see Ref. 7)

$$k_x = \frac{\omega}{c}\sqrt{\frac{\epsilon_1 + \epsilon_2}{\epsilon_1 \epsilon_2}} = \frac{\omega}{c}\sqrt{\epsilon_0}\,\sin(\alpha), \qquad (1)$$

where ϵ_i is the optical constant of medium i (see Fig. 1). Using Fresnel equations by the matrix formalism from the optical constants at a given wavelength, the reflectivity and field enhancement of the SPP for a multilayered system (which consists of the prism substrate ϵ_0, metal film ϵ_1, sample molecules ϵ_2, and additional layers such as a passivating layer) can be calculated.[8] Following the creation of the SPP, its consequential decay may occur by the emission of photons under equivalent conditions. More precisely, the photons have identical wavelengths and after reflection they proceed with the same angle with respect to the metal surface. Due to scattering processes in the metal layer (e.g., surface roughness or impurities), the emitted photons partially lose their spatial coherence, but the angle with respect to the surface is conserved. This leads to the so-called ATR ring which is shown in Fig. 2. The intensity of the displayed ATR ring depends strongly on the roughness of the surface, the quality of which has been additionally controlled by atomic force measurements (AFM).[9] In connection to this publication[9] an interesting property of the emitted light in the ATR cone was discovered—namely, its polarization dependence—the results of which can be found in Ref. 10. Consequently, this paper will investigate the causality and time dependence of interactions between an SPP and those molecules, which have been introduced into its enhanced evanescent electromagnetic field, thus resulting in a wavelength-shifted reemission of photons.

II. MEASUREMENTS

In order to investigate the resonant coupling of plasmon polaritons, excited by an ATR optical configuration, and fluorescent molecules in the near field, the first concern is to investigate the spatial dependence of the spectral emission of the chosen fluorescent dye. Rhodamin 6G was used as dye for the experiments due to its high stability and because it is a strong emitter with a broad spectral emission. Prior to the

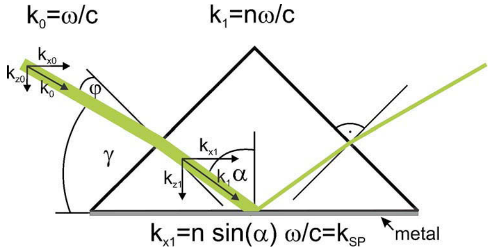

FIG. 1. (Color online) The ATR-SPP setup (Kretschmann type). Note the differences in definition between angles α, γ, and φ.

1098-0121/2006/73(3)/033408(4)/$23.00

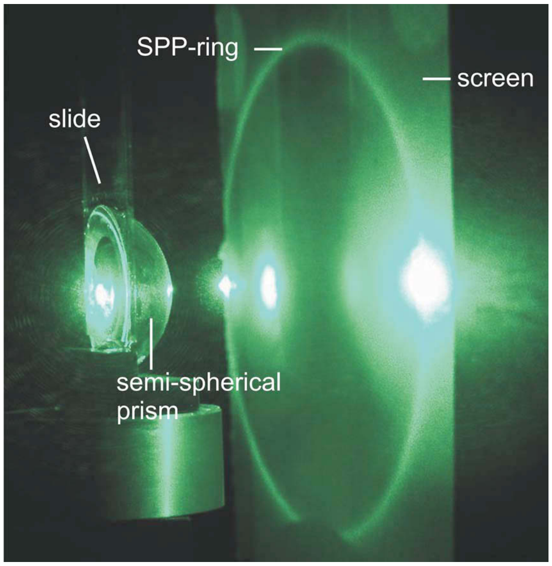

FIG. 2. (Color online) The ATR-SPP setup (Kretschmann type). Plasmon excitation at 514.5 nm on an evaporated silver film. The ATR SPP cone is projected onto a screen and is visible as a bright circle. The "spots" are a result of the unscattered strong laser light and its partial reflections, while the brightness of the circle in respect to the spots is a measure of the silver surface roughness. For the sake of illustrating the phenomenon an untypical rough silver film and a semispherical prism were used.

SPP experiments the spatial dependence of the dissolved dye excited at 514.5 nm was tested. The outcome proved that the spectral emission is isotropic after subtraction of the elastically scattered background. Following this first experiment, the setup was transformed into a Kretschmann-type ATR setup. In order to prevent quenching, charge-transfer reactions, and so-called SERS first-layer (hot-spot) effects, the thin silver layer (thickness 50 nm) was passivated with a hexadecanethiol self-assembling monolayer. This monolayer is stable, dense, and well ordered so that the rhodamin molecules are effectively blocked from reaching the Ag surface.[11,12] Optimized parameters for the excitation of the SPP prevented the laser photons from reaching the dye molecules directly; rather, excitation occurred through the excited plasmon. Following the excitation of the dye via the SPP an intense fluorescent signal was detected and analyzed, showing that the strong evanescent field of the SPP was the source of the excitation of the dye.

The investigations focused mainly on the angular distribution of the emitted fluorescence photons. In a simple model, one would expect that the SPP decays radiatively followed by photon absorption via the dye molecules. The response would be a redshifted fluorescent emission. Assuming that no coupling between the excitation and emission processes of the photons occurs, the emission would be of an isotropic nature.

However, if a coupling via the evanescent field were postulated, the angular intensity distribution would predict maxima at the same angles as the SPP photon emission—i.e., similar to forward and backward scattering. In particular, this distribution is expected to be independent of the emitted (redshifted) wavelength but to have its maximum for an angle, which would still be valid for the SPP excitation with the 514.5-nm laser photons.

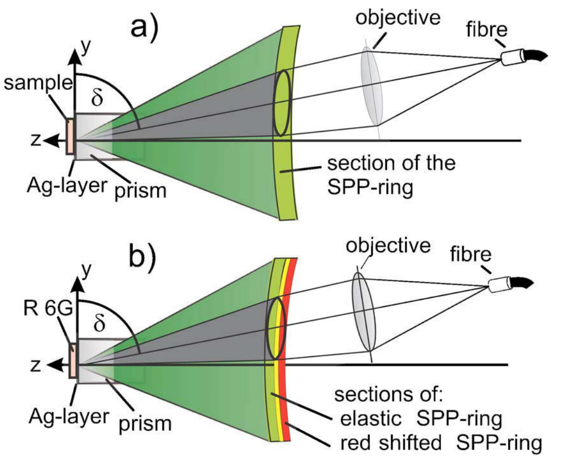

FIG. 3. (Color online) (a) Sketch for the detection of elastically scattered photons within the ATR cone. (b) Sketch of the wavelengths distribution and its detection within the ATR cone.

Nevertheless, the physical measurements show a different behavior. The angular distributions of the emitted photons are sharply defined and depend on the respective emitted wavelength. The case for the simple ATR cone is shown in Fig. 3(a) while the results of the fluorescent emission are displayed in Fig. 3(b). In order to quantify the results in a more precise way, interference filters have been used to investigate spectral parts of the broad rhodamin 6G emission. The filters have maximum transmissions for redshifted wavelengths of 534.7 nm (shift 752 cm^{-1}) and 583.9 nm (shift 2330 cm^{-1}). Together with the elastically Rayleigh-scattered light at 514.5 nm (shift 0 cm^{-1}), three different wavelengths were chosen to illustrate the following facts:

According to these conditions the relative change in azimuth for the maximum of the shifted emission at 752 cm^{-1} is $1.5° \pm 0.5°$ with respect to the Rayleigh-scattered light. For the shifted emission at 2330 cm^{-1} the deviation is $3.7° \pm 0.5°$ with respect to the Rayleigh-scattered photons. The changes in azimuth for the three wavelengths are shown in Fig. 4.

The energy spacings are not uniform for the three used filters. Also, it is reasonable to compare the measured results with simulations of the excitation of an SPR for the three wavelengths (see Fig. 5). The simulations show that the angle with respect to the surface normal is decreased for longer wavelengths, as shown in the measurements. The relative shifts are $\Delta\alpha_{1,2}=0.7°$ and $\Delta\alpha_{2,3}=0.9°$, respectively.

For comparison with the experimental data one also has to take the dispersive properties of the ATR prism into account and to transform the internal ATR angle α (within the prism) into the external angle φ or γ by means of applying simple ray optics and geometrical considerations according to the optical constants $\epsilon(\lambda)$: $\varphi=\arcsin[\sqrt{\epsilon_{prism}(\lambda)}\,\sin(\alpha-45°)]$.[13] The results of this transformation are shown in Table I. The changes in azimuth according to calculations are now 1.3° (for 752 cm^{-1}) and 3.1° (for 2330 cm^{-1}) both with respect to the Rayleigh-scattered photons. This is in very good agreement with the recorded measurements, especially if one takes into account that surface plasmon resonance is extremely

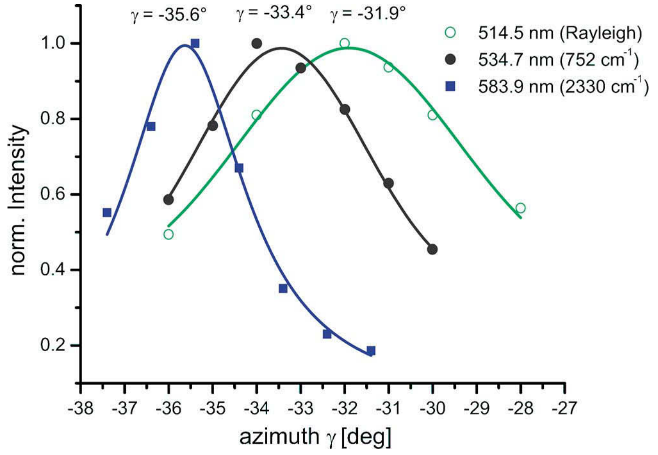

FIG. 4. (Color online) Measured angular dependence of the fluorescent emission with respect to its wavelength.

sensitive to changes in thickness as well as reactions involving sulphur and oxygen with the silver layer.

While the transformation from internal angles α to external angles φ already contains the refraction of the photons at the prism-air interface, all remaining effects (besides the SPP) connected to the total reflection at the prism-metal interface and its evanescent field have been so far neglected. The total internal reflection from the rear facet of the prism causes a small but measurable displacement of the light. A comprehensive analysis of this phenomenon, which is known as the Goos-Hänchen effect, can be carried out by decomposition of the incident beam into its plane-wave spectrum, computation of the Fresnel reflection coefficients for each such plane wave, and superposition of the reflected plane waves.[14–17] The Goos-Hänchen effect is a direct consequence of the evanescent field. The resulting effect is of the order of the chosen wavelength and is a pure displacement and not a change in angle.[17] For this reason this effect can be neglected. This is still true if the light undergoes a change in wavelengths within the evanescent field as happens here due to the fluorescence. Emile *et al.* showed that even a second-harmonic generation process in a nonlinear medium does not change the angle of reflection[18] and even investigations of this effect with surface plasmons have been carried out.[19,20] These experiments produced positive or negative lateral optical beam displacements but again no change in angle was observed.

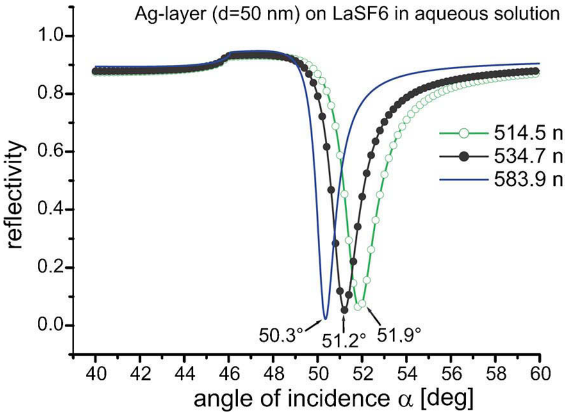

FIG. 5. (Color online) Calculation of the SPP excitation with respect to the angle α for the selected three wavelengths.

TABLE I. Results of the ATR-SPP calculations and their transformation into external azimuth angles in comparison to the measurements.

cm^{-1}	α_{calc}	φ_{calc}	γ_{calc}	γ_{meas}	$\Delta\gamma_{calc}$	$\Delta\gamma_{meas}$
0	51.9°	12.9°	32.1°	31.9°	—	—
752	51.2°	11.6°	33.4°	33.4°	1.3°	1.5°
2330	50.3°	9.8°	35.2°	35.6°	3.1°	3.7°

As a consequence, the measured and simulated azimuth angles can only be derived by applying the SPP dispersion relation for the different reemitted wavelengths.

III. CONCLUSION

The fluorescent emission, excited in the near field of the evanescent SPP field, remains a coherent process and therefore obeys the new conditions for the excitation of the plasmons as a result of the changed wavelength. By doing this it allows us to determine the causality of the underlying mechanisms of the entire process. It is shown experimentally that depending on the wavelength of the incident photons there is exactly one angle of incidence which will excite an SPP. This SPP has a strong, evanescent field. Instead of releasing a photon that is subsequently absorbed by a molecule, the SPP field directly interacts with the molecule in the near field, thereby maintaining its SPP character. The process might generate the equivalence of a fluorescent photon which still follows the SPP conditions in combination with the properties of its evanescent field. The fluorescent photons are then coherently emitted in wavelength dependent azimuth angles on the prism side of the metal film, in accordance with the SPP conditions.

---

*Electronic address: dominic.zerulla@ucd.ie

[1] K. Kneipp, Y. Wang, H. Kneipp, L. T. Perelman, I. Itzkan, R. R. Dasari, and M. S. Feld, Phys. Rev. Lett. **78**, 1667 (1997).
[2] A. P. Hibbins, B. R. Evans, and J. R. Sambles, Science **308**, 670 (2005).
[3] J.-N. Lin and C. J. Wilson, U.S. Patent No. 5,776,785 (1998).
[4] J. Malicka, I. Gryczynski, and J. R. Lakowicz, J. Biomol. Screening **9**, 208 (2004).
[5] E. Kretschmann and H. Raether, Z. Naturforsch. A **23**, 2135 (1968).
[6] A. Otto, Z. Phys. **216**, 398 (1968).
[7] H. Raether, *Surface Plasmons* (Springer Verlag, Berlin, 1988), Vol. 111.
[8] C. E. Reed, J. Giergiel, J. C. Hemminger, and S. Ushioda, Phys.

Rev. B **36**, 4990 (1987).

[9] G. Isfort, Ph.D. thesis, Universität Düsseldorf, 2005.

[10] D. Zerulla, G. Isfort, and K. Schierbaum (unpublished).

[11] D. Zerulla, I. Uhlig, R. Szargan, and T. Chasse, Surf. Sci. **402-404**, 604 (1998).

[12] D. Zerulla and T. Chasse, Langmuir **18**, 5392 (2002).

[13] E. D. Palik, *Handbook of Optical Properties of Solids* (Academic Press, Orlande, FL, 1985).

[14] F. Goos and H. Hänchen, Ann. Phys. **1**, 333 (1947).

[15] H. K. V. Lotsch, Optik (Stuttgart) **32**, 299 (1971).

[16] H. K. V. Lotsch, Optik (Stuttgart) **32**, 116 (1970).

[17] F. Bretenaker, A. Le Floch, and L. Dutriaux, Phys. Rev. Lett. **68**, 931 (1992).

[18] O. Emile, T. Galstyan, A. Le Floch, and F. Bretenaker, Phys. Rev. Lett. **75**, 1511 (1995).

[19] C. Bonnet, D. Chauvat, O. Emile, F. Bretenacker, and A. Le Floch, Opt. Lett. **26**, 666 (2001).

[20] X. Yin, L. Hesselink, Z. Liu, N. Fang, and X. Zhang, Appl. Phys. Lett. **85**, 372 (2004).

PHYSICAL REVIEW B **74**, 033404 (2006)

Polarization dependence of surface plasmon polariton emission

G. Isfort and K. Schierbaum
Heinrich-Heine Universität Düsseldorf, Institut für Physik der kondensierten Materie, Abteilung für Materialwissenschaft, Germany

D. Zerulla[*]
University College Dublin, UCD, Physics, Belfield, Dublin 4, Ireland

(Received 25 April 2006; published 11 July 2006)

Surface plasmon polaritons (SPP's) need specific conditions for excitation by photons. In order to fulfill the dispersion relation of the SPP's the photons are required to approach the metal interface from an optically denser medium. For this an attenuated reflection setup (ATR) of a so-called Kretschmann type is used. The excited plasmon may decay by the emission of photons with the same angle with respect to the surface normal. Deliberately using rough metal films the surface plasmon polariton is elastically scattered at the interface. This results in a partial loss of coherence of the reemitted photons. While the angle in respect to the surface normal is conserved, a fraction of the emitted photons leave the plane of incidence, resulting in the so-called ATR cone. Upon analysis of the polarization dependence of light from the ATR cone, an exceptionally clear polarization dependence has been found. The observed behavior is the complete linear polarization of the light in the plane of emission, thus resulting in continuously changed polarization in respect to the polar coordinates within the ATR ring.

DOI: 10.1103/PhysRevB.74.033404 PACS number(s): 73.20.Mf

I. INTRODUCTION

Surface plasmon polaritons (SPPs) play an important role in a variety of modern applications, such as surface enhanced Raman scattering[1] (SERS), surface plasmon-coupled emission[2–5] (SPCE), surface plasmon resonance[6–9] (SPR), and subwavelength optics.[10,11] It is therefore expected that progress in the understanding of its mechanism will unlock prospective novel approaches. Here we report on the polarization dependence of the elastically reemitted photons, which permits us to draw important conclusions in conjunction with inelastically re-emitted photons used, e.g., in SPCE.[2–5]

The dispersion relation of a SPP dictates the conditions under which it is excited. One result is that its excitation cannot be achieved by direct irradiation of photons on a metal surface but requires special optical configurations, including those initially proposed by Kretschmann and Raether[12] and Otto.[13] Their common property is that the photons approach from an optically denser medium before impinging on the metal, using an attenuated total reflection (ATR) setup.[12,13] In this paper we use exclusively the Kretschmann configuration.

The use of a semispherical prism, as shown in Fig. 1, has two intrinsic advantages. First, the light path can be used in such a fashion that the incident and outgoing photons are always normal on the prism surface, i.e., refraction at this air glass interface may be neglected. Second, the rotational symmetry of the prism permits unperturbed observation of the scattered light unlike a triangular prism. For SPP's excited by photons with angular frequency ω on thin, smooth metal surfaces, the wavelength-dependent dispersion relation of a SPP is given by the following equation:[14]

$$k_x = \frac{\omega}{c}\sqrt{\frac{\epsilon_1 \epsilon_2}{\epsilon_1 + \epsilon_2}} = \frac{\omega}{c}\sqrt{\epsilon_3}\,\sin\alpha \qquad (1)$$

with $\epsilon_i = \epsilon_i' + i\epsilon_i''$ complex optical constant of layer i and α photon angle of incidence.

The above equation (1) assigns exactly one unique **k** vector to each wavelength involved in the excitation of a SPP. The photons then need a specific angle of incidence with respect to the surface normal and within the plane of incidence. Furthermore, in order to satisfy the dispersion relation, modification of the **k** vector can only occur if the incident photons are linearly polarized parallel to the plane of incidence. On a perfect, single crystalline, metal surface where scattering events due to imperfections can be considered negligible, the SPP may decay by the emission of photons which are still within the plane of incidence and with the same absolute angle with respect to the surface normal that were needed for their excitation.

On an evaporated and therefore imperfect metal film the propagating surface plasmon polariton is in part elastically scattered from its original direction. This results in a partial loss of coherence of the reemitted photons. While the angle with respect to the surface normal is conserved, most of the emitted photons may no longer be located in the plane of incidence. This results in the so-called ATR cone (Fig. 1). It should be noted that the aperture angle of the reemitted photons is only then unchanged if the total process can be con-

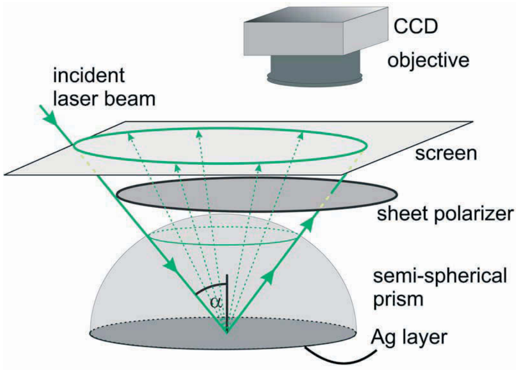

FIG. 1. (Color online) Sketch of the Kretschmann-type ATR setup with a semispherical prism and an additional polarizer.

1098-0121/2006/74(3)/033404(4)

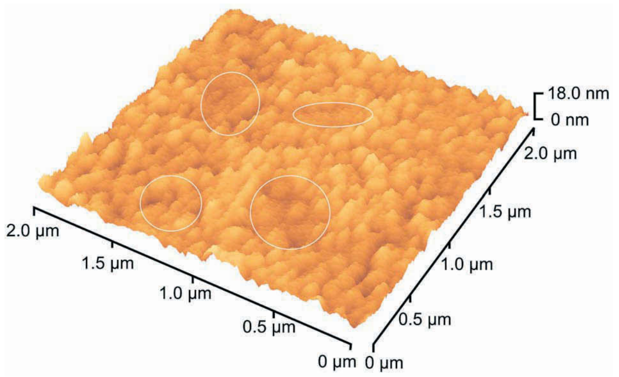

FIG. 2. (Color online) AFM image of the evaporated silver film.

sidered to be elastic. If an inelastic process such as fluorescence or Raman scattering is introduced, the aperture angle of the ATR cone is changed according to the dispersion relation[2–5,15] [see Eq. (1)].

The ratio between the number of reemitted photons situated in the plane of incidence and those detected beyond the plane of incidence is a function of the roughness δ of the metal film.[14,16,17] The roughness also influences the angular position of the reflectivity minimum $\Delta\alpha$ and the ATR curve half-width $\Delta\alpha_{1/2}$ compared to a smooth interface.[14,16,17]

$$\Delta\alpha = \tan(\alpha_{SP})\mathrm{Re}\left[\frac{\Delta k_{SP}}{k'_{SP}}\right] \tag{2}$$

$$\Delta\alpha_{1/2} = -2\tan(\alpha_{SP})\mathrm{Im}\left[\frac{\Delta k_{SP}}{k'_{SP}}\right] \tag{3}$$

with $k'_{SP}=(2\pi/\lambda)\sqrt{\epsilon_3}\sin(\alpha_{SP})$. The quality of the model depends crucially on the definition of Δk_{SP} for which we refer to the literature.[17]

II. EXPERIMENTAL

The excitation of the SPP's was achieved with the green 514.5 nm line of a Coherent Innova 70-4 laser in single line configuration. To prevent distortion of the ATR ring a semispherical prism (BK7, Schott) was used. The prism was cleaned prior to its use by a successive multistep treatment with Ethanol (purity: 99.98% for spectroscopy, Merck), Deconex (Borer Chemie), Neodisher (Dr. Weigert), and Acetone (99.98% pro Analysis, Merck) at 70 °C after finally having dried in a flow of nitrogen (purity: 99.999%, Messer Griesheim). The procedure is explained in greater detail in (Ref. 18). The use of Carot's acid as a standard cleaning procedure for glass surfaces was discontinued due to the irreversible corrosion of the surfaces for some of the chosen glass types. The silver (purity: 99.99%, Goodfellow) was thermally evaporated on the cold prism, in order to increase the roughness of the film. The enhanced roughness gives rise to a very pronounced ATR ring. The degree of roughness was controlled with an AFM (Explorer 2000, Topometrix) and is shown in Fig. 2.

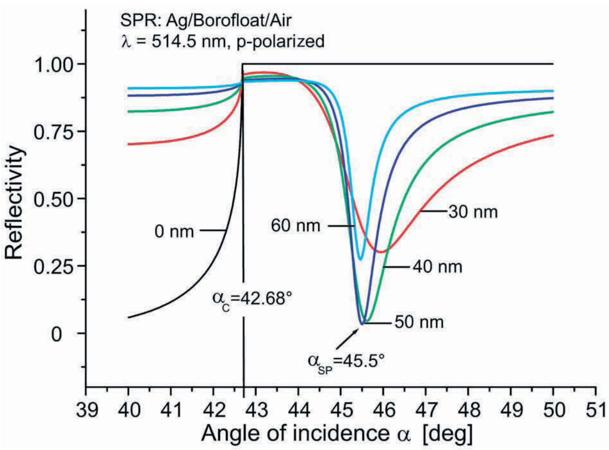

FIG. 3. (Color online) Simulations of reflectivity vs angle of incidence α of a Borofloat-glass/silver/air system with varying silver thicknesses in a Kretschmann-type ATR configuration.

The maximum height deviation in a representative 2 μm × 2 μm area, as shown in the AFM scan above, is approximately 18 nm. However, the average roughness δ_{RMS} observed is 2–3 nm. The white circles denote larger depressions in the 50 nm thick layer of typical diameters of 200–400 nm.

III. MEASUREMENTS

The aperture angle of the ATR cone (with best visibility on a rough silver film) is identical to the angle for the maximum SPP excitation which can be found by observing the reflectivity curve. Solving the Fresnel equations by means of a matrix formalism for a multilayered system, with respect to the optical constants,[19] allows the reflectivity with respect to the angle of incidence to be simulated.[20] Figure 3 shows the results of a set of simulations compiled to describe a three-layer Borfloat-glass/silver/air system. The outcome for several different thicknesses of silver coating are also displayed in Fig. 3.

The curve for 0 nm shows the behavior of the system in the absence of a silver coating, where the critical angle α_c specifies the angle at which the total reflection initiates. Furthermore, this graph is lacking an SPP excitation. The remaining four curves (30 nm–60 nm silver thickness) show the excitation of an SPP. This is evident by the clear minima present in their reflectivities located between 45° and 46°. The quality of the excitation can be deduced from the sharpness and depth of the minima. For the above-described system, excited at 514.5 nm, the optimum silver thickness is approximately 50 nm. These results imply that the optimum angle is influenced by the excitation wavelengths, the wavelength-dependent optical constants, and the thickness of the individual layers. This provides an explanation for the highly delicate and extremely sensitive nature of surface plasmon resonance (SPR). In order to fulfill the dispersion relation, only the parallel component k_{par} of the incoming photons can satisfy the inherent conditions of this relation. Therefore, one prerequisite is the sole usage of linearly po-

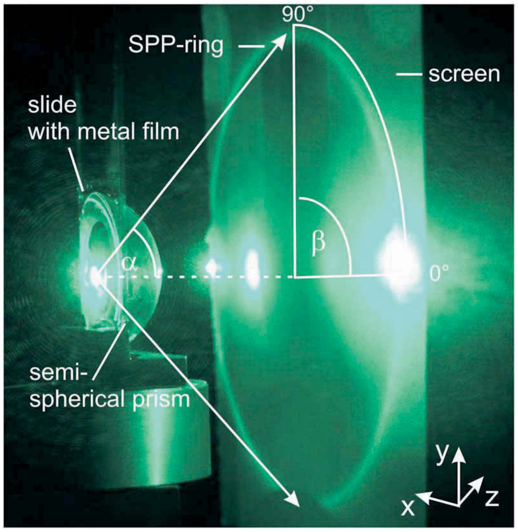

FIG. 4. (Color online) Projection of the ATR cone on a screen.

larized photons within the plane of incidence. The focus of this Brief Report is to analyze the polarization of the light, reemitted directly by the SPP into the ATR cone. An article on the polarization dependence of SPP excited fluorescent emissions (SPCE) has been published by Gryczynski *et al.*[2] An image of the projection of the ATR cone from a semispherical prism onto a screen is depicted in Fig. 4.

Due to the symmetry properties of the ATR ring evident in the above image, it is sufficient to confine our analysis to a quarter of the actual ATR ring. Furthermore, it is advantageous to use a reversed gray-scale image in order to show the distribution of light on the projection screen. Please refer also to the notation of the polarization as shown in Fig. 5.

In Fig. 6 a full set of ten measurements is displayed, where the polarization analyzer has been changed from 0° to 90° in consecutive steps of 10°. The light responsible for the excitation and the nonscattered, total reflected light are linearly polarized at 0°.

The result of the analysis is summarized in Fig. 7. It definitively shows that the polarization of the emitted light is not in accordance with the SPP exciting photons, but changes with its origin on the ATR ring. More precisely, the polarization of the light is always perpendicular to the tangent of the ATR ring at this coordinates.

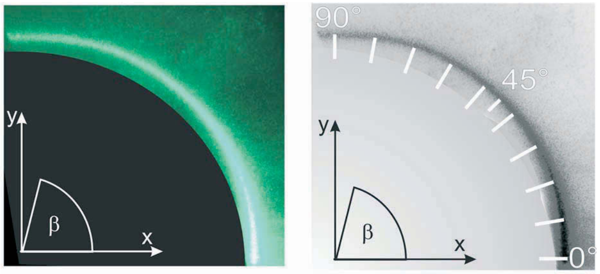

FIG. 5. (Color online) Left: Upper right quarter of the projected ATR cone. Right: Notation of the polarization on an inverted gray-scale image.

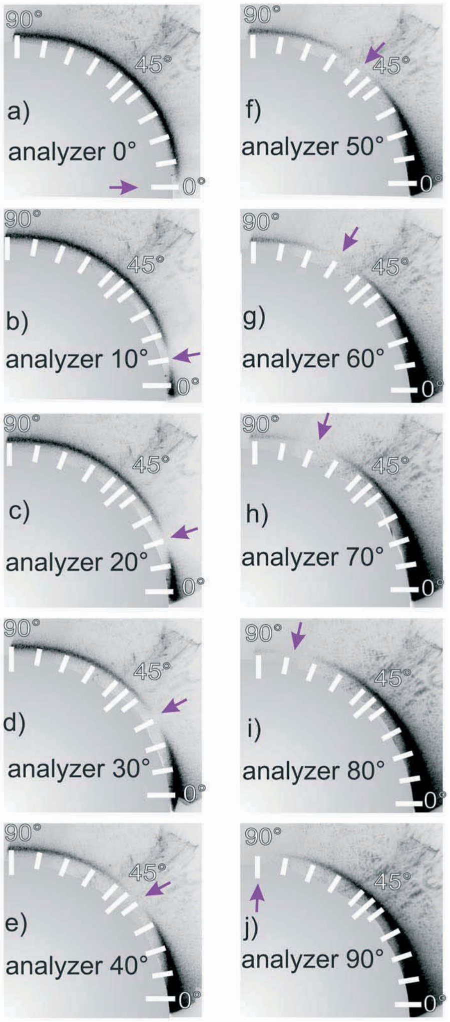

FIG. 6. (Color online) Behavior of the polarization within the ATR ring. The arrows denote the positions of the intensity minima, respectively.

IV. CONCLUSION

The way the orientation of the light vector changes sheds light on the origin of the effect. While a mere reflection would conserve the polarization of light, the changes are clearly due to the effects of the SPP. Following the

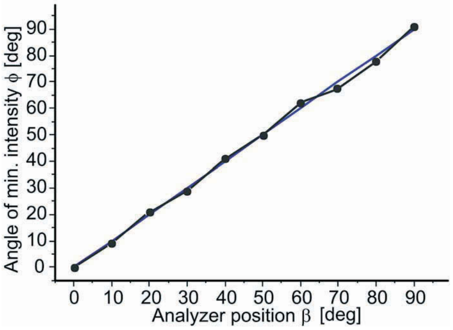

FIG. 7. (Color online) Polarization vs position.

transformation of light into an electron density wave, these propagating electrons are scattered at the imperfections of the metal surface. This changes the direction of propagation. Upon retransformation of the surface plasmon polariton wave into photons, these are emitted with a well-defined angle in the plane between the surface normal and the new electron propagation direction according to the SPP conditions. In order to obey the SPP dispersion relation which has to be valid for the excitation as well as for the deexcitation of the surface plasmon, the polarization of the reemitted light has to be parallel to the above-mentioned new plane and therefore results in the observed effect.

---

*Electronic address: dominic.zerulla@ucd.ie

[1] K. Kneipp, Y. Wang, H. Kneipp, L. T. Perelman, I. Itzkan, R. R. Dasari, and M. S. Feld, Phys. Rev. Lett. **78**, 1667 (1997).

[2] I. Gryczynski, J. Malicka, K. Nowaczyk, Z. Gryczynski, and J. R. Lakowicz, J. Phys. Chem. B **108**, 12073 (2004).

[3] J. R. Lakowicz, Y. Shen, S. D'Auria, J. Malicka, J. Fang, Z. Gryczynski, and I. Gryczynski, Anal. Biochem. **301**, 261 (2002).

[4] J. R. Lakowicz, Anal. Biochem. **324**, 153 (2004).

[5] I. Gryczynski, J. Malicka, Z. Gryczynski, and J. R. Lakowicz, Anal. Biochem. **324**, 170182 (2004).

[6] A. P. Hibbins, B. R. Evans, and J. R. Sambles, Science **308**, 670 (2005).

[7] D. Zerulla, G. Isfort, M. Kölbach, A. Otto, K. Schierbaum, Electrochim. Acta **48**, 2943 (2003).

[8] J.-N. Lin and C. J. Wilson, U.S. Patent No. 5,776,785 (1998-07-07).

[9] J. Malicka, I. Gryczynski, and J. R. Lakowicz, J. Biomol. Screening **9**, 208 (2004).

[10] S. I. Bozhevolnyi, V. S. Volkov, E. Deveaux, J. Y. Laluet, and T. W. Ebbesen, Nature (London) **440**, 508 (2006).

[11] W. L. Barnes, A. Dereux, and T. W. Ebbesen, Nature (London) **424**, 824 (2003).

[12] E. Kretschmann and H. Raether, Z. Naturforsch. A **23**, 2135 (1968).

[13] A. Otto, Z. Phys. **216**, 398 (1968).

[14] H. Raether, *Surface Plasmons* (Springer-Verlag, Berlin, 1988), Vol. 111.

[15] G. Isfort, K. Schierbaum, and D. Zerulla, Phys. Rev. B **73**, 033408 (2006).

[16] R. G. Llamas and L. E. Regalado, Opt. Commun. **142**, 167 (1997).

[17] E. Fontana and R. H. Pantell, Phys. Rev. B **37**(7), 3164 (1988).

[18] G. Isfort, Ph.D. thesis, Universität Düsseldorf, 2005.

[19] E. D. Palik, *Handbook of Optical Properties of Solids* (Academic Press, Orlando, FL, 1985).

[20] C. E. Reed, J. Giergiel, J. C. Hemminger, and S. Ushioda, Phys. Rev. B **36**, 4990 (1987).

PHYSICAL REVIEW B **76**, 085420 (2007)

Tunable nanowires: An additional degree of freedom in plasmonics

Stephanie Rehwald,[1,2] Michael Berndt,[1,2] Frank Katzenberg,[3] Stephan Schwieger,[4] Erich Runge,[4]
Klaus Schierbaum,[2] and Dominic Zerulla[1]
[1]*School of Physics, University College Dublin (UCD), Science Center North, Dublin 4, Ireland*
[2]*IPkM, Heinrich-Heine-Universität Düsseldorf, D-40225 Düsseldorf, Germany*
[3]*FB Bio- und Chemieingenieurwesen, Universität Dortmund, D-44227 Dortmund, Germany*
[4]*Theoretische Physik I, Technische Universität Ilmenau, D-98684 Ilmenau, Germany*

(Received 14 June 2007; published 17 August 2007)

We report on the excitation of surface plasmon polaritons (SPP's) on a periodic arrangement of metallic ribbons with tunable periodicity. The ability to vary its lattice constant results in an additional degree of freedom, permitting excitation of SPP's for any combination of wavelength and angle of incidence within the tuning range of the system. Moreover, the designed smart material allows fundamental questions to be answered regarding SPP propagation and localization. Finally, the concept opens vistas in the development of other methodologies in spectroscopy including plasmonic sensors and chips.

DOI: 10.1103/PhysRevB.76.085420 PACS number(s): 73.20.Mf, 73.63.Nm

I. INTRODUCTION

Planar waveguides and photonic crystal structures are being intensively investigated as key components for future integrated photonic devices. However, there may be an alternative approach to the manufacturing of highly integrated optical devices with structural elements smaller than the wavelength, which, nevertheless, enables strong guidance and manipulation of light—the use of metallic and metallodielectric nanostructures in conjunction with surface plasmon polaritons (SPP's). They are now considered as possibly "the next big step" in nanotechnology. Here, we present a device that allows freedom to choose the properties of excited SPP's to a certain degree at will. It is based on a smart, adaptive material which consists of a periodic arrangement of metallic, ribbonlike wires on a tunable polymer substrate, which allows tuning the periodicity of this structure over a wide range.

SPP's are mixed states of photons and electron density waves which propagate along the surface of a conductor. Their favorable properties allow strong guidance and manipulation of light on very small scales. This has led to a new branch of photonics called plasmonics.[1] Today SPP's are already playing an important role in the fundamental understanding of quantum behavior at nano- and mesoscales,[2–6] in subwavelength optics,[7] as well as in the development of ultra-surface-sensitive techniques like surface plasmon resonance,[8,9] and surface enhanced Raman scattering.[10]

Conventionally, SPP's are excited using an attenuated total reflection setup[11,12] or modulated metal surfaces with a fixed geometry.[11,13–17] Considering the latter case, the SPP excitation condition $k_{xl}^{light}(\omega)=k_x^{SPP}(\omega)$ can be approximated for a metal/air interface with a periodic modulation (periodicity d) by

$$\frac{\omega}{c}\sin(\alpha_{inc})+l\frac{2\pi}{d}\overset{!}{=}\frac{\omega}{c}\sqrt{\frac{\epsilon_m}{\epsilon_m+1}}, \qquad (1)$$

where ϵ_m is the real part of the metallic dielectric constant, c is the vacuum velocity of light, α_{inc} is the polar angle of incidence, ω is the angular frequency, and l is an integer characterizing the diffraction order of the light in the periodic structure. Henceforth, an SPP which is excited using the lth diffraction order will be referred to as lth order SPP. The corresponding angle $\alpha_{inc}=\alpha_{SPP}$ will be called the resonance angle (of the lth order). Unfortunately, setups with fixed geometry confine and limit the experiment to a unique combination of frequency and incidence angle of the exciting light [see Eq. (1)]. In addition, for any given excitation frequency and angle, the properties of the SPP (as, e.g., its lifetime) are determined unambiguously.

These severe limitations are overcome by tunable gratings demonstrated in the present work. Tunable gratings not only allow selection of the incidence angle at will (e.g., normal incidence) but (as will be shown below) also give the freedom to tailor SPP properties such as group velocity and lifetime. Thus they give the possibility to isolate and study, e.g., ultraslow plasmons or to produce ultradispersive gratings[18] for a desired wavelength range. The tunable gratings consist of metallic wires separated by slits with adjustable width. Therefore, they can further be used to address fundamental questions connected with the transition of a propagating SPP excitation to a set of interacting but localized particle-plasmon excitations. Additionally, the geometry dependence of the plasmon-light coupling strength, (i.e., details of the SPP formation) can be studied systematically. In this paper, we want to present the proof of principle of such a device and show its impact on fundamental physics by comparing measurements and numerical simulations of SPP's on such systems.

II. TUNABLE SMART MATERIALS

The synthesis of the desired tunable structures is a multistep procedure described in great detail in Ref. 19. In brief, polydimethyl siloxane (PDMS) is cast to an approximately 1 mm thick rubber film. A uniaxial strain is then applied to the sample while an argon plasma truncates and cross-links the upper surface of the film. This leads, due to the fragmentation of macromolecular segments and renewed cross-linking, to relaxation processes in this thin surface region. After the strain is removed, the lower nonrelaxed part of the sample shrinks and causes compressive stress to the upper

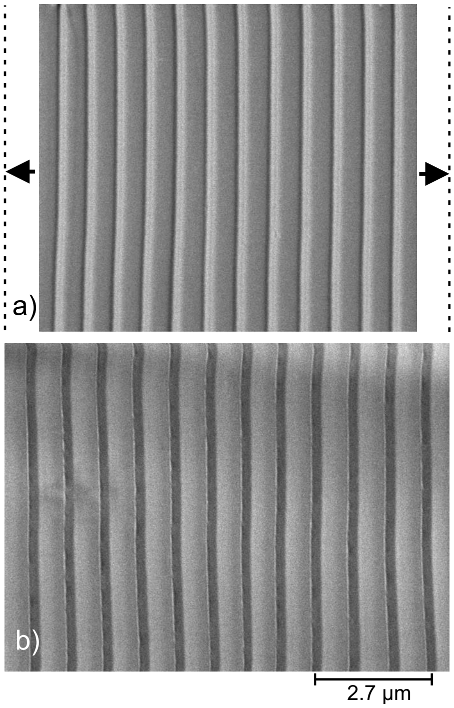

FIG. 1. Scanning electron micrograph of a silver coated periodic polymer structure with average silver thickness of 50 nm: (a) unstretched, periodicity 750 nm; (b) 20% stretched, periodicity 900 nm.

relaxed part. This produces sinusoidal ripples at the surface in order to compensate for the consequent length differences between the two layers. The sinusoidal profile is subsequently silver coated at an oblique angle of typically 45° in the plane perpendicular to the grooves, which results in a thickness modulated silver film at the surface. A scanning electron micrograph of such a surface is shown in (Fig. 1(a)).

Reapplication of strain leads to fractures along the thin metal regions parallel to the grooves. Such a film stretched by 20% is shown in Fig. 1(b). After an initial strain, a threshold is surpassed and, consequently, all the grooves break and the resulting metallic ribbonlike structures are almost perfectly aligned parallel to each other. The spacing, and hence fundamental periodicity of the grating, depends linearly on the applied strain. This was checked locally in the laser spot, as will be explained below. The separation of the metallic wires can be reversibly adjusted, thus allowing for dynamical changes in the grating constant. The initial value of the grating depends on the chosen PDMS, the stretching prior to the argon plasma treatment, and the plasma parameters. This procedure so far allows periodicities between 350 nm and 2 μm, while the separation can be fine tuned from 0 to above 50% of the initial periodicity.

III. TUNABLE SURFACE PLASMON EXCITATION

The silver/PDMS wire grating is used to demonstrate the tunability of the SPP resonance. As a first proof of principle, angle-dependent reflectivities for s and p polarizations have been recorded as a function of incidence angle α_{inc}. The light source used was a He-Ne laser ($\lambda_0=632.8$ nm). Figure 2(a) shows the reflectivities detected in the -1st diffraction order of an unstretched grating: the s-polarized curve does not show any minima, while the p-polarized curve has two pronounced minima at 15° and 36°. Note that only p-polarized light, with its polarization direction perpendicular to the wires, can excite SPP's. Therefore, we can conclude that these minima are caused by SPP's which extract energy from the propagating modes (light). The minima are found at the resonance angles, predicted by Eq. (1) for the 1st and -2nd order ($l=1, l=-2$) ($\epsilon_M=-15.87+1.08i$). Having demonstrated SPP excitation, the next important step is to prove the promised tunability. Figure 3(a) shows reflectivity measurements for six different grating periods ranging from the unstretched sample to about 7% prolongation. The grating periods have been determined independently by using diffraction techniques (locally in the laser spot) and have additionally been verified by scanning electron micrographs. The two minima of the 1st and -2nd order plasmons are clearly visible in each case. Their positions coincide reasonably well with the predictions of Eq. (1). Almost perfect agreement is obtained for the slightly modified estimation described below. In summary, we have shown that the elastic silver wire/PDMS grating is, indeed, a tunable SPP system.

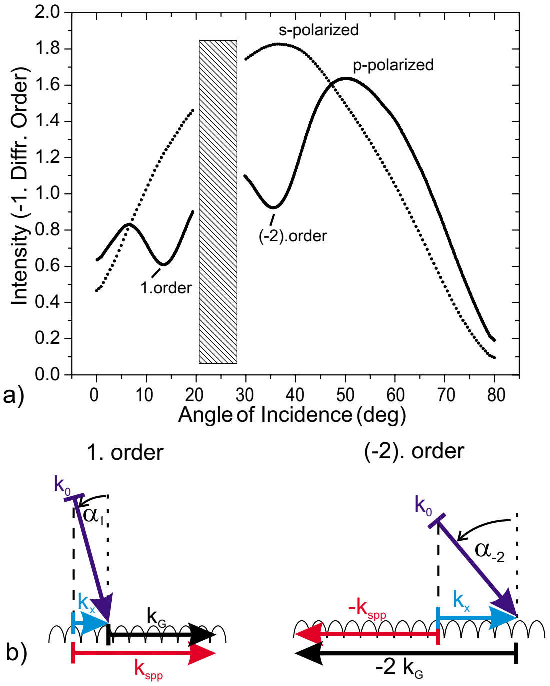

FIG. 2. (Color online) (a) Scan of the intensity of the −1 diffraction order versus angle of incidence of s-polarized and p-polarized light. Lattice constant is fixed at 780 nm. The experimental setup does not allow measurements in the shaded area. (b) **k**-vector diagram of the SPP excitation: 1st order (left) and −2nd order (right).

IV. PROPAGATION AND LOCALIZATION OF SURFACE PLASMON POLARITONS

The focus up to now was the possibility of tuning SPP resonance angles via the grating period. However, the poly-

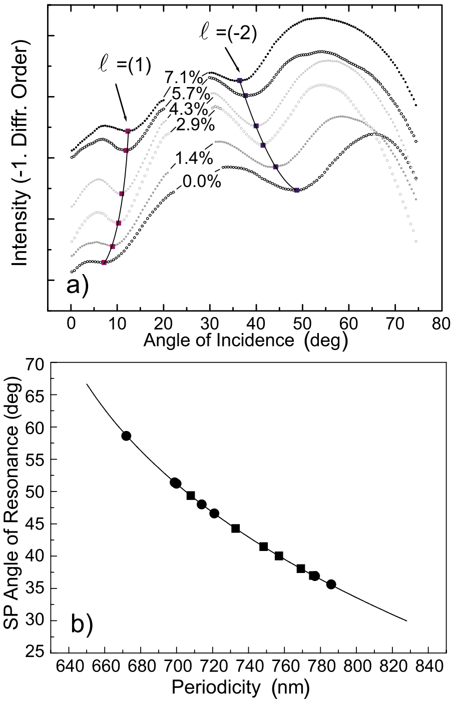

FIG. 3. (Color online) (a) Angular scan of the reflectivity of the tunable system for six different lattice constants, recorded for the −1 diffractive order. (b) Development for the (−2) plasmonic order. The solid line represents a prediction of the plasmon excitation, which proves to be accurate within the limits of the experimental errors; squares show data taken from (a), circles from additional measurements.

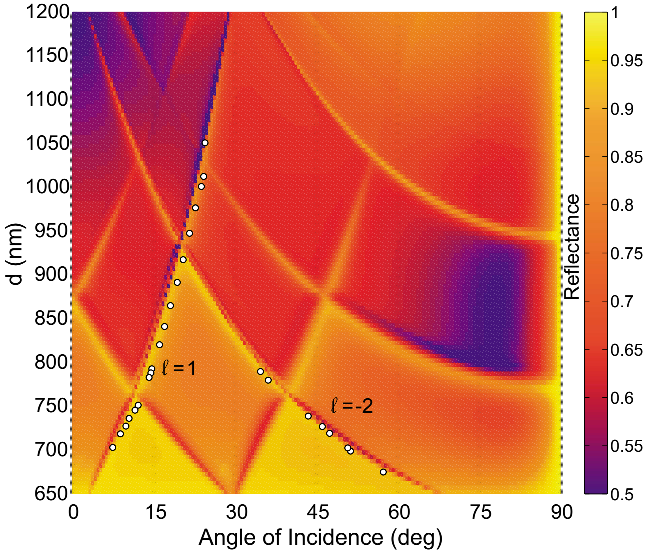

FIG. 4. (Color online) Simulation of the specular reflection of a tunable PDMS based grating with initial periodicity of 640 nm and 40 nm silver thickness. The excitation wavelength is 632.8 nm. The dots indicate the experimentally measured SPP excitations from three different samples.

mer matrix based metallic wire arrays also allow the study of fundamental questions related to the propagation and localization of SPP's during the transition from a cohesive metallic surface with periodic corrugation to an array of separated silver wires with adjustable distance. Of particular interest is whether the properties of the SPP's can be described by the response of individual wires or whether collective effects involving all wires play the major role. The latter picture underlies the SPP excitation condition given in Eq. (1). However, this equation only defines the possible resonance angles but does not predict the actual magnitude and sharpness of the SPP resonances.

The width and depth of the SPP resonance are mainly determined by the coupling of the SPP to the radiation field. This coupling increases with the spatial variation of the dielectric constant ϵ along the SPP propagation direction.[20,21] It is proportional to the ratio of the spacing between the wires and the period of the grating. Thus, larger slits are expected to cause deeper and broader minima. This trend is, indeed, corroborated by our data, namely by the increasing depth of the minima for stretching up to about 5% [see Fig. 3(a)]. A localization of the plasmon excitation is expected for very large slit widths. This would cause clear deviations from the resonance conditions which are, however, not found in our experiment. We conclude that SPP localization does not occur for the investigated range of wire spacings.

The dependence of the measured minima positions on the grating constant d can be understood in a rather simple picture: To account for the finite slit width, the dielectric constant of the metal ϵ_m is replaced by a spatially averaged effective dielectric constant ϵ_{av} (which depends on the dielectric constants of the metal and the polymer, and on the period to slit width ratio) in Eq. (1). Figure 3(b) shows that this yields a remarkably good description.

However, this approach is not sufficient to describe details such as the SPP lifetime as a function of the slit width and the period. Consequently, we have performed simulations of metal wires with variable polymer slits between them using a theory developed by Lochbihler and Depine,[22] which is applicable provided that the conductivity of the metal is very high. Above and below the grating, the electromagnetic field is expanded in plane waves. The metallic character of the wire surface is accounted for by the surface impedance boundary conditions. Within the slits, the field is expanded in slit eigenmodes. The continuity conditions at the grating interfaces determine the field amplitudes and, finally, via Maxwell equations, the electric and magnetic fields above or below the grating. Note that the finite slit width, finite height of the grating, and the dielectric constants of the different media (air and PDMS) at both sides of the grating are taken into account explicitly.

Figure 4 shows calculated specular reflectance for systems with an initial periodicity of 640 nm and stretching up to 1200 nm. A rich SPP "band structure" $d(\alpha_{inc})$ and the formation of gaps in the vicinity of crossings of two respective plasmon modes can be seen. The calculations can be compared directly with the resonance angle measurements, which have been added to Fig. 4 as black dots. Theory and experiment agree within the experimental error, so that we may conclude that our variable spacing system is fully predictable and, therefore, permits the excitation of SPP's for any given wavelength within the tuning range of the system.

Combining theory and experiment opens the possibility to excite and investigate SPP's with special, selected properties.

V. CONCLUSION

This paper clearly shows that excitations of SPP's in different orders can be achieved on the described tunable, smart materials made from metal-coated polymer substrates. Our design allows for the fine control of the lattice constant by simple mechanical means. It was shown that we can adjust the angle of incidence for SPP excitation continuously. This allows one to choose a special point in the band structure $d(\alpha_{inc})$ to excite SPP's and, therefore, to select SPP's with certain desired properties. We have performed simulations that predict SPP properties such as lifetime, group velocity, and emission characteristics at certain combinations of the grating period and the angle of incidence. Combining theory and experiments on tunable lattices allows the potential to study fundamental questions concerning the light-plasmon coupling (i.e., SPP formation) as well as basic properties of SPP's on periodic structures. We found, that simulations compare very well with resonance angle measurements, which is the precondition for subsequent, more detailed investigations.

On a separate viewpoint, the presented tunable systems allow for the design of previously unknown types of spectroscopic methods. The ability to tune the wavelength of the exciting photons while maintaining SPP excitation results in extreme surface sensitive and selective variants of major techniques. The spatial confinement of the generated optical near field and the SPP sensitivity are further arguments along this line. Due to the inexpensive production of the tunable chips, they can also be targeted for a mass production market, for example, in the life sciences.

ACKNOWLEDGMENTS

The authors thank Gillian Doyle and Brian Ashall for their assistance in the preparation of this manuscript.

---

[1] I. Gryczynski, J. Malicka, K. Nowaczyk, Z. Gryczynski, and J. R. Lakowicz, J. Phys. Chem. B **108**, 12073 (2004).

[2] A. P. Hibbins, B. R. Evans, and J. R. Sambles, Science **308**, 670 (2005).

[3] P. Andrew and W. L. Barnes, Science **306**, 1002 (2004).

[4] S. I. Bozhevolnyi, V. S. Volkov, E. Deveaux, J. Y. Laluet, and T. W. Ebbesen, Nature (London) **440**, 508 (2006).

[5] G. Isfort, K. Schierbaum, and D. Zerulla, Phys. Rev. B **73**, 033408 (2006).

[6] G. Isfort, K. Schierbaum, and D. Zerulla, Phys. Rev. B **74**, 033404 (2006).

[7] W. L. Barnes, A. Dereux, and T. W. Ebbesen, Nature (London) **424**, 824 (2003).

[8] D. Zerulla, G. Isfort, M. Kölbach, A. Otto, and K. Schierbaum, Electrochim. Acta **48**, 2943 (2004).

[9] E. Ozbay, Science **311**, 189 (2006).

[10] K. Kneipp, Y. Wang, H. Kneipp, L. T. Perelman, I. Itzkan, R. R. Dasari, and M. S. Feld, Phys. Rev. Lett. **78**, 1667 (1997).

[11] E. K. Kretschmann and H. Z. Raether, Z. Naturforsch. A **23A**, 2135 (1968).

[12] A. Otto, Z. Phys. **216**, 398 (1968).

[13] U. Fano, J. Opt. Soc. Am. **31**, 213 (1941).

[14] G. Schider, J. R. Krenn, A. Hohenau, H. Ditlbacher, A. Leitner, F. R. Aussenegg, W. L. Schaich, I. Puscasu, B. Monacelli, and G. Boreman, Phys. Rev. B **68**, 155427 (2003).

[15] M. B. Sobnack, W. C. Tan, N. P. Wanstall, T. W. Preist, and J. R. Sambles, Phys. Rev. Lett. **80**, 5667 (1998).

[16] R. A. Watts, T. W. Preist, and J. R. Sambles, Phys. Rev. Lett. **79**, 3978 (1997).

[17] K. Wang and D. M. Mittleman, Phys. Rev. Lett. **96**, 157401 (2006).

[18] V. Mikhailov, J. Elliot, G. Wurtz, P. Bayvel, and A. V. Zayats, arXiv:cond-mat/0509222 (unpublished).

[19] F. Katzenberg, Nanotechnology **14**, 1019 (2003).

[20] C. Ropers, D. J. Park, G. Stibenz, G. Steinmeyer, J. Kim, D. S. Kim, and C. Lienau, Phys. Rev. Lett. **94**, 113901 (2005).

[21] K. G. Lee and Q. Han Park, Phys. Rev. Lett. **95**, 103902 (2005).

[22] H. Lochbihler and R. Depine, Appl. Opt. **32**, 3459 (1993).